

Composition tuning microstructure and magnetic properties of High Entropy Alloys and MnNiSi-based compounds

Bruno G. F. Eggert

Supervisors:
Bjørn C. Hauback
Helmer Fjellvåg
Christoph Frommen

Department of Chemistry
Faculty of Mathematics and Natural Sciences

© **Bruno G. F. Eggert, 2024**

*Series of dissertations submitted to the
Faculty of Mathematics and Natural Sciences, University of Oslo
No. 2715*

ISSN 1501-7710

All rights reserved. No part of this publication may be
reproduced or transmitted, in any form or by any means, without permission.

Cover: UiO.

Print production: Graphic center, University of Oslo.

Preface

This thesis is submitted in partial fulfillment of the requirements for the degree of *Philosophiae Doctor* at the University of Oslo. The research presented here was conducted at the Institute for Energy Technology and University of Oslo, under the supervision of Professor Bjørn Christian Hauback, Professor Helmer Fjellvåg and Dr. Christoph Frommen. Their insightful assistance and support have assisted me during the last years. For that, I am really grateful.

The work was partially performed at the Institute for Energy Technology and a couple of central facilities, like the European Synchrotron Radiation Facility (ESRF) and the Paul Scherrer Institute (PSI). This work was supported by the HI-ENTROPY project, part of the NANO2021 programme funded by Norwegian Research Council (grant 287150).

It is necessary to acknowledge people that greatly assisted in discussions, modeling and/or characterization efforts: **Erna** at Uppsala, **Christian** at DTU in Lyngby, **Fernando** at TUD in Darmstadt, **João** at IFIMUP in Porto, **Øystein** at PSI in Villigen, **Susmit** at UiO in Oslo, and **Valmir** at IFE. Thank you for all the assistance.

Also, special thanks to my **my parents**, and my wife **Camila** for encouraging me through this whole journey. You cheered me up when I doubted myself, and never hesitated in showing your support for my decision, even if it meant being a continent away from home. I really appreciate all you have done.

Preface

Abstract

This thesis is concerned with the synthesis and characterization of novel magnetocaloric materials. FeCoNi-based High Entropy Alloys (HEAs) have been evaluated, where all atoms occupy the same crystallographic site in metallic solid solutions. When producing FeCoNi-based solid solutions, alloys with a high magnetization can be obtained. If alloyed with antiferromagnetic elements, the resulting product may feature magnetic ordering transition temperatures at room temperature, a requirement for room temperature magnetocaloric materials. This will only translate to a large magnetocaloric effect if an abrupt change in magnetization as a function of temperature is achieved. Considering the nearly endless compositional space, a magnetocaloric HEA may be designed to display such features. While Mn and Cr have already been studied, Vanadium (V) has not been explored as an alloying element in FeCoNi-based solid solutions for magnetocaloric applications.

To explore magnetocaloric V-containing HEAs, VFeCoNi(Al/Cu) solid solutions were synthesized by arc melting, and studied in this metastable state. These compositions were chosen as they meet a series of HEA literature parameters to yield solid solutions. The produced equiatomic alloys have transitions below room temperature, so nonequiatomic compositions were produced with reduced V contents, resulting in $V_{1-x}\text{FeCoNi(Al)}_{1+x}$ ($x= 0.2$ to 0.75) and $V_{1-y}\text{FeCoNi(Cu)}_{1+y}$ ($y= 0.15$ to 0.75) keeping the ferromagnetic element content intact. The magnetic results showcase the possibility of increasing the magnetic transition temperatures of the studied solid solutions with decreasing V contents, from 150/200 K to over 400 K within the specified composition ranges. The evaluated absolute isothermal entropy change of 0.15 J/kg.K for a 0 to 1 Tesla magnetic field variation in $V_{0.85}\text{FeCoNiCu}_{1.15}$ is comparable to Cr and Mn-based HEAs, but low when compared to common magnetocaloric materials.

The cause of such performance was further evaluated through subsequent synthesis of FeCoNi solid solutions with V and Cu. The results stress the strong effect of disorder in broadening the magnetic transition, and the effect of V to decrease magnetic transition temperatures and magnetization values. Still, the use of Cu as a dilutant to the ferromagnetic exchange interactions has increased the abruptness of the magnetic transition while keeping low transition temperatures.

The second group of novel magnetocaloric materials studied in this thesis were MnNiSi-based compounds. They are intermetallics with ordered transition metal (Mn,Ni) and p-block (Si) sites. By convenient Fe and Al modifications, an abrupt magnetization variation as a function of temperature can be achieved in coupled magnetic and structural transitions. The properties of $\text{Mn}_{1-w}\text{Ni}_{1-w}\text{Fe}_{2w}\text{Si}_{0.95}\text{Al}_{0.05}$ compounds where $w=0.28$ to 0.35 were evaluated. The simultaneous substitution of both transition metal sites by Fe imposes a large magnetic transition temperature variation of over 200 K, from 420 K in $w=0.28$ to 215 K in 0.35 . The absolute isothermal entropy change of 4.2 J/kg.K for a 0 to 1 Tesla magnetic field variation in $\text{Mn}_{0.7}\text{Ni}_{0.7}\text{Fe}_{0.6}\text{Si}_{0.95}\text{Al}_{0.05}$ is larger than the studied V-containing HEAs, and similar to other MnNiSi-based compounds with no critical elements as constituents.

The structural and magnetic properties of $\text{MnNiSi}_{0.95}\text{Al}_{0.05}$ with Fe substitutions on Mn and Ni sites were also compared with MnNiSi compounds with substitutions on Mn sites. Macroscopic magnetic measurements as well as powder neutron diffraction experiments and density functional theory calculations evidence a larger total magnetic moment in $\text{Mn}_{1-w}\text{Ni}_{1-w}\text{Fe}_{2w}\text{Si}_{0.95}\text{Al}_{0.05}$ compounds than in $\text{Mn}_{1-z}\text{Fe}_z\text{NiSi}_{0.95}\text{Al}_{0.05}$. However, in this comparison, different degrees of local disorder impact the magnetostructural transition, and hint at a better magnetocaloric effect in the latter composition. To alter the degree of disorder, different heat treatments can be explored to modify the abruptness of the magnetic transition. Two different heat treatments were then compared in $\text{Mn}_{1-w}\text{Ni}_{1-w}\text{Fe}_{2w}\text{Si}_{0.95}\text{Al}_{0.05}$ compounds.

The introduction of a short high-temperature step accounting for less than 3 % of the regular heat treatment period led to substantial changes in the compounds, specially in crystallite/grain morphology and magnetic properties. The combined effect of these changes increased the isothermal entropy change up to 7.2 J/kg.K for a 0 to 1 Tesla magnetic field change.

Sammendrag

Denne avhandlingen handler om syntese og karakterisering av nye magnetokaloriske materialer. FeCoNi-baserte høyentropi-legeringer (HEL-er) er evaluert, der alle atomene okkuperer samme krystallografiske sted i metalliske faste løsninger. Når FeCoNi-baserte faste løsninger produseres, kan legeringer med høy magnetisering oppnås. Hvis de legeres med antiferromagnetiske elementer, kan det resulterende produktet ha magnetisk ordensovergangstemperatur ved romtemperatur, en nødvendighet for romtemperatur magnetokaloriske materialer. Dette vil kun gi en stor magnetokalorisk effekt hvis en brå endring i magnetisering som funksjon av temperatur oppnås. Med tanke på den nesten uendelige sammensetningsrommet kan en magnetokalorisk HEL skreddersys til å oppnå slike egenskaper. Mens Mn og Cr allerede har blitt studert, har ikke Vanadium (V) blitt utforsket som et legeringselement i FeCoNi-baserte faste løsninger for magnetokaloriske anvendelser.

For å utforske magnetokaloriske V-inneholdende HEL-er, ble faste løsninger av $V\text{FeCoNi}(\text{Al}/\text{Cu})$ syntetisert ved lysbuesmelting og studert i denne metastabile tilstanden. Disse sammensetningene ble valgt da de oppfyller en rekke parametere fra HEL-litteraturen for å danne faste løsninger. De produserte likeatomære-legeringene har overganger under romtemperatur, så likeatomære sammensetninger ble produsert med redusert V-innhold, noe som resulterer i $V_{1-x}\text{FeCoNi}(\text{Al})_{1+x}$ ($x=0.2$ til 0.75) og $V_{1-y}\text{FeCoNi}(\text{Cu})_{1+y}$ ($y=0.15$ til 0.75) mens innholdet av ferromagnetisk element holdes intakt. De magnetiske resultatene viser muligheten for å øke de magnetiske overgangstemperaturene til de studerte faste løsningene ved å redusere V-innholdet, fra 150/200 K til over 400 K innenfor de angitte sammensetningsområdene. Den vurderte absolutte isoterme entropiendringen på $0.15 \text{ J/kg} \cdot \text{K}$ for en magnetisk feltvariasjon på 0 til 1 Tesla i $V_{0.85}\text{FeCoNiCu}_{1.15}$ er sammenlignbar med Cr- og Mn-baserte HEL-er, men lav sammenlignet med vanlige magnetokaloriske materialer.

Årsaken til en slik ytelse ble videre evaluert gjennom påfølgende syntese av FeCoNi-faste løsninger med V og Cu. Resultatene understreker den sterke effekten av uorden som utvider den magnetiske overgangen, og effekten av V på å redusere magnetiske overgangstemperaturer og magnetiseringsverdier. Bruken av Cu som en fortyner til de ferromagnetiske utvekslingsinteraksjonene økt bråheten til den

magnetiske overgangen samtidig som lave overgangstemperaturer opprettholdes.

Den andre gruppen av nye magnetokaloriske materialer som ble studert i denne avhandlingen, var MnNiSi-baserte forbindelser. De er intermetalliske forbindelser med ordnede overgangsmetall (Mn, Ni) og p-blokk (Si) steder. Ved hjelp av praktiske Fe- og Al-modifikasjoner kan en brå endring i magnetisering som funksjon av temperatur oppnås i sammenkoblede magnetiske og strukturelle overganger. Egenskapene til $\text{Mn}_{1-w}\text{Ni}_{1-w}\text{Fe}_{2w}\text{Si}_{0.95}\text{Al}_{0.05}$ forbindelser der $w=0.28$ til 0.35 ble evaluert. Den samtidige substitusjonen av begge overgangsmetall-stedene med Fe pålegger en stor variasjon i magnetisk overgangstemperatur på over 200 K, fra 420 K ved $w=0.28$ til 215 K ved 0.35 . Den absolutte isoterme entropiendringen på $4.2 \text{ J/kg} \cdot \text{K}$ for en magnetisk feltvariasjon på 0 til 1 Tesla i $\text{Mn}_{0.7}\text{Ni}_{0.7}\text{Fe}_{0.6}\text{Si}_{0.95}\text{Al}_{0.05}$ er større enn de studerte V-inneholdende HEL-ene og lik andre MnNiSi-baserte forbindelser uten kritiske elementer som bestanddeler.

De strukturelle og magnetiske egenskapene til $\text{MnNiSi}_{0.95}\text{Al}_{0.05}$ med Fe-substitusjoner på Mn- og Ni-steder ble også sammenlignet med MnNiSi-forbindelser med substitusjoner på Mn-steder. Makroskopiske magnetiske målinger, samt pulvernøytron-diffraksjonseksperimenter og tetthetsfunksjonelle teoriberegninger, viser et større totalt magnetisk moment i $\text{Mn}_{1-w}\text{Ni}_{1-w}\text{Fe}_{2w}\text{Si}_{0.95}\text{Al}_{0.05}$ forbindelser enn i $\text{Mn}_{1-z}\text{Fe}_z\text{NiSi}_{0.95}\text{Al}_{0.05}$. Imidlertid påvirker ulike grader av lokal uorden overgangen mellom magnetisk og strukturell tilstand, og antyder en bedre magnetokalorisk effekt i sistnevnte sammensetning. For å endre graden av uorden, kan ulike varmebehandlinger utforskes for å modifisere bråheten til den magnetiske overgangen. To forskjellige varmebehandlinger ble deretter sammenlignet i $\text{Mn}_{1-w}\text{Ni}_{1-w}\text{Fe}_{2w}\text{Si}_{0.95}\text{Al}_{0.05}$ forbindelser.

Innføringen av et kort høyt trinn med temperaturer på mindre enn 3 % av den vanlige varmebehandlingsperioden førte til betydelige endringer i forbindelsene, spesielt i krystallitt-/kornmorfologi og magnetiske egenskaper. Den kombinerte effekten av disse endringene økte den isoterme entropiendringen til $7.2 \text{ J/kg} \cdot \text{K}$ for en magnetisk feltendring på 0 til 1 Tesla.

List of Papers

Paper I

Bruno G. F. Eggert, Erna K. Delczeg-Czirjak, Fernando Maccari, Susmit Kumar, Oliver Gutfleisch, Helmer Fjellvåg, Bjørn C. Hauback, Christoph Frommen 'Exploring V-Fe-Co-Ni-Al and V-Fe-Co-Ni-Cu high entropy alloys for magnetocaloric applications'. In: *Journal of Alloys and Compounds*. Volume 921, (2022), <https://doi.org/10.1016/j.jallcom.2022.166040>.

Paper II

Bruno G. F. Eggert, Erna K. Delczeg-Czirjak, Bjørn C. Hauback, Christoph Frommen 'Magnetic transitions in V-Fe-Co-Ni-Cu-based high entropy alloys'. In *Materials Today Physics*. Volume 35, (2022), <https://doi.org/10.1016/j.mtphys.2023.101116>.

Paper III

Bruno G. F. Eggert, João Horta Belo, João P. Araújo, Bjørn C. Hauback, Christoph Frommen 'Structural transitions and magnetocaloric properties of low-cost MnNiSi-based intermetallics' In: *Intermetallics*. Volume 154, (2022), <https://doi.org/10.1016/j.intermet.2023.107823>

Paper IV

Bruno G. F. Eggert, Erna K. Delczeg-Czirjak, Øystein S. Fjellvåg, Bjørn C. Hauback, Christoph Frommen 'Structure and Magnetism of Fe-substituted MnNiSi_{0.95}Al_{0.05}' *To be submitted*.

Paper V

Bruno G. F. Eggert, Kun Wang, Sina Jafarzadeh, Christian R. Bahl, Bjørn C. Hauback, Christoph Frommen 'Study of the magnetostructural transition in critical-element free Mn_{1-x}Ni_{1-x}Fe_{2x}Si_{0.95}Al_{0.05}' In: *API Advances*. Volume 13, (2023), <https://doi.org/10.1063/9.0000511>

Preface

List of Abbreviations and Acronyms

ΔT_{ad}	Adiabatic temperature change
ΔS_m	Isothermal entropy change
δ	Atomic size difference
bcc	body-centered cubic
BSE	Backscattered Electron Mode - Scanning Electron Microscopy
CALPHAD	Calculation of Phase Diagram
ccp	cubic-close packed
C_P	Heat capacity at constant pressure
DSC	Differential Scanning Calorimeter
<i>i.e.</i>	<i>id est</i> (lat. that is)
FOPT	First Order Phase Transition
HEA	High-Entropy alloy
H_f^{IM}	Enthalpy of formation of intermetallics
H_{mix}^{SS}	Enthalpy of mixing of solid solutions
MEA	Medium-entropy Alloy
PND	Powder Neutron Diffraction
PXD	Powder X-ray Diffraction
R_{wp}	weighted R profile
S_f^{IM}	Entropy of formation of intermetallics
S_{mix}^{SS}	Entropy of mixing of solid solutions
SEM	Scanning Electron Microscopy
SOPT	Second Order Phase Transition
SR-PXD	Synchrotron Radiation Powder X-ray Diffraction
T_C	Curie temperature
T_{hys}	Thermal hysteresis between heating and cooling transitions
T_{str}	Structural transition temperature
T_t	Magnetostructural transition temperature
$T_{t_{o-h}}$	Magnetostructural transition temperature during heating
$T_{t_{h-o}}$	Magnetostructural transition temperature during cooling
VEC	Valence Electron Concentration

Preface

Contents

1	Introduction and motivation	1
1.1	Prospects of heating and cooling of areas and caloric cooling	1
1.2	Magnetocaloric materials	2
1.3	High Entropy Alloys	4
1.4	Magnetocaloric High Entropy Alloys	7
1.5	MM'X-type compounds as magnetocaloric materials	8
1.6	Scope of the work	11
2	Theory and characterization methods	13
2.1	Synthesis and processing of alloys and intermetallics	13
2.2	CALPHAD modeling of equilibrium phase-diagrams	14
2.3	Thermodynamics of phase transitions	14
2.4	Thermal analysis	17
2.4.1	Low temperature commercial DSC	17
2.4.2	High temperature commercial DSC - magnetic balance	18
2.4.3	Custom-built DSC with magnetic field	19
2.5	Ferromagnetism and estimation of magnetic properties by Density Functional Theory	20
2.6	Magnetic characterization methods	22
2.6.1	Field dependent curves	22
2.6.2	Temperature-dependent curves	23
2.6.3	Magnetocaloric property determination and analysis	23
2.7	Powder diffraction	25
2.7.1	Rietveld Analysis	29
2.8	X-ray and Neutron sources	31
2.8.1	Laboratory x-ray diffractometer	31
2.8.2	Synchrotron radiation x-ray	31
2.8.3	Neutron sources	31
2.9	Microstructure observation methods	32
2.9.1	Optical light microscopy	32
2.9.2	Scanning Electron Microscopy and Energy Dispersive X-ray Spectroscopy	32

Contents

3	Paper summary	35
3.1	Exploring V-containing High Entropy Alloys (Paper I)	35
3.2	Magnetic transitions of V-Fe-Co-Ni-Cu-based alloys (Paper II)	37
3.3	MnNiSi-based intermetallics with Fe and Al (Paper III)	39
3.4	Structure and magnetism of Fe-substituted MnNiSi _{0.95} Al _{0.05} (Paper IV)	42
3.5	Study of the magnetostructural transition in critical-element free Mn _{1-w} Ni _{1-w} Fe _{2w} Si _{0.95} Al _{0.05} (Paper V)	44
4	Conclusion	47

I Exploring V-Fe-Co-Ni-Al and V-Fe-Co-Ni-Cu High Entropy Alloys for Magnetocaloric Applications 59

II Magnetic transitions in V-Fe-Co-Ni-Cu-based high entropy alloys 73

III Structural transitions and magnetocaloric properties of low-cost MnNiSi-based intermetallics 85

IV Structure and magnetism of Fe-substituted MnNiSi_{0.95}Al_{0.05} compounds 97

V Study of the magnetostructural transition in critical-element free Mn_{1-x}Ni_{1-x}Fe_{2x}Si_{0.95}Al_{0.05} 119

Chapter 1

Introduction and motivation

1.1 Prospects of heating and cooling of areas and caloric cooling

The technological use of materials is directly linked to the progress of civilization. In recent years, the constant pursuit of progress lead to an accelerated warming of the planet due to anthropogenic causes. A paradigm shift must therefore occur towards renewable energy production. Examples include photovoltaic solar panels and wind turbines, together with other renewable sources.

Besides energy production, energy consumption should also be optimized by using better technologies. As of 2016, around 50 % of household energy in Europe was employed for heating and cooling [1]. Furthermore, future energy demand for cooling technologies is expected to double until 2050 worldwide, according to the estimates of the International Institute of Refrigeration [2].

The most employed regular cooling technologies, based on vapor compression, can feature high efficiencies in large-scale setups, close to 60 % of the second law of thermodynamic efficiencies [3]. In small-scale domestic appliances, however, the efficiencies drop to an average of 20 % of the Carnot cycle, which demonstrates the need for improvement [3]. On top of efficiency issues in small units for air conditioners and refrigerators, typical vapor compression products exploit gaseous hydrofluorocarbon refrigerants. Their use in such cooling technologies is harmful to the environment, being responsible for 7.8 % of the total global greenhouse gas emissions [4]. Therefore, new technologies must aim to improve energy efficiency without negative environmental impact.

Caloric cooling is an alternative concept for heat conversion that can be exploited to heat or cool. The method is based on solid state materials that undergo phase transitions due to different stimuli. Examples include elastocaloric and electrocaloric materials, where heat is generated from the material due to the modification of internal stresses and electric fields, respectively. This leads to an increase in temperature, exemplified in Figure 1.1. This increase in temperature can then be used to extract heat from an area using a fluid such as water, in a cycle analogous to vapor compression [5, 6, 3].

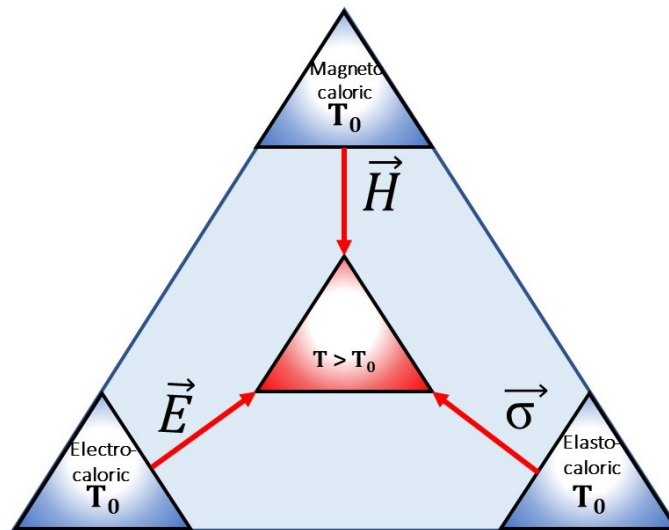


Figure 1.1: Representation of caloric effects induced in electrocaloric, magnetocaloric, and elastocaloric materials, respectively, as different stimuli such as electrical fields (E), stress (σ), and magnetic fields (H) inducing a temperature increase $T > T_0$.

1.2 Magnetocaloric materials

Another alternative for caloric cooling uses magnetic fields as external stimuli, in materials known as magnetocalorics. Large temperature variations happen during magnetization due to an exchange between the magnetic entropy and the lattice and electronic entropy contributions. When a material is magnetized, its magnetic moments align, giving a decrease in magnetic entropy. As a response to this event, the other entropy contributions will be increased, and the temperature of the material is changed [7, 6]. Generally, the larger the degree of alignment of magnetic moments during magnetization, the stronger this variation will be.

A typical representation of a temperature-dependent magnetization in a common magnetocaloric material is shown in Figure 1.2(a). At low temperatures, it is ferromagnetic, with a large magnetization. The magnetization decreases slightly until the vicinity of its magnetic transition temperature T_t , where it decreases rapidly. After reaching T_t , most of the ferromagnetic moment vanishes, becoming a paramagnetic material.

Let us assume that the temperature of the material is just below T_t , seen in point 1 in Figure 1.2(a). If an external magnetic field $H > 0$ is applied, the magnetic fields stabilize the ferromagnetic state. This shifts the hypothetical magnetic transition curve to higher temperatures, see the red dashed line in Figure 1.2(a). Due to the ferromagnetic state being stabilized, the material undergoes a large magnetization change, towards point 2 in the Figure. If this process is performed isothermally, with exchange of heat with the medium, the total entropy curve decreases, exemplified in the vertical black line in Figure 1.2(b). This describes the isothermal entropy change ΔS_m between the two states, and corresponds to the amount of heat that can be transferred for the given magnetic field change. The ΔS_m is a figure of merit in magnetocaloric materials research. It is calculated

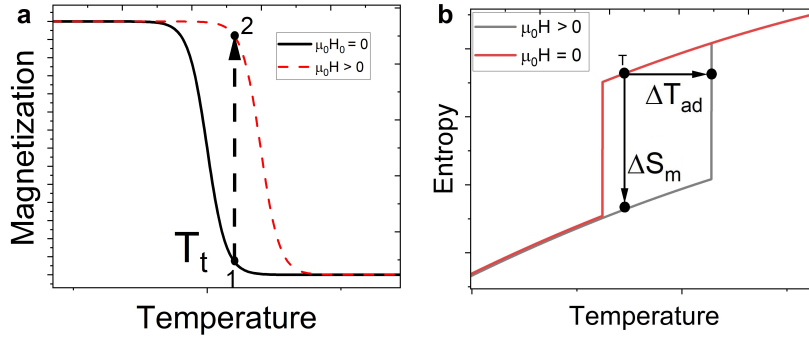


Figure 1.2: (a) Hypothetical magnetization curve of a ferromagnetic material around the magnetic ordering temperature, displaying the abrupt loss of magnetization. The red dashed curve represents the magnetization curve when the material is inside an external field H . (b) Hypothetical entropy curve in the vicinity of a transition temperature T_t with and without the influence of an external magnetic field.

by a numerical integration of a Maxwell relation [5]:

$$\Delta S_m(T, \Delta H) = \mu_0 \int_{H_i}^{H_f} \left(\frac{\partial M(T, H)}{\partial T} \right)_H dH \quad (1.1)$$

where T is the temperature, μ_0 the magnetic permeability, H_i and H_f the initial and final magnetic fields, and M the magnetization.

On the other hand, if the magnetization process is performed adiabatically, i.e., with no exchange of heat with the medium, it induces a temperature change ΔT_{ad} , seen in the horizontal black line in Figure 1.2(b). It is correlated to how fast heat transfer can occur for a magnetic field change, as the induced temperature difference is directly correlated to the heat flux between the material and the medium [8]. ΔT_{ad} is obtained by measuring the temperature before and after in a nearly adiabatic magnetization process, according to the following relation:

$$\Delta T_{ad}(T, \Delta H) = -\mu_0 \int_{H_i}^{H_f} \left(\frac{T}{C_p(T, H)_H} \right) \left(\frac{\partial M(T, H)}{\partial T} \right)_H dH \quad (1.2)$$

where C_p is the heat capacity at constant pressure.

Among the alternative caloric cooling technologies that have been developed for household applications, magnetocaloric cooling/heating technology is the one that has seen the most improvements during the last 25 years [3]. Initially there were demonstrators and test-bench setups [9, 10]. Now, household magnetocaloric heat pumps, wine-coolers, and air conditioning systems have been assessed to replace vapor compression technologies [11, 12, 13, 14]. Most of the initial prototypes used Gd as a magnetocaloric material. This is due to its reasonably high magnetocaloric effect around room temperature. Its ΔT_{ad} amounts to 5.8 K, for a magnetic field change of $\mu_0 H = 0 - 2$ T [15]. Materials such as Gd undergo a second order phase transition (SOPT). This is a continuous decrease of magnetization over temperature. The magnetic transition temperature is thus known as the *Curie* temperature T_C .

The recent study of magnetocaloric materials for room temperature magnetic cooling started with the discovery of a giant ΔS_m in $Gd_5(Si,Ge)_4$ at room

temperature [16]. This was the first magnetocaloric material featuring a concurrent structural and magnetic transition, a first order phase transition (FOPT). In it, the magnetization shows a discontinuity as a function of temperature, and thus decreases to very low values in an abrupt manner, due to the sudden atomic rearrangement. Instead of using T_C , the transition temperature for such materials is named T_t , as it corresponds to a change from a ferromagnetic structure to a different structure that is paramagnetic. These classifications will be explained in detail in the next chapter.

The temperature change of 5.8 K in a $\mu_0 H = 0 - 2$ T field change for Gd is considered high compared to most ferromagnetic materials. As a comparison, the pioneering discovery of Weiss and Picard on the magnetocaloric effect of metallic Ni showed an increase of approximately 0.7 K for a magnetic field change of 1.5 T [17]. However, these temperature changes would not be capable of inducing the temperature span needed for heating and cooling. Therefore, an active regeneration cycle must be used, in which the material undergoes a series of cycles exchanging heat with a heat transfer fluid to be able to generate the large temperature span seen in refrigerators or air conditioners [10, 18].

Such operating conditions with high number of (de)magnetization cycles entail a series of requirements for magnetocaloric materials to maximize the heat transfer while lowering its environmental impact [19]:

- A high ΔS_m and ΔT_{ad}
- Chemically and mechanically stable
- Easily conformed to desired shapes to maximize surface area
- Produced from abundant, inexpensive raw materials

These requirements are important in the search for new magnetocaloric compounds, since Gd is an expensive, non-abundant and toxic rare-earth element. In recent years, the most studied and promising compounds are $\text{La}_1(\text{Fe},\text{Mn},\text{Si})_{13}\text{H}_y$ [20, 21, 22, 23], NiMn-based Heusler alloys [24, 25, 26, 27], and $(\text{Mn}_{2-x}\text{Fe}_x)(\text{P}_{1-y}\text{Si}_y)$ intermetallics [6, 28, 29, 30]. A comparison between those materials is shown in Table 1.1. While the reported $\text{La}_1(\text{Fe},\text{Mn},\text{Si})_{13}\text{H}_y$ alloy exhibits high ΔS_m values, its low chemical stability leads to destabilization of the compound and ultimately loss of performance [31]. Other materials such as Gd in $\text{Gd}_5(\text{Si},\text{Ge})_4$, or In in the case of $\text{Ni}_{45.7}\text{Mn}_{36.6}\text{In}_{13.5}\text{Co}_{4.2}$ Heusler alloys use Gd and In, which are expensive. On top of this, irreversibilities associated with thermal hysteresis T_{hys} also lower the reversible effect. Recent studies also state the need of larger magnetocaloric effects to allow for comparable performances with the same machine sizes as regular compression devices [32, 18, 33]. Based on these requirements, new materials should be investigated.

1.3 High Entropy Alloys

An alloy design concept that has gained attention in the last couple of years are high entropy alloys (HEAs). They can fulfill most of the requirements needed for

Table 1.1: Properties of selected magnetocaloric materials. Taken from [30, 34, 35]

Composition	T_t / T_C (K)	ΔS_m (J/kg.K)	ΔT_{ad} (K)	T_{hys} (K)	$\mu_0 H$ (T)
Gd	292	2.8	2.9	-	1
$Gd_5(Si,Ge)_4$	262	7.1	1.3	5	1
$La_1Fe_{11.83}Mn_{0.32}Si_{1.3}H_x$	297	11.1	2.5	1.3	1
$Ni_{45.7}Mn_{36.6}In_{13.5}Co_{4.2}$	301	5	0.2	3.6	1
$(Mn_1Fe_{0.95})(P_{0.585}Si_{0.34}B_{0.075})$	290.5	9.1	2.5	1.5	1
MnFeCoNiCu	395	0.115			0.5
$Mn_{1.05}FeCoNiCu_{0.95}$	297	0.32	-	-	0.55
$Cr_{0.5}FeCoNi_{0.5}$	270	0.32	-	-	1

magnetocaloric materials and are produced from inexpensive transition metals. In HEAs, five or more elements are mixed in similar contents, close to equiatomic ratios. This is a different approach from traditional alloys where one element typically has a much larger fraction than the other elements. This leads to a large number of alloy design possibilities. As an example, if one tries to produce an equiatomic 5-element alloy using five of the first ten transition metals in the Periodic Table (from Sc to Zn), there are 252 possible combinations to explore. If one deviates from equiatomic ratios, it leads to nearly endless 5-d compositional spaces.

The first HEAs were developed 15-20 years ago by Cantor and Yeh, concurrently [36, 37]. The work of Cantor was centered around CrMnFeCoNi-based alloys, while Yeh focused on CrFeCoNiCu. From the Gibbs phase rule, the maximum expected equilibrium phases is $p=c+1$, c is the number of component. This would give a maximum of 6 different phases in the case of alloys with five elements. A surprising result was the possibility for biphasic (for CrMnFeCoNi) and monophasic (for CrFeCoNiCu) alloys [36, 37]. These findings initiated a substantial research effort to understand thermodynamic aspects of phase formation in multicomponent alloys. Analyses were conducted taking into consideration the Gibbs energy of a solid solution (SS) G^{SS} :

$$G^{SS} = H_{mix}^{SS} - T(S_{mix}^{SS}) \quad (1.3)$$

where H_{mix}^{SS} is the ideal enthalpy of mixing of solid solutions, T the temperature, and S_{mix}^{SS} the ideal entropy of mixing of solid solutions. S_{mix}^{SS} itself can be calculated as follows:

$$S_{mix}^{SS} = -R \sum_{i=1}^N c_i \ln c_i \quad (1.4)$$

R is the universal gas constant, 8.314 J/K/mol, and N is the number of elements, each with a concentration c_i . The alloys were termed "High Entropy Alloys" due to the resulting high S_{mix}^{SS} that stabilized solid solutions [38, 39]. To explain the small number of phases formed with the large number of elements, Yeh argued that "Based on Boltzmann's hypothesis concerning the relationship between the entropy and the complexity of the system, the high S_{mix}^{SS} with multiprincipal elements lowers the tendency to order and segregate" [36]. From this analysis, a HEA was

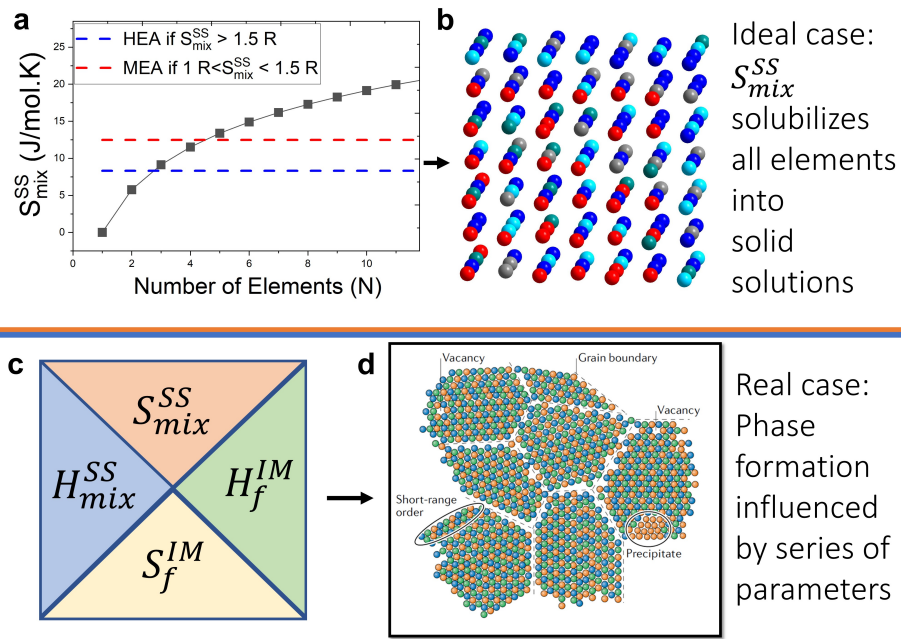


Figure 1.3: (a) S_{mix}^{SS} as a function of the number n of elements in an equiatomic alloy. According to the initial HEA definition of $n > 5$, S_{mix}^{SS} helps to stabilize a monophasic solid solution. (b) Representation of a monophasic, disordered solid solution stabilized by S_{mix}^{SS} . (c) Factors impacting the formation of solid solutions and intermetallics. (d) Real case of the impact of different thermodynamic properties on HEAs, creating precipitates, ordering, and defects in solid solutions. Adapted from [41].

defined by values of S_{mix}^{SS} above $1.5R$. This was one of the earliest definitions of HEAs, known as the entropy definition [40] (see Figure 1.3(a)). In the case of equiatomic compositions, HEAs were formed when $N \geq 5$, and Medium Entropy Alloys (MEAs), when N was between 3 and 4. This property was then linked to solid solution formation, stabilizing monophasic solid solutions, see Figure 1.3(b).

Besides S_{mix}^{SS} and H_{mix}^{SS} The following additional parameters were found to be of guideline relevance when designing HEAs [42, 43]:

- Atomic size difference (δ): An estimation of the variation of atomic size in a solid solution, indicating the amount of lattice misfit. δ can be correlated with H_{mix}^{SS} to display the trend for precipitating amorphous phases versus solid solutions and intermetallics. Large δ s combined with largely negative H_{mix}^{SS} tended to form amorphous phases, while small δ s combined with positive or close to null H_{mix}^{SS} stabilized ordered, crystalline solid solutions [42].
- Valence Electron concentration (VEC), which influences the formation of body centered cubic (bcc) or cubic-close packed (ccp) phases in transition metal based alloys [43].

Initially, alloys were only termed as "HEAs" if samples were monophasic and equiatomic; Later, S_{mix}^{SS} was found not to be the main descriptor of solid solution

formation [40, 44]. The calculation of S_{mix}^{SS} seen in Equation 1.4 assumes an ideal, random solution between the constituents. In reality, ideal solutions are rarely seen - they consist of 4 % of the high entropy alloys reported in Miracle's study [40, 44]. The calculation of entropy in regular and subregular solutions is not straightforward as in Equation 1.4. In addition, early alloy systems were reported in as-cast conditions, i.e., quickly cooled, metastable states which are away from thermodynamic equilibrium [40]. In thermodynamic equilibrium, most HEAs are multiphase alloys [40, 44]. The determination of phase fractions in thermodynamic equilibrium is influenced by several parameters such as the enthalpy and entropy of formation of the intermetallics (H_f^{IM} and S_f^{IM}) and H_{mix}^{SS} and S_{mix}^{SS} , illustrated in the bottom part of Figure 1.3(c). It follows that ordered phases, pure precipitates, and intermetallics can be formed together with solid solutions, illustrated in Figure 1.3(d) [41]. The relationships between thermodynamics of solid solutions and HEA phase stability is well covered by Miracle D. and Senkov O.N. [40]. A more tolerant definition based on composition is now adopted, known as the composition definition. It consists of a number n_{major} of major alloying elements, as well as a number of n_{minor} minor alloying elements, as follows:

$$n_{major} \geq 5, 5at. \leq \%c_i \leq 35 at. \%, n_{minor} \geq 0, c_j \leq 5 at. \% \quad (1.5)$$

where c_i and c_j are the atomic percentages of the i th major and j th minor elements [45, 46].

In the beginning, HEA research was motivated by understanding phase formation, correlating it to thermodynamic properties. Now, interest has grown motivated by its load bearing capacities in unusual conditions: some HEAs have unusually high ductility at low temperatures, or high-temperature yield strengths, which are not common in metallic materials [41]. The concept was also envisioned for functional applications [47], where HEAs would present specifically tailored properties for applications such as soft magnetism, hydrogen storage, catalytic applications, and superconductivity [47]. The main HEA research areas include:

- Refractory HEAs: based on early transition metals, such as Cr, Hf, Mo, Nb, Ta, Ti, V, W, and Zr. Studied for structural properties at high temperatures, superconductivity and hydrogen storage applications.
- Low-density HEAs: based on low specific weight elements such as Al, Be, Li, Mg, Sc, Si, Sn, Ti, and Zn. Investigated for applications in the aerospace industry.
- 3d transition metal HEAs: The most common group of HEAs studied, typically involving at least 4 of the following elements: Al, Co, Cr, Cu, Fe, Mn, Ni, Ti, and V. This system is studied for structural and soft magnetism applications.

1.4 Magnetocaloric High Entropy Alloys

Lucas et al. evaluated the magnetocaloric potential of HEAs by producing and studying $Cr_xFeCoNi$ alloys in a 3d-metal based MEA in 2013 [48]. Despite the

modest magnetocaloric effect, a high degree of tunability was demonstrated by changing the Cr content. Nonequiatomic Cr_xFeCoNi alloys were synthesized from arc melting, and had T_C 's ranging from 50 to 190 K, with higher Cr contents stabilizing T_C 's towards lower temperatures [48].

In 2015, Belyea et al. explored the addition of different amounts of Pd to CrFeCoNi , resulting in CrFeCoNiPd_x HEAs [49]. The authors report an increase of the T_C as a function of Pd content, which is counter-intuitive at first as Pd is not ferromagnetic. This was correlated to an increase in "magnetic homogeneity", reducing the distribution of T_C 's in the system. However, the prohibitive cost of Pd was a serious hindrance to the application. The authors suggested that a similar effect could be obtained using Cu instead of Pd [49].

Kurniawan followed this approach by producing XFeCoNiCu alloys, where X are elements replacing Cr, namely Mn, Pt, Ag, and Mo, in equiatomic compositions [50]. By using quick solidification techniques, the samples become monophasic. Among all studied alloys in Kurniawan's work, MnFeCoNiCu had T_C closest to room temperature, at 400 K. They proceeded to study offstoichiometric $\text{Mn}_{1+x}\text{FeCoNiCu}_{1-x}$ alloys, and found transitions close to room temperature in $\text{Mn}_{1.05}\text{FeCoNiCu}_{0.95}$ (280 K) and $\text{Mn}_{1.1}\text{FeCoNiCu}_{0.90}$ (265 K) [34]. Alice Perrin's PhD thesis studied HEA's for magnetocaloric applications comprehensively [51]. One of her studies are related to Mn off-stoichiometries for MnFeCoNiCu HEA's, also produced by quick solidification techniques [34]. $\text{Mn}_{1+x}\text{FeCoNiCu}_{1-x}$ and $\text{Mn}_{1+x}\text{Fe}_{1-x}\text{CoNiCu}$ allowed for tuning of T_C 's. The compositions $\text{Mn}_{1.05}\text{FeCoNiCu}_{0.95}$ and $\text{Mn}_{1.025}\text{Fe}_{0.975}\text{CoNiCu}$ displayed transitions around 300 K [34].

Quintana-Nedelcos et al. presented a different approach for production of magnetocaloric HEAs, aiming to increase the magnetocaloric effect based on microstructure modification [35]. They explored non equiatomic $\text{Cr}_{0.5}\text{FeCoNi}_{0.5}\text{Al}_x$ alloys that were biphasic. Heat treatments after casting were used to precipitate FeCr nanoparticles in a AlNiCo matrix. Given the right radius and distribution for the observed NPs, ferromagnetic exchange bias from the AlNiCo matrix forced the FeCr nanoparticles to behave as ferromagnets [35].

1.5 MM'X-type compounds as magnetocaloric materials

MM'X are intermetallic compounds with 3 elements in equiatomic ratios, with largely covalent bonds between metallic (M, M') and p-block (X) elements. Typical MM'X studied for magnetocaloric applications are MnCoGe , MnNiGe , MnNiSi , and MnCoSi [52, 53, 54, 55, 56]. In some compositions such as MnCoGe and MnNiSi , the intermetallics display two different crystal structures, depending on the temperature. At low temperatures, the structure-type of TiNiSi is observed with an orthorhombic unit cell. It is a modification of the MnP -type structure, where a vacancy is filled with a second transition metal atom. At high temperatures, the hexagonal Ni_2In structure-type is seen (Figure 1.4(a)) [57]. The TiNiSi and Ni_2In structures are depicted in Figure 1.4(b).

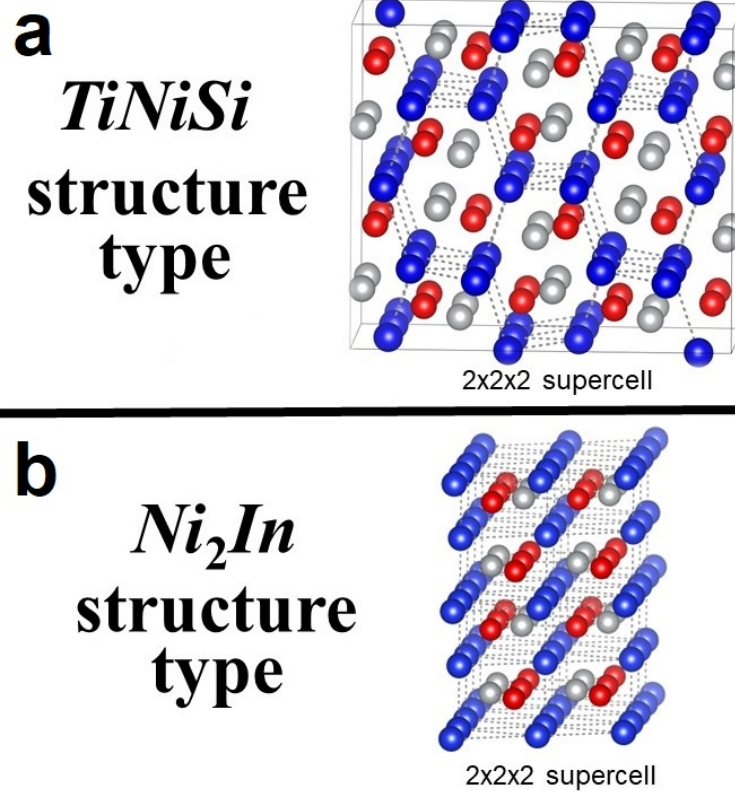


Figure 1.4: Representation of the (a) *TiNiSi* and (b) *Ni₂In* structures present in MM'X materials

The transformation between both structures is known as a martensitic transformation, happening at a transformation temperature T_{str} . Such a transformation is independent of thermal activation (diffusion) [52, 57]. The most known example of a martensitic transformation is in Fe-C alloys, where the presence of interstitial C hinders the transformation of ccp Fe "austenite" to the bcc structure [58]. The result is a distorted variation of the bcc structure, a body-centered tetragonal structure also known as "martensite". The nomenclature used in the Fe-C martensitic transformation is also utilized in MM'X compounds. The high temperature hexagonal structure is named austenite, and the low temperature orthorhombic structure is called martensite. In MM'X compounds, the transition signals a change in the coordination environment between the atoms: For the *TiNiSi*-type, there are two additional M-type bonds (such as Co or Ni bonds) per formula unit, while for the *Ni₂In*-type there are one additional Mn-p block, one M-p block and two Mn-Mn bonds [59]. This will create differences in the required energies to break such bonds and transform from one structure to another. Due to this, there will be differences between the heating (martensite to austenite) and cooling (austenite to martensite) transformations. This creates thermal hysteresis, i.e., a difference between the heating and cooling transformation temperatures. However, there are ways to reduce hysteresis. From the crystallographic theory of martensite, the thermal hysteresis can be reduced, and the geometrical compatibility improved, if the ratio between c_{orth} and $\sqrt{3}a_{hex}$

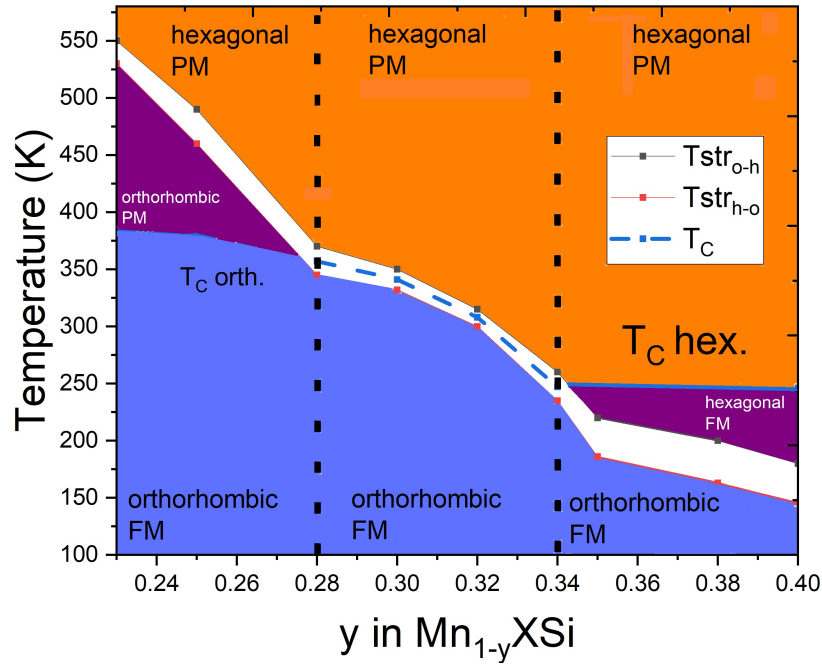


Figure 1.5: Hypothetical representation of a temperature-composition diagram for a substitution of element y in $MnNiSi$. In the composition region between $y=0.28$ to 0.34 , a concurrent structural-magnetic transition occurs.

is close to 1, i.e., $c_{orth}/\sqrt{3}a_{hex} = 1$ [60, 61, 62, 63].

While studying substitutions of $MnNiGe$ with Si in the Ge site, Bazela et al. discovered an abrupt magnetization change as a function of temperature [64]. This was later understood as a coupling of the magnetic transition and the martensitic transformation, similar to $Gd_5(SiGe)_4$ compounds [6]. The coupled magnetic and structural transition temperature is denoted as T_t .

This coupling of transitions could be obtained in other $MnM'X$ materials, where it was discovered that it can exist in a composition region in a phase diagram. This is exemplified in a diagram of a hypothetical modification of an element Y modifying Mn sites in $MnNiSi$, seen in Figure 1.5. In lower degrees of substitution, the T_C of the orthorhombic phase is below the T_{str} . With larger amounts of substitution, the ferromagnetic orthorhombic phase is stable up until the T_{str} , while the theoretical T_C of the hexagonal structure stands at temperatures below T_{str} . This creates a transition from ferromagnetic, orthorhombic structure to paramagnetic hexagonal structure in the magnetostructural transition temperature T_t . In larger degrees of substitution, T_{str} becomes lower than the hexagonal T_C , and both the orthorhombic and hexagonal phases are ferromagnetic.

When the search for feasible magnetocaloric materials began, such $MnM'X$ compounds were considered due to the tunability of T_t by partial element substitutions [65, 66]. $MnCoGe$ for example can be easily modified to display magnetostructural transitions at room temperature, due to a T_{str} which resides between 400 and 458 K, and a T_C of the orthorhombic phase at approximately 350 K [59]. However, since Ge and Co are considered critical elements [67], a shift towards $MnNiSi$ -based $MM'X$ compounds is occurring aiming to reduce or remove

Ge and Co. MnNiSi exhibits an orthorhombic T_C around 600 K, and a T_{str} of 1200 K [68, 64]. This requires a larger amount of element substitutions, with two or more site substitutions in MnNiSi. The use of large quantities of alloying elements can make it difficult to achieve complete local order, and local inhomogeneities can impact the observed T_t . Therefore, attention to the thermal history of MM'X compounds is important to achieve a large degree of order in the structure [69].

Another very important aspect of the magnetostructural FOPTs happening in MM'X compounds is the relationship with pressure/mechanical stress. It is well known that external pressure modifies T_t in MM'X compounds [70, 71, 72]. However, internal stresses also modify T_t . As the change between crystal structures creates a volume change, it induces internal stresses that impact T_t in neighbouring grains [27]. Different grain sizes will exert different internal stress fields in the grains, and therefore a distribution of T_t can be expected also based on the particle sizes.

The volume changes occurring during the transition also leads to embrittlement. After several cycles, it leads to pulverization of the sample which is detrimental to the application [73, 27]. An attempt at circumventing the brittleness is to use ductile metal composites (with In or Sn matrices) with MM'X particles. This creates MM'X / ductile metal composites, which are reported to keep their mechanical integrity after 500 cycles [74].

1.6 Scope of the work

Considering the aforementioned challenges in section 1.2, there is a need to discover and optimize novel magnetocaloric materials. Hence, establishing structure-property relationships in new magnetocaloric HEAs and MM'X compounds is important. Based on the state of the art perspectives described in this chapter, the present work aims to:

- Synthesize high entropy alloys for magnetocaloric energy conversion at room temperature;
- Analyze their magnetocaloric potential;
- Produce transition-metal based MM'X intermetallics with inexpensive, abundant materials;
- Characterize their properties when different levels of substitution occur in low-cost MM'X;
- Investigate the impact of thermal history on the magnetocaloric properties of low-cost MM'X.

Chapter 1. Introduction and motivation

Chapter 2

Theory and characterization methods

This chapter aims to introduce the reader to the topics necessary to understand the magnetocaloric materials studied in this thesis. The synthesis and processing methods will be briefly detailed. The following section will describe an introduction of the Calculation of Phase Diagram (CALPHAD) method, used to estimate phase diagrams and other thermodynamic properties. Subsequently, theoretical aspects on the thermodynamics of phase transitions will be outlined, and used to define the figures of merit of magnetocaloric materials. To measure magnetocaloric properties, methods of characterization of caloric and magnetic properties will be presented. In the second half, the emphasis is placed on the description and characterization of the average structures studied by diffraction methods. Finally, a brief description of microstructure will be discussed.

2.1 Synthesis and processing of alloys and intermetallics

All alloys and intermetallics in this thesis were prepared using a custom-built arc melter, see Figure 2.1. This process involves mixing of the starting elements in powder or ingot form into a Cu hearth, i.e., a Cu area that is continuously cooled by water. A high current is then passed through a tungsten tip placed in close proximity over the hearth. This creates an electric arc that melts the elements together, and mixes them on an atomic level. To increase the homogeneity, the alloys are turned over, and remelted several times.

The cooling of the product is very fast due to the contact with the cooled Cu hearth. This usually leads to a metastable alloy or compound. In some cases, it is beneficial to further process the ingot by normalizing or modifying the microstructure through an additional heat treatment.

To perform such heat treatments, ingots or powders are sealed under vacuum in quartz tubes and placed in resistance furnaces at certain temperatures for given periods of time. After the end of the heat treatment, samples can be quenched in water to preserve the structural and microstructural characteristics at high temperatures, away from thermodynamic equilibrium.

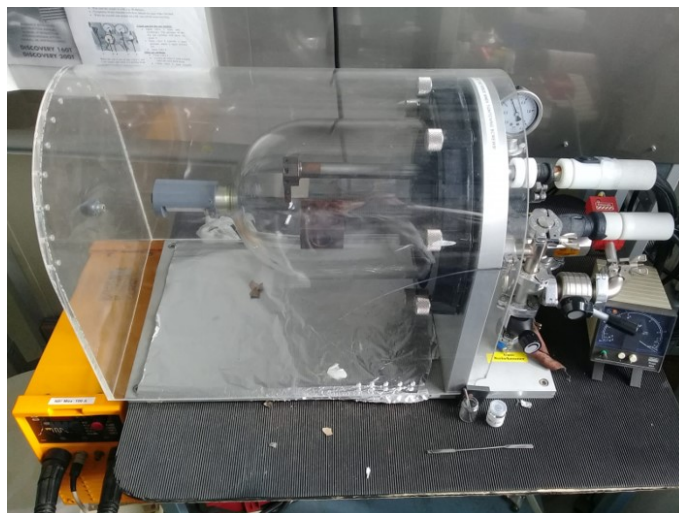


Figure 2.1: Custom-built arc melter used in the synthesis of HEAs and MM'X intermetallics.

2.2 CALPHAD modeling of equilibrium phase-diagrams

A robust method for alloy screening is the Calculation of Phase Diagrams (CALPHAD), which utilizes thermodynamic experimental data from binary and ternary alloys that is extrapolated to n-element alloys [75]. Here, the software Thermocalc 2021 TM was employed, together with the TCHEA3 database package. An example of a CALPHAD calculation showing the phase presence in thermodynamic equilibrium as a function of temperature for the VFeCoNiCu HEA is depicted in Figure 2.2.

2.3 Thermodynamics of phase transitions

Substances can exist as liquids, gases or solids. Due to different temperatures, pressures and volumes, a substance can undergo a phase transition from one allotrope to another in a solid, or from a gas to a liquid for example. The specific conditions (temperature, pressure, volume) involving a transition from one phase to another are known as critical points [76]. In 1933, Paul Ehrenfest detailed an early method for classifying phase transitions, known as the "Ehrenfest classification" [76]. An illustration is depicted in Figure 2.3. In this approach the derivatives of the Gibbs free energy G are analyzed. G is defined in a substance as:

$$G = U - Ts + pV - \mu_0 MH \quad (2.1)$$

U is the internal energy, T the temperature in Kelvin, s the specific entropy, p the pressure, V the volume, M the magnetization of the material, μ_0 the vacuum magnetic permeability, and H the magnetic field [8].

When the first derivative of G is discontinuous, the material undergoes a first order phase transition (FOPT) as depicted in the top part of Figure 2.3. Examples of FOPTs are changes in the state of matter (liquid to solid, or between allotropes),

2.3. Thermodynamics of phase transitions

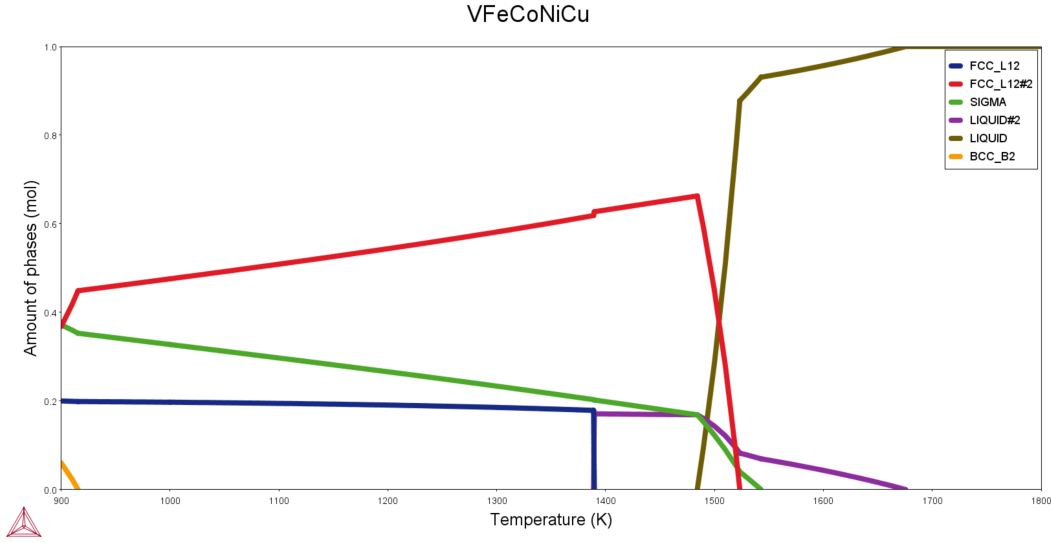


Figure 2.2: Calculated thermodynamic phase equilibrium as a function of temperature produced by the ThermoCalc software.

with a latent heat associated to the transition. A Second Order Phase Transition (SOPT) occurs if the first derivative of G is continuous, and the second derivative is discontinuous, as shown in the bottom part of Figure 2.3. Both types of phase transitions are important for magnetocaloric materials: Gd exhibits a SOPT [15], while FOPTs are observed for $\text{La}(\text{Fe},\text{Mn},\text{Si})_{13}\text{H}_y$, $\text{MM}'\text{X}$ compounds and others [6]. First order magnetocaloric materials undergo by a discontinuity in magnetization as a function of temperature, while second order magnetocaloric materials have no discontinuity in magnetization [5]. In both cases, the figures of merit ΔS_m and ΔT_{ad} can be determined from experiment. The theoretical approach to obtain the magnetocaloric properties will be defined by differentiating Equation 2.1 as follows:

$$dG = V dp - s dT - \mu_0 M dH \quad (2.2)$$

If the pressure and volume are kept constant, M will be the partial derivative of G with respect to H :

$$\mu_0 M(T, H) = - \left(\frac{\partial G}{\partial H} \right)_T \quad (2.3)$$

The entropy S will be the partial derivative of G with respect to T :

$$S(T, H) = - \left(\frac{\partial G}{\partial T} \right)_H \quad (2.4)$$

As both partial derivatives of the previous equations are the second partial derivatives of G , they can be related, with respect to H and T :

$$\left(\frac{\partial M}{\partial T} \right)_H = \left(\frac{\partial S}{\partial H} \right)_T \quad (2.5)$$



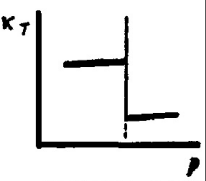


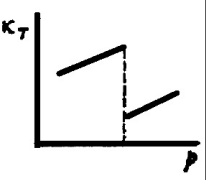
Order of Transition	g	Derivatives of g	
		first	second
First			
Second			

Figure 2.3: Illustration for the Ehrenfest classification of phase transitions. Adapted from [76].

By integrating both terms of the previous equation, ΔS_m between two different fields H_i and H_f becomes:

$$\Delta S_m(T, \Delta H) = \mu_0 \int_{H_i}^{H_f} \left(\frac{\partial M(T, H)}{\partial T} \right)_H dH \quad (2.6)$$

Equation 2.6 shows why the magnetocaloric effect is larger closer to the magnetic ordering temperatures such as T_C , since $\frac{\partial M}{\partial T}$ is large close to these temperatures. It also shows why a large $\frac{\partial M}{\partial T}$ is desired.

For an adiabatic process of magnetization, i.e., with no exchange of heat with the medium, the increase of temperature ΔT_{ad} is expressed by:

$$\Delta T_{ad}(T, \Delta H) = -\mu_0 \int_{H_i}^{H_f} \left(\frac{T}{C_p(T, H)_H} \right) \left(\frac{\partial M(T, H)}{\partial T} \right)_H dH \quad (2.7)$$

C_p is the heat capacity at a constant pressure and magnetic field. From Equation 2.7, the smaller the heat capacity, the stronger the adiabatic temperature change. However, in magnetocaloric materials with FOPTs, the magnetization contribution to the heat capacity creates an infinitely sharp peak [77]. This decreases the effect of the strong $\frac{\partial M}{\partial T}$ in ΔT_{ad} of materials with first order phase transitions, compared to second order phase transitions.

The peak position of C_p is mostly insensitive to magnetic fields in materials undergoing SOPTs. In this case, ΔT_{ad} can be determined from Equation 2.7 [6]. In materials undergoing FOPTs, the C_p peak is modified by magnetic fields [5], therefore another method has to be utilized. They are usually measured in built-in devices such as the one reported by Trevizoli et al. [78], with samples mounted in an actuator system. The materials can be cycled in and out of a magnetic field in a nearly adiabatic condition. The sample actuation occurs while the sample temperature is recorded. The magnetic fields are generated from a Hallbach-configuration magnet, and the whole system is usually enclosed in a thermal bath with controlled temperatures. This allows probing different temperatures.

Magnetization processes do not occur isothermally (very slow magnetization) or adiabatically (very fast magnetization) during magnetocaloric device operation. In reality, the magnetization process takes a finite amount of time, in the order of seconds, and a temperature change in the material occurs while it exchanges heat with the medium. The real magnetocaloric effect is therefore a midpoint between the two properties, dependent on both the magnetization process, and the design of the prototype. In summary, the two figures of merit provide a prototype-independent, simple method to characterize how fast a certain quantity of heat can be transferred to the medium for a given change in the magnetic field.

Besides ΔT_{ad} and ΔS_m , other properties are relevant for the characterization of magnetocaloric materials, such as the heat capacity. Thermal analyses permit examination of the heat capacity of transitions, and to understand transition kinetics in detail. Thus, the following section will present the characterization of the phase transitions by thermal analyses.

2.4 Thermal analysis

One method to capture phase transitions in materials is to analyse the change in heat flow, or specific heat as a function of temperature. In this thesis, two thermal analyses methods have been used: A DSC to capture phase transitions at lower temperatures, and a high temperature simultaneous Thermogravimetric analysis and differential scanning calorimeter, working as a magnetic balance to screen magnetic transitions.

2.4.1 Low temperature commercial DSC

A Differential Scanning Calorimeter (DSC) from TA instruments was used to measure the heat flux on samples undergoing phase transitions, shown in Figure 2.4(a). The instrument consists of a single furnace where the specimen and the reference materials undergo a controlled heating or cooling program. The sample is encapsulated in an Al pan which is placed on a thermoelectric disk inside the furnace, together with an empty reference pan highlighted in Figure 2.4(a). As the furnace temperature changes, heat is transferred to the sample and the reference. The heat flow is captured by area thermocouples. The material's heat flow is defined as:

$$q = C_p(dT/dt) + f(T, t) \quad (2.8)$$

q is the sample heat flow, C_p is the sample's specific heat capacity, dT/dt the heating rate and $f(T,t)$ is the kinetic response at a specific temperature and time [79].

When a transformation of the sample occurs, such as a SOPT or a FOPT, their heat flux being correlated to changes in the heat capacity is measured. Kinetic responses are mostly correlated to other events such as crystallization, evaporation of volatile species or decomposition reactions. Examples of the heat flux captured from a FOPT from $(\text{MnNiSi})_{0.66}(\text{Fe}_2\text{Ge})_{0.34}$ and a SOPT from Gd are shown in 2.4(b). For Gd, a small amount of heat flow occurs, distributed across

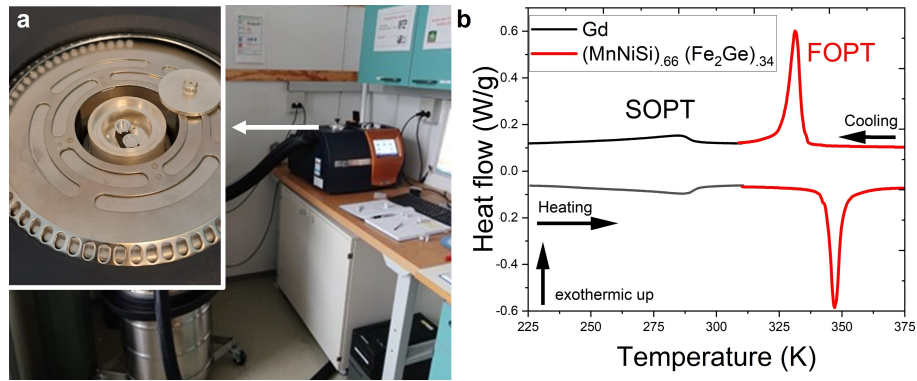


Figure 2.4: (a) The TA instruments DSC25 equipment, with the Aluminum pan setup in the inset. (b) Heat flow curves as a function of temperature that can be obtained through DSC measurements. The curves display examples of SOPT transitions such as Gd in black, and a FOPT in a MnNiSi-based material

a large temperature range. In the example of the magnetostructural transition of $(\text{MnNiSi})_{0.66}(\text{Fe}_2\text{Ge})_{0.34}$, an intense sharp peak occurs, attributed to the structural transition between the two crystal structures of MnNiSi. This kind of transition presents thermal hysteresis, i.e., a difference in T_t 's during heating and cooling transitions.

It is also possible to probe the heat capacity of the materials by the use of a "classical three step procedure" [79], based on the ASTM E1269 norm. It requires that three measurements with the exact same heating or cooling rates are executed:

- (1) With an empty sample holder;
- (2) with a sapphire standard;
- (3) with the specimen.

Isotherms before and after must be performed on each measurement. The heat capacity of the sample $C_p(s)$ can be determined as follows:

$$C_p(s) = C_p(st) \cdot \frac{Ds \cdot Wst}{Dst \cdot Ws} \quad (2.9)$$

$C_p(st)$ expresses the heat capacity of the sapphire standard, Ds the difference in heat flow between the specimen and the empty holder at a given time, Wst the weight of the sapphire standard, Dst the difference in heat flow between the sapphire standard and the empty holder at a given time, and Ws is the mass of the specimen.

2.4.2 High temperature commercial DSC - magnetic balance

By applying a magnetic field in a specific configuration on a NETZSCH STA 449 F3 Jupiter simultaneous thermal analyzer, the change in internal magnetic field of the sample produces a magnetic force which adds to the weight measured by the balance used. As the sample is heated up during the measurement, the

internal magnetization decreases, which modifies the measured weight. This occurs until the magnetic transition is reached, where no further contribution from the magnetization is recorded. It is therefore an indirect measurement of the internal magnetization, comparable to a temperature-dependent magnetization experiment. This temperature-dependent magnetization experiment will be specified in section 2.6.2.

2.4.3 Custom-built DSC with magnetic field

Measurements of heat capacity were carried out at the Department for Energy Conversion and Storage at the Technical University of Denmark (DTU), using a custom-built DSC with applied magnetic field, see Figure 2.5(a). A Peltier element is a thermoelectric device which can heat or cool an area by application of electric current by the Peltier Effect, or generate an electric current by a temperature difference between its two sides, in a phenomenon called the Seebeck effect. It allows for heating and cooling of the Cu finger between 250 and 320 K by the use of a Pt-100 temperature sensor. The sample area is also evacuated to pressures below 10^{-5} mbar, which greatly reduces heat transfer by conduction and convection from the surroundings. To measure the heat flux of a material, two additional smaller Peltier thermoelectric devices are used to detect temperature differences due to the Seebeck effect [80]. By this method, with one Peltier serving as a Reference, and a second for placing the material, phase transitions occurring in the material can be recorded by the voltage difference across the two Peltiers. After a series of corrections to remove the effect of thermal paste (used to increase thermal conductivity) and accurate calibrations which require additional measurements, the specific heat capacity $c_{P,H}$ can be obtained using the following relation:

$$c(T, H)_{P,H} = \frac{A_c k U_s(T, H) - U_{ref}(T)}{LS m_s T} \quad (2.10)$$

where A_c is the contact area, L is the Peltier length, S is the Seebeck Coefficient, k is the thermal conductivity coefficient, m_s is the mass of the sample, and U_s and U_{ref} are the voltages generated on the sample's Peltier and reference, respectively. Such a custom-built setup enables precise measurements of the heat associated with magnetic and/or structural transitions around room temperature, from 250 to 320 K [80].

With the use of different magnetic fields, it is also possible to investigate the effect of different magnetic fields on magnetic transition temperatures, see Figure 2.5(b). In addition to qualitative evaluations of the phase transitions, one can also obtain ΔS_m values by analysis of the heat capacity for different magnetic fields. The maximum applied fields possible in this device are close to 1.5 T, which limits the evaluation of ΔS_m for higher magnetic field changes.

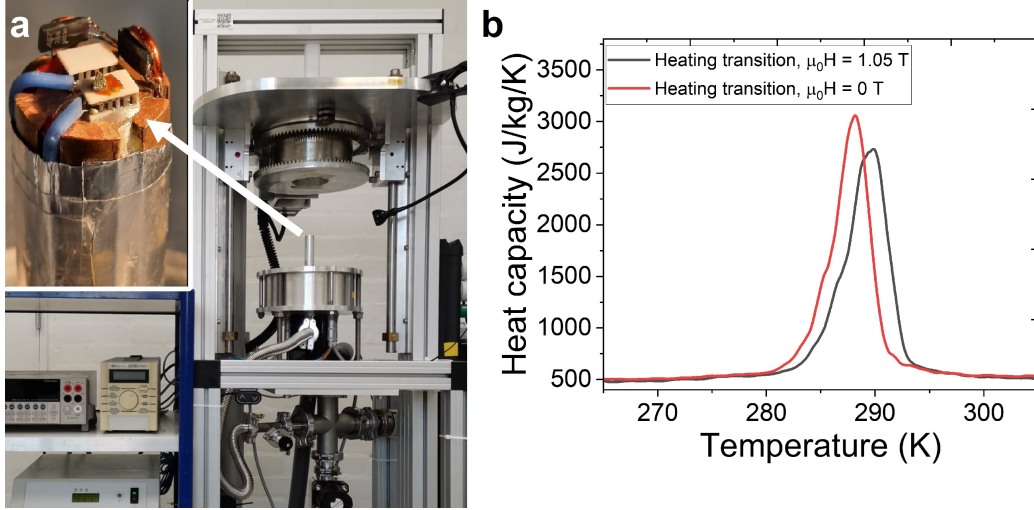


Figure 2.5: (a) Custom-built DSC setup at DTU, with the control unit and thermal bath in the lower left, the vacuum system in the lower right, and the main heating unit and Hallbach magnet system in the middle and upper right, respectively. The inset in the upper left shows the cold finger where the two peltier elements are used to measure the heat associated in samples with phase transitions around RT. (b) Heat capacity of a MnNiSi-based intermetallic with applied fields of $\mu_0 H = 0$ and 1.05 T.

2.5 Ferromagnetism and estimation of magnetic properties by Density Functional Theory

The studied materials in this thesis are ferromagnetic in lower temperatures, and undergo pure magnetic or magnetostructural transitions to paramagnetic states. The origin of the magnetic moments in HEA's and MM'X studied in this thesis are the unpaired 3d electrons in transition metals. For ferromagnetism to exist, the spins in these electrons must be aligned in parallel. Using a quantum mechanics approach, the Heisenberg model describes an exchange interaction (J_{ex}) term between nearest neighbors [77]. J_{ex} then gives rise to a potential energy E_{ex} term by taking into account the adjacent spin vectors S_i and S_j , and the angle between them:

$$E_{ex} = -J_{ex} \vec{S}_i \vec{S}_j = -J_{ex} S_i S_j \cos \phi \quad (2.11)$$

If the J_{ex} between nearest neighbors is positive, there is parallel alignment and collectively a ferromagnetic ground state is observed. If J_{ex} is negative, there is antiparallel alignment, and the resulting magnetic ground state will be antiferromagnetic. The J_{ex} term is dependent on the interplay between the Coulomb interaction and Pauli's exclusion principle [77, 81], and positive J_{ex} can only be obtained for specific interatomic distances and 3d orbitals, see the Bethe-Slater curve in Figure 2.6. Positive J_{ex} 's are observed when Fe, Co and Ni are alloyed with each other, in direct exchange. In such materials, there is a correlation between J_{ex} and T_C [77].

Due to the delocalized nature of the 3d electrons in Fe/Co/Ni, and high J_{ex} 's, T_C in Fe-Co-Ni alloys is high (far above RT). To bring it to RT, Fe, Co and Ni

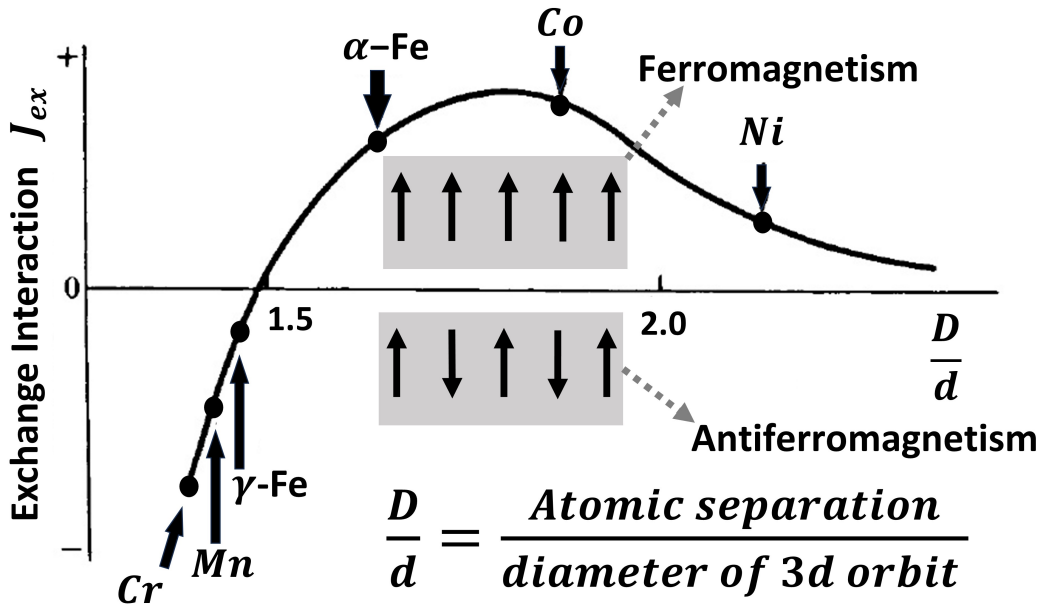


Figure 2.6: Schematic variation of the exchange interaction as a function of the ratio D/d . Adapted from [82].

needs to be alloyed with elements that induce negative J_{ex} 's such as Cr or Mn to reduce T_C to RT (see Figure 2.6). The resulting macroscopic magnetic behavior will be a function of the ratio between positive and negative J_{ex} 's seen in the resulting disordered solid solutions.

Manganese can induce antiparallel exchange interactions as seen in Figure 2.6. However, given the right interatomic distances, Mn can induce positive J_{ex} due to indirect exchange between Mn and a p-block element [77]. This behavior is theorized to occur in $MM'X$ compounds. However, the complete description of magnetism in $MM'X$ (and MnP -type) compounds is not completely explained by indirect exchange [83, 84], as several nearest neighbors have to be considered to correctly describe the magnetism in the $TiNiSi$ -type structure (and related MnP) [69, 84, 85]. Macroscopically, $MM'X$ can have ferromagnetic or antiferromagnetic ground states, where the latter can occur with different magnetic structures associated with the Mn atom [69, 64, 83].

J_{ex} 's and T_C 's are properties that can be evaluated by Density Functional Theory, a quantum mechanical modeling method to evaluate the electronic structure of molecules or compounds. In Papers I, II and IV, compounds have been evaluated with the exact muffin-tin orbital (EMTO) method by a researcher in the University of Uppsala. In papers I and II, T_C is estimated by Monte Carlo simulations taking into account the J_{ex} 's obtained by the EMTO method. In paper IV, a Mean field approach is considered to calculate T_C from the following equation:

$$k_b T_C = 2/3(E^{PM} - E^{FM}) \quad (2.12)$$

where k_b is the Boltzmann constant, and E^{PM}/E^{FM} the energies of the para- and ferromagnetic states respectively. The energies are obtained from the EMTO method.

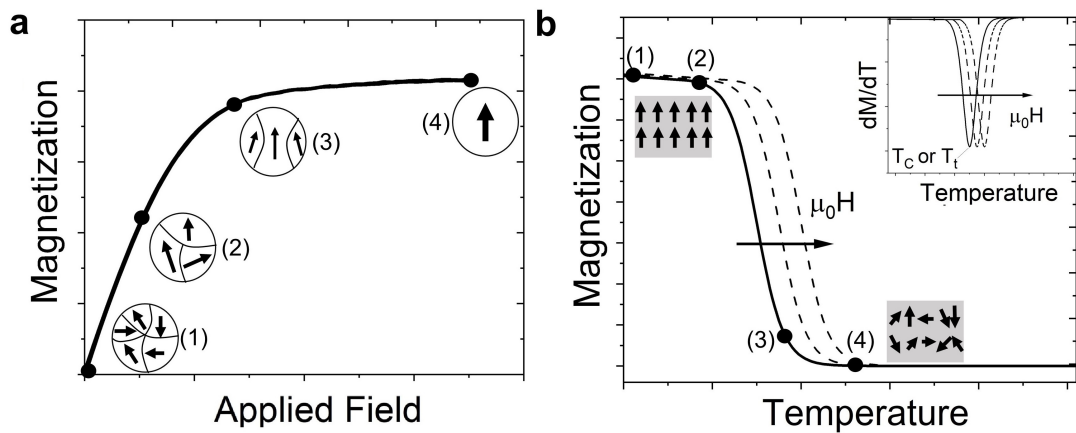


Figure 2.7: Magnetic measurements performed in VSMS. (a) Magnetization behavior in field-dependent curves, illustrating the effect of external applied field on the magnetic domain alignment. (b) Magnetic transitions are displayed in temperature-dependent curves, showing how a transition occurs between high and a low magnetization states. The effect of larger magnetic fields $\mu_0 H$ on the transition temperature are also shown, shifting the transition to higher temperatures.

2.6 Magnetic characterization methods

To measure macroscopic magnetic properties in a material, one of the most common methods is the use of a Vibrating Sample Magnetometer (VSM). It can be a stand-alone instrument, or a module inside a Physical Property Measurement System (PPMS). As the name VSM implies, the materials (typically powders or ingots in the milligram range) are placed between a pair of coils by a rod, vibrating at a specific frequency within an enclosed space. When an external magnetic field is applied from the coil pair, the material is magnetized, creating its own stray field. This field vibrating with a known frequency will induce a signal on a sensor, transforming it into a magnetization value assigned to the applied field. With the sample in a cryostat or a furnace, one can extend the temperature range of measurements significantly. In a PPMS, the VSM module can be cooled and heated from around 1 K to 390 K. In stand-alone VSMS with furnaces, measurements can be carried out in temperatures from 300 to 1100 K. Typical measurements include temperature-dependent magnetization measurements, and applied field dependent curves, which are illustrated in Fig 2.7 (a) and (b), respectively. Both temperature and field-dependent measurements are relevant for the study of magnetocaloric materials, and will be outlined in the upcoming sections.

2.6.1 Field dependent curves

A VSM is mostly used to measure field dependent curves, observed in Figure 2.7(a). It consists in the recording of magnetization values as the applied magnetic field is changed, with a constant temperature. For a ferromagnetic material, with $\mu_0 H = 0$ T, all magnetic domains are randomly oriented, see point (1) in Figure 2.7(a). With larger external magnetic fields, magnetic domains aligned with the external

field grow in (2). After a certain applied field, most of the magnetic domains are oriented parallel to the applied field in (3), and finally, all domains are aligned parallel to the external magnetic field in (4). This last point is known as the saturation magnetization [86].

2.6.2 Temperature-dependent curves

For magnetization measured as a function of temperature exemplified in Figure 2.7(b), an external magnetic field is kept constant, and the temperature is varied at a constant rate. For typical ferromagnetic materials, the magnetic domains will align at lower temperatures, and the material exhibits a large magnetization, see (1). As the temperatures increases, atomic agitation increases, and gradually the magnetic moment alignment in the magnetic domains diminishes (2). In materials undergoing SOPTs, when the temperature approaches T_C , the alignment of moments can not be kept due to the large thermal agitation, and a large decrease in magnetization is observed, see point (3). Theoretically, T_C is then determined as the point where the spontaneous magnetization no longer changes with temperature [86]. In materials with FOPTs, the large decrease in magnetization occurs due to the structural transition between a ferromagnetic and a paramagnetic structure, also in (3). Experimentally, both T_C and T_t are defined as the minimum derivative of magnetization as a function of temperature, shown in the inset of Figure 2.7(b). After T_C and T_t , the sample remains in a paramagnetic state (4), where the magnetization remains constant. For both SOPT and FOPTs, the transition temperatures are shifted towards higher temperatures with higher magnetic fields.

2.6.3 Magnetocaloric property determination and analysis

As explained in section 2.3, the most important descriptors of the magnetocaloric performance of a material are ΔT_{ad} and ΔS_m [5]. The entropy change can be determined by two methods: in direct measurements of heat capacity with applied magnetic fields by equipments as the one detailed in section 2.4.3; or indirectly by the use of field-dependent curves in VSM measurements, as seen in Figure 2.7(a). In SOPTs, field-dependent curves are obtained isothermally at temperatures surrounding T_C . This allows for a straightforward determination of ΔS_m by numerically integrating Equation 2.6 using the trapezoidal rule [87, 88, 7].

The determination of ΔS_m in materials with a FOPT and thermal hysteresis also uses field-dependent magnetization curves, but it demands more attention. A "thermal reset" procedure has been developed by Caron et al. [87], in order to avoid mixed magnetic states that generate incorrect ΔS_m values. The procedure consists of controlling the temperature and magnetic field of the sample. An illustration for the thermal reset procedure for obtaining field dependent curves around a cooling transition is observed in Figure 2.8, which are used to determine ΔS_m .

In a magnetic field as a function of temperature plot, the sample sits at the temperature T_i in (0). A magnetization process is thus executed at temperature

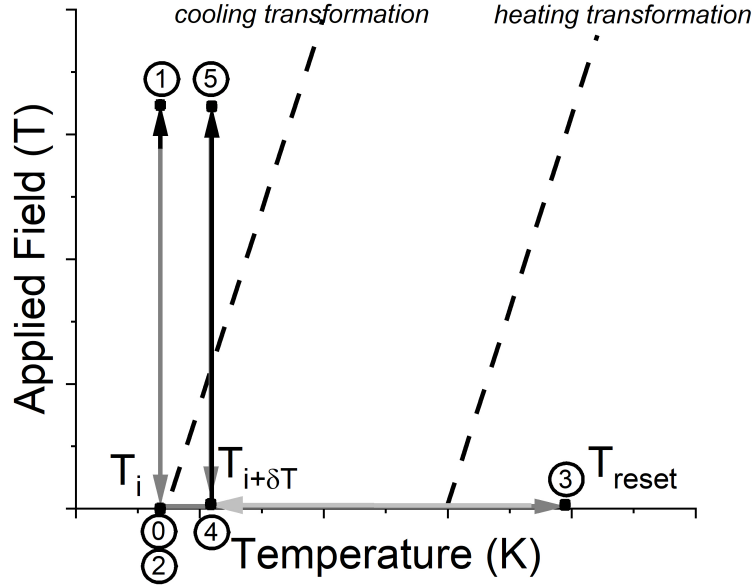


Figure 2.8: Depiction of magnetic field and temperature control procedure used to reset magnetic and thermal history states in FOPT materials. The specified procedure is for the determination of ΔS_m in cooling transitions.

T_i in (1). After the demagnetization (2), the sample must be heated up to ensure a full paramagnetic state at the reset temperature T_{reset} in (3). Subsequently, the sample can be cooled down (4) to the next field dependent measurement at $T_i + \delta T$ in (5). All field dependent curves should be obtained through this thermal reset procedure. The magnetization section of the field dependent curves obtained by this method can be numerically integrated to ensure the correct ΔS_m values. In the case of capturing heating transitions, the temperature is decreased, and the magnetic field remains applied, ensuring a full ferromagnetic state. The field dependent measurement used for determining ΔS_m in heating transitions should be the demagnetization step [89].

Analysis of magnetic data allows for further understanding of the order of the magnetic transitions. A qualitative evaluation of the order of the magnetic transition can be performed by the Banerjee criterion analysis: By graphing the square of the magnetization (M^2) as a function of the Applied field - magnetization ratio (H/M) (Figure 2.9), a negative slope in this curve (such as the one exemplified at in Figure 2.9 at $T = 272$ K) signals a first order character [90]. This method is widely employed, however it can present discrepancies between other methods, such as specific heat data [91].

A quantitative analysis to determine the order of magnetic transitions has recently been reported by Law et al. [92]. It consists of the study of the field dependence of ΔS_m as follows:

$$\Delta S_m \propto H^n \quad (2.13)$$

where n is a magnetic field and temperature dependent exponent. It is calculated

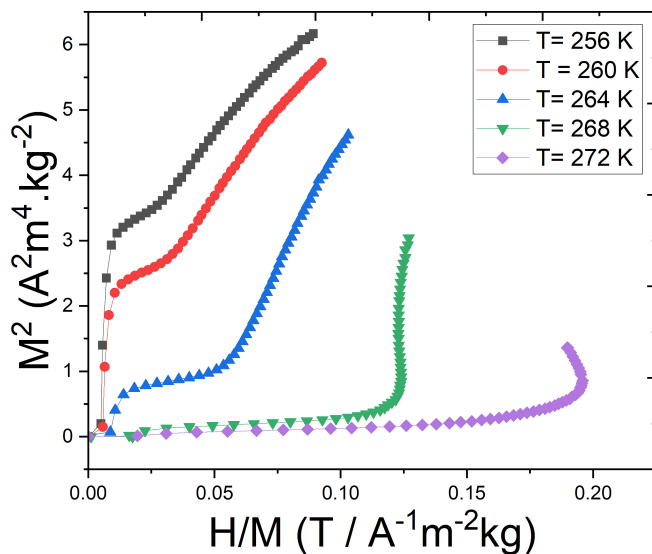


Figure 2.9: Representation of Arrott plots ($M^2(H/M)$) in a MnNiSi-based composition around its transition temperature. The negative slope is a qualitative indication of a FOPT, according to the Banerjee criterion.

as follows:

$$n(T, H) = \frac{d \ln |\Delta S_m|}{d \ln H} \quad (2.14)$$

For temperatures below the transition temperature, n is expected to be around 1. For temperatures far above the transition, n tends to 2. Around the transition region, the n exponent maximum varies as a function of the applied field. Inside this region, an overshoot of the n value above 2 is a clear indication of a FOPT around the transition region [92].

The structure and microstructure need to be characterized to be able to create structure-property relationships. These methods will be detailed in the next section.

2.7 Powder diffraction

For crystalline compounds, atoms are periodically arranged in 3 dimensions. The atoms or molecules in the crystal can be represented by an array of motifs arranged in space, the lattice. A crystalline material consists of a big number of equal units repeating in 3 dimensions. This unit is termed a unit cell. It is represented by a set of 3 basis vectors \mathbf{a} , \mathbf{b} and \mathbf{c} with angles α , β , and γ between them. The relationships between basis vector lengths and angles describe the seven different crystal systems, see Figure 2.10 [93].

The atoms in the unit cells are related to each other by a set of symmetry operations. The symmetry operations that work on the atoms in the unit cell

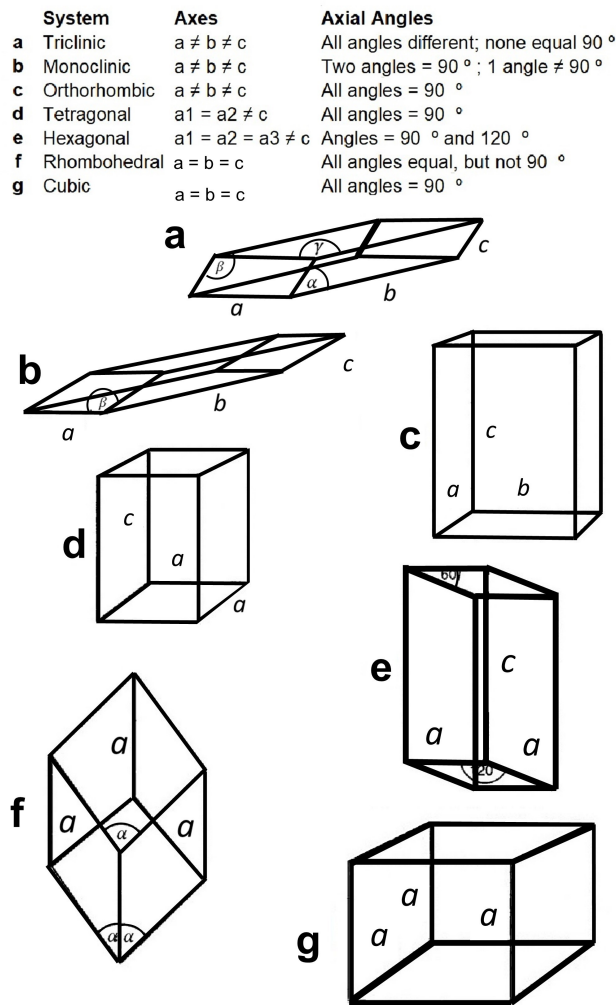


Figure 2.10: Description of the seven crystal systems, from lower (top) to higher (bottom) symmetry: (a) Triclinic, (b) Monoclinic, (c) Orthorhombic, (d) Tetragonal, (e) Hexagonal, (f) Rhombohedral, (g) cubic. Adapted from [58].

define what is known as a space group. There are 230 possible space groups in the 3-d space, distributed across the seven crystal systems.

These arrangements of the atoms in space groups can be explored using electromagnetic waves, for example x-rays. Some particles such as neutrons and electrons can also be used, due to the wave particle duality.

If X-rays or neutrons with a wavelength similar to a crystal's interatomic spacings are targeted towards a crystal, there will be coherent scattering by the crystal over specific directions, in a constructive interference process. This is also known as diffraction. A crystal will have a series of interatomic spacings determined by the lattice planes. A family of lattice planes can be described by a *Miller index*, with integers hkl , representing how many times the planes cut the **a**, **b**, or **c** axis, respectively. Diffraction occurs when the scattered beams from neighbouring lattice planes are in phase, giving rise to strong scattering. The geometrical relationship that expresses this phenomenon is known as *Bragg's law* [93]. For a wavelength λ it gives the scattering angle 2θ corresponding to the

lattice plane d_{hkl} :

$$\lambda = 2d_{hkl}\sin\theta \quad (2.15)$$

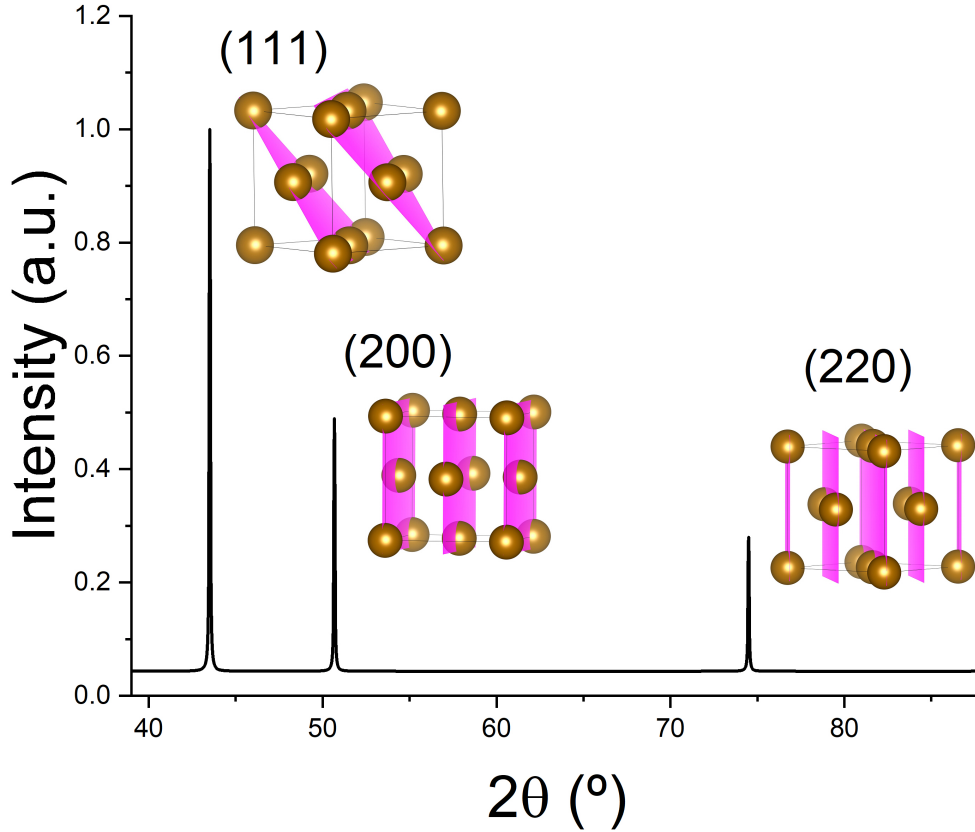


Figure 2.11: Calculated intensity in a Cu powder diffraction experiment as a function of 2θ for a ccp structure, with $a = 3.6 \text{ \AA}$ and $\lambda = 1.5406 \text{ \AA}$.

A diffraction pattern for the ccp lattice is exemplified in Figure 2.11. The most intense peak depicts the (111) planes, with the biggest planar atomic density. The other peaks in the figure represent the scattering from the (200) and (220) plane, with smaller atomic planar densities. Bragg's law allows description of the unit cell axis and angles from the positions of the Bragg peaks as a function of 2θ , d_{hkl} or the wavevector transfer \mathbf{Q} [93].

The intensities of the reflections are determined from the positions of the atoms in the unit cell. It is proportional to the square modulus of the structure factor F_{hkl} which describes the amplitude and phase of the scattered beam for a given hkl reflection:

$$I_{hkl} \propto |F_{hkl}|^2 = \left| \sum_{j=1}^N f_j \exp(2\pi i(hx_j + ky_j + lz_j)) \right|^2 \quad (2.16)$$

The sum occurs over all N atoms in the unit cell, while x_j , y_j , and z_j are the fractional coordinates of the j 'th atom, and f_j is its atomic scattering factor, which

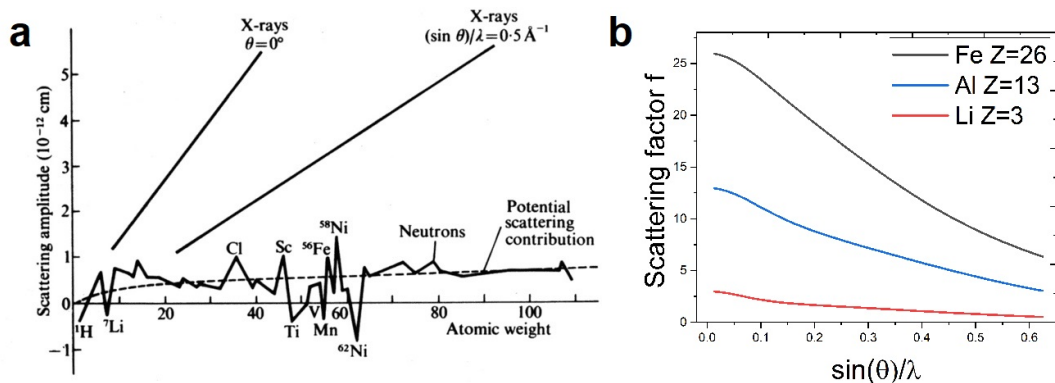


Figure 2.12: (a) The lines show scattering amplitude for X-rays with $\theta = 0$ and $\sin\theta/\lambda = 0.5 \text{ \AA}^{-1}$, respectively. At the bottom, scattering amplitude for neutrons. (b) The scattering amplitude for X-rays for Li, Al and Fe as a function of $\sin\theta/\lambda$.

is given by the scattering from the elements and depends on the type of radiation [93]. The photons in X-ray scattering experiments interact with the electrons of the sample. Each element scatters more or less depending on the number of electrons (and atomic weight), giving out different scattering amplitudes that influences 2.16, see Figure 2.12(a). X-rays will therefore present a very good contrast between elements of very different atomic numbers. The scattering factor also changes with the angle in relationship with the beam. It starts with a maximum value correspondent to the number of electrons of each element, and decays considerably as the angle increases, as shown in Figure 2.12(b) with Li ($Z=3$), Al ($Z=13$) and Fe ($Z=26$). It is seen that as $\sin(\theta)/\lambda$ increases to higher angles, destructive interference increases, and the number of electrons observed decrease. This is why intensities in X-rays decrease in higher 2θ values [94].

In neutron diffraction, neutrons interact basically with the nuclei of atoms, which are much smaller than the electron clouds. Due to this, the average number of interactions of neutrons with matter is much smaller than with X-rays. Besides this, the scattering amplitude (or scattering length) is not correlated to atomic number, with specific values for each nuclear configuration. It follows that the scattering amplitude of neutrons does not increase with larger atomic weight as X-rays, depicted in the bottom of Figure 2.12(a). Due to this, large contrasts can exist between neighbors in the Periodic Table or between isotopes of the same element. One example is the significant difference in scattering between Fe and Mn. The scattering amplitude does not depend on the $\sin(\theta)/\lambda$, and in general high angle neutron data are as intense as at lower angles. The two techniques are, therefore, complementary.

Another important feature with neutrons (spin 1/2) and unpaired electrons in compounds is magnetic scattering. Figure 2.13 exemplifies neutron diffraction experiments with (a) ferromagnetic and (b) antiferromagnetic materials. In the case of ferromagnetic interactions, the magnetic moments create reflections in the same positions as the nuclear ones, increasing the overall intensity. For antiferromagnetic materials, there are magnetic reflections at positions different from the Bragg peaks from the crystal structure. Magnetic space groups, size and

orientation of the magnetic moments can be determined from the powder neutron diffraction patterns.

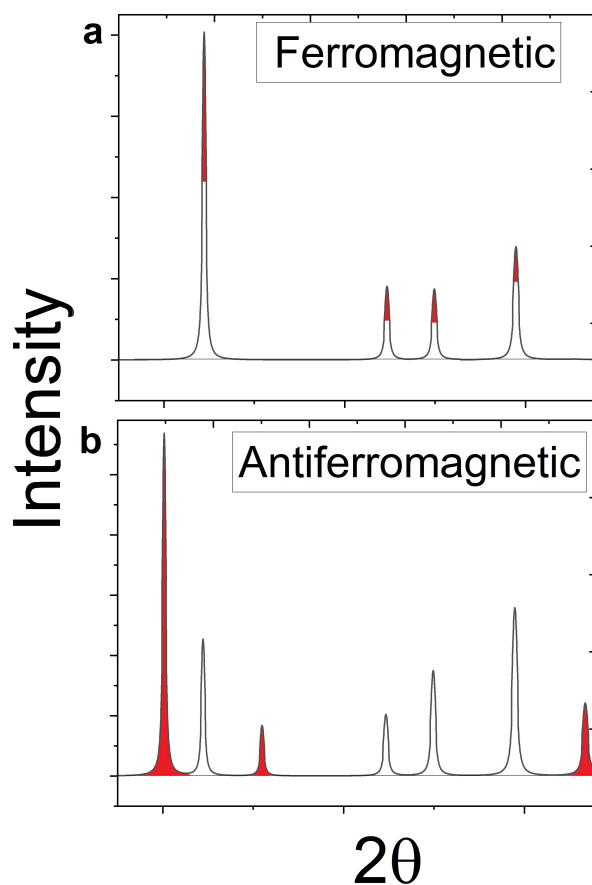


Figure 2.13: Hypothetical neutron diffraction patterns demonstrate the influence of different magnetic contributions in ferromagnetic materials (a), which add intensity to nuclear Bragg reflections, and antiferromagnetic materials (b), which add new reflections from the magnetic scattering

2.7.1 Rietveld Analysis

In some cases where Bragg peaks are overlapping, it becomes difficult and often impossible to extract intensities for each hkl . In 1969, Hugo Rietveld developed a method where the diffraction profiles were represented as a sum of Gaussian peaks [95]. It made possible to account for overlapping peaks. The peaks are modeled in order to represent the observed structural information in each Bragg reflection. The so-called Rietveld method has been further developed to characterize not only Gaussian peaks, but also taking into account microstructural and instrumental features [94]. The calculated intensities are described as follows:

$$Y_{calc}(hkl) = \mathbf{b}(hkl) + \sum_p \left(S_p \sum_{s(p)} (|F_{calc,hkl,p}|^2 2\theta_c \text{Corr}_{\mathbf{hkl},s,p}) \right) \quad (2.17)$$

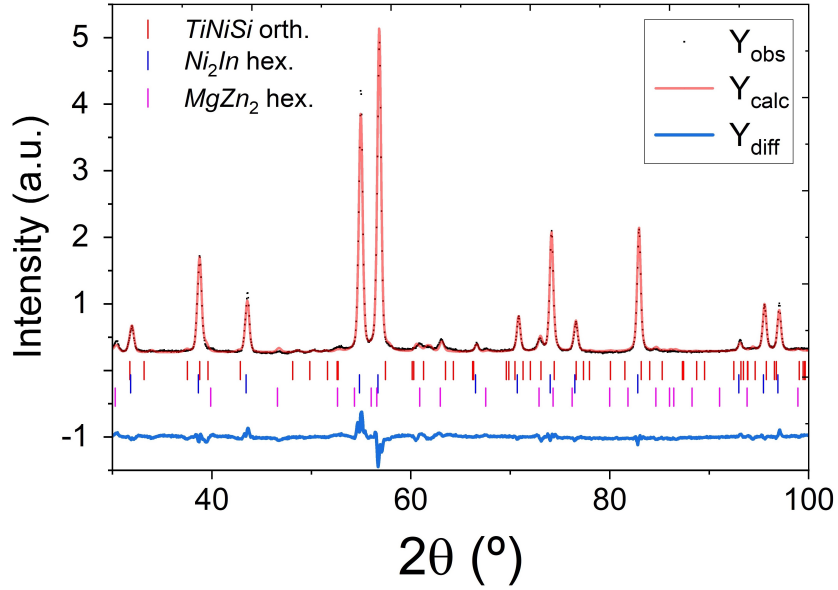


Figure 2.14: Example of a Rietveld refinement from Powder neutron diffraction data for a MnNiSi-based compound. Black points indicate the observed intensities. Red line displays the modeled intensities from the Rietveld refinement. The blue line indicates the difference between the observed and modeled intensities. The used wavelength was $\lambda = 1.89 \text{ \AA}$.

$b(hkl)$ is a polynomial function accounting for the background; the outer sum is for the different phases p . The sum $s(p)$ is for all Bragg reflections with indices hkl of the phase p . S_p is a scaling factor for phase p . $2\theta_c$ is the scattering angle with account instrumental zero-point offset and cosine dependency corrections, $\text{Corr}_{s,p,hkl}$ takes into account a series of correction parameters, and $|F_{hkl,s,p}|^2$ is the structure factor presented on Equation 2.16 [94].

A least-square algorithm aims to minimize the differences between the calculated intensities Y_{calc} and the observed intensities Y_{obs} , as follows:

$$\frac{\sum_i w_i |Y_{obs} - Y_{calc}|^2}{\sigma^2} \rightarrow 0 \quad (2.18)$$

where σ is the squared measurement uncertainties. An example of a Rietveld refinement is depicted in Figure 2.14. The goodness of fit can be evaluated by a series of figures of merit, such as the weighted R profile R_{wp} , comparing observed intensities Y_{obs} and calculated intensities Y_{calc} as follows:

$$R_{wp} = \sqrt{\frac{\sum_i w_i (Y_{obs} - Y_{calc})^2}{\sum_i w_i (y_{O,i})^2}} * 100\% \quad (2.19)$$

There are several software packages being used for the Rietveld refinements. In this thesis, the Fullprof Suite [96] and the TOPAS academic V6 software packages were used [94].

2.8 X-ray and Neutron sources

Powder X-ray Diffraction (PXD) can be performed both with laboratory diffractometers and by use of synchrotron facilities. Powder Neutron Diffraction (PND) are carried out using either reactor or accelerator-based international facilities.

2.8.1 Laboratory x-ray diffractometer

Most diffraction experiments are carried out using laboratory X-ray diffractometers. Such instruments consist of a filament (typically W) working as a cathode, and a water cooled anode made of a metal, typically Cu, Mo or Co. By the discharge, electrons are ejected from the W filament, accelerated and hit the metal target. The collisions create a spectrum of radiation, with sharp lines corresponding to the ejection of electrons from inner shells, with distinct energies for each atom and shell. For example, Cu $K\alpha$ X-rays have a distinct wavelength of $\lambda = 1.5406 \text{ \AA}$. With the help of filters and monochromators, the $K\alpha$ incident radiation can be used to probe a powder in the case of reflection (Bragg-Brentano flat plate geometry) mode, or a powder encapsulated in a capillary, for example made of borosilicate, in transmission (Debye-Scherrer geometry) mode. The scattering as a function of 2θ is typically measured with a 1D detector. The laboratory X-ray diffraction patterns seen in this thesis were obtained in a Bruker D2 in Bragg Brentano geometry, with Cu- $K\alpha$ radiation.

2.8.2 Synchrotron radiation x-ray

Synchrotron Radiation Powder X-ray Diffraction (SR-PXD) are carried out at facilities where the X-rays are produced by acceleration of electrons moving at nearly relativistic speeds. A major European facility is the European Synchrotron Radiation Facility (ESRF), in Grenoble, France. The wavelength of incoming X-rays can easily be changed, giving more versatility in the experiments. It also allows for significantly better resolution than laboratory x-rays, with a more intense beam. It can measure complete diffraction patterns in seconds. One possible type of experiment is temperature-dependent diffraction, to characterize structural transitions and thermal expansion behavior during heating or cooling. In the studies for this thesis, a series of experiments were performed in the BM-01 at the Swiss-Norwegian Beamline (SNBL) at the ESRF. The Bending Magnet source BM-01 has a spectral range of 10 to 22 keV ($\lambda = 1.24$ to 0.56 \AA). It employs a PILATUS2M 2-D pixel area detector, and can be used for high resolution single crystal and powder diffraction.

2.8.3 Neutron sources

Neutrons are subatomic particles used to probe the structures and dynamics of materials. Neutrons can be produced during nuclear fission, or by a spallation method where neutrons are generated from the collision of accelerated protons

into a metal target (typically tungsten or lead). Such facilities are known as spallation sources. In this thesis, PND experiments were carried out using the High Resolution Powder diffractometer for Thermal neutrons (HRPT) at SINQ, PSI. It uses thermal Neutrons that enable high resolutions [97].

The HRPT is a multidetector diffractometer, with a wide range of possible wavelengths, from $\lambda = 0.84$ to 2.96 \AA . The neutrons are monochromised with a focusing Ge-monochromator. The detection is done by 1600 detectors with 0.1 degree separations, contained in a single detector bank, thus covering 160 degrees in 2θ . The large number of possible wavelengths paired with a large number of possible sample environments such as cryostats, furnaces, pressure cells, etc. makes the HRPT a versatile instrument for PND experiments [97].

2.9 Microstructure observation methods

Diffraction is the main method to describe the average structure of materials. In order to discover where different crystallites and phases are located or arranged, microscopic methods are needed. Understanding of this is of great importance for the macroscopic properties. By analysis of the microstructure, the phase morphology and large defects can be evaluated. To do this, the surface area of a sample must be carefully prepared by grinding and polishing, enabling a microscopic visualization of the grains of the material.

It is performed by selecting a fracture surface of an ingot, and grinding the surface with sandpaper until a flat surface is achieved. In subsequent steps, the sample is grinded with finer mesh sandpapers until the surface becomes nearly mirrored. To be able to visualize microstructural features, polishing is needed. In this thesis, colloidal diamond particles were used with mean particle sizes of 3 , 1 , and $1/4 \mu\text{m}$. This step creates a mirrored surface, allowing for microstructural features to be discerned using light (light microscopy) or electrons (electron microscopy) are used.

2.9.1 Optical light microscopy

In the case of light microscopy, usually smaller magnifications are used, ranging from 5 to 1000 times. The use of polarized lenses in addition to regular objective lenses allows to discriminate different grain orientations. An polarized optical micrograph is exemplified in Figure 2.15.

2.9.2 Scanning Electron Microscopy and Energy Dispersive X-ray Spectroscopy

Larger magnifications can be obtained with electron microscopy. In Scanning Electron Microscopy (SEM), electrons are produced from a W filament and collimated through a series of magnetic lenses, that can then be used to scan a specific area selected by the user. The electrons interact with the sample, knocking out other electrons from the atoms of the sample, emitting photons. The photons

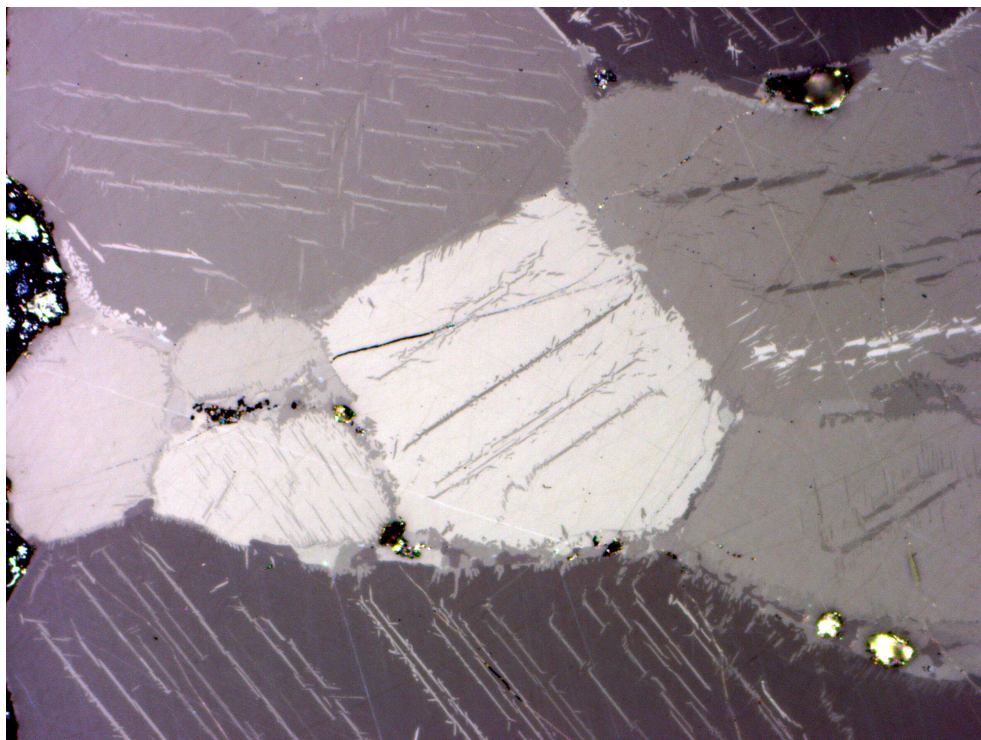


Figure 2.15: An example of an optical micrography employing polarized light for a MnNiSi intermetallic microstructure with a magnification of 31.5 times. Different grain orientations are seen as different grey hues.

can be captured by sensors, creating detailed images of the topography of the sample in secondary electron mode. Other sensors create images correlated to the atomic density of the sample, in back-scattered electron (BSE) mode, see Figure 2.16(a). In electron microscopes, much larger magnifications are possible, from 250 up to 1 million times magnification. The BSE mode is especially useful as it allows for the identification of different phases in the samples, since different phases will exhibit different atomic densities.

Another useful tool present in most SEMs is an Energy Dispersive X-ray Spectroscopy (EDS) probe. It allows to evaluate the local chemical composition from X-rays emitted by the samples atoms. They are emitted when inner-shell electrons are scattered by the SEM's electron beam. When an electron is ejected, the electron is replaced and thus emits radiation with specific energies given by the energy level it was occupying and the final energy level. The number (counts) of such events can be plotted as a function of the measured energy (unit eV).

From the resulting energy-dependent intensity plots, the chemical composition of the scanned area can be evaluated. Given the right conditions of electron beam and sample preparation, this technique allows for good accuracy (close to 2 weight % for each element) in determination of overall chemical composition. At the same time, it can also be used for determination of smaller areas, which enables measurements of chemical composition of individual phases such as the example on the right side of Figure 2.16(b).

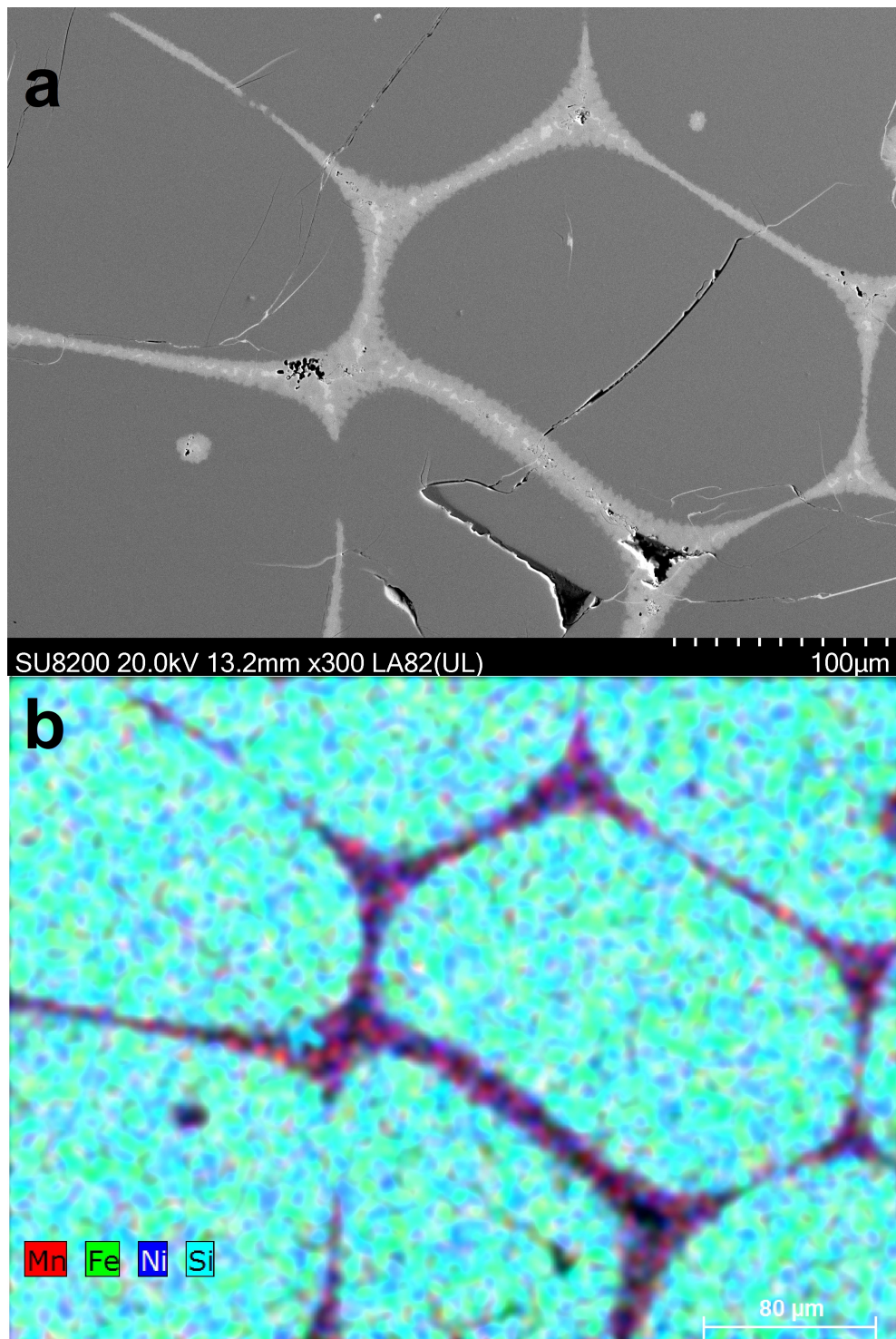


Figure 2.16: (a) SEM micrograph in BSE mode of a MnNiSi intermetallic with 300 times magnification. It unveils different atomic densities with different grey hues, which can be used to differentiate between phases. (b) In EDS elemental mapping mode, different color hues represent different atomic elements, contributing to understanding of the atomic distribution in different phases.

Chapter 3

Paper summary

The results in this thesis are divided between the study of magnetocaloric properties in high entropy alloys, which undergo typical SOPTs from ferro-to-paramagnetic states, and transition metal based intermetallics with FOPTs. The order of results is as follows: section 3.1 details the work from paper I, on the exploration of HEAs containing V/Al and V/Cu solid solutions with Fe, Co and Ni. Section 3.2 deals with magnetic transitions in the V-Fe-Co-Ni-Cu system (see paper II). Section 3.3 (corresponding to paper III) introduces the novel $\text{Mn}_{1-w}\text{Ni}_{1-w}\text{Fe}_{2w}\text{Si}_{0.95}\text{Al}_{0.95}$ intermetallics, with Fe as substituent on the two transition metal sites, and Al on the p-block site. Section 3.4 (paper IV) details the structural and magnetic properties of different Fe substitutions in $\text{MnNiSi}_{0.95}\text{Al}_{0.95}$. In section 3.5 a summary of paper V is presented, where the effects of different heat treatments on the magnetocaloric properties of novel $\text{Mn}_{1-w}\text{Ni}_{1-w}\text{Fe}_{2w}\text{Si}_{0.95}\text{Al}_{0.95}$ compounds are evaluated.

3.1 Exploring V-containing High Entropy Alloys (Paper I)

Bruno G. F. Eggert, Erna K. Delczeg-Czirjak, Fernando Maccari, Susmit Kumar, Oliver Gutfleisch, Helmer Fjellvåg, Bjørn C. Hauback, Christoph Frommen ‘**Exploring V-Fe-Co-Ni-Al and V-Fe-Co-Ni-Cu high entropy alloys for magnetocaloric applications**’. In: *Journal of Alloys and Compounds*. Volume 921, (2022), <https://doi.org/10.1016/j.jallcom.2022.166040>.

Paper I is a preliminary exploration of the magnetocaloric properties of two novel series of HEAs: V-Fe-Co-Ni-Al and V-Fe-Co-Ni-Cu. They were selected following the work of Alice Perrin which concluded on the necessity of 5-element alloys, with one element inducing antiferromagnetic interactions (with strong negative J_{ex} 's), Fe, Co, Ni, and a fifth element that dilutes the magnetic exchange interactions [51]. This first section is dedicated to a preliminary exploration of the magnetocaloric properties of two novel series of HEAs, V-Fe-Co-Ni-Al and V-Fe-Co-Ni-Cu. They were selected following the work of Alice Perrin's PhD thesis, which did a preliminary study on magnetocaloric HEA's and concluded on

the necessity of 5-element alloys, with one element inducing strong negative J_{ex} 's, Fe, Co, Ni, and a fifth element that dilutes the system [51].

To follow it up, a screening of thermodynamic properties of 36 different 5-element systems, combining one early transition metal element (between V, Cr, Mn, Ti, Zr, Nb) and one "dilution element" (Cu, Al, Zn, Pd, Sn, Si), together with Fe, Co and Ni, in equiatomic composition. From the 36 possible combinations, 8 systems have thermodynamic properties relevant for "solid solution formation" [38, 39]. Out of these 8 compositions, V-Fe-Co-Ni-Al and V-Fe-Co-Ni-Cu were selected since they weren't explored in the literature, and Cu/Al have very different VEC values, that might induce different bcc or ccp structures. Samples were synthesized by arc melting, and turned 5 times to ensure homogeneity. Nominal compositions of $V_{1-x}FeCoNiAl_{1+x}$ were $x=0.2, 0.4, 0.5, 0.75$, and $x=0.15, 0.2, 0.4, 0.5, 0.75$ for $V_{1-x}FeCoNiCu_{1+x}$.

By using the CALPHAD method implemented in the Thermo-Calc 2021 software package, pseudobinary diagrams for $V_{1-x}FeCoNiAl_{1+x}$ and $V_{1-x}FeCoNiCu_{1+x}$ were obtained considering all possible phases formed. The CALPHAD method predictions are comparable to the results obtained by PXD and SEM investigations in $V_{1-x}FeCoNiAl_{1+x}$, but are dissimilar in $V_{1-x}FeCoNiCu_{1+x}$. This can be correlated to the metastable states induced by the fast cooling during the arc-melting process. This reinforces the role of thermodynamic properties as guidelines for solid solution formation in HEA systems.

To understand the impact of alloying elements on the magnetic ordering temperature T_C , samples were evaluated by a magnetic balance between 300 and 1200 K, and by low-field magnetization measurements in a PPMS between 100 and 390 K. The magnetic transitions for equiatomic VFeCoNiAl and VFeCoNiCu are presented as red and black curves in Figure 3.1(a), respectively. Obtained T_C s are of 155 K, 200 K, and 456 K for VFeCoNiAl, $V_{0.8}FeCoNiAl_{1.2}$ and $V_{0.25}FeCoNiAl_{1.75}$, respectively. In the $V_{1-x}FeCoNiCu_{1+x}$ system, the measured T_C s are 230 K, 329 K, 345 K, 440 K, 521 K and 736 K for $x=0, 0.15, 0.2, 0.4, 0.5$ and 0.75 , respectively. The magnetic properties of $V_{0.85}FeCoNiCu_{1.15}$, with a T_C s close to room temperature, were further investigated by field-dependent magnetization measurements. Relatively small ΔS_m values of -0.15, -0.3 and -0.75 for a field change of $\mu_0 H = 0 - 1, 0 - 2$ and $0 - 5$ T, see Figure 3.1(b), can be partly attributed to the large number of exchange interactions. To gain further insight into the strength and character of the different exchange interactions, Density functional theory calculations were conducted, where the detrimental effect of V, together with the dilution effect of Cu and Al were shown to greatly reduce the ferromagnetic behavior of the Fe-Co-Ni based solid solutions.

In conclusion, this paper reports on novel $V_{1-x}FeCoNiAl_{1+x}$ and $V_{1-x}FeCoNiCu_{1+x}$ HEA's, their (micro)structure and magnetic properties. The experimental results were complemented by CALPHAD predictions and DFT calculations. The shift in V/Al and V/Cu content modifies T_C s, from below to above room temperature. However, the broad magnetic transitions are detrimental for magnetocaloric applications, as showcased by low ΔS_m values of -0.75 J/kg.K for a $\mu_0 H = 0-5$ T field change. This result was similar to other reported HEAs such as Cr-Fe-Co-Ni-Al and Mn-Fe-Co-Ni-Cu [48, 35, 34]. These values are still

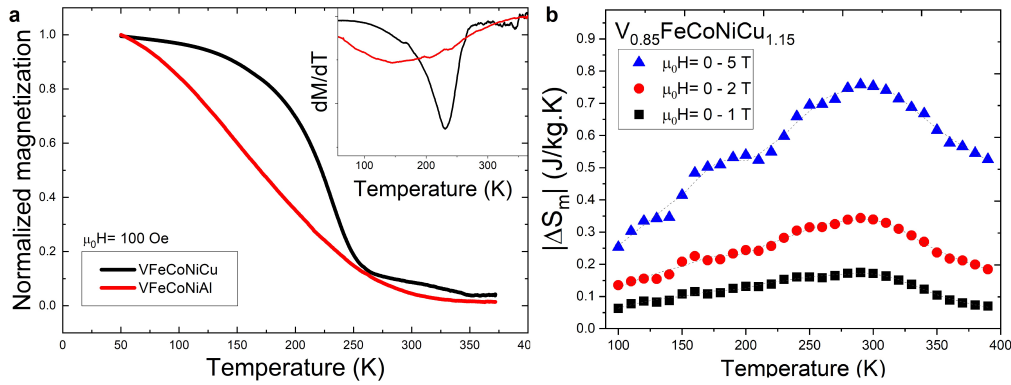


Figure 3.1: (a) Temperature dependent magnetization curves with applied field of $\mu_0 H = 100$ Oe in equiatomic VFeCoNiCu and VFeCoNiAl samples with transitions below room temperature, illustrating the broadness of the magnetic transitions across the observed temperature range. (b) ΔS_m measured in $V_{0.85}FeCoNiCu_{1.15}$ in applied field changes of $\mu_0 H = 0-1, 0-2$ and $0-5$ T.

small compared to other common magnetocaloric materials which range from $\Delta S_m = 5 - 15$ J/kg.K for a $\mu_0 H = 0 - 1$ T magnetic field change [30].

Contributions My contributions in this paper relate to the synthesis of the compounds, CALPHAD predictions, PXD experiments and subsequent analysis, magnetic balance measurements, and magnetic data analysis. Low temperature magnetic measurements were carried out by coauthors in Darmstadt and Oslo. Density Functional Theory calculations were performed by coauthors at the University of Uppsala. I was the writer of the original manuscript, and received contributions to the preparation of further iterations of the manuscript.

3.2 Magnetic transitions of V-Fe-Co-Ni-Cu-based alloys (Paper II)

Bruno G. F. Eggert, Erna K. Delczeg-Czirjak, Bjørn C. Hauback, Christoph Frommen ‘Magnetic transitions in V-Fe-Co-Ni-Cu-based high entropy alloys’. In *Materials Today Physics*. Volume 35, (2022), <https://doi.org/10.1016/j.mtphys.2023.101116>.

In paper I, small ΔS_m values and broad magnetic transitions were attributed to the large number of exchange interactions, and disorder at a local level. With this in mind, a subsequent study was performed to understand the specific roles of Cu and V in the structure, microstructure and magnetic properties of $V_{1-x}FeCoNiCu_{1+x}$ alloys. This system was chosen over $V_{1-x}FeCoNiAl_{1+x}$ since it presented more abrupt magnetic transitions. The following four specific compositions were investigated by PXD, Electron microscopy and magnetic measurements: FeCoNi, FeCoNiCu_{1.15}, V_{0.85}FeCoNi, and V_{0.85}FeCoNiCu_{1.15}. This study did not only confirm the individual roles of Cu and V for the modification of T_{CS} , but also provided insight on the role of different alloying elements on the abruptness of the magnetic transitions (dM/dT), which is relevant for

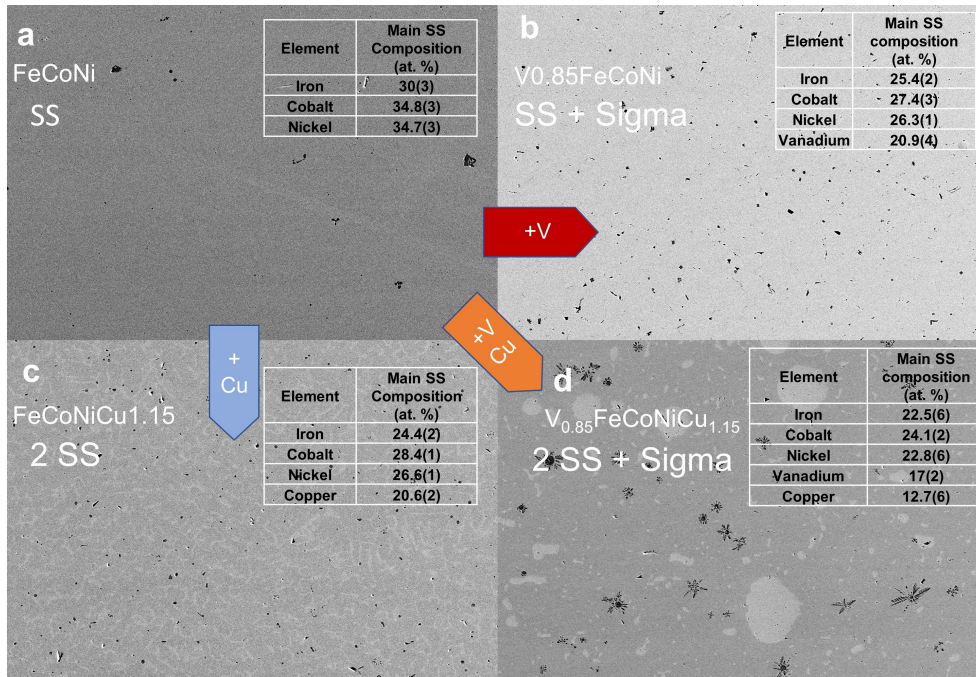


Figure 3.2: Scanning electron micrographs obtained in BSE mode with a magnification of 250x, showing the microstructure of four solid solutions: (a) FeCoNi, (b) V_{0.85}FeCoNi, (c) FeCoNiCu_{1.15} and (d) V_{0.85}FeCoNiCu_{1.15}. Either one or two solid solutions (SS) or a mix of SS and a sigma intermetallic are observed. The atomic compositions of the main ccp solid solution are shown in the insert for each of the four studied alloys.

magnetocaloric properties.

The investigated alloys presented only ccp reflections in their diffraction patterns, thus all samples were nearly monophasic with disordered ccp phases. While analysing the microstructure (Figure 3.2) of V_{0.85}FeCoNiCu_{1.15} however, in Figure 3.2(d), a multiphasic material was observed in electron microscopy. This is correlated to the lack of solubility between V and Cu that yields formation of a secondary liquid phase before solidification. This is also predicted by CALPHAD assessments.

The magnetic transitions observed in Figure 3.3(a) in the vicinity of T_C highlight the impact of Cu and V on absolute magnetization values and the thermal dependence on the magnetization: FeCoNi and FeCoNiCu_{1.15} show the same transition behavior. When V is introduced in V_{0.85}FeCoNi, and V_{0.85}FeCoNiCu_{1.15}, the slope of the curves are modified and they become much broader. This is also visualized by the absolute derivative of the magnetization ($|dM/dT|$) in Figure 3.3(b), where the values of V-containing samples are much smaller than FeCoNi and FeCoNiCu_{1.15}. DFT evaluations of the exchange interactions disclose the role of V: it dilutes the ferromagnetic elements, it couples antiparallel to them, and leads to a decrease of the magnetic exchange interactions in the ferromagnetic elements; J_{Fe-Fe} , J_{Fe-Co} and J_{Co-Co} for example, are strongly reduced.

This comprehensive study sheds light into the impact of Cu and V into the thermal dependence of the magnetization in FeCoNi-based alloys. It is demonstrated that the introduction of V is deleterious for the absolute

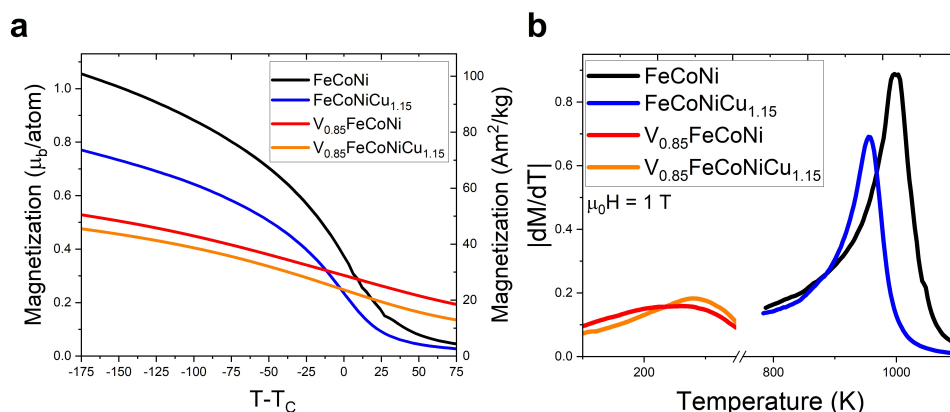


Figure 3.3: (a) Magnetization as a function of temperature for the four studied alloys with applied fields of $\mu_0 H = 1$ T, in Bohr magneton/atom on the left, and in Am^2/kg on the right. (b) Absolute derivative of magnetization as a function of temperature for the studied alloys, allowing one to compare the transitions with each modification. With the introduction of Cu, a decrease in absolute magnetization is observed, but the overall behaviour is unchanged. In V-containing alloys, absolute magnetization, and derivatives of magnetization (dM/dT) are strongly modified.

magnetization and the abruptness of the transition, which is correlated to the magnetocaloric effect. However, V is crucial to lower the transition temperature. **Contributions** My contributions in this paper relate to the synthesis of the compounds, CALPHAD predictions, PXD experiments, microscopic sample preparation, electron microscopy, high temperature magnetic measurements, and subsequent data analysis. Low temperature magnetic measurements were conducted by Prof. Martin Valldor in Oslo. Density Functional Theory calculations were performed by one of the coauthors at the University of Uppsala. I was the writer of the original manuscript, and received contributions to the preparation of further iterations of the manuscript.

3.3 MnNiSi-based intermetallics with Fe and Al (Paper III)

Bruno G. F. Eggert, João Horta Belo, João P. Araújo, Bjørn C. Hauback, Christoph Frommen ‘**Structural transitions and magnetocaloric properties of low-cost MnNiSi-based intermetallics**’ In: *Intermetallics*. Volume 154, (2022), <https://doi.org/10.1016/j.intermet.2023.107823>

Even though magnetic ordering temperatures in HEAs can be easily tuned, their ΔS_m values are not competitive compared to La-Fe-Si or Heusler alloys. On the other hand, MM’X compounds are also based on transition metals, can be synthesized with non-critical elements, and undergo a magnetostructural transition with large ΔS_m . With this in mind, the following study was suggested to create the most affordable MM’X compound possible, with magnetostructural transitions at room temperature which resulted in paper III. For the first time, the triple

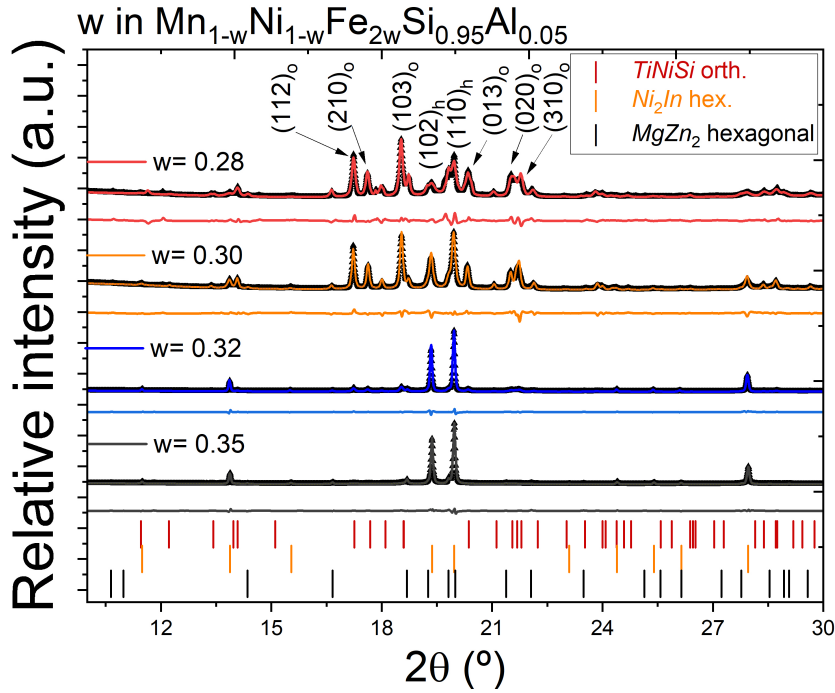


Figure 3.4: Rietveld refinements of $\text{Mn}_{1-w}\text{Ni}_{1-w}\text{Fe}_{2w}\text{Si}_{0.95}\text{Al}_{0.05}$, with $w=0.28, 0.30, 0.32$, and 0.35 at $T=300$ K. Black points display the observed intensities, while colored curves exhibit the calculated intensities for each composition. The light colored curve in the bottom is the difference between observed and calculated intensities. The red ticks below observed/calculated intensities represent the orth. structure, yellow ticks the Ni_2In -type hex. structure, and in black ticks, the MgZn_2 -type hex. structure.

substituted $\text{Mn}_{1-w}\text{Ni}_{1-w}\text{Fe}_{2w}\text{Si}_{0.95}\text{Al}_{0.05}$ compounds with $w=0.28, 0.3, 0.32$, and 0.35 were investigated with respect to their structural, microstructural, caloric, and magnetic properties. They were synthesized by arc melting, and undergone heat treatment for 1 week at 1073 K. The samples were then quenched in water.

Rietveld refinements from SR-PXD data at $T=300$ K in Figure 3.4 indicate an increasing amount of the hexagonal Ni_2In -type phase (named as hex.) in detriment of the orthorhombic TiNiSi -type phase (named as orth.), with increasing Fe contents. All of the samples depict the presence of a third phase with hexagonal MgZn_2 structure in the diffraction patterns. For $w=0.28$, an additional fourth phase with hexagonal Fe_5Si_3 structure was found.

From DSC measurements, all 4 compositions of $\text{Mn}_{1-w}\text{Ni}_{1-w}\text{Fe}_{2w}\text{Si}_{0.95}\text{Al}_{0.05}$ are shown in Figure 3.5(a) where latent heat peaks during heating and cooling are associated to the structural transitions. Variations in the magnetostructural transition temperature during heating T_{t_o-h} occur from 419 K in $w=0.28$ to 217 K in $w=0.35$. Therefore, larger w contents in $\text{Mn}_{1-w}\text{Ni}_{1-w}\text{Fe}_{2w}\text{Si}_{0.95}\text{Al}_{0.05}$ shift T_t to lower temperatures. The transitions observed by DSC are generally broad, and hint at a high level of atomic disorder. Another characteristic is the large hysteresis between heating and cooling transitions, ranging between 34 to 46 K. The structural transition was also confirmed by in-situ SR-PXD during heating, where the TiNiSi orth. reflections vanish as the Ni_2In hex. appear.

3.3. MnNiSi-based intermetallics with Fe and Al (Paper III)

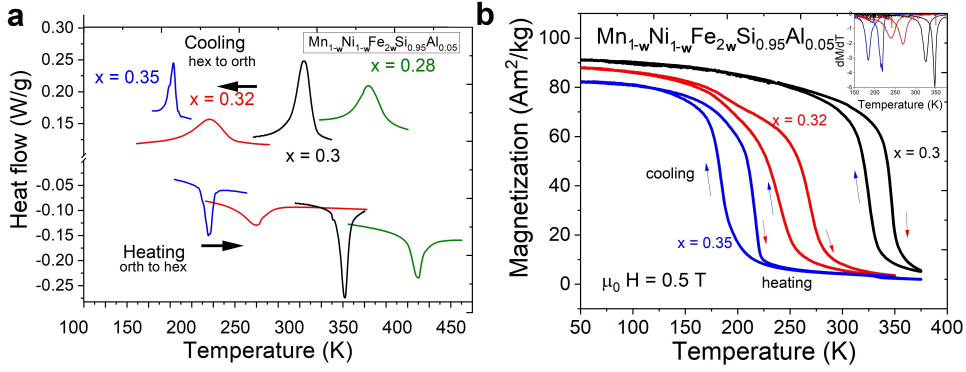


Figure 3.5: a) DSC analysis in $\text{Mn}_{1-w}\text{Ni}_{1-w}\text{Fe}_{2w}\text{Si}_{0.95}\text{Al}_{0.05}$, with $w=0.28, 0.30, 0.32$, and 0.35 . b) Temperature dependent magnetization displaying the MST in $w=0.3, 0.32$ and 0.35 .

Temperature-dependent magnetization curves show abrupt magnetization changes during heating and cooling, at temperatures that match the structural transition temperatures observed in the DSC, Figure 3.5(b). This confirms coupled magnetic and structural transitions across three of the observed compositions ($\text{Mn}_{0.72}\text{Ni}_{0.72}\text{Fe}_{0.56}\text{Si}_{0.95}\text{Al}_{0.05}$ had T_t beyond the temperature limit of the equipment).

$\text{Mn}_{0.7}\text{Ni}_{0.7}\text{Fe}_{0.6}\text{Si}_{0.95}\text{Al}_{0.05}$ to examine the magnetocaloric effect of the cooling transition in detail. Isotherms were obtained around the cooling transition (T_{h-o}) from 310 to 364 K, with 2 K temperature steps employing the thermal reset procedure described in section 2.6.3. The peak ΔS_m values are -4.2, -8.15, -19.15 and -26.45 J/Kg.K for magnetic field changes of $\mu_0 H = 0-1, 0-2, 0-5$ and $0-7$ T, respectively. Analysis using the Banerjee criterion lead one to conclude a FOPT due to a slight negative slope on the $M^2(H/M)$ curves. Further analysis of the magnetic isotherms using the n-criterion analysis disclosed a n-exponent overshoot above 2 in the transition region for magnetic field changes above $\mu_0 H = 0-3$ T, which confirms a FOPT.

In summary, the novel $\text{Mn}_{1-w}\text{Ni}_{1-w}\text{Fe}_{2w}\text{Si}_{0.95}\text{Al}_{0.05}$ compounds have transitions at room temperature, and comparable ΔS_m values to some of the best magnetocaloric materials known in the literature while only featuring common elements such as Fe, Ni and Mn. The reported ΔS_m values are higher than melt-spun $\text{Mn}_{1-x}\text{Fe}_x\text{NiSi}_{1-y}\text{Al}_y$ ribbons or arc melted $\text{MnNi}_{1-x}\text{Fe}_x\text{Si}_{1-y}\text{Al}_y$, but lower than other arc-melted $\text{Mn}_{1-x}\text{Fe}_x\text{NiSi}_{1-y}\text{Al}_y$ compounds [98, 99, 100, 101]. The associated thermal hysteresis severely hinders its reversible effect. To understand this discrepancy between compositions, $\text{MnNiSi}_{0.95}\text{Al}_{0.05}$ compounds with different Fe substitutions were compared and discussed in paper IV (next section).

Contributions My contributions in this paper relate to synthesis and processing of the compounds, room temperature and in-situ heating SR-PXD experiments, DSC experiments, microscopic sample preparation, light and electron microscopy experiments, and subsequent data analysis. Low temperature magnetic measurements were completed by a coauthor in Porto. I was the writer of the original manuscript, and received contributions to the preparation of further iterations of the manuscript.

3.4 Structure and magnetism of Fe-substituted MnNiSi_{0.95}Al_{0.05} (Paper IV)

Bruno G. F. Eggert, Erna K. Delczeg-Czirjak, Øystein S. Fjellvåg, Bjørn C. Hauback, Christoph Frommen ‘Structure and Magnetism of Fe-substituted MnNiSi_{0.95}Al_{0.05}’ *To be submitted.*

Paper IV investigates in detail how Fe-substitution on the different transition metal sites affects the structural and magnetic transitions in the following series of MnNi(SiAl) compounds: Mn_{1-x}Fe_xNiSi_{0.95}Al_{0.05}, MnNi_{1-y}Fe_ySi_{0.95}Al_{0.05} and Mn_{1-w}Ni_{1-w}Fe_{2w}Si_{0.95}Al_{0.05}, where x= 0.45,0.5, and 0.55, y= 0.55,0.6,0.65, and w=0.3,0.32, and 0.35.

SR-PXD was done at 310 K for all compounds. In paper III, Rietveld refinement was done on Mn_{1-w}Ni_{1-w}Fe_{2w}Si_{0.95}Al_{0.05} at a temperature of T=300 K. Recognizing the influence of temperature on phase fraction near phase transformation temperatures, this data are gathered at the temperature of 310 K to match experimental conditions of PND experiments and away from transition temperatures. The diffraction patterns analysed by Rietveld refinement disclose that similarly to Mn_{1-w}Ni_{1-w}Fe_{2w}Si_{0.95}Al_{0.05} reported in the previous section, larger Fe contents stabilize the *Ni₂In*-type hexagonal structure in Mn_{1-x}Fe_xNiSi_{0.95}Al_{0.05}. The *MgZn₂*-type hexagonal structure was also observed across all studied compositions.

In the case of MnNi_{1-y}Fe_ySi_{0.95}Al_{0.05} compounds, only trace amounts of the orth. *TiNiSi* was observed. Instead, a majority of Mn₅Si₃-type (S.G. *P6₃/mcm*) and *MgZn₂* phases matched most of the reflections observed in the diffraction patterns. Other peaks correspond to *TiNiSi*-type (also known as *Co₂Si*) and PbCl₂-type orthorhombic phases, which are reported in the Mn-Ni-Si diagram [102]. Similar compositions were already investigated by Nuendute et al. where drastic differences in phase formation were reported depending on different thermal histories of MnNi_{1-y}Fe_ySi_{1-p}Al_p [100].

To assess occupancies and possible intermixing between atomic sites, PND is executed in the studied Mn_{0.45}Fe_{0.55}NiSi_{0.95}Al_{0.05} and Mn_{0.68}Ni_{0.68}Fe_{0.64}Si_{0.95}Al_{0.05} compositions. Two neutron experiments were carried out for both samples, with different thermal histories:

- 1) Refinement of nuclear structure: the sample is heated up to 340 K so that a majority of the sample retains a hexagonal (*P6₃/mmc*) phase, and later cooled to 310 K, where data acquisition takes place. This is done to measure the occupancies in the hex. phase, and check for intermixing between Mn and Ni sites;
- 2) Refinement of magnetic structure: A low temperature measurement, with a orth. (*Pnma*) phase majority at 240 K, yields information about the magnetic scattering of the orth. phase and magnetic moments associated to the transition metal sites.

3.4. Structure and magnetism of Fe-substituted $\text{MnNiSi}_{0.95}\text{Al}_{0.05}$ (Paper IV)

To lower the uncertainties in peak intensities associated with magnetic scattering and the atomic coordinates, neutron and x-ray powder diffraction patterns were used in combined refinements. The refined occupancy values in the Ni_2In hex. phase reveal a slightly larger Fe content than their nominal compositions. This can be correlated to the presence of the secondary MgZn_2 hex. phase, which are a Mn-Ni-Si rich composition. Therefore, the main phases (TiNiSi orth./ Ni_2In hex.) retain a larger amount of Fe. Regarding intermixing, no substantial improvement of the refinement fits was observed in the combined refinements at $T=310$ K with Mn in Ni sites, and vice-versa. Therefore, there are no evident signs of intermixing.

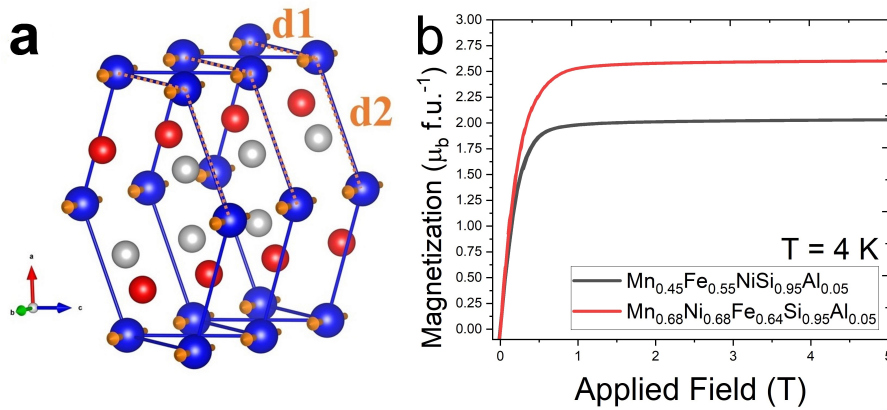


Figure 3.6: (a) Illustration of the TiNiSi -type orthorhombic structure depicting the $d1$ (out-of-plane) and $d2$ (in-plane) distances. (b) Magnetization as a function of applied field for $\text{Mn}_{0.45}\text{Fe}_{0.55}\text{NiSi}_{0.95}\text{Al}_{0.05}$ and $\text{Mn}_{0.68}\text{Ni}_{0.68}\text{Fe}_{0.64}\text{Si}_{0.95}\text{Al}_{0.05}$.

The absence of large peaks at low angles that are not from the TiNiSi , Ni_2In or MgZn_2 structures in PND patterns indicate that both samples are ferromagnetic. Refinement of the magnetic moments is performed by symmetry analysis, in search for Shubnikov magnetic space groups with a propagation vector $k(0,0,0)$. Eight space groups exist where $4c$ sites carry a magnetic moment in this configuration: #62.441, #62.443, #62.444, #62.445, #62.446, #62.447, #62.448, and #62.449. When testing the space groups, the $\text{Pn}'\text{ma}'$ (62.448) magnetic space group, with Mn and Ni site moments parallel to the b axis of the orthorhombic structure, similarly to the MnNiSi parent compound [64]. This is illustrated in Figure 3.6(a). The local magnetic moments obtained by PND agree well with those calculated within the framework of DFT and macroscopic measurements. The total magnetic moment is larger for $\text{Mn}_{0.68}\text{Ni}_{0.68}\text{Fe}_{0.64}\text{Si}_{0.95}\text{Al}_{0.05}$ than for $\text{Mn}_{0.45}\text{Fe}_{0.55}\text{NiSi}_{0.95}\text{Al}_{0.05}$, see Figure 3.6(b). This can be attributed to the presence of Fe in Ni sites, which raises the Ni site moment. The larger overall moment is an important result, as it indicates that a higher magnetocaloric effect can be obtained for $\text{Mn}_{1-w}\text{Ni}_{1-w}\text{Fe}_{2w}\text{Si}_{0.95}\text{Al}_{0.05}$ than on $\text{Mn}_{1-x}\text{Fe}_x\text{NiSi}_{0.95}\text{Al}_{0.05}$. However, the overall MCE can be affected by transition kinetics.

Contributions My contributions in this paper relate to synthesis and processing of the compounds, room temperature and in-situ heating SR-PXD experiments, DSC experiments, microscopic sample preparation, electron microscopy experiments, and subsequent data analysis. Low temperature magnetic

measurements were performed by Prof. Martin Valldor in Oslo. Powder Neutron diffraction experiments and analysis were conducted by one of the coauthors at Villigen. Density Functional Theory calculations were performed by a coauthor at the University of Uppsala. I was the writer of the original manuscript, and received contributions to the preparation of further iterations of the manuscript.

3.5 Study of the magnetostructural transition in critical-element free $\text{Mn}_{1-w}\text{Ni}_{1-w}\text{Fe}_{2w}\text{Si}_{0.95}\text{Al}_{0.05}$ (Paper V)

Bruno G. F. Eggert, Kun Wang, Sina Jafarzadeh, Christian R. Bahl, Bjørn C. Hauback, Christoph Frommen ‘**Study of the magnetostructural transition in critical-element free $\text{Mn}_{1-w}\text{Ni}_{1-w}\text{Fe}_{2w}\text{Si}_{0.95}\text{Al}_{0.05}$** ’ In: *API Advances*. Volume 13, (2023), <https://doi.org/10.1063/9.0000511>

A low magnetostructural coupling is seen in the $\text{Mn}_{1-w}\text{Ni}_{1-w}\text{Fe}_{2w}\text{Si}_{0.95}\text{Al}_{0.05}$ samples, compared to $\text{Mn}_{1-x}\text{Fe}_x\text{NiSi}_{0.95}\text{Al}_{0.05}$. This was partly attributed, in papers III and IV, to inhomogeneity at a local level. To address this issue, modifying the thermal history of the compounds is important for establishing local homogeneity in MM’X compounds. Therefore, a different heat treatment procedure was suggested for $\text{Mn}_{1-w}\text{Ni}_{1-w}\text{Fe}_{2w}\text{Si}_{0.95}\text{Al}_{0.05}$ compounds, and the impact of the heat treatment was compared to the regular heat treatment used in papers III and IV. The resulting alloys’ structure and microstructure are evaluated, together with magnetic and caloric properties.

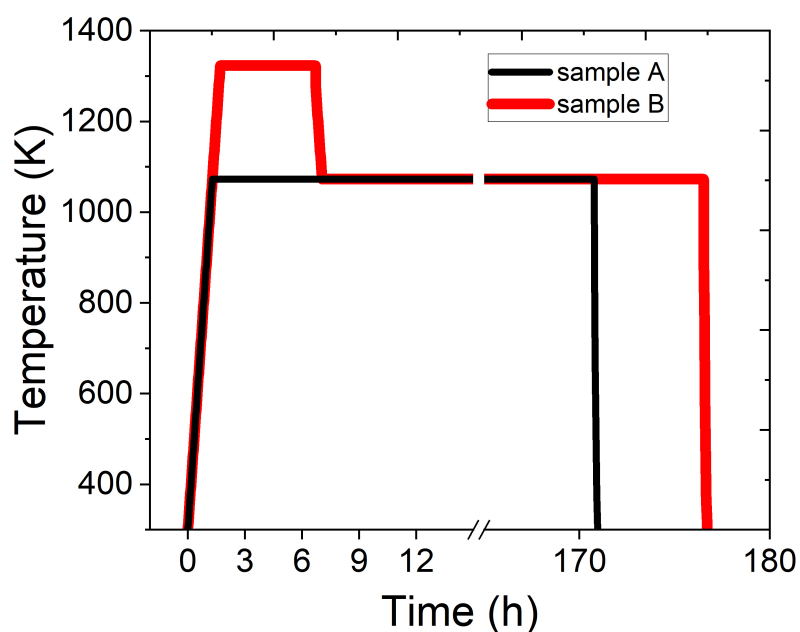


Figure 3.7: Heat treatment profile used for samples A and B.

3.5. Study of the magnetostructural transition in critical-element free $\text{Mn}_{1-w}\text{Ni}_{1-w}\text{Fe}_{2w}\text{Si}_{0.95}\text{Al}_{0.05}$ (Paper V)

$\text{Mn}_{1-w}\text{Ni}_{1-w}\text{Fe}_{2w}\text{Si}_{0.95}\text{Al}_{0.05}$ intermetallics were synthesized with pre-alloyed MnNiSi intermetallic ingots, together with Fe, Si and Al in a Ti-gettered arc melting furnace. Ingots were later sealed in quartz tubes under vacuum, and heat treated according to the two different routes depicted in Figure 3.7: In sample A, the ingot was kept at 1073 K for 7 days and quenched in water. In sample B, the sample was heated to a high temperature step at 1323 K for 5 hours, and then kept at 1073 K for 7 days (168 hours), followed by quenching. We selected two samples with T_t around room temperature, with slightly different nominal compositions, namely $\text{Mn}_{1-w}\text{Ni}_{1-w}\text{Fe}_{2w}\text{Si}_{0.95}\text{Al}_{0.05}$, with $w=0.32$ for Sample A, and $w=0.31$ for Sample B.

By using EDS area measurements, the compositions of the hex./orth. phases of samples A and B were obtained, and the results point to the same composition, if considering the associated errors of the EDS probe. Furthermore, the magnetic properties of samples A and B are evaluated by temperature-dependent magnetization in Figure 3.8(a). The transitions in sample A are broad, with large hysteresis, spanning from 314 K during heating to 286 K during cooling, respectively. Magnetization values change from 55 to 8 Am^2/kg in a temperature span of 57 K during heating. In sample B, with the additional high temperature step prior to the regular heat treatment, transitions occur between 290 and 278 K during heating and cooling, respectively, with a similar net magnetization change from 66 to 17 Am^2/kg , albeit in a much smaller temperature span of 15 K, see Figure 3.8(a). A series of isotherms are obtained for samples A and B surrounding their cooling transitions, and their ΔS_m values during the cooling transformation are 4.15 and 12.5 $\text{J}/\text{kg}\cdot\text{K}$ for samples A and B, respectively, for field changes of $\mu_0 H$ 0 - 1.8 T, see Figure 3.8(b).

The microstructures of both samples have the hex./orth. majority with the unwanted MgZn_2 phases. The morphologies of the phases are different on both samples: in sample A, the grains present a dispersion of sizes, whereas the grain sizes are homogeneous and large in sample B. In addition, the MgZn_2 phase is only visible as lines inside the grains and grain boundaries, while in sample B it is arranged in lines but also as rounded precipitates.

The difference in microstructure can influence the measured heat capacity during heating and cooling captured by the home-built DSC. In sample A, transitions are broad, spanning between 25-30 K, while the overall latent heat peaks reach values up to 700 $\text{J}/\text{K}\cdot\text{Kg}$, while sample B appears to have sharper transitions, spanning 7 to 10 K. The latent heat peaks are also much higher, reaching up to 5000 $\text{J}/\text{K}\cdot\text{Kg}$. Both samples have similar hysteresis of about 16 K. By comparing both curves, a cause for this discrepancy could be correlated to different local order, but also due to the average grain sizes, since the grain sizes could impact transition kinetics, modifying T_t locally.

Most of the reports in the literature in MM'X compounds employ relatively low temperatures compared to their melting points, with temperatures ranging from 973 to 1173 K. This study was the first to exploit less conventional heat treatments in Mn-Ni-Fe-Si-Al MM'X compounds, which improves ΔS_m values.

Contributions My contributions in this paper relate to synthesis and processing of the compounds, performing room temperature PXD, magnetic

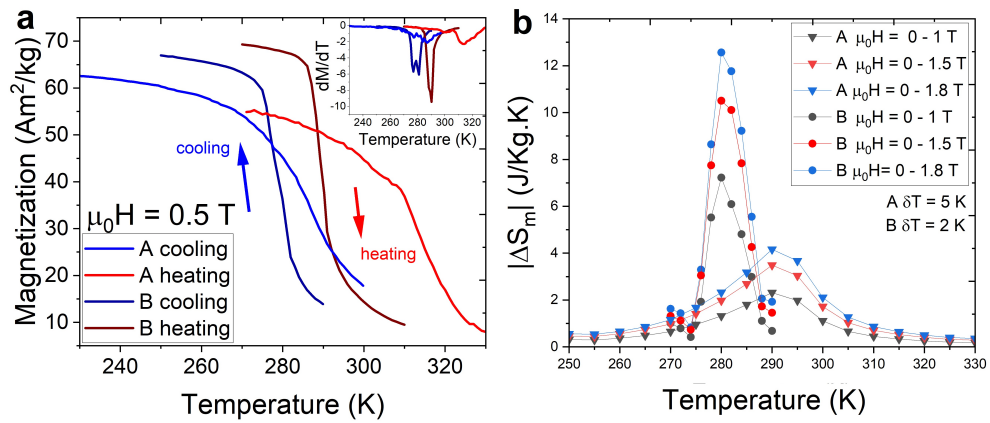


Figure 3.8: (a) Temperature-dependent magnetization for samples A and B, respectively, showcasing the effect of different heat treatments on the steepness and temperature span of the transitions. (b) ΔS_m values obtained correlated to the cooling transition in samples A and B in magnetic fields ranging from $\mu_0 H = 0 - 1.8$ T.

property measurements, and calorimetry experiments with the home-built device at DTU. Also, Microscopic sample preparation, light and electron microscopy experiments, with subsequent data analysis. I was the writer of the original manuscript, and received contributions to the preparation of further iterations of the manuscript.

Chapter 4

Conclusion

This chapter summarizes the work devoted to the synthesis and characterization of High Entropy Alloys and MnNiSi-based compounds for magnetocaloric applications. Suggestions for future work are also highlighted in this section. The main achievements of this research (related to the objectives cited in section 1.6) are:

- High Entropy Alloys were explored for magnetocaloric applications, based on V-Fe-Co-Ni-(Al/Cu) alloys. Their structure and microstructure were evaluated.
- The magnetic properties of the composition with transition around room temperature ($V_{0.85}FeCoNiCu_{1.15}$) presents modest ΔS_m values compared to the most commonly employed magnetocaloric materials like La-Fe-Si or Heusler alloys (see Table 4.2).
- MnNiSi-based materials with inexpensive, abundant Fe and Al were synthesized in $Mn_{1-w}Ni_{1-w}Fe_{2w}Si_{0.95}Al_{0.05}$ compounds, with different levels of Fe substitution in transition metal sites. A Curie Temperature window was established spanning between 373 (w= 0.28) and 183 K (w=0.35) where a magnetostructural transition was confirmed, with comparable ΔS_m (see Table 4.2) values to the state of the art. Nevertheless, a large thermal hysteresis of over 20 K hinders the application of these materials in actual prototypes.
- The orthorhombic and hexagonal structures of $Mn_{1-w}Ni_{1-w}Fe_{2w}Si_{0.95}Al_{0.05}$ were compared with $Mn_{1-x}Fe_xNiSi_{0.95}Al_{0.05}$ with different amounts of Fe substitution. By the joint use of PND and magnetic measurements, a larger saturation magnetization was found in $Mn_{1-w}Ni_{1-w}Fe_{2w}Si_{0.95}Al_{0.05}$ compounds, and supported by Density Functional Theory calculations. Despite this, the right microstructure and/or local order is needed to induce a large ΔS_m .
- The impact of a different heat treatment in $Mn_{1-w}Ni_{1-w}Fe_{2w}Si_{0.95}Al_{0.05}$ compounds increased the ΔS_m values by 72 % from 4.3 J/kg.K to 7.2 % for a $\mu_0H = 0 - 1$ T field change(see Table 4.2). The high temperature step used to increase homogeneity corresponds to less than 3 % of the overall processing time of the alloy.

Chapter 4. Conclusion

Regarding the studied High Entropy Alloys, new compositions of Fe-Co-Ni based materials can lead to better ΔS_m values due to a an optimization of the dilution and antiferromagnetic interactions created by V and (Al/Cu). In these new compositions, elements that create monophasic solutions should be preferred. In this endeavor, the use of CALPHAD methods are crucial to enable monophasic HEA's.

The MM'X compounds synthesized in this research endeavor show that magnetocaloric materials produced from inexpensive transition metal elements can be comparable to the best rare-earth containing magnetocaloric materials, given the right compositions and thermal histories. However, the large thermal hysteresis present in the studied compounds highlight the need for additional composition tuning in MM'X compounds.

Table 4.2: Properties of selected magnetocaloric materials taken from [30, 34, 35] and results obtained in this thesis.

Composition	T_t (K)	ΔS_m (J/kg.K)	ΔT_{ad} (K)	T_{hys} (K)	$\mu_0 H$ (T)
Gd	292	2.8	2.9	-	1
Gd ₅ (Si,Ge) ₄	262	7.1	1.3	5	1
La ₁ Fe _{11.83} Mn _{0.32} Si _{1.3} H _x	297	11.1	2.5	1.3	1
Ni _{45.7} Mn _{36.6} In _{13.5} Co _{4.2}	301	5	0.2	3.6	1
(Mn ₁ Fe _{0.95})(P _{0.585} Si _{0.34} B _{0.075})	290.5	9.1	2.5	1.5	1
MnFeCoNiCu	395	0.115	-	-	0.5
Mn _{1.05} FeCoNiCu _{0.95}	297	0.32	-	-	0.55
Cr _{0.5} FeCoNi _{0.5}	270	0.32	-	-	1
V _{0.85} FeCoNiCu _{1.15}	290	0.15	-	-	1
Mn _{0.7} Ni _{0.7} Fe _{0.6} Si _{0.95} Al _{0.05}	330	4.3	-	20	1
Mn _{0.69} Ni _{0.69} Fe _{0.62} Si _{0.95} Al _{0.05}	279	7.2	-	11	1

Bibliography

- [1] The European Commission. *An EU Strategy on Heating and Cooling*. Tech. rep. (2016).
- [2] Dupont, J.-L., Domanski, P., Lebrun, P. and Ziegler, F. ‘The role of refrigeration in the global economy-38. Informatory Note on Refrigeration Technologies’ (2019).
- [3] Kitanovski, A. ‘Energy Applications of Magnetocaloric Materials’. *Advanced Energy Materials* **10** (2020), p. 1903741.
- [4] Coulomb, D., Jean-Luc, D. and Valentin, M. *The impact of the refrigeration sector on climate change - Informatory Note on refrigeration technologies*. (2017).
- [5] Smith, A., Bahl, C. R., Bjørk, R., Engelbrecht, K., Nielsen, K. K. and Pryds, N. ‘Materials Challenges for High Performance Magnetocaloric Refrigeration Devices’. *Advanced Energy Materials* **2** (2012), p. 1288–1318.
- [6] Franco, V., Blázquez, J. S., Ipus, J. J., Law, J. Y., Moreno-Ramírez, L. M. and Conde, A. ‘Magnetocaloric effect: From materials research to refrigeration devices’. *Progress in Materials Science* **93** (2018), p. 112–232.
- [7] Pecharsky, V., Gschneidner, K., Pecharsky, a. and Tishin, a. ‘Thermodynamics of the magnetocaloric effect’. *Physical Review B* **64** (2001), p. 144406.
- [8] Çengel, Y. A. and Boles, M. A. ‘Thermodynamics : An Engineering Approach’. 1989.
- [9] Brown, G. V. ‘Magnetic heat pumping near room temperature’. *Journal of Applied Physics* **47**, no. 8 (1976), p. 3673–3680.
- [10] Pecharsky, V. K. and Gschneidner, K. A. ‘Advanced magnetocaloric materials : What does the future hold ?’ *International Journal of Refrigeration* **29** (2006), p. 1239–1249.
- [11] Jacobs, S, Auringer, J, Boeder, A, Chell, J, Komorowski, L, Leonard, J, Russek, S and Zimm, C. ‘The performance of a large-scale rotary magnetic refrigerator’. *International Journal of Refrigeration* **37** (2013), p. 84–91.
- [12] Johra, H., Filonenko, K., Heiselberg, P., Veje, C., Dall’Olio, S., Engelbrecht, K. and Bahl, C. ‘Integration of a magnetocaloric heat pump in an energy flexible residential building’. *Renewable Energy* **136** (2019), p. 115–126.

Bibliography

- [13] Nakashima, A. T., Fortkamp, F. P., Sá, N. M. de, Santos, V. M. dos, Hoffmann, G., Peixer, G. F., Dutra, S. L., Ribeiro, M. C., Lozano, J. A. and Barbosa, J. R. ‘A magnetic wine cooler prototype’. *International Journal of Refrigeration* **122** (2021), p. 110–121.
- [14] Peixer, G. F., Silva, M. C. R., Lorenzoni, A. and Hoffmann, G. ‘Evaluating the Performance of a TRL-6 Magnetic Air Conditioner Prototype’. *Proceedings of the 19th International Refrigeration and Air-Conditioning Conference at Purdue*. 2022.
- [15] Dan’kov, S., Tishin, a., Pecharsky, V. and Gschneidner, K. ‘Magnetic phase transitions and the magnetothermal properties of gadolinium’. *Physical Review B* **57** (1998), p. 3478–3490.
- [16] Pecharsky, V. K. and Gschneidner, K. a. ‘Giant Magnetocaloric Effect in $Gd_5Si_2Ge_2$ ’. *Physical Review Letters* **78**, no. 23 (1997), p. 3–6.
- [17] Smith, A. ‘Who discovered the magnetocaloric effect ?’ *European Physical Journal H* **517** (2013), p. 507–517.
- [18] Sajid, M., Ozair, H. and Sheng, H. ‘Review on the developments of active magnetic regenerator refrigerators – Evaluated by performance’. *Renewable and Sustainable Energy Reviews* **133**, no. August (2020), p. 110247.
- [19] Yu, B. F., Gao, Q., Zhang, B., Meng, X. Z. and Chen, Z. ‘Review on research of room trmperature magnetic refrigeration’. *International Journal of Refrigeration* **26**, no. 6 (2003), p. 622–636.
- [20] Fujita, A., Fujieda, S., Fukamichi, K., Mitamura, H. and Goto, T. ‘Itinerant-electron metamagnetic transition and large magnetovolume effects $La(Fe_xSi_{1-x})_{13}$ compounds’. *Physical Review B* **65**, no. 1 (2001), p. 014410.
- [21] Shen, B. G., Sun, J. R., Hu, F. X., Zhang, H. W. and Cheng, Z. H. ‘Recent Progress in Exploring Magnetocaloric Materials’. *Advanced Materials* **21**, no. 45 (2009), p. 4545–4564.
- [22] Barcza, A, Katter, M, Zellmann, V, Russek, S, Jacobs, S, Zimm, C, Gmbh, V. and Kg, C. ‘Stability and Magnetocaloric Properties of Sintered $La(Fe, Mn, Si)_{13}H_z$ Alloys’. **47**, no. 10 (2011), p. 3391–3394.
- [23] Lovell, E., Pereira, A. M., Caplin, A. D., Lyubina, J. and Cohen, L. F. ‘Dynamics of the first-order metamagnetic transition in magnetocaloric $La(Fe,Si)_{13}$: Reducing hysteresis’. *Advanced Energy Materials* **5**, no. 6 (2015), p. 1–9.
- [24] Krenke, T., Duman, E., Acet, M., Wassermann, E. F., Mañosa, L. and Planes, A. ‘Inverse magnetocaloric effect in ferromagnetic Ni – Mn – Sn alloys’. **4**, no. June (2005).
- [25] Mañosa, L., González-alonso, D., Planes, A., Bonnot, E., Barrio, M., Tamarit, J.-l., Aksoy, S. and Acet, M. ‘Giant solid-state barocaloric effect in the Ni – Mn – In magnetic shape-memory alloy’. **9**, no. April (2010).

- [26] Liu, J., Scheerbaum, N., Lyubina, J. and Gutfleisch, O. ‘Reversibility of magnetostructural transition and associated magnetocaloric effect in Ni-Mn-In-Co’. *Applied Physics Letters* **93**, no. 10 (2008), p. 2006–2009.
- [27] Gottschall, T., Benke, D., Fries, M., Taubel, A., Radulov, I. A., Skokov, K. P. and Gutfleisch, O. ‘A Matter of Size and Stress : Understanding the First-Order Transition in Materials for Solid-State Refrigeration’. **1606735** (2017), p. 1–6.
- [28] Guillou, F., Porcari, G., Yibole, H., Van Dijk, N. and Brück, E. ‘Taming the first-order transition in giant magnetocaloric materials’. *Advanced Materials* **26**, no. 17 (2014), p. 2671–2675.
- [29] Lai, J., You, X., Law, J., Franco, V., Huang, B., Bessas, D., Maschek, M., Zeng, D., Dijk, N. V. and Brück, E. ‘Ultra-low hysteresis in giant magnetocaloric Mn_{1-x}V_xFe_{0.95}(P,Si,B) compounds’. *Journal of Alloys and Compounds* **930** (2023), p. 167336.
- [30] Gottschall, T., Skokov, K. P., Fries, M., Taubel, A., Radulov, I., Scheibel, F., Benke, D., Riegg, S. and Gutfleisch, O. ‘Making a Cool Choice: The Materials Library of Magnetic Refrigeration’. *Advanced Energy Materials* **9** (2019), p. 1901322.
- [31] Rocabert, U., Muench, F., Fries, M., Beckmann, B., Loewe, K., Vieyra, H. A., Katter, M., Barcza, A., Ensinger, W. and Gutfleisch, O. ‘Electrochemical corrosion study of La(Fe_{11.6-x}Si_{1.4}Mn_x)H_{1.5} in diverse chemical environments’. *Electrochimica Acta* **434** (2022), p. 1–8.
- [32] Monfared, B. and Palm, B. ‘Material requirements for magnetic refrigeration applications’. *International Journal of Refrigeration* **96** (2018), p. 25–37.
- [33] Greco, A., Aprea, C., Maiorino, A and Masselli, C. ‘A review of the state of the art of solid-state caloric cooling processes at room-temperature before 2019’. *International Journal of Refrigeration* **106** (2019), p. 66–88.
- [34] Perrin, A., Sorescu, M., Burton, M. T., Laughlin, D. E. and McHenry, M. ‘The Role of Compositional Tuning of the Distributed Exchange on Magnetocaloric Properties of High-Entropy Alloys’. *The Journal of The Minerals, Metals Materials Society* **69** (2017), p. 2125–2129.
- [35] Leong, Z and Morley, N. A. ‘Study of dual-phase functionalisation of NiCoFeCr-Al_x multicomponent alloys for the enhancement of magnetic properties and magneto-caloric effect’. *Materials Today Energy* **20** (2021), p. 100621.
- [36] Yeh, J.-w., Chen, S.-k., Gan, J.-y., Lin, S.-j. and Chin, T.-s. ‘Formation of Simple Crystal Structures in Cu-Co-Ni-Cr-Al-Fe-Ti-V Alloys with Multi-principal Metallic Elements’. *Metallurgical and Materials Transactions A* **35** (2010), p. 2533–2536.

Bibliography

- [37] Cantor, B., Chang, I. T. and Knight, P. ‘Microstructural development in equiatomic multicomponent alloys’. *Materials Science and Engineering A* **375** (2004), p. 213–218.
- [38] MacDonald, B. E., Fu, Z., Zheng, B., Chen, W., Lin, Y., Chen, F., Zhang, L., Ivanisenko, J., Zhou, Y., Hahn, H. and Lavernia, E. J. ‘Recent Progress in High Entropy Alloy Research’. *The Journal of The Minerals, Metals Materials Society* **69** (2017), p. 2024–2031.
- [39] Gao, M. C., Zhang, C., Gao, P., Zhang, F., Ouyang, L. Z., Widom, M. and Hawk, J. A. ‘Thermodynamics of concentrated solid solution alloys’. *Current Opinion in Solid State and Materials Science* **21** (2017), p. 238–251.
- [40] Miracle, D. B. and Senkov, O. N. ‘A critical review of high entropy alloys and related concepts’. *Acta Materialia* **122** (2017), p. 448–511.
- [41] George, E. P., Raabe, D. and Ritchie, R. O. ‘High-entropy alloys’. *Nature Reviews Materials* **4** (2019), 515–534.
- [42] Guo, S., Hu, Q., Ng, C. and Liu, C. T. ‘Intermetallics more than entropy in high-entropy alloys : Forming solid solutions or amorphous phase’. *Intermetallics* **41** (2013), p. 96–103.
- [43] Wang, Z., Guo, S. and Liu, C. T. ‘Phase Selection in High-Entropy Alloys: From Nonequilibrium to Equilibrium’. *The Journal of The Minerals, Metals Materials Society* **66** (2014), p. 1966–1972.
- [44] Pickering, E. J. and Jones, N. G. ‘High-entropy alloys : a critical assessment of their founding principles and future prospects’. *International Materials Reviews* **61** (2016).
- [45] Law, J. Y. and Franco, V. ‘Pushing the limits of magnetocaloric high-entropy alloys’. *APL Materials* **9** (2021), p. 080702.
- [46] Law, J. Y., Díaz-garcía, Á., Moreno-ramírez, L. M. and Franco, V. ‘Increased magnetocaloric response of FeMnNiGeSi high-entropy alloys’. *Acta Materialia* **212** (2021), p. 116931.
- [47] Gao, M. C., Miracle, D. B., Maurice, D., Yan, X., Zhang, Y. and Hawk, J. A. ‘High-entropy functional materials’. *Journal of Materials Research* **33** (2018), p. 3138–3155.
- [48] Lucas, M. S., Belyea, D., Bauer, C., Bryant, N., Michel, E., Turgut, Z., Leontsev, S. O., Horwath, J., Semiatin, S. L., McHenry, M. E. and Miller, C. W. ‘Thermomagnetic analysis of FeCoCr_xNi alloys: Magnetic entropy of high-entropy alloys’. *Journal of Applied Physics* **113** (2013), p. 2011–2014.
- [49] Belyea, D. D., Lucas, M. S., Michel, E., Horwath, J. and Miller, C. W. ‘Tunable magnetocaloric effect in transition metal alloys’. *Scientific Reports* **5** (2015), p. 15755.
- [50] Kurniawan, M., Perrin, A., Xu, P., Keylin, V. and McHenry, M. ‘Curie Temperature Engineering in High Entropy Alloys for Magnetocaloric Applications’. *IEEE Magnetism Letters* **7** (2016), p. 6105005.

- [51] Perrin, A. E. ‘Characterization of High Entropy Alloys for Magnetocaloric Applications’. PhD thesis. Carnegie Mellon University, 2019.
- [52] Johnson, V. and Frederick, C. G. ‘Magnetic and crystallographic properties of ternary manganese silicides with ordered Co₂P structure’. *Physica Status Solidi (a)* **20** (1973), p. 331–335.
- [53] Quetz, A., Samanta, T., Dubenko, I., Kangas, M. J., Chan, J. Y., Stadler, S. and Ali, N. ‘Phase diagram and magnetocaloric effects in aluminum doped MnNiGe alloys’. *Journal of Applied Physics* **114**, no. 15 (2013).
- [54] Morrison, K., Barcza, A., Moore, J. D., Sandeman, K. G., Chattopadhyay, M. K., Roy, S. B., Caplin, A. D. and Cohen, L. F. ‘The magnetocaloric performance in pure and mixed magnetic phase CoMnSi’. *Journal of Physics D: Applied Physics* **43**, no. 19 (2010).
- [55] Pal, S. K., Frommen, C., Kumar, S., Hauback, B. C., Fjellvåg, H., Woodcock, T. G., Nielsch, K. and Helgesen, G. ‘Comparative phase transformation and magnetocaloric effect study of Co and Mn substitution by Cu in MnCoGe compounds’. *Journal of Alloys and Compounds* **775** (2019), p. 22–29.
- [56] Hassan, N. ul, Chen, F., Zhang, M., Shah, I. A., Liu, J., Gong, Y., Xu, G. and Xu, F. ‘Realisation of magnetostructural coupling and a large magnetocaloric effect in the MnCoGe_{1+x} system’. *Journal of Magnetism and Magnetic Materials* **439** (2017), p. 120–125.
- [57] Johnson, V. ‘Diffusionless Orthorhombic to Hexagonal Transitions in Ternary Silicides and Germanides’. *Inorganic Chemistry* **14** (1975), p. 1117–1120.
- [58] Smallman, R. and Bishop, R. J. *Modern Physical Metallurgy and materials engineering*. 1999.
- [59] Jeitschko, W. ‘A high-temperature X-ray study of the displacive phase transition in MnCoGe’. *Acta Crystallographica Section B Structural Crystallography and Crystal Chemistry* **31** (1975), p. 1187–1190.
- [60] Zhang, Z., James, R. D. and Müller, S. ‘Energy barriers and hysteresis in martensitic phase transformations’. *Acta Materialia* **57** (2009), p. 4332–4352.
- [61] Liu, J., Gong, Y., You, Y., You, X., Huang, B., Miao, X., Xu, G., Xu, F. and Brück, E. ‘Giant reversible magnetocaloric effect in MnNiGe-based materials: Minimizing thermal hysteresis via crystallographic compatibility modulation’. *Acta Materialia* **174** (2019), p. 450–458.
- [62] Chen, X., Song, Y., Tamura, N. and James, R. D. ‘Determination of the stretch tensor for structural transformations’. *Journal of the Mechanics and Physics of Solids* **93** (2016), p. 34–43.

Bibliography

- [63] Guo, Y., Zhang, T., Zhang, Z., Chen, B., Guo, W., Pan, S., Gong, Y., Bai, Y., Gong, Y., Liu, J., Miao, X. and Xu, F. ‘Large reversible magnetocaloric effect in high-entropy MnFeCoNiGeSi system with low-hysteresis magnetostructural transformation’. *APL Materials* **10** (2022), p. 091107.
- [64] Bażela, W., Szytula, A., Todorović, J. and Zięba, A. ‘Crystal and magnetic structure of the NiMnGe₁Sn System’. *Physica Status Solidi (a)* **64** (1981), p. 367–378.
- [65] Lin, S., Tegus, O., Brück, E., Dagula, W., Gortenmulder, T. J. and Buschow, K. H. J. ‘Structural and Magnetic Properties of MnFe_{1-x}Co_xGe Compounds’. *IEEE Transactions on Magnetics* **42** (2006), p. 3776–3778.
- [66] Fang, Y.-k., Yeh, J.-c., Chang, W.-c., Li, X.-m. and Li, W. ‘Structures, magnetic properties, and magnetocaloric effect in MnCo_{1-x}(0.02 ≤ x ≤ 0.2) Ge compounds’. *Journal of Magnetism and Magnetic Materials* **321** (2009), p. 3053–3056.
- [67] Gauß, R., Homm, G. and Gutfleisch, O. ‘The Resource Basis of Magnetic Refrigeration’. *Journal of Industrial Ecology* **21**, no. 5 (2017), p. 1291–1300.
- [68] Landrum, G. A., Hoffmann, R., Evers, J. and Boysen, H. ‘The TiNiSi Family of Compounds: Structure and Bonding’. *Inorganic Chemistry* **37** (1998), p. 5754–5763.
- [69] Fjellvåg, H. and Andresen, A. ‘On the crystal structure and magnetic properties of MnNiGe’. *Journal of Magnetism and Magnetic Materials* **50** (1985), p. 291–297.
- [70] Samanta, T., Lepkowski, D. L., Saleheen, A. U., Shankar, A., Prestigiacomo, J., Dubenko, I., Quetz, A., Oswald, I. W., McCandless, G. T., Chan, J. Y., Adams, P. W., Young, D. P., Ali, N. and Stadler, S. ‘Hydrostatic pressure-induced modifications of structural transitions lead to large enhancements of magnetocaloric effects in MnNiSi-based systems’. *Physical Review B - Condensed Matter and Materials Physics* **91**, no. 2 (2015).
- [71] Taubel, A., Gottschall, T., Fries, M., Faske, T., Skokov, K. P. and Gutfleisch, O. ‘Influence of magnetic field, chemical pressure and hydrostatic pressure on the structural and magnetocaloric properties of the Mn-Ni-Ge system’. *Journal of Physics D: Applied Physics* **50**, no. 46 (2017).
- [72] Shen, F. R., Hu, F. X., Yu, Z. B., Zhou, H. B., Wu, H., Huang, Q. Z., Hao, J. Z., Gao, Y. H., Qiao, K. M., Li, J., Zhang, C., Liang, W. H., He, L. H., Wang, J., Liang, T. J., Sun, J. R. and Shen, B. G. ‘Neutron diffraction study on hydrostatic pressure regulated magnetostructural transition and magnetocaloric effect in MnNi_{1-x}Fe_xSi_{1-y}Ge_y alloys’. *Journal of Applied Physics* **127**, no. 13 (2020).
- [73] Bruno, N. M. and Yuce, S. ‘On the instability of the giant direct magnetocaloric effect in CoMn_{0.915}Fe_{0.085}Ge at. % metamagnetic compounds’. *Scientific Reports* **10** (2020).

- [74] Zhou, H., Tao, K., Chen, B., Chen, H., Qiao, K., Yu, Z., Cong, J., Huang, R., Taskaev, S. V. and Zhang, H. ‘Low-melting metal bonded MMX/In composite with largely enhanced mechanical property and anisotropic negative thermal expansion’. *Acta Materialia* **229** (2022), p. 117830.
- [75] Andersson, J. O., Helander, T., Höglund, L., Shi, P. and Sundman, B. ‘Thermo-Calc and DICTRA, computational tools for materials science’. *Calphad: Computer Coupling of Phase Diagrams and Thermochemistry* **26** (2002), p. 273–312.
- [76] Jaeger, G. ‘The ehrenfest classification of phase transitions: Introduction and evolution’. *Archive for History of Exact Sciences* **53** (1998), p. 51–81.
- [77] Morrish, A. H. *The Physical Principles of Magnetism*. John Wiley and Sons, Ltd, 2001. Chap. 6, p. 259–331.
- [78] Trevizoli, P., Barbosa Jr, J., Oliveira, P. de, Prata, A. and Ferreira, R. ‘Direct measurements of the magnetocaloric effect of gadolinium samples at near room temperature’. *Proceedings of the 20th International Congress of Mechanical Engineering*. 2009.
- [79] Höhne, G. W. H., Hemminger, W and Flammersheim, H.-J. *Differential Scanning Calorimetry*. Springer Berlin Heidelberg, 1996.
- [80] Neves Bez, H. ‘Magnetocaloric materials and first order phase transitions’. PhD thesis. 2016.
- [81] McHenry, M. E., Willard, M. A. and Laughlin, D. E. *Amorphous and nanocrystalline materials for applications as soft magnets*. Vol. 44. 4. 1999, p. 291–433.
- [82] Maccari, F. ‘Investigations on ThMn₁₂-type and Mn-Al compounds as permanent magnet candidates’. PhD thesis. Technische Universität Darmstadt, 2022.
- [83] Niziol, S., Bombik, A., Bazela, W., Szytula, A. and Fruchart, D. ‘Crystal and magnetic structure of Co_xNi_{1-x}MnGe system’. *Journal of Magnetism and Magnetic Materials* **27** (1982), p. 281–292.
- [84] Dobrzynski, L. and Andresen, A. F. ‘On the magnetic double helical structure in MnP- and MnAs- based alloys’. *Journal of Magnetism and Magnetic Materials* **82** (1989), p. 67–76.
- [85] Gercsi, Z. and Sandeman, K. G. ‘Structurally driven metamagnetism in MnP and related Pnma compounds’. *Physical Review B - Condensed Matter and Materials Physics* **81** (2010), p. 224426.
- [86] Cullity, B. and Graham, C. *Introduction to magnetic materials*. Vol. 12. 2009, p. 45.
- [87] Caron, L., Ou, Z., Nguyen, T., Cam Thanh, D., Tegus, O. and Brück, E. ‘On the determination of the magnetic entropy change in materials with first-order transitions’. *Journal of Magnetism and Magnetic Materials* **321** (2009), p. 3559–3566.

Bibliography

- [88] Neves Bez, H., Yibole, H., Pathak, A., Mudryk, Y. and Pecharsky, V. K. 'Best practices in evaluation of the magnetocaloric effect from bulk magnetization measurements'. *Journal of Magnetism and Magnetic Materials* **458** (2018), p. 301–309.
- [89] Moreno-Ramírez, L. M., Díaz-García, Law, J. Y., Giri, A. K. and Franco, V. 'Hysteresis, latent heat and cycling effects on the magnetocaloric response of $(\text{MnNiSi})_{0.66}(\text{Fe}_2\text{Ge})_{0.34}$ alloy'. *Intermetallics* **131** (2021), p. 107083.
- [90] Banerjee, B. K. *On a generalised approach to first and second order magnetic transitions*. 1964.
- [91] Herrero-albillos, J., Bartolomé, F. and García, L. M. 'Nature and entropy content of the ordering transitions in R Co_2 ' (2006), p. 1–10.
- [92] Law, J. Y., Franco, V., Moreno-Ramírez, L. M., Conde, A., Karpenkov, D. Y., Radulov, I., Skokov, K. P. and Gutfleisch, O. 'A quantitative criterion for determining the order of magnetic phase transitions using the magnetocaloric effect'. *Nature Communications* **9**, no. 1 (2018).
- [93] Sørby, M. H. 'Status on Existing Technologies'. *Hydrogen Technology: Mobile and Portable Applications*. Ed. by Leon, A. Berlin, Heidelberg: Springer Berlin Heidelberg, 2008, p. 523–537.
- [94] Leineweber, A., Dinnebier, R. and Evans, J. *Rietveld Refinement Practical Powder Diffraction Pattern Analysis using TOPAS*. 2018.
- [95] Rietveld, H. M. 'A profile refinement method for nuclear and magnetic structures'. *Journal of Applied Crystallography* **2** (1969), p. 65–71.
- [96] Rodriguez-Carvajal, J. 'Recent developments of the program FULLPROF, commission on powder diffraction'. *IUCr Newsl.* **26** (2001), p. 12–19.
- [97] Fischer, P., Frey, G., Koch, M., Könnecke, M., Pomjakushin, V., Schefer, J., Thut, R., Schlumpf, N., Bürge, R., Greuter, U., Bondt, S and Berruyer, E. 'High-resolution powder diffractometer HRPT for thermal neutrons at SINQ'. *Physica B: Condensed Matter* **276-278** (2000), p. 146–147.
- [98] Zhang, C. L., Shi, H. F., Nie, Y. G., Ye, E. J., Han, Z. D. and Wang, D. H. 'Thermal-cycling-dependent magnetostructural transitions in a Ge-free system $\text{Mn}_{0.5}\text{Fe}_{0.5}\text{Ni}(\text{Si},\text{Al})$ '. *Applied Physics Letters* **105** (2014), p. 242403.
- [99] Biswas, A., Pathak, A. K., Zarkevich, N. A., Liu, X., Mudryk, Y., Balema, V., Johnson, D. D. and Pecharsky, V. K. 'Designed materials with the giant magnetocaloric effect near room temperature'. *Acta Materialia* **180** (2019), p. 341–348.
- [100] Nuendute, B., Hanggai, W., Yibole, H., Tana, B., Tegus, O. and Guillou, F. 'Drastic Influence of Synthesis Conditions on Structural, Magnetic, and Magnetocaloric Properties of $\text{Mn}(\text{Fe},\text{Ni})(\text{Si},\text{Al})$ Compounds'. *Crystals* **12** (2022), p. 233.
- [101] Arreguín-Hernández, M. L., Sánchez-Valdés, C. F. and Sánchez Llamazares, J. L. 'Magnetostructural transition and magnetocaloric effect in thermally annealed $\text{Mn}_{0.5}\text{Fe}_{0.5}\text{NiSi}_{0.945}\text{Al}_{0.55}$ melt-spun ribbons'. *Journal of Magnetism and Magnetic Materials* **533** (2021), p. 168021.

- [102] Gupta, K. P. 'The Mn-Ni-Si (manganese-nickel-silicon) system'. *Journal of Phase Equilibria and Diffusion* **27**, no. 5 (2006), p. 529–534.

Bibliography

Paper I

Exploring V-Fe-Co-Ni-Al and V-Fe-Co-Ni-Cu High Entropy Alloys for Magnetocaloric Applications



Exploring V-Fe-Co-Ni-Al and V-Fe-Co-Ni-Cu high entropy alloys for magnetocaloric applications

Bruno G.F. Eggert^a, Erna K. Delczeg-Czirjak^b, Fernando Maccari^c, Susmit Kumar^d,
Oliver Gutfleisch^c, Helmer Fjellvåg^d, Bjørn C. Hauback^a, Christoph Frommen^{a,*}

^a Department for Hydrogen Technology, Institute for Energy Technology (IFE), P.O. Box 40, NO-2027 Kjeller, Norway

^b Department of Physics and Astronomy, Uppsala University, Box 516, 751 20 Uppsala, Sweden

^c Functional Materials, Materials Science, Technical University of Darmstadt, 64287 Darmstadt, Germany

^d Department of Chemistry, University of Oslo, Sem Sælands vei 26, 0371 Oslo, Norway

ARTICLE INFO

Article history:

Received 23 February 2022

Received in revised form 21 June 2022

Accepted 23 June 2022

Available online 29 June 2022

Keywords:

Magnetocaloric

Transition metal alloys and compounds

X-ray diffraction

Scanning electron microscopy

Computer simulations

Magnetism

ABSTRACT

A series of $V_{1-x}\text{-Fe-Co-Ni-Al}_{1+x}$ and $V_{1-x}\text{-Fe-Co-Ni-Cu}_{1+x}$ high entropy alloys with varying compositions ($0 \leq x \leq 0.75$) has been investigated for magnetocaloric applications. Compositions were selected according to established properties, such as configurational entropy, atomic size difference, and enthalpy of mixing. To study the influence of composition on magnetic ordering temperatures, the V and (Al/Cu) contents were changed while the content of Fe, Co and Ni was retained at 20 at. % each. The crystal structure and microstructure of the as-cast alloys were compared to literature phase guidelines and thermodynamic calculations based on the CALPHAD approach. The V-Fe-Co-Ni-Al compounds are monophasic and crystallize in a disordered body centered cubic structure or its ordered B2 variant, while the V-Fe-Co-Ni-Cu compounds are all multiphasic. Magnetic transitions in the V-Fe-Co-Ni-Al system span over 400 K, with Curie temperature ranging from 155 K in equiatomic VFeCoNiAl, to 456 K in non-equiatomic $V_{0.25}\text{FeCoNiAl}_{1.75}$. The V-Fe-Co-Ni-Cu alloys display magnetic transitions that span about 150 K, with Curie temperature ranging from 230 K for equiatomic VFeCoNiCu to 736 K for non-equiatomic $V_{0.25}\text{FeCoNiCu}_{1.75}$. The magnetic properties of the V-Fe-Co-Ni-Cu compounds were evaluated by means of density functional theory. Individual element-specific moments, magnetic exchange integrals between atomic pairs, and Curie temperatures were calculated. $V_{0.85}\text{FeCoNiCu}_{1.15}$ is selected due to its Curie temperature of 329 K, and its calculated isothermal entropy change of 0.75 J/kg·K for a field change of 5 T is comparable to other 3d metal-based high entropy alloys that form disordered solid solutions.

© 2022 The Author(s). Published by Elsevier B.V.
CC BY 4.0

1. Introduction

As climate change tends to raise average temperatures and increases the occurrence of temperature anomalies, cooling and heating of common areas will play a crucial role in future worldwide energy demand [1,2]. In that regard, more efficient technologies will allow for lower stress on energy grids. Amongst the more promising alternatives to current domestic vapor compression technologies for refrigeration or air conditioning solutions, magnetocaloric devices stand out, as they use less environmentally deleterious substances whilst providing better efficiency during thermal cycling [3,4]. At the core of these devices are materials that heat or cool due to changes in their internal magnetizations; they are called magnetocaloric

materials. The most common properties used to measure the intensity of the magnetocaloric effect in a compound for a given magnetic field, are the adiabatic temperature change (dT_{ad}) and the isothermal entropy change (ΔS_m) [5,6]. The former can be obtained directly from specialized devices measuring the compound's temperature during a near-adiabatic magnetization/demagnetization cycle, while the latter can be calculated indirectly by magnetization measurements across a magnetic transition temperature, such as the Curie temperature (T_C) in ferromagnetic (FM) systems, by adaptation of a Maxwell relation:

$$\Delta S_m = \mu_0 \int_{H_i}^{H_f} \left(\frac{\partial M}{\partial T} \right)_H dH \quad (1)$$

Here, μ_0 is the vacuum permeability constant, H_i and H_f are the minimum and maximum applied magnetic fields, and $\left(\frac{\partial M}{\partial T} \right)_H$ denotes the derivative of mass magnetization with respect to temperature

* Corresponding author.

E-mail address: christoph.frommen@ife.no (C. Frommen).

under a constant magnetic field. Among the most studied magnetocaloric compound classes are $\text{La}(\text{Fe,Si})_{13}$, Fe_2P , magnetic shape memory alloys and $\text{MM}'\text{X}$ compounds, where M, M' are transition metals and X is a p-block element. These materials are attractive for magnetocaloric energy conversion due to their high ΔS_m values [5–7]. Such high ΔS_m values are ascribed to their First Order Phase Transitions (FOPT), which occur either due to concurrent structural and magnetic transitions (e.g., in $\text{MM}'\text{X}$ and magnetic shape memory alloy compounds), or during magnetoelastic phase transitions (e.g., in $\text{La}(\text{Fe,Si})_{13}$ and Fe_2P). However, the presence of hysteresis lowers the reversibility during a FOPT and hinders the application potential of such materials [8,9]. Therefore, it is crucial to lower the hysteresis. An alternative would be to develop new compounds with Second Order Phase Transitions (SOPT), that exhibit no hysteresis, with a reasonable ΔS_m , thus exhibiting a bigger reversible effect.

In this context, a new promising alloy concept that is drawing attention are High Entropy Alloys (HEA); they are disordered solid solutions (SS) formed by four or more metallic elements in similar proportions, ranging from 5 to 35 at. % [10,11]. Given the number of possible combinations due to such boundary conditions for the compositions, a trial-and-error approach would be an arduous process. Therefore, research has focused on identifying trends in phase formation by assessing a series of thermodynamic parameters. Several of them influence the number of phases, and phase structure in such disordered solutions. MacDonald et al. argue that a configurational entropy ($S_{\text{conf}} \geq 12.465 \text{ J/mol}\cdot\text{K}$ (1.5 R, where R is the universal gas constant) favours the formation of disordered SSs [12]. Besides S_{conf} , atomic size difference ($\delta \leq 6.6 \%$) and enthalpy of mixing (ΔH_{mix}) between -15 and $+5 \text{ kJ/mol}$ are property values that are said to help stabilize SSs in HEAs [13]. Guo [14] also argues on the role of Valence Electron Concentrations (VEC), where VECs < 6.87 tend to form body-centered cubic (bcc) alloys, $6.87 \leq \text{VEC} \leq 8$ stabilize a mixture of bcc and cubic close packed (ccp) structures, and VECs > 8 fully stabilize ccp structures.

Such properties mentioned above help to provide guidelines for solid solution formation. Another method for prediction of structure and phase presence in alloys is the CALculation of PHase Diagram (CALPHAD) method, which relies on data derived from experimental thermodynamic databases for binary and ternary alloys [15].

Investigations of HEAs were initially aimed at understanding phase formation and mechanical properties, primarily for structural applications. In recent years, their distinct electronic configurations sparked interest for applications such as hydrogen storage [16], thermoelectricity [17], and magnetism [18]. In the latter field, HEAs are explored for their soft and semi-hard properties, as their crystal structures, microstructures and electronic configurations can be easily modified towards the desired properties [19]. As candidates for magnetocaloric materials, HEAs based on 3d ferromagnetic transition metal elements could have great advantages, as they feature good chemical stability, high ductility, and could easily be processed into different shapes [20,21]. However, the lack of solubility between certain elements, varying degrees of short range ordering and ultimately a low ΔS_m have so far prevented HEAs from becoming serious candidates for magnetic cooling applications [22–24].

A combined approach employing computational and experimental methods is advantageous for identifying new combinations of metallic elements that may yield the desired (micro)structure and magnetic properties. In this respect, a thorough understanding of the microstructural features of HEAs is crucial. While monophasic alloys were initially sought after, reports on multiphasic HEA systems have been showcasing a strong interplay between different phases,

that can yield unexpected beneficial magnetic and mechanical properties [25–28].

To adjust the Curie temperature (T_C) towards room temperature (RT) in alloys based on ferromagnetic transition metals, elements that create antiferromagnetic exchange interactions are used. Recent explorations include melt-spun MnFeCoNiCu and heat-treated CrFeCoNiAl , which employ mainly Mn and Cr, respectively to decrease T_C [29,30].

In contrast, little attention has been given to V-containing HEAs. V can also induce antiferromagnetic interactions with Fe/Co/Ni, which lower T_C to RT. In addition, little is known about its influence on the properties, structure and microstructure of Fe/Co/Ni-based HEAs to be used as magnetocaloric materials. Thus, the potential of V-containing HEAs remains unexplored. To bridge this knowledge gap, we present experimental and computational results regarding phase formation, (micro)structure, and magnetism for two different V-containing alloy systems: $\text{V}_{1-x}\text{FeCoNiAl}_{1+x}$ and $\text{V}_{1-x}\text{FeCoNiCu}_{1+x}$ ($0 \leq x \leq 0.75$), with Al or Cu as fifth elements. Cu and Al are employed in this study as they are abundant elements, that enable the formation of solid solutions by raising S_{conf} while having very distinct number of valence electrons, which modify the VEC. They also dilute the magnetic moments in the solid solutions, aiding in lowering T_C towards RT. These systems are chosen as the equimolar compositions feature suitable ΔH_{mix} , δ and VEC values to form SSs. We study the influence of composition on magnetic ordering temperatures and magnetic exchange interactions. This is achieved by a systematic variation of the V/Al and V/Cu ratios while retaining a content of 20 at. % for Fe, Co, and Ni each (60 at. % in total). The experimental results are complemented by CALPHAD modelling and density functional theory (DFT) to elucidate structural and magnetic properties in the studied alloys.

2. Materials and methods

Metallic powders of Fe, Ni, Co, V, Cu and Al of 99.9 % purity were weighed, mixed and arc melted in a Ti-gettered home-built arc melter in argon atmosphere. The samples were remelted and turned 5 times to ensure homogeneity. Nominal compositions are described in Table 1. Phase presence and constitution were predicted by the CALPHAD method implemented by the Thermocalc 2021 software in combination with the TCHEA3 high entropy alloy database package. Property diagrams were obtained by considering all the possible phases, including intermetallic and intermediate compounds formed by the constituent elements.

Table 1

Selected properties for a series of V-Fe-Co-Ni-(Al/Cu) HEAs: configurational entropy (S_{conf}), atomic size difference (δ), enthalpy of mixing (ΔH_{mix}), and Valence Electron Concentration (VEC). The table also displays the refined lattice parameters (a) and standard deviations (σ) in brackets.

Composition	S_{conf} (J/mol·K)	δ (%)	ΔH_{mix} (kJ/mol)	VEC	a (σ) (Å)
$\text{V}_1\text{FeCoNiAl}_1$	13.38	5.38	-13.87	7.0	2.881(1)
$\text{V}_{0.8}\text{FeCoNiAl}_{1.2}$	13.31	5.63	-13.03	6.92	2.886(1)
$\text{V}_{0.6}\text{FeCoNiAl}_{1.4}$	13.11	5.86	-11.85	6.84	2.885(1)
$\text{V}_{0.5}\text{FeCoNiAl}_{1.5}$	12.95	5.96	-11.14	6.8	2.884(2)
$\text{V}_{0.25}\text{FeCoNiAl}_{1.75}$	12.33	6.21	-8.96	6.7	2.8815(3)
$\text{V}_1\text{FeCoNiCu}_1$	13.38	2.88	-1.28	8.6	3.6108(9)
$\text{V}_{0.85}\text{FeCoNiCu}_{1.15}$	13.34	2.72	0.32	8.78	3.604(1)
$\text{V}_{0.8}\text{FeCoNiCu}_{1.2}$	13.31	2.66	0.84	8.84	3.606(1)
$\text{V}_{0.6}\text{FeCoNiCu}_{1.4}$	13.11	2.4	2.92	9.08	3.601(1)
$\text{V}_{0.5}\text{FeCoNiCu}_{1.5}$	12.95	2.25	3.93	9.2	3.5981(9)
$\text{V}_{0.25}\text{FeCoNiCu}_{1.75}$	12.33	1.79	6.38	9.5	3.5960(9)

Crystal structure characterization was carried out by a Bruker D2 Phaser Cu-K α X-ray diffractometer ($\lambda = 1.5406 \text{ \AA}$) in Bragg-Brentano configuration. Rietveld refinements were done using the Fullprof Suite software [31]. Scanning electron microscopy (SEM) and energy dispersive X-ray spectroscopy (EDS) were carried out in a Hitachi SU8230 ultra-high resolution cold-field emission scanning electron microscope.

Magnetic balance measurements were done on a modified Netzsch STA 449 – F3 Jupiter thermogravimetry / differential scanning calorimetry device. Magnetic balance measurements are a valuable tool for obtaining knowledge on the magnetic transitions present in the alloys, and for the determination of trends caused by compositional variations. Furthermore, the presence of different magnetic phases can be detected by changes in slopes of descent of magnetization and/or by steps in the curves.

By applying a magnetic field in a specific configuration on a thermogravimetry analysis device, the change in internal magnetic field of the sample produces a magnetic force which adds to the weight measured by the thermobalance. As the sample is heated up during the measurement, the internal magnetic field is weakened by the thermal energy, thereby lowering the measured weight until the magnetic ordering temperature T_C is reached, and no further contribution to the weight exists. It is an indirect measurement of internal magnetization, comparable to a magnetization measurement with a small applied magnetic field. Measurements were carried out in the temperature range from 300 K to 1273 K, with heating rates of 1 or 5 K/min. Magnetic balance data was normalized with respect to mass change in the samples and plotted as a function of temperature. The mass changes were normalized since the absolute values of mass change are dependent on factors such as sample shape and mass itself, which could influence the assessment of each composition.

Magnetic measurements were carried out by either a Quantum Design Magnetic Property Measurement system or a Physical Property Measurement System. Measurements as a function of temperature were carried out in a persistent applied field of $\mu_0 H = 0.01 \text{ Tesla (T)}$, and temperatures ranging from 10 to 370 K. Field dependent measurements were performed at 10, 50, 250, 350 and 370 K, respectively, and applied fields in the range $\mu_0 H = 0\text{--}5 \text{ T}$. Field dependent measurements for the determination of the isothermal magnetic entropy change, ΔS_m , were carried out across the magnetic transition with 10 K intervals.

Ground state magnetic properties were investigated using DFT [32,33] formulated within the Lyngby version [34] exact muffin-tin orbital method [35–39]. The chemical disorder was treated within the coherent potential approximation (CPA) [40,41]. The electrostatic correction to the single-site CPA was described using the screened impurity model with a screening parameter of 0.6. The one-electron Kohn-Sham equations were solved within the soft-core and scalar-relativistic approximations. s , p , d and f orbitals were included in the basis set. The Green's function was calculated for 16 complex energy points distributed exponentially on a semi-circular contour including states within 1.1 Ry below the Fermi level. The presented results are obtained using the local spin density approximation (LSDA) to describe the exchange correlation effects. [42,43]. For the one-center expansion of the full charge density a $I_{max}^h = 8$ cutoff was used. The magnetic exchange interactions were calculated within the magnetic force theorem [44] for the ferrimagnetic configuration. The calculated exchange interactions were further utilized to estimate the Curie temperature (T_C) via Monte Carlo (MC) simulations implemented within the Uppsala atomistic spin dynamics (UppASD) software [45,46]. Such simulations were performed on a $40 \times 40 \times 40$ supercell with periodic boundary conditions. The size and direction of the magnetic moments were chosen randomly at each MC trial and 10,000 MC steps were used for equilibration followed by 50,000 steps for obtaining thermodynamic averages.

3. Results and discussion

3.1. Evaluation of the thermodynamic parameters from nominal compositions

The formation of disordered SSs in HEAs is ascribed mainly to the role of configurational entropy, where S_{conf} values $\geq 12.465 \text{ J/mol}\cdot\text{K}$ ($1.5 R$) help to stabilize SSs. In addition to the role of S_{conf} , properties such as δ , ΔH_{mix} and VEC are of value as important guidelines for SS formation. Table 1 summarizes thermodynamic properties of V-containing HEAs reported in literature to date. With respect to the enthalpy of mixing, ΔH_{mix} , we observe values ranging from -13.87 to $+6.38 \text{ kJ/mol}$, thus almost all compositions have values that favor SS formation, except for $V_{0.25}FeCoNiCu_{1.75}$. As for δ , differences are small and thus also favour the formation of solid solutions. When comparing the values of S_{conf} in the two systems, we find that compounds with V content < 0.25 are below the reported guideline, while those with $V \geq 0.25$ have S_{conf} large enough to be considered HEAs according to the “configurational entropy definition”. By evaluating the influence of VEC it can be concluded that except for $V_{0.25}FeCoNiAl_{1.75}$, all other compositions in the V-Fe-Co-Ni-Al system could be ccp, bcc or a mixture of these structures. In the V-Fe-Co-Ni-Cu system, all compositions should be ccp. To compare the literature guideline evaluations with thermodynamic database models, the compositions are modelled in CALPHAD and their expected structure and phase presence are described in detail in the next section.

Equilibrium phases have been determined in the isopleths of phase diagram using CALPHAD, with Al and Cu substitutions as a function of V reduction, shown in Fig. 1. As can be seen from (a), the equilibrium phases present in the V-Fe-Co-Ni-Al system at RT are 2

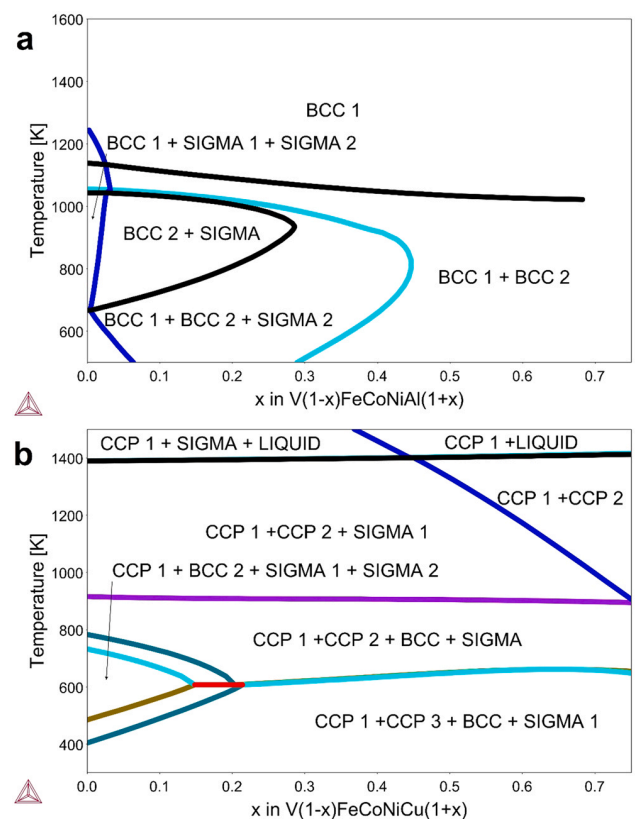


Fig. 1. Isoleth of V-Fe-Co-Ni-Al and V-Fe-Co-Ni-Cu phase diagrams, with the modifications proposed in this article produced by the CALPHAD method.

ordered bcc phases (in B2 ordering), and a sigma phase intermetallic, a tetragonal V-rich phase seen in V-rich compositions, that is not present in the predictions featuring higher Al concentrations. At temperatures above 1000 K, only one bcc phase dominates since Fe and V solubilities in the V-Fe-Co-Ni-Al main solid solution increase in equilibrium [47].

In the V-Fe-Co-Ni-Cu system, shown in Fig. 1(b), CALPHAD predicts the presence of 2 ccp phases, one bcc and one sigma phase in lower V concentrations at RT. With higher V concentrations, there is the formation of a secondary sigma phase at the expense of the ccp phase, thus forming a (ccp + bcc + sigma1 + sigma2) phase composition. At higher temperatures, the sigma phases get solubilized into a SS phase, with the formation of a secondary SS (one disordered V-Fe-Co-Ni-Cu SS and a Cu-rich phase). This secondary ccp phase is present up to 1400 K, at which point it is liquified. In summary, the CALPHAD method provides a more detailed picture of the system after the initial evaluation based on thermodynamic properties. To assess the phases, present in the as-cast V-containing alloys, we turn our attention to the analysis of their crystal structure and microstructure using X-ray diffraction and scanning electron microscopy, respectively.

3.2. Crystal structure and microstructure

The V-Fe-Co-Ni-Al alloys were brittle in the as-cast state, thus for the X-ray diffraction (XRD) measurements the samples were pulverized with a mortar and pestle. The patterns are shown in Fig. 2a. For all samples, the diffraction data could be indexed as disordered bcc or ordered B2 alloys, as indicated by the (100) reflection around

$2\theta = 30^\circ$. The respective lattice parameters are given in Table 1. Except for the V-Fe-Co-Ni-Al equiatomic composition, the non-equiatomic compositions follow a trend towards smaller lattice constants, when the V content is lowered. Note, that the higher Al compositions (up to the $V_{0.25}FeCoNiAl_{1.75}$ composition) result in B2-ordered phase with clearly visible (100) superstructure reflections, corresponding to the end of the phase diagram seen in Fig. 1a. In this B2 ordering, symmetry is lowered towards the $Pm-3m$ space group. Thus certain atoms remain in specific positions, modifying the structure factors influencing the diffraction pattern. The structure factors with the best description of the patterns occur when 1a positions are taken by V, Al and half of the Fe, whereas the remaining Fe, Co and Ni atoms occupy the 1b position [48].

To gain insight into the phase and element distribution after the solidification process for the as-cast V-containing alloys, SEM imaging and EDS were carried out on $V_{0.8}FeCoNiAl_{1.2}$ and $V_{0.85}FeCoNiCu_{1.15}$. For compositions containing Al, the data shows a dendritic microstructure, see Fig. 2b. The composition measured with EDS in dendritic (clear) and interdendritic (dark) areas are displayed in Table 2, with no clear formation of secondary phases.

Dendritic and interdendritic areas display very different compositions, which can be attributed to constitutional supercooling. This phenomenon occurs during cooling of alloys when local solubility differences at solid/liquid interfaces result in a liquid that is poorer in certain elements. This creates an undercooling effect, leading to the formation of compositional gradients between dendritic (first solidification product) and interdendritic areas (solute-poor liquids that solidify in a later stage). In the V-Fe-Co-Ni-Al alloys, constitutional supercooling acts to form dendritic areas richer in Ni,

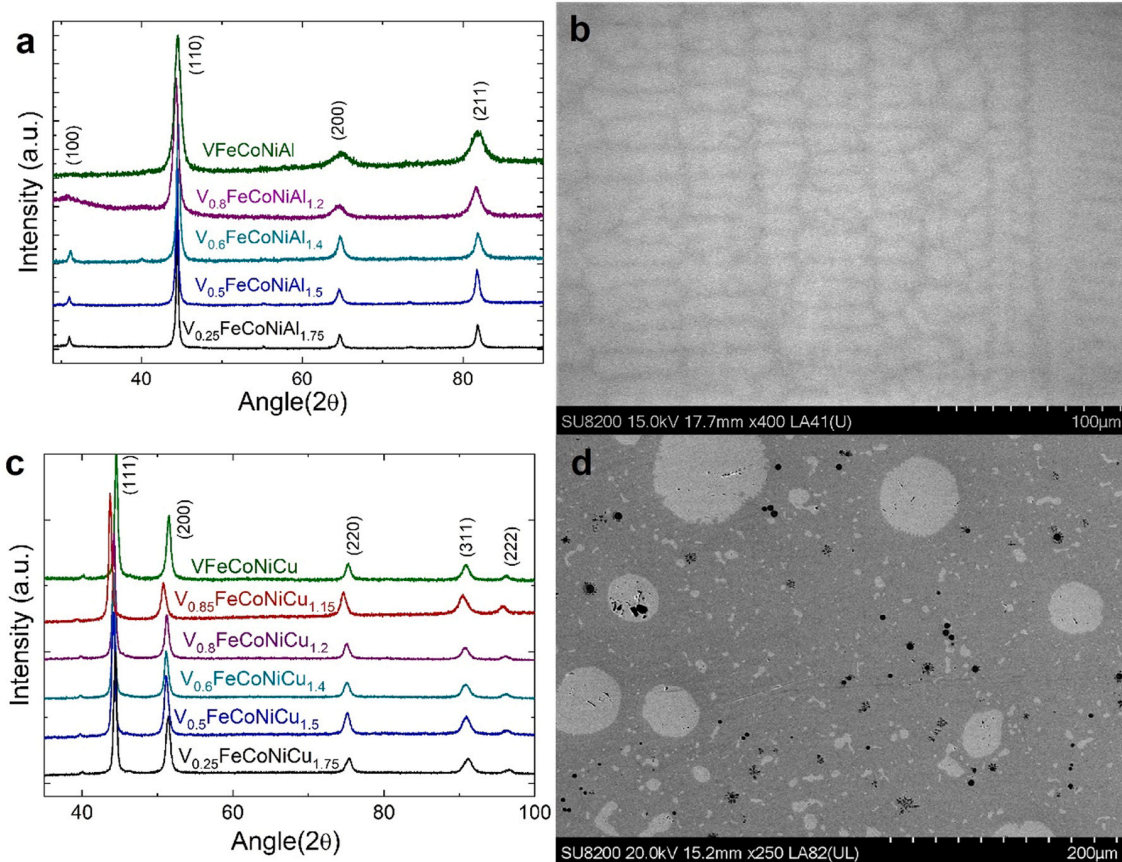


Fig. 2. a) XRD patterns for a series of V-Fe-Co-Ni-Al high entropy alloys (Cu $K\alpha$; $\lambda = 1.5406 \text{ \AA}$); b) SEM image in Back-scattered mode for $V_{0.8}FeCoNiAl_{1.2}$ displaying a dendritic microstructure; c) XRD patterns for a series of V-Fe-Co-Ni-Cu compounds (Cu $K\alpha$; $\lambda = 1.5406 \text{ \AA}$); d) SEM image in Backscattered Electron mode for $V_{0.8}FeCoNiCu_{1.2}$ exhibiting the main SS in gray, the Cu-rich phase in clear regions and the areas in black where the sigma intermetallic phase was precipitated and removed during preparation.

Table 2

Composition of dendritic areas, interdendritic areas, and the average composition measured in $V_{0.8}FeCoNiAl_{1.2}$ as determined by EDS. As a comparison, the nominal composition is displayed as well.

Element	Dendrite (%)	Interdendrite (%)	Average (%)	Nominal (%)
Fe	17.2 ± 0.8	24.0 ± 2.3	20.6 ± 3.8	20
Co	21.8 ± 0.2	21.0 ± 0.1	21.4 ± 0.4	20
Ni	22.2 ± 0.4	18.8 ± 0.9	20.5 ± 1.9	20
V	12.4 ± 0.6	18.1 ± 1.9	15.3 ± 3.2	16
Al	26.3 ± 0.9	18.0 ± 3.4	22.1 ± 4.8	24

Co and Al, with a higher solidification temperature, and interdendrites richer in Fe and V in $V_{0.8}FeCoNiAl_{1.2}$ which solidify later. The trend of Fe and V to be expelled from an early solidification front at lower temperatures is also proposed by CALPHAD as V and Fe tend to form a secondary bcc phase at lower temperatures (see Fig. 1a).

The V-Fe-Co-Ni-Cu HEAs were ductile, so the alloys were filed into fine powders. XRD patterns are shown in Fig. 2c. V-Fe-Co-Ni-Cu alloys display only ccp reflections in their as-cast state with no signs of ordering. Note, that due to a different sample height, a different sample displacement factor occurs in the $V_{0.85}FeCoNiCu_{1.15}$ sample, thus shifting its diffraction pattern slightly to the left. An example of the Rietveld refinement performed for $V_{0.85}FeCoNiCu_{1.15}$ is seen in Fig. 3a. The observed reflection peaks evidence shifts from their expected positions, as well as broadening that cannot be modeled by FWHM Caglioti function or strain contributions described by regular Pseudo-Voigt profile functions. Instead, it is concluded that this is the result of stacking faults. Stacking faults in HEAs are quite common as a higher number of elements tend to reduce the stacking fault energy [49–51]. To correctly describe the influence of stacking faults in the diffraction pattern, the FAULTS program was used. FAULTS employs a Levenberg–Marquardt algorithm to model stacking faults and is part of the Fullprof suite. It is based itself on the DIFFaX program which computes diffraction from layered crystals that contain stacking faults [52]. The best fit to the data with FAULTS for $V_{0.85}FeCoNiCu_{1.15}$ is presented in Fig. 3a. The difference in the (200) peak position for a perfectly stacked ccp lattice, and one featuring stacking faults is exemplified in Fig. 3b. Note the improved peak shift description for the FAULTS refinement compared to Fullprof, which is obtained by employing a mixture of intrinsic and extrinsic stacking faults, in a ratio between 50 % and 65 % intrinsic stacking faults, with stacking faults present from 6 % to 9 % of the ccp planes.

The lattice parameters in $V_{1-x}FeCoNiCu_{1+x}$ are lower with reduced V content, since Cu has smaller radius than V (see Table 1) [11]. The SEM micrograph for $V_{0.85}FeCoNiCu_{1.15}$ in Fig. 2d obtained in backscattered electron mode evidences two SS phases. During later stages of sample preparation, a third phase is removed from the matrix. During grinding and polishing, the surface of the sample is submitted to high stress locally. In the case of microstructures

featuring brittle phases or low coherence between the phases, some areas can be pulled out of the microstructure. Therefore, to gain insight about this phase, the chemical composition was determined by EDS during the intermediate stages of metallographic preparation. The results point towards the sigma phase, commonly formed between V, Fe, Co, Ni and Cu in HEAs [53]. Table 3 lists the compositions of different phases present in $V_{0.85}FeCoNiCu_{1.15}$, together with their average measured composition as determined by EDS and the nominal composition.

The main phase is a SS that is poor in copper (12.7 at. %) but retains most of the ferromagnetic transition metals and V. The remaining Cu segregates into a secondary phase, whose formation can be ascribed to a lack of solubility of Cu in the main SS with V-Fe-Co-Ni-Cu. A subsequent diffusion of Fe, Co and Ni during cooling into the Cu-rich phase is also observed. Possible reasons for the poor solubility of Cu in the matrix can be related to an immiscibility between Cu and V, or low solubility of Cu with Fe and Co [24,47,54]. Despite the presence of a Cu-rich phase in the micrographs, the diffraction patterns of the V-Fe-Co-Ni-Cu samples appear to be monophasic. As the Cu-rich phase exhibits a ccp structure whose atoms are very similar in size to the main SS (Cu has atomic radius comparable to Fe, Co and Ni), the diffraction patterns for these two phases would show a significant overlap, especially considering peak broadening effects associated with lattice distortions in as-cast HEAs. The present findings illustrate, why complementary techniques such as XRD and SEM are needed to fully describe the phase content, structure, and microstructure in HEAs.

When evaluating the role of the literature parameters (S_{conf} , δ , ΔH_{mix} and VEC), one can conclude that they enable early screening of SS compositions. Both systems contain SSs as majority phases: a monophasic bcc SS in the case of V-Fe-Co-Ni-Al alloys, and two ccp SSs in the V-Fe-Co-Ni-Cu system. It is important to highlight some specific property correlations, such as ΔH_{mix} and δ for instance, which can be used together to determine mono and multiphase solid solution fields [13,14]. VEC is also a relevant descriptor of possible structures in HEAs [14].

Nevertheless, they cannot be taken as the sole descriptors for phase presence and structure in HEAs. The S_{conf} property value used in the HEA literature assumes a completely random SS and neglects the possibility of a SS with a non-random distribution (sub-regular type solution). This is the dominant case in binary metallic systems [55]. The determination of S_{conf} in such sub-regular systems is not easily performed. Likewise, the Miedema model, commonly used for the determination of ΔH_{mix} , is also only accurate in certain systems as it assumes liquid mixing of the binaries, not solid ones [11,56]. Their role is, therefore, mainly to guide the early composition screening.

The experimentally observed phases at RT are also different from the ones predicted by CALPHAD. Instead, the samples are very similar to the phase content seen in the CALPHAD predictions in temperatures above 1000 K. This is caused by the metastability of the as-cast HEAs. As-cast samples withstand cooling rates of hundreds of degrees per second inside the Cu hearth during arc melting, enabling a metastable state. In this condition, only phases with a high thermal activation are formed, which are still present during the cooling process. At lower temperatures, thermodynamic equilibrium cannot be reached due to the lack of diffusivity during regular solidification processes.

In practical terms, this means that only phases seen in as-cast V-Fe-Co-Ni-Al and V-Fe-Co-Ni-Cu are phases present in diffusion active temperatures, above 1000 K. In summary, for the present HEAs in equilibrium, the literature parameters are a first step for determination of possible solid solutions, and in a subsequent step the CALPHAD method provides accurate information of phase presence. Therefore, CALPHAD can be considered as a valuable tool for the prediction of phases in multicomponent alloys.

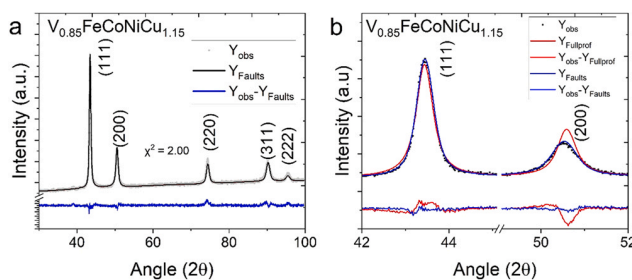


Fig. 3. a) Rietveld refinements of $V_{0.85}FeCoNiCu_{1.15}$ XRD pattern performed with the FAULTS program. b) comparison between the refinement with and without stacking faults performed with FAULTS and Fullprof, respectively. Observed intensities as dots, refined intensities as coloured lines, and difference plots on the bottom of each graph.

Table 3

Composition of main SS and Cu-rich SS phases in $V_{0.85}FeCoNiCu_{1.15}$, as well as the average composition for the alloy as determined by EDS. Nominal composition shown for comparison.

Element	Main SS (%)	Cu-rich SS (%)	Sigma (%)	Average (%)	Nominal (%)
Fe	22.5 ± 0.6	2.5 ± 0.3	14.5 ± 1.4	18.3 ± 0.3	20
Co	24.1 ± 0.2	1.9 ± 0.3	15.1 ± 1.2	21.4 ± 0.4	20
Ni	22.8 ± 0.6	6.4 ± 0.2	13.7 ± 1.2	22.8 ± 0.2	20
V	17.9 ± 2.0	0.3 ± 0.1	48.3 ± 3.4	15.0 ± 0.7	17
Cu	12.7 ± 0.5	88.9 ± 0.3	8.4 ± 1.4	22.5 ± 1.5	23

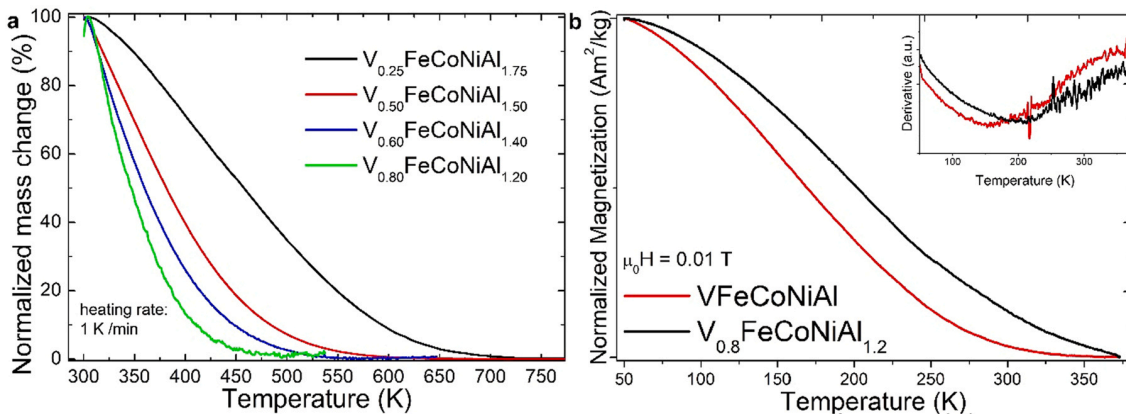


Fig. 4. (a) Indirect magnetization from magnetic balance measurements; (b) magnetization as a function of temperature for the $V_{1-x}FeCoNiAl_{1+x}$ system.

3.3. Establishment of composition trends: magnetic balance and magnetic characterization

The $V_{1-x}FeCoNiAl_{1+x}$ as-cast samples feature a broad transition, spanning more than 300 K, as seen from the magnetic balance measurements in Fig. 4a. The $V_{0.25}FeCoNiAl_{1.75}$ sample is the only composition where magnetization reduction begins above RT, spanning from 300 to 723 K. In other compositions studied, it was not possible to infer where the reduction in magnetization begins, i.e., where the transition begins. The normalized curves in Fig. 4a feature different slopes. This can be a sign of inhomogeneities modifying local average exchange interactions and the local T_C values, and then change the slope of the curves. To determine the behaviour in some compositions below RT, thermomagnetic measurements were performed for $VFeCoNiAl$ and $V_{0.8}FeCoNiAl_{1.2}$, see Fig. 4b. Curves were normalized in order to ease visualization. Absolute magnetization values at different temperatures are better displayed in field-dependent measurements seen in Fig. 6a.

Both equimolar and $V_{0.8}FeCoNiAl_{1.2}$ samples feature the same behavior seen in magnetic balance measurements with broad

transitions spanning more than 300 K. As expected, samples with higher V content have their transitions shifted towards lower temperatures. The T_C values are determined from the derivative values of magnetization as a function of temperature, see the inset of Fig. 4b for $VFeCoNiAl$ and $V_{0.8}FeCoNiAl_{1.2}$, respectively. For $VFeCoNiAl$, $V_{0.8}FeCoNiAl_{1.2}$ and $V_{0.25}FeCoNiAl_{1.75}$, T_C values were determined as 155, 200 and 456 K, respectively. Compositions featuring transitions above or below the equipment's temperature threshold did not have their T_C measured, as it was not possible to capture the full extent of the transition.

This continuous decrease of magnetization as a function of temperature is further evidenced in field-dependent magnetization $M(H)$ measurements shown in Fig. 6a for the equimolar $VFeCoNiAl$ composition. The saturation magnetization (M_S) drops with temperature, from 38 Am^2/kg at 10 K to around 5 Am^2/kg at 370 K. The magnetization shows a linear increase at higher fields, indicating a possible PM contribution to the ferromagnetic signal.

The magnetic balance measurements for the $V_{1-x}FeCoNiCu_{1+x}$ as-cast alloys, shown in Fig. 5a, feature narrower magnetic transitions compared to the V-Fe-Co-Ni-Al samples, spanning only around

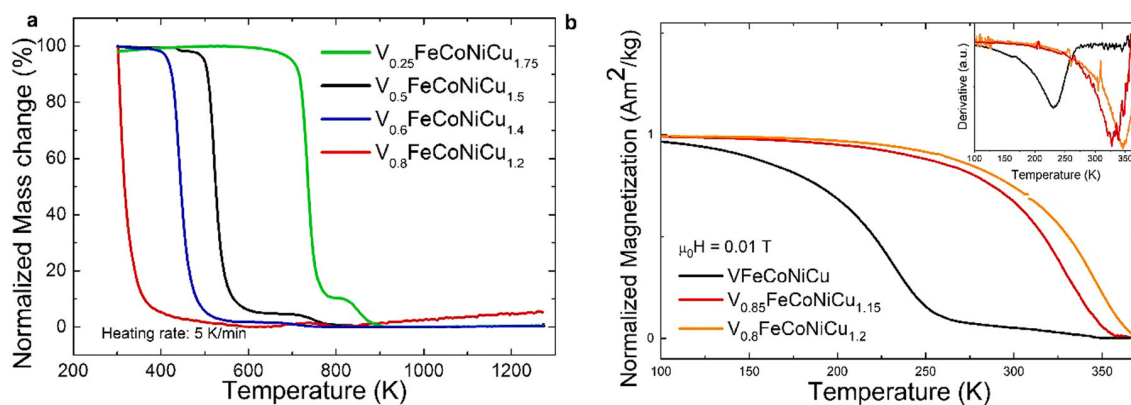


Fig. 5. (a) Indirect magnetization from magnetic balance measurements; (b) magnetization as a function of temperature for the $V_{1-x}FeCoNiCu_{1+x}$ system.

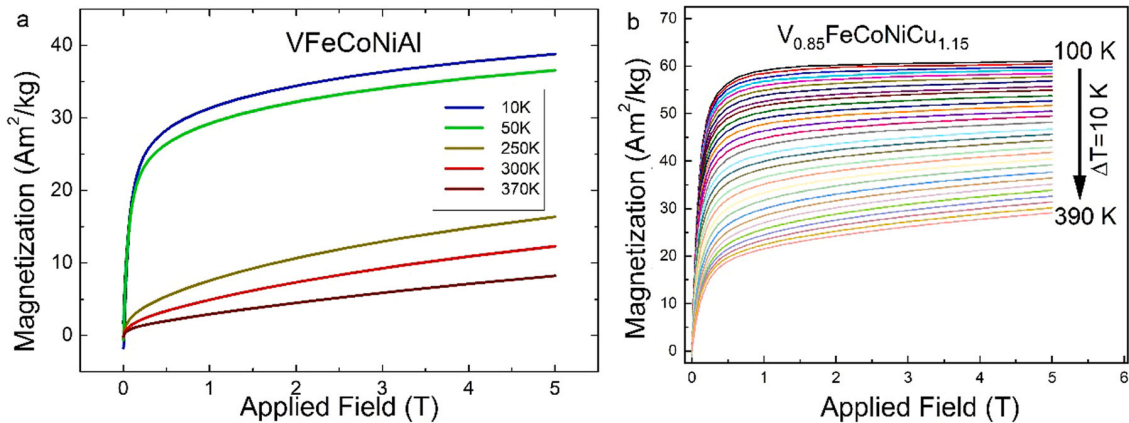


Fig. 6. Magnetization as a function of applied field for (a) VFeCoNiAl and (b) $V_{0.85}FeCoNiCu_{1.15}$.

150 K. Similar to the V-Fe-Co-Ni-Al samples, a reduction in V content and increase in the fifth element content (Cu) raises T_C to higher temperatures. Note, that the onset of the magnetic transition for the $V_{0.8}FeCoNiCu_{1.2}$ sample lies below RT (outside our measurement range). It is therefore not possible to correctly evaluate its transition temperature by the magnetic balance measurements. It can be concluded that samples containing 16 at. % V or more feature part of their magnetic transitions around RT and below. Therefore, additional temperature-dependent magnetization measurements were performed. Fig. 5b shows the normalized magnetization obtained for three samples: $V_{1-x}FeCoNiCu_{1+x}$ ($x = 0.0, 0.15$ and 0.2) measured between 100 K and 400 K in an external field of 0.01 T. The insert in Fig. 5b shows the derivative of magnetization as a function of temperature and is used to determine T_C .

Experimental T_C values for the V-Fe-Co-Ni-Cu samples are shown in Table 4. A secondary step or a slight slope shift after the main magnetization decrease is observed, which evidences the presence of a secondary magnetic phase both in high and low temperature measurements. This response can be attributed to the secondary Cu-rich phase, with small concentration of FM 3d elements. As the magnetocaloric effect in such SOPT is directly related to the sharpness of the magnetic transition, it is possible to conclude that the V-Fe-Co-Ni-Cu system is more promising for magnetocaloric applications than the V-Fe-Co-Ni-Al system under the current conditions. To shed more light on the role of each element on the magnetic properties of $V_{1-x}FeCoNiCu_{1+x}$ alloys, DFT calculations were performed.

The total and element resolved magnetic moments of $V_{1-x}FeCoNiCu_{1+x}$ alloys as a function of V and Cu concentrations are listed in Table 4 in units of Bohr magnetons, μ_B . We can observe that the total magnetic moment per unit cell m_{tot} increases from $0.59 \mu_B$ for the equiatomic alloy to $0.82 \mu_B$ for $V_{0.25}FeCoNiCu_{1.75}$. This can be attributed to the change of the element resolved magnetic moments with V and Cu concentration. Fe, Co and Ni couple parallel to each other in all alloys and their moments increase with increasing Cu content. This is in line with the slight re-population of the 3d orbitals

plotted in Fig. 7 due to a relative change in V/Cu concentration. It increases the population of the spin-up channel and decreases the population of the spin-down channel as observed for Fe, Co and Ni in $V_{0.25}FeCoNiCu_{1.75}$, compared with spin channel occupations in $V_1FeCoNiCu_1$. Due to a hybridisation of the 3d orbitals of V and Cu with the 3d orbitals of Fe, Co and Ni, induced magnetic moments appear on V as well as on Cu. While the magnetic moment on Cu is small and couples parallel to the moments of Fe, Co and Ni, the magnetic moment developed on V is larger and antiparallel to the rest of the moments. The small magnitude of m_{Cu} is due to the fully filled 3d-orbitals as presented in Fig. 7, which is a direct consequence of the *sd*-hybridisation present in Cu. In contrast, V has a less than half-filled 3d orbital and therefore a large number of states at the Fermi energy (see Fig. 7). This makes V to be easily polarised and results in a moment of $-0.48 \mu_B$, for $V_1FeCoNiCu_1$ which increases to $-0.93 \mu_B$, for $V_{0.25}FeCoNiCu_{1.75}$. This increase of the magnetic moment is a consequence of the migration of the spin-up electrons into the spin-down channel. We then proceed to estimate T_C and compare it to the experimental values.

The calculated T_C values are increasing with decreasing V concentration, from 220 K for the equiatomic alloy to 520 K for $V_{0.25}FeCoNiCu_{1.75}$, as shown in Table 4. This agrees with experimental findings and is a consequence of the dilution of V in the SS [39]. The calculated Curie temperatures in Table 4 are consistently lower than the measured ones, and the difference increases with decreasing vanadium content, from 10 K for the equiatomic alloy to 216 K for $V_{0.25}FeCoNiCu_{1.75}$. Results presented here are obtained using LSDA, that is regarded as giving the lower bound for the values describing the magnetic properties. The generalized gradient approximations, for example the Perdew-Burke-Ernzerhof exchange-correlation functional [57], gives larger values for calculated magnetization and estimated Curie temperatures. For the investigated alloys, we observe a 1.2 % constant shift towards higher moments and T_C for each composition, and therefore the slope for the T_C variation with V/Cu concentration is not affected. Two factors may account for this discrepancy: (1) the difference between the ideal

Table 4

Total (m_{tot}) and element resolved ($m_{element}$) magnetic moments in units of Bohr magnetons, μ_B , calculated and experimental Curie temperatures (T_C) in K for a series of $V_{1-x}FeCoNiCu_{1+x}$ alloys.

Composition	$m_{tot}(\mu_B)$	$m_V(\mu_B)$	$m_{Fe}(\mu_B)$	$m_{Co}(\mu_B)$	$m_{Ni}(\mu_B)$	$m_{Cu}(\mu_B)$	calc. T_C (K)	exp. T_C (K)
$V_1FeCoNiCu_1$	0.59	-0.48	2.10	1.07	0.23	0.01	220	230
$V_{0.85}FeCoNiCu_{1.15}$	0.62	-0.53	2.17	1.14	0.26	0.01	260	329
$V_{0.8}FeCoNiCu_{1.2}$	0.64	-0.56	2.20	1.17	0.27	0.01	290	345
$V_{0.6}FeCoNiCu_{1.4}$	0.70	-0.67	2.29	1.27	0.31	0.01	360	440
$V_{0.5}FeCoNiCu_{1.5}$	0.73	-0.73	2.34	1.31	0.33	0.01	400	521
$V_{0.25}FeCoNiCu_{1.75}$	0.82	-0.93	2.46	1.43	0.40	0.02	520	736

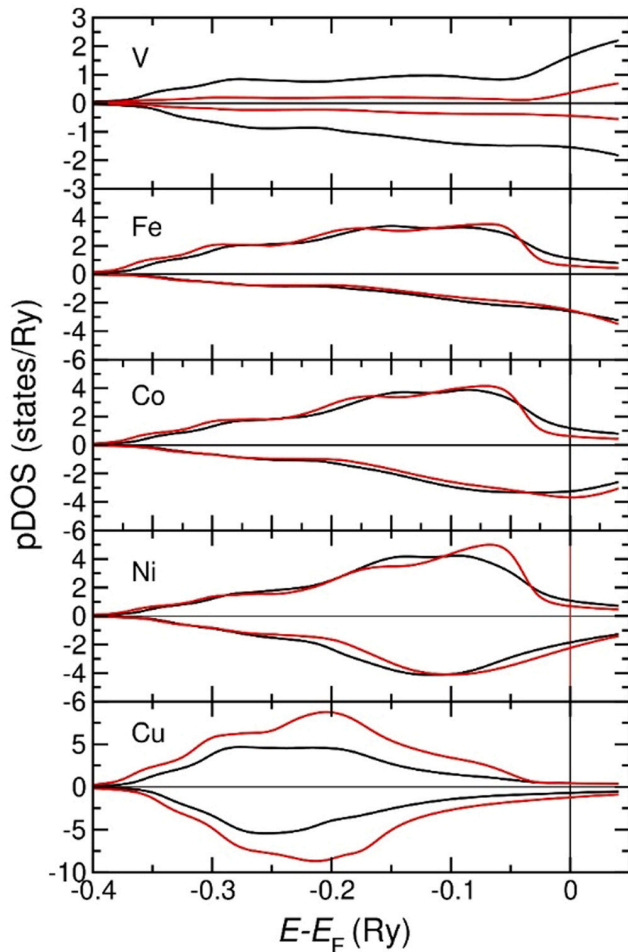


Fig. 7. Element resolved density of states. Black lines represent VFeCoNiCu and red lines represent $V_{0.25}\text{FeCoNiCu}_{1.75}$. Density of states are weighted with the concentration of each element.

equilibrium alloys modelled by the theory and the multi-phase experimental samples. The change in V/Cu ratio affects the phase ratio between the main SS, Cu-rich SS and sigma-phase. This in turn modifies the composition of the main SS, further diverging from the nominal composition. The model also does not take into account the influence of defects i.e. local composition variations, local lattice relaxations, vacancies, stacking faults, etc.; (2) temperature-induced longitudinal fluctuations of the magnetic moments are not accounted for, even though they are important to properly describe high temperature magnetism of 3d alloys [34]. However, while the above-mentioned factors may be important, the trend in the T_C variation with concentration is well captured without taking them into account. Therefore, the complex description of high temperature magnetism and the effect of structural complexity on the magnetic properties of these alloys are left to another study.

Field dependent measurements were carried out with an applied field of $\mu_0 H = 0-5$ T at selected temperatures between 10 K and 390 K in $V_{0.85}\text{FeCoNiCu}_{1.15}$, and are displayed in Fig. 6b. The magnetization as a function of applied field for the V-Fe-Co-Ni-Cu samples is different from the V-Fe-Co-Ni-Al sample shown in Fig. 6a, as purely FM behaviour is seen in the measurements at 10 K. This is evidenced by a plateau at high magnetic fields, i.e., the sample reaches its saturation magnetization, M_s . In the isothermal measurements performed at higher temperatures, magnetization displays a more paramagnetic character, as magnetization begins to increase linearly with the applied field. Note the presence of a

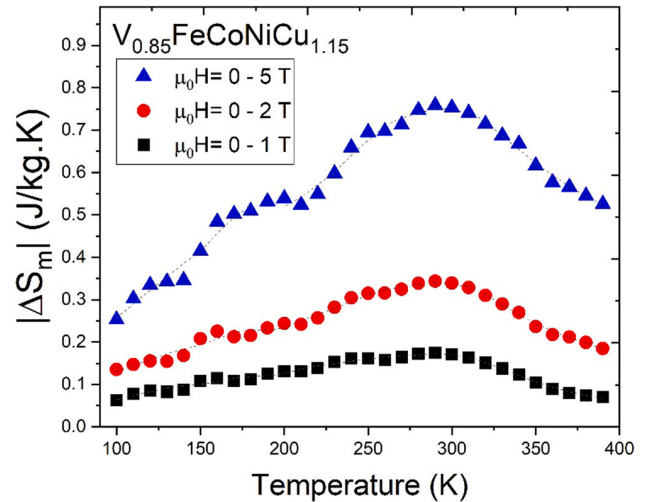


Fig. 8. Isothermal magnetic entropy change for $V_{0.85}\text{FeCoNiCu}_{1.15}$ between 100 and 390 K.

secondary ferromagnetic phase in the $M(H)$ curves as well, as some magnetization is retained at 390 K. Saturation magnetization values for $V_{0.85}\text{FeCoNiCu}_{1.15}$ are higher than for the 5-element equiatomic alloy with Al; with M_s reaching up to $61 \text{ Am}^2/\text{kg}$ at 100 K, to approximately $29 \text{ Am}^2/\text{kg}$ at 390 K. We attribute this to the presence of the secondary phase with higher M_s .

3.4. $V_{0.85}\text{FeCoNiCu}_{1.15}$ magnetocaloric properties and magnetic system description

From the field dependent data shown previously, one can indirectly obtain ΔS_m from Eq. 1 between 100 and 390 K, and the results are shown in Fig. 8 for field changes of 0–1, 0–2 and 0–5 T, respectively. The whole transition from the main SS phase branches over this wide temperature range, peaking around RT (the biggest values are seen at $T = 290$ K). The maximum values are approximately 0.15, 0.3 and 0.75 J/kg.K for the 0–1, 0–2 and 0–5 T changes, respectively. Even though at higher temperatures a complete paramagnetic state is not yet reached (as seen by the remaining magnetization in the field dependent magnetization curves in Fig. 6b), most of the sample has transitioned, leading to smaller ΔS_m values after the peak around RT. Small variations between each temperature step can be seen that gives small deviations throughout the temperature range, which stems from a non-normalized microstructure with compositional variations across the main SS phase. However, the trend of the transition can be clearly seen across the studied temperature range. A similar behavior of ΔS_m variations between temperature steps is seen in as-cast $\text{Mn}_{0.89}\text{Cr}_{0.3}\text{Fe}_{0.5}\text{Co}_{0.2}\text{Ni}_{0.5}\text{Al}_{0.3}$ HEA where despite these variations, the behavior of the transition is captured [20,58].

This influences the dM/dT values, which in turn causes a gradual decrease of the ΔS_m curve, as seen from Eq. (1). The highest value of 0.75 J/kg.K for a field change of 5 T is comparable to what has been reported for ccp HEAs featuring a SOPT, such as Cr-containing CrFeCoNiPd_x and CrFeCoNiAl_x [20,59]. Nevertheless, the value is lower than the $\text{Mn}_{27}\text{Cr}_7\text{Ni}_{33}\text{Ge}_{25}\text{Si}_8$ SOPT HEA and $\text{Mn}_{22}\text{Fe}_{22}\text{Ni}_{22}\text{Ge}_{17}\text{Si}_{17}$ FOPT HEA, which are modifications of the MMX alloy systems containing hexagonal or orthorhombic structures [60,61]. In order to gain a better understanding of the magnetic order in the as-cast V-Fe-Co-Ni-Cu alloys, pair exchange integrals (J_{ij}) were calculated by means of DFT.

In metals featuring SOPTs, ΔS_m values arise from the demagnetization of the magnetic moments from direct exchange interactions

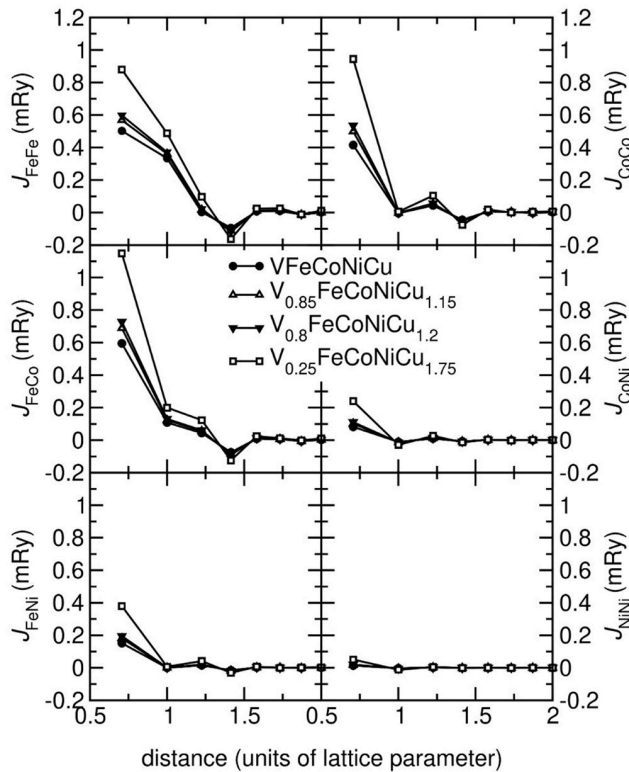


Fig. 9. Magnetic exchange integrals between the magnetic elements Fe, Co and Ni as a function of atomic distance for a series of $V_{1-x}FeCoNiCu_{1+x}$ ($x = 0, 0.15, 0.2,$ and 0.75) samples.

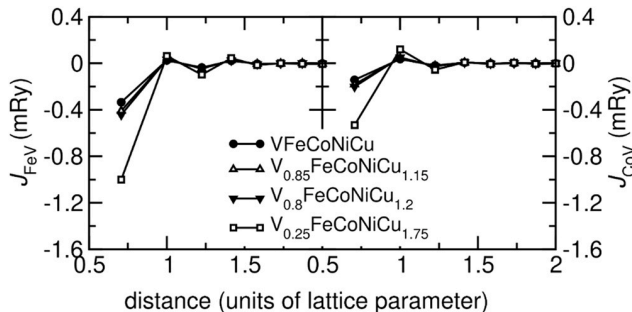


Fig. 10. Magnetic exchange integrals between Fe and V, and Co and V, respectively, as a function of atomic distance for a series of $V_{1-x}FeCoNiCu_{1+x}$ ($x = 0, 0.15, 0.2,$ and 0.75) samples.

between the atom pairs at T_C . To describe the V-Fe-Co-Ni-Cu system, the calculated magnetic exchange integrals are plotted in Figs. 9 and 10. A general observation is that the exchange integrals show an oscillatory behaviour with distance and decay after about 1.5 lattice parameter units (5th coordination shell). Also, all interactions increase with decreasing V content. The strongest FM couplings can be found between the magnetic elements Fe and Co, i.e., J_{FeFe} , J_{FeCo} and J_{CoCo} (see Fig. 9). They become stronger with decreasing V concentration, which is in line with the increase of local magnetic moments of these elements. Since Ni possesses only a small magnetic moment, it also shows a weaker FM coupling with itself and with Fe and Co (see Fig. 9 for J_{FeNi} , J_{CoNi} and J_{NiNi}).

The magnetic coupling between Cu, V, and the magnetic elements as well as for Cu-Cu, Cu-V and V-V pairs is negligible and

therefore not shown. However, we find a large negative nearest neighbour coupling for Fe and Co with V (see Fig. 10) that increases with decreasing V content that becomes comparable in size to the J_{FeFe} , J_{FeCo} and J_{CoCo} exchange integrals for $V_{0.25}FeCoNiCu_{1.75}$.

In disordered materials such as HEAs, the high number of possible parallel and antiparallel magnetic couplings surrounding each element creates different magnetic configurations in neighbouring coordination shells. This leads to a distribution of exchange interactions and consequently magnetic ordering temperatures that result in broad magnetic transitions that span a large range of temperatures. This behaviour may be further complicated by non-normalized microstructures common in regular solidification processes. In them, a deviation from a random SS occurs leading to inhomogeneities or ordering. This results in micro segregation in clusters within a SS phase or in some cases, the formation of secondary phases. All of this can contribute negatively, lowering the total entropy change. This non-normalized microstructure featuring composition gradients within the SS yields a distribution of T_C values, which in turn lowers the maximum ΔS_m values. This negative influence of microstructure can be minimized by applying different processing routes, as has been reported for rapidly-solidified MnFeCoNiCu [29]. The use of processes inducing fast cooling can minimize the dwelling time in such diffusion-activated regimes, and thus reducing inhomogeneities.

On the other hand, adequate heat treatments can be employed on certain alloys to increase the change in magnetization with respect to temperature ($\frac{\partial M}{\partial T}$). By inducing the formation of intermetallics or ordered phases that enable strong ferromagnetic interactions, it is possible to modify the material and thus increase ($\frac{\partial M}{\partial T}$). In the Cr-based HEA $Cr_{0.5}FeCoNi_{0.5}Al_x$, the neighborhood of Fe changes from a disordered SS that contains Fe, Co, Ni, Cr and Al to one where Fe is precipitated into Fe-Cr nanoparticles [26,30]. This precipitate contributes ferromagnetically due to an exchange coupling with the surrounding FM Al-Ni-Co matrix. Due to this particular microstructure, ΔS_m values are higher (~ 0.5 J/kg.K at $\mu_0 H = 2$ T) than for HEAs that feature completely disordered structures. We believe that similar strategies can be employed to improve the characteristics of the magnetic SOPTs in the V-Fe-Co-Ni-Cu HEAs presented here.

4. Conclusions

$V_{1-x}FeCoNiAl_{1+x}$ and $V_{1-x}FeCoNiCu_{1+x}$ HEAs were explored as candidates for magnetic refrigeration applications. Compositions were chosen in agreement with well-known properties in the literature. SS phase formation guidelines based on literature results were compared with the CALPHAD method and with experimental results of the processed alloys. The alloys studied were all in an as-cast state. Compounds in the V-Fe-Co-Ni-Al system are monophasic and crystallize in a bcc lattice and tend to order themselves as B2 structures as Al content increases. The V-Fe-Co-Ni-Cu system features a main SS, a Cu-rich SS, and a V-containing intermetallic phase. Due to a limit of Cu solubility in the main SS, Cu segregates into a secondary Cu-rich phase.

The thermodynamic parameters help to establish a first evaluation of proposed V-Fe-Co-Ni-Al and V-Fe-Co-Ni-Cu HEAs before processing, thus helping to determine mono/multiphase compositions that can yield interesting properties. The CALPHAD calculations differ from experimental results due to samples being in a metastable condition in their as-cast state. However, the predictions made from CALPHAD for phase composition and presence in diffusion activated regimes (high temperatures) is very similar to what is seen in the as-cast samples.

A substitution of V by Al or Cu raises magnetic transition temperatures for both systems. The Al-containing alloys feature a broad

magnetic transition that spans more than 400 K. They also exhibit lower magnetization change values than the Cu-containing alloys. This is attributed to the presence of paramagnetic Al and V, as well as big compositional gradients in their microstructure. The Cu-containing samples feature a magnetic transition that spans 150 K with higher magnetization value changes, which makes the V-Fe-Co-Ni-Cu alloys better candidates for magnetocaloric applications than the V-Fe-Co-Ni-Al alloys. An analysis of the magnetic exchange interactions in the V-Fe-Co-Ni-Cu alloys by means of DFT shows strong FM interactions between Fe, Co and Ni and negligible interactions between Cu-Cu, Cu-V and V-V pairs. There exists a large antiferromagnetic coupling between Fe-V and Co-V pairs that tends to lower the ferromagnetic character of the samples.

As it is known, derivatives of magnetization with temperature are an adequate indication of the magnetocaloric effect in SOPT materials; rather low derivative values for Al and Cu containing samples lead to isothermal magnetic entropy changes, ΔS_m , that are comparable to those observed in Mn- and Cr-containing HEAs. However, the values are lower when compared to the magnetocaloric effect of orthorhombic/hexagonal HEAs featuring p-block elements.

HEAs for magnetocaloric applications are typically employed in their as-cast state, which might not yield the best results. Thermo-mechanical treatments may change phase morphology and control metallurgical processes such as recovery, recrystallization or precipitation, which can lead to different magnetic exchange phenomena in multiphasic systems. Such possibilities are not common in rare earth intermetallics, which are typically brittle. This could lead to improved magnetocaloric properties in such versatile transition metal systems. Furthermore, the low manufacturing cost of 3d metal based HEAs compared to rare earth-based materials should make them attractive candidates for magnetocaloric energy devices.

The search for new HEA candidate materials with suitable MCE properties could be performed by a combined CALPHAD and DFT methodology. In the first step, CALPHAD calculations are performed to predict compositions of solid solutions present and possible intermetallics. In the second step, DFT calculations are employed to estimate the magnetic moments from equilibrium phases. However, only through experimental work on promising candidates will it be possible to evaluate the true performance of HEAs for magnetocaloric energy conversion.

The field of HEA research for magnetocaloric applications is still very young. The complex magnetic interactions in such disordered systems are still not completely understood, while crystal structures and microstructures depend strongly on processing conditions and are easily modifiable. The full potential of HEAs for magnetocaloric energy conversion around RT can only be reached through careful control of their elemental composition and microstructure.

CRedit authorship contribution statement

Bruno G. F. Eggert: Conceptualization, Investigation, Writing – original draft, Visualization, Writing – review & editing, Erna K. Delczeg-Czirjak: Software, Methodology, Formal analysis, Resources, Visualization, Writing – review & editing, Fernando Maccari: Investigation, Resources, Susmit Kumar: Investigation, Resources, Oliver Gutfleisch: Writing – review & editing, Resources, Helmer Fjellvåg: Writing – review & editing, Resources, Bjørn C. Hauback: Writing – review & editing, Supervision, Christoph Frommen: Writing – review & editing, Supervision, Project administration, Funding acquisition.

Data availability

Data will be made available on request.

Declaration of Competing Interest

The authors declare that they have no known competing financial interests or personal relationships that could have appeared to influence the work reported in this paper.

Acknowledgements

This work was financed by The Research Council of Norway through the NANO2021 program, Project No. 287150. E.K.D-Cz. acknowledges STandUPP and eSENCE for financial support and the Swedish National Infrastructure for Computing (SNIC) for computational resources.

The authors acknowledge Magnus H. Sørby for fruitful discussions and his skilful assistance with structural characterization and modelling.

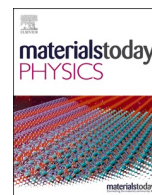
References

- [1] C.K. Folland, T.R. Karl, M. Jim Salinger, Observed climate variability and change, *Weather* 57 (2002) 269–278, <https://doi.org/10.1256/004316502320517353>
- [2] L. Cozzi, T. Gould, S. Bouckart, D. Crow, T.-Y. Kim, C. McGlade, P. Olejarnik, B. Wanner, D. Wetzel, *World Energy Outlook 2020*, 2050 (2020) 1–461. (https://www.oecd-ilibrary.org/energy/world-energy-outlook-2020_557a761b-en).
- [3] V.K. Pecharsky, K. a Gschneidner, Giant magnetocaloric effect in $Gd_5Si_2Ge_2$, *Phys. Rev. Lett.* 78 (1997) 3–6, <https://doi.org/10.1103/PhysRevLett.78.4494>
- [4] T. Gottschall, A. Gràcia-Condal, M. Fries, A. Taubel, L. Pfeuffer, L. Mañosa, A. Planes, K.P. Skokov, O. Gutfleisch, A multicaloric cooling cycle that exploits thermal hysteresis, *Nat. Mater.* 17 (2018) 929–934, <https://doi.org/10.1038/s41563-018-0166-6>
- [5] O. Gutfleisch, T. Gottschall, M. Fries, D. Benke, I. Radulov, K.P. Skokov, H. Wende, M. Gruner, M. Acet, P. Entel, M. Farle, Mastering hysteresis in magnetocaloric materials, *Philos. Trans. R. Soc. A Math. Phys. Eng. Sci.* 374 (2016), <https://doi.org/10.1098/rsta.2015.0308>
- [6] V. Franco, J.S. Blázquez, J.J. Ipus, J.Y. Law, L.M. Moreno-Ramírez, A. Conde, Magnetocaloric effect: From materials research to refrigeration devices, *Prog. Mater. Sci.* 93 (2018) 112–232, <https://doi.org/10.1016/j.pmatsci.2017.10.005>
- [7] T. Gottschall, K.P. Skokov, M. Fries, A. Taubel, I. Radulov, F. Scheibel, D. Benke, S. Riegg, O. Gutfleisch, Making a cool choice: the materials library of magnetic refrigeration, *Adv. Energy Mater.* 9 (2019), <https://doi.org/10.1002/aenm.201901322>
- [8] F. Scheibel, T. Gottschall, A. Taubel, M. Fries, K.P. Skokov, A. Terwey, W. Keune, K. Ollefs, H. Wende, M. Farle, M. Acet, O. Gutfleisch, M.E. Gruner, Hysteresis design of magnetocaloric materials—from basic mechanisms to applications, *Energy Technol.* 6 (2018) 1397–1428, <https://doi.org/10.1002/ente.201800264>
- [9] T. Hess, L.M. Maier, N. Bachmann, P. Corhan, O. Schäfer-Welsen, J. Wollenstein, K. Bartholomé, Thermal hysteresis and its impact on the efficiency of first-order caloric materials, *J. Appl. Phys.* 127 (2020), <https://doi.org/10.1063/1.5132897>
- [10] R. Kozak, A. Sologubenko, W. Steurer, Single-phase high-entropy alloys – an overview, *Z. Fur Krist.* 230 (2015) 55–68, <https://doi.org/10.1515/zkri-2014-1739>
- [11] D.B. Miracle, O.N. Senkov, A critical review of high entropy alloys and related concepts, *Acta Mater.* 122 (2017) 448–511, <https://doi.org/10.1016/j.actamat.2016.08.081>
- [12] B.E. MacDonald, Z. Fu, B. Zheng, W. Chen, Y. Lin, F. Chen, L. Zhang, J. Ivanisenko, Y. Zhou, H. Hahn, E.J. Lavernia, Recent progress in high entropy alloy research, *JOM* 69 (2017) 2024–2031, <https://doi.org/10.1007/s11837-017-2484-6>
- [13] M.C. Gao, C. Zhang, P. Gao, F. Zhang, L.Z. Ouyang, M. Widom, J.A. Hawk, Thermodynamics of concentrated solid solution alloys, *Curr. Opin. Solid State Mater. Sci.* 21 (2017) 238–251, <https://doi.org/10.1016/j.cossms.2017.08.001>
- [14] Z. Wang, S. Guo, C.T. Liu, Phase selection in high-entropy alloys: from nonequilibrium to equilibrium, *JOM* 66 (2014) 1966–1972, <https://doi.org/10.1007/s11837-014-0953-8>
- [15] H. Mao, H.L. Chen, Q. Chen, TCHEA1: a thermodynamic database not limited for “High Entropy”, *Alloy. J. Phase Equilibria Diffus* 38 (2017) 353–368, <https://doi.org/10.1007/s11669-017-0570-7>
- [16] M.M. Nygård, W.A. Sławiński, G. Ek, M.H. Sørby, M. Sahlberg, D.A. Keen, B.C. Hauback, Local order in high-entropy alloys and associated deuterides – a total scattering and Reverse Monte Carlo study, *Acta Mater.* 199 (2020) 504–513, <https://doi.org/10.1016/j.actamat.2020.08.045>
- [17] H.P. Chou, Y.S. Chang, S.K. Chen, J.W. Yeh, Microstructure, thermophysical and electrical properties in $AlxCoCrFeNi$ ($0 \leq x \leq 2$) high-entropy alloys, *Mater. Sci. Eng. B Solid-State Mater. Adv. Technol.* 163 (2009) 184–189, <https://doi.org/10.1016/j.mseb.2009.05.024>
- [18] Q. Zhang, H. Xu, X.H. Tan, X.L. Hou, S.W. Wu, G.S. Tan, L.Y. Yu, The effects of phase constitution on magnetic and mechanical properties of $FeCoNi(CuAl)_x$ ($x = 0-1.2$) high-entropy alloys, *J. Alloy. Compd.* 693 (2017) 1061–1067, <https://doi.org/10.1016/j.jallcom.2016.09.271>
- [19] M.C. Gao, D.B. Miracle, D. Maurice, X. Yan, Y. Zhang, J.A. Hawk, High-entropy functional materials, *J. Mater. Res.* 33 (2018) 3138–3155, <https://doi.org/10.1557/jmr.2018.323>

- [20] S.M. Na, P.K. Lambert, H. Kim, J. Paglione, N.J. Jones, Thermomagnetic properties and magnetocaloric effect of FeCoNiCrAl-type high-entropy alloys, *AIP Adv.* 9 (2019), <https://doi.org/10.1063/1.5079394>
- [21] B.F. Yu, Q. Gao, B. Zhang, X.Z. Meng, Z. Chen, Review on research of room temperature magnetic refrigeration, *Int. J. Refrig.* 26 (2003) 622–636, [https://doi.org/10.1016/S0140-7007\(03\)00048-3](https://doi.org/10.1016/S0140-7007(03)00048-3)
- [22] F. Körmann, D. Ma, D.D. Belyea, M.S. Lucas, C.W. Miller, B. Grabowski, M.H.F. Sluiter, “Treasure Maps” for magnetic high-entropy-alloys from theory and experiment, *Appl. Phys. Lett.* 107 (2015), <https://doi.org/10.1063/1.4932571>
- [23] M. Kurniawan, A. Perrin, P. Xu, V. Keylin, M. McHenry, Curie temperature engineering in high entropy alloys for magnetocaloric applications, *IEEE Magn. Lett.* 7 (2016) 1–5, <https://doi.org/10.1109/LMAG.2016.2592462>
- [24] Z. Rao, B. Dutta, F. Körmann, D. Ponge, L. Li, J. He, L. Stephenson, L. Schäfer, K. Skokov, O. Gutfleisch, D. Raabe, Z. Li, Unveiling the mechanism of abnormal magnetic behavior of FeNiCoMnCu high-entropy alloys through a joint experimental-theoretical study, *Phys. Rev. Mater.* 4 (2020), <https://doi.org/10.1103/PhysRevMaterials.4.014402>
- [25] J.K.-P. E-Wen Huang, Guo-Yu Chang, Yeol Hung Soo, Lee, W.-C.Y. Jayant, P.K.L. Jing, J. Chou, Mechanical and magnetic properties of the high-entropy alloys for combinatorial approaches, 697–697, *J. A. I. E. E* 46 (2013), <https://doi.org/10.1109/jaiee.1927.6535544>
- [26] N.A. Morley, B. Lim, J. Xi, A. Quintana-Nedelcos, Z. Leong, Magnetic properties of the complex concentrated alloy system CoFeNi_{0.5}Cr_{0.5}Al_x, *Sci. Rep.* 10 (2020) 1–12, <https://doi.org/10.1038/s41598-020-71463-3>
- [27] L. Han, Z. Rao, I.R. Souza Filho, F. Maccari, Y. Wei, G. Wu, A. Ahmadian, X. Zhou, O. Gutfleisch, D. Ponge, D. Raabe, Z. Li, Ultrastrong and ductile soft magnetic high-entropy alloys via coherent ordered nanoprecipitates, *Adv. Mater.* 33 (2021) 3–12, <https://doi.org/10.1002/adma.202102139>
- [28] Z. Li, K.G. Pradeep, Y. Deng, D. Raabe, C.C. Tasan, Metastable high-entropy dual-phase alloys overcome the strength-ductility trade-off, *Nature* 534 (2016) 227–230, <https://doi.org/10.1038/nature17981>
- [29] A. Perrin, M. Sorescu, M.T. Burton, D.E. Laughlin, M. McHenry, The role of compositional tuning of the distributed exchange on magnetocaloric properties of high-entropy alloys, *JOM* 69 (2017) 2125–2129, <https://doi.org/10.1007/s11837-017-2523-3>
- [30] A. Quintana-Nedelcos, Z. Leong, N.A. Morley, Study of dual-phase functionalisation of NiCoFeCr-Alx multicomponent alloys for the enhancement of magnetic properties and magneto-caloric effect, *Mater. Today Energy* 20 (2021) 100621, <https://doi.org/10.1016/j.mtener.2020.100621>
- [31] J. Rodriguez-Carvajal, Recent developments of the program FULLPROF, commission on powder diffraction, *IUCr Newsl.* 26 (2001) 12–19 (<http://www.iucr.org/iucr-top/comm/cpd/html/newsletter26.html>).
- [32] P. Hohenberg, W. Kohn, Inhomogeneous Electron Gas, *Phys. Rev.* 136 (n.d.) B864–B871, <https://link.aps.org/doi/10.1103/PhysRev.136.B864>.
- [33] W. Kohn, L.J. Sham, Self-consistent equations including exchange and correlation effects, A1133–A1138, *Phys. Rev.* 140 (1965), <https://doi.org/10.1103/PhysRev.140.A1133>
- [34] A.V. Ruban, M. Dehghani, Atomic configuration and properties of austenitic steels at finite temperature: Effect of longitudinal spin fluctuations, *Phys. Rev. B* 94 (2016) 1–10, <https://doi.org/10.1103/PhysRevB.94.104111>
- [35] O.K. Andersen O. Jepsen, G. Krier, Lectures on Methods of Electronic Structure Calculation, 1994.
- [36] L. Vitos, H.L. Skriver, B. Johansson, J. Kollár, Application of the exact muffin-tin orbitals theory: the spherical cell approximation, *Comput. Mater. Sci.* 18 (2000) 24–38, [https://doi.org/10.1016/S0927-0256\(99\)00098-1](https://doi.org/10.1016/S0927-0256(99)00098-1)
- [37] L. Vitos, Total-energy method based on the exact muffin-tin orbitals theory, *Phys. Rev. B* 64 (2001) 14107, <https://doi.org/10.1103/PhysRevB.64.014107>
- [38] L. Vitos, The EMTO Method and Applications in Computational Quantum Mechanics for Materials Engineers, Springer-Verlag, London, 2007.
- [39] P.A. Korzhavyi, A.V. Ruban, I.A. Abrikosov, H.L. Skriver, Madelung energy for random metallic alloys in the coherent potential approximation, *Phys. Rev. B* 51 (1995) 5773–5780, <https://doi.org/10.1103/PhysRevB.51.5773>
- [40] P. Soven, Coherent-potential model of substitutional disordered alloys, *Phys. Rev.* 156 (1967) 809–813, <https://doi.org/10.1103/PhysRev.156.809>
- [41] B.L. Gyorffy, Coherent-potential approximation for a nonoverlapping-muffin-tin-potential model of random substitutional alloys, *Phys. Rev. B* 5 (1972) 2382–2384, <https://doi.org/10.1103/PhysRevB.5.2382>
- [42] J.P. Perdew, Y. Wang, Accurate and simple analytic representation of the electron-gas correlation energy, *Phys. Rev. B* 45 (1992) 13244–13249, <https://doi.org/10.1103/PhysRevB.45.13244>
- [43] D.M. Ceperley, B.J. Alder, Ground state of the electron gas by a stochastic method, *Phys. Rev. Lett.* 45 (1980) 566–569, <https://doi.org/10.1103/PhysRevLett.45.566>
- [44] A.I. Liechtenstein, M.I. Katsnelson, V.A. Gubanov, Exchange interactions and spin-wave stiffness in ferromagnetic metals, L125–L128, *J. Phys. F. Met. Phys.* 14 (1984), <https://doi.org/10.1088/0305-4608/14/7/007>
- [45] B. Skubic, J. Hellsvik, L. Nordstrom, O. Eriksson, A method for atomistic spin dynamics simulations: implementation and examples, *J. Phys. Condens. Matter* 20 (2008) 315203, <https://doi.org/10.1088/0953-8984/20/31/315203>
- [46] O. Eriksson, A. Bergman, L. Bergqvist, J. Hellsvik, Atomistic Spin Dynamics, Oxford University Press, 2016, (<https://global.oup.com/academic/product/atomistic-spin-dynamics-9780198788669>).
- [47] J.O. Andersson, T. Helander, L. Höglund, P. Shi, B. Sundman, Thermo-Calc & DICTRA, computational tools for materials science, *Calphad Comput. Coupling Phase Diagr. Thermochem* 26 (2002) 273–312, [https://doi.org/10.1016/S0364-5916\(02\)00037-8](https://doi.org/10.1016/S0364-5916(02)00037-8)
- [48] C. Li, M. Zhao, J.C. Li, Q. Jiang, B2 structure of high-entropy alloys with addition of Al, *J. Appl. Phys.* 104 (2008), <https://doi.org/10.1063/1.3032900>
- [49] J.D. Makinson, J.S. Lee, S.H. Magner, R.J. De Angelis, W.N. Weins, A.S. Hieronymus, X-ray diffraction signatures of defects in nanocrystalline materials, *Adv. X-Ray Anal.* 42 (2000) 407–411.
- [50] S.F. Liu, Y. Wu, H.T. Wang, J.Y. He, J.B. Liu, C.X. Chen, X.J. Liu, H. Wang, Z.P. Lu, Stacking fault energy of face-centered-cubic high entropy alloys, *Intermetallics* 93 (2018) 269–273, <https://doi.org/10.1016/j.intermet.2017.10.004>
- [51] A.J. Zaddach, C. Niu, C.C. Koch, D.L. Irving, Mechanical properties and stacking fault energies of NiFeCrCoMn high-entropy alloy, *JOM* 65 (2013) 1780–1789, <https://doi.org/10.1007/s11837-013-0771-4>
- [52] M. Casas-Cabanas, M. Reynaud, J. Rikarte, P. Horbach, J. Rodríguez-Carvajal, FAULTS: a program for refinement of structures with extended defects, *J. Appl. Crystallogr.* 49 (2016) 2259–2269, <https://doi.org/10.1107/S1600576716014473>
- [53] G. Laplanche, S. Berglund, C. Reinhart, A. Kostka, F. Fox, E.P. George, Phase stability and kinetics of α -phase precipitation in CrMnFeCoNi high-entropy alloys, *Acta Mater.* 161 (2018) 338–351, <https://doi.org/10.1016/j.actamat.2018.09.040>
- [54] Q. Yu, W.W. Xu, C. Cui, X. Gong, W. Li, L. Chen, X. Li, L. Vitos, Unveiling segregation-induced evolution in phase constitution of Cu-containing high-entropy alloys, *J. Alloy. Compd.* 843 (2020) 156109, <https://doi.org/10.1016/j.jallcom.2020.156109>
- [55] A. Takeuchi, A. Inoue, Mixing enthalpy of liquid phase calculated by miedema’s scheme and approximated with sub-regular solution model for assessing forming ability of amorphous and glassy alloys, *Intermetallics* 18 (2010) 1779–1789, <https://doi.org/10.1016/j.intermet.2010.06.003>
- [56] A.K. Boer, F.R. de, Mattens, W.C.M. Boom, R. Miedema, A.R. Niessen, Cohesion in metals, *Transit. Met. Alloy.* (1988) 774.
- [57] J.P. Perdew, K. Burke, M. Ernzerhof, Generalized gradient approximation made simple, *Phys. Rev. Lett.* 77 (1996) 3865–3868, <https://doi.org/10.1103/PhysRevLett.77.3865>
- [58] Z. Dong, S. Huang, V. Ström, G. Chai, L.K. Varga, O. Eriksson, L. Vitos, MnxCr_{0.3}Fe_{0.5}Co_{0.2}Ni_{0.5}Al_{0.3} high entropy alloys for magnetocaloric refrigeration near room temperature, *J. Mater. Sci. Technol.* 79 (2021) 15–20, <https://doi.org/10.1016/j.jmst.2020.10.071>
- [59] D.D. Belyea, M.S. Lucas, E. Michel, J. Horwath, C.W. Miller, Tunable magnetocaloric effect in transition metal alloys, *Sci. Rep.* 5 (2015) 1–8, <https://doi.org/10.1038/srep15755>
- [60] K. Sarlar, A. Tekgul, I. Kucuk, Magnetocaloric properties of rare-earth-free Mn₂₇Cr₇Ni₃₃Ge₂₅Si₈ high-entropy alloy, *IEEE Magn. Lett.* 10 (2019) 8–12, <https://doi.org/10.1109/LMAG.2019.2955667>
- [61] J.Y. Law, L.M. Moreno-Ramírez, Á. Díaz-García, A. Martín-Cid, S. Kobayashi, S. Kawaguchi, T. Nakamura, V. Franco, MnFeNiGeSi high-entropy alloy with large magnetocaloric effect, *J. Alloy. Compd.* 855 (2021), <https://doi.org/10.1016/j.jallcom.2020.157424>

Paper II

Magnetic transitions in V-Fe-Co-Ni-Cu-based high entropy alloys



Magnetic transitions in V-Fe-Co-Ni-Cu-based high entropy alloys

B.G.F. Eggert^a, E.K. Delczeg-Czirjak^b, B.C. Hauback^a, C. Frommen^{a,*}

^a Department for Hydrogen Technology, Institute for Energy Technology (IFE), P.O. Box 40, NO-2027, Kjeller, Norway

^b Department of Physics and Astronomy, Uppsala University, Box 516, 751 20, Uppsala, Sweden

ARTICLE INFO

Keywords:

Magnetocaloric
High entropy alloys
Density functional theory
Microstructure
Scanning electron microscopy

ABSTRACT

FeCoNi, $V_{0.85}\text{FeCoNi}$, $\text{FeCoNiCu}_{1.15}$ and $V_{0.85}\text{FeCoNiCu}_{1.15}$ alloys have been synthesized by arc melting and analyzed by powder X-ray diffraction, electron microscopy, magnetic measurements, and density functional theory (DFT). The influence of each alloying element on the magnetic exchange interaction, Curie temperature (T_C) and magnetocaloric effect is evaluated. The experimental results show that Cu and V “dilute” the magnetic properties and couple antiferromagnetically to Fe, Co, and Ni. Analysis of the microstructure reveals a lack of solubility between V and Cu with FeCoNi, and between themselves, thus lowering the concentration of V and Cu in the main solid solution of the 5-element alloy $V_{0.85}\text{FeCoNiCu}_{1.15}$. T_C decreases significantly from 997 K in FeCoNi to 245 K in $V_{0.85}\text{FeCoNi}$ and 297 K in $V_{0.85}\text{FeCoNiCu}_{1.15}$, respectively. The derivative of magnetization as a function of temperature (dM/dT) in the vicinity of T_C is drastically reduced due to the presence of V which indicates a reduced magnetocaloric effect. DFT calculations confirm antiferromagnetic coupling of V to the ferromagnetic FeCoNi-base and predict a similar behavior for other transition metal elements (e.g., Ti, Cr, Mn). This leads to a lowering of T_C , which is needed to establish the magnetocaloric effect at room temperature. However, it comes at a cost of reduced magnetic moments. Nevertheless, the use of V and Cu has shown possible routes for tuning the magnetocaloric effect in FeCoNi-based high entropy alloys.

1. Introduction

Solid-state magnetocaloric devices aim to deliver more efficient refrigeration with less environmental impact [1,2]. When considering material challenges, high entropy alloys (HEAs) containing 3d metals could meet several of the demands that magnetic heat conversion devices require. They offer corrosion resistance, long-term cyclability, and ease of production, while being produced from abundant, non-expensive materials [3,4]. The core of the magnetocaloric effect (MCE) in these HEAs originates from the use of Fe, Co and Ni, with strong magnetic moments, and magnetic ordering temperatures (T_C) of 1043 K (Fe), 1400 K (Co) and 627 K (Ni), respectively.

Since the T_C s of the pure elements are far above room temperature (RT), it is necessary to decrease them by alloying Fe, Co, and Ni with other elements [5–8]. This can be achieved by two main approaches: (i) dilution of ferromagnetic exchange interactions via elements such as Cu/Al that induce a zero or close-to-zero exchange interaction with the ferromagnetic transition metals (FMTM), and (ii) use of elements such as Cr, V, Ti etc. that induce antiparallel coupling with the FMTMs. To conveniently bring T_C to RT, both kinds of elements are typically used in

FeCoNi-based HEAs [7]. This raises the number of possible magnetic interactions between all elements. Due to an equilibrium between enthalpy and entropy, sub-regular solid solutions are commonly formed. This creates some degree of inhomogeneity or ordering in bulk HEAs [9] that leads to a distribution of T_C s. As a result, the magnetic transition becomes broadened and ultimately results in a reduced MCE. How elements that induce dilution and/or couple antiferromagnetically impact T_C is not well understood, except for Cr and Mn [7,10–13].

In a previous report, we considered V, Al and Cu as alloying elements in $V_{1-x}\text{FeCoNi}(\text{Al}/\text{Cu})_{1+x}$ HEAs [14]. In $V_{0.85}\text{FeCoNiCu}_{1.15}$, a multiphase microstructure was found, that impacted the composition of the main solid solution compared to the nominal composition. The investigation also uncovered an isothermal entropy change (ΔS_m) of 0.17 J/kg.K for a magnetic field change of $\mu_0 H = 0\text{--}1$ T at room temperature in $V_{0.85}\text{FeCoNiCu}_{1.15}$, or 0.75 J/kg.K for $\mu_0 H = 0\text{--}5$ T, which are low values compared to regular magnetocaloric materials [15]. This result is understood as the combined effect of V and Cu in the ferromagnetic transition of FeCoNi. However, since two alloying elements are present, the individual influence of each alloying element on the magnetic transition is not possible to determine.

* Corresponding author.

E-mail address: christoph.frommen@ife.no (C. Frommen).

<https://doi.org/10.1016/j.mtphys.2023.101116>

Received 20 March 2023; Received in revised form 5 May 2023; Accepted 19 May 2023

Available online 20 May 2023

2542-5293/© 2023 The Authors. Published by Elsevier Ltd. This is an open access article under the CC BY license (<http://creativecommons.org/licenses/by/4.0/>).

In this article, we investigate how the individual and combined addition of V and Cu affects the (micro)structure and magnetic properties of FeCoNi-based solid solutions. A disordered ferromagnetic FeCoNi base alloy is compared to: (i) a magnetically diluted Cu-doped compound (FeCoNiCu_{1.15}), (ii) a V-containing compound (V_{0.85}FeCoNi) with ferromagnetic and antiferromagnetic interactions, and (iii) the combined effect of V and Cu in V_{0.85}FeCoNiCu_{1.15}, with dilution and antiparallel interactions. This non-equiatom ratio has been selected as the 5-element alloy displays a magnetic transition around RT [14]. The same ratio is also kept for the respective FeCoNi–Cu and V–FeCoNi 4-element alloys. We pay special attention to the solidification path and metallurgy of the alloys and how they enable an optimized microstructure which is essential for obtaining efficient magnetocaloric materials. The magnetic properties of the alloys are assessed through magnetization measurements, and experimental results are compared to DFT calculations in order to gain better insight into magnetic ordering temperatures, element-resolved magnetic moments, and exchange interactions. Finally, we briefly evaluate by DFT the use of other elements such as Ti, Cr, and Mn to induce antiferromagnetic coupling in FeCoNi-based solid solutions.

2. Materials and methods

Metallic powders of Fe, Ni, Co, V, Cu and Al of 99.9% purity were weighed, mixed and arc melted in a Ti-gettered home-built arc melter in argon atmosphere. The samples were remelted and turned 5 times to ensure homogeneity. Nominal compositions are described in Table 1. Powder X-ray diffraction (PXRD) was carried out by a Bruker D2 Phaser Cu–K α diffractometer ($\lambda = 1.5406 \text{ \AA}$) in Bragg-Brentano configuration. Rietveld refinements were done using the Fullprof Suite [16]. The presence of stacking faults was modelled by the FAULTS software package, where lattice parameters, crystallite size, and stacking fault probabilities were refined [17]. Scanning electron microscopy (SEM) and energy dispersive X-ray spectroscopy (EDS) were carried out in a Hitachi SU8230 ultra-high-resolution cold-field emission scanning electron microscope used in backscattered electron (BSE) mode. On samples containing the sigma phase, its phase fraction was determined by area analysis using the ImageJ software [18] using three micrographs with 250 times magnification, scanning an area over 0.2 mm^2 per image. As the samples show no signs of preferential orientation, it is possible to extrapolate the area percentage to volumetric percentage. Chemical compositions were obtained by area measurements. Magnetic measurements were carried out by a Quantum Design Physical Property Measurement System (PPMS) and a LakeShore Vibrating Sample Magnetometer (VSM). Measurements as a function of temperature were

Table 1

Atomic concentration of the elements for the nominal compositions of the alloys, together with the compositions for the main ccp solid solutions obtained from EDS measurements.

Nominal composition (formula units)	Fe (at. %)	Co (at. %)	Ni (at. %)	V (at. %)	Cu (at. %)
FeCoNi	33	33	33	–	–
FeCoNiCu _{1.15}	24.1	24.1	24.1	–	27.7
V _{0.85} FeCoNi	26	26	26	22	–
V _{0.85} FeCoNiCu _{1.15}	20	20	20	17	23
main phase composition (formula units)	Fe (at. %)	Co (at. %)	Ni (at. %)	V (at. %)	Cu (at. %)
Fe ₁ Co _{1.14} Ni _{1.14}	30.5 (30)	34.8 (3)	34.7 (3)	–	–
FeCo _{1.16} Ni _{1.09} Cu _{0.84}	24.4 (2)	28.4 (1)	26.6 (1)	–	20.6 (2)
V _{0.82} FeCo _{1.07} Ni _{1.03}	25.4 (2)	27.4 (3)	26.3 (1)	20.9 (4)	–
V _{0.75} FeCo _{1.07} Ni _{1.01} Cu _{0.56}	22.5 (6)	24.1 (2)	22.8 (6)	17.9 (20)	12.7 (6)

performed in a persistent applied field of $\mu_0 H = 1 \text{ T}$, and temperatures ranging from 10 to 375 K in the PPMS, and from 300 to 1100 K in the VSM. Field dependent magnetization was performed with applied fields of $\mu_0 H = 0\text{--}1 \text{ T}$.

2.1. Theoretical methodology

Phase presence and compositions were predicted by the CALPHAD method implemented in the Thermo-Calc 2021 software in combination with the TCHEA3 high entropy alloy database package. Property diagrams were obtained by considering all the possible phases, including intermetallic and intermediate compounds formed by the constituent elements.

Electronic structure calculations were done by the exact muffin-tin orbital (EMTO) method [19,20] where the chemical and magnetic disorder is treated within the coherent potential approximation (CPA) [21, 22] (EMTO-CPA [23]). The electrostatic correction to the single-site CPA was considered as implemented in the Lyngby version of the EMTO code [24]. For details the reader is referred to Refs. [24,25], and [26].

The one-electron Kohn-Sham equations were solved within the soft-core and scalar-relativistic approximations, with $l_{m \max} = 3$ for partial waves and $l_{m \max}^{\text{rel}} = 5$ for their “tails”. The Green’s function was calculated for 16 complex energy points distributed exponentially on a semi-circular contour including states within 1 Ry below the Fermi level. The exchange-correlation effects were described within the Generalized Gradient Approximation (GGA) in Perdew, Burke, and Ernzerhof (PBE) form [16]. Magnetic exchange interactions were calculated within the magnetic force theorem, implemented in the Lyngby version of the EMTO-CPA [24] code for the ferromagnetic state.

Total energies were calculated within the full-charge density technique [27] using PBE [16] to describe the exchange-correlation effects. For the one-center expansion of the full charge density a cut-off of $l_{m \max} = 8$ was used. $\alpha_i^0 = 0.7$ for the on-site screening constant, and $\beta_{scr} = 1.1$ for the average screening parameter [25,26] was used to account for the contributions of the screened Coulomb interactions to the one-electron potential of the alloy components and the total energy of the system [25,26]. A $12 \times 12 \times 12$ Monkhorst-Pack [28] k -mesh grid was used for the Brillouin zone integration. The equilibrium volume (lattice parameter) for the nominal compositions were determined from a Morse [29] equation of state fitted to the *ab initio* total energies of fcc structures for 5 different atomic volumes. Statistical thermodynamics simulations of the magnetic phase transition were done by MC method implemented within the Uppsala atomistic spin dynamics (UppASD) software [30,31]. MC simulations were performed on a $40 \times 40 \times 40$ supercell with periodic boundary conditions. The size and direction of the magnetic moments were chosen randomly at each MC trial and 10000 MC steps were used for equilibration followed by 50000 steps for obtaining thermodynamic averages.

3. Results and discussion

3.1. Solidification of FeCoNi alloys with V and Cu

FeCoNi-based HEAs are typically ferromagnetic with T_C 's in the order of several hundred degrees Kelvin. To tune T_C towards RT, the average exchange interaction needs to be altered by use of other elements. This modifies the liquid and solid solution properties, influencing the morphology of the phases during common (non-equilibrium) solidification processes. To correctly assess the potential of magnetocaloric high entropy alloys, a detailed understanding of the factors that determine phase formation in those materials is essential for tailoring their magnetic properties and microstructure.

Solidification of the FeCoNi parent alloy proceeds without macroscopic segregation, see Fig. 1(a). This indicates a good solubility between the three ferromagnetic elements. The corresponding CALPHAD

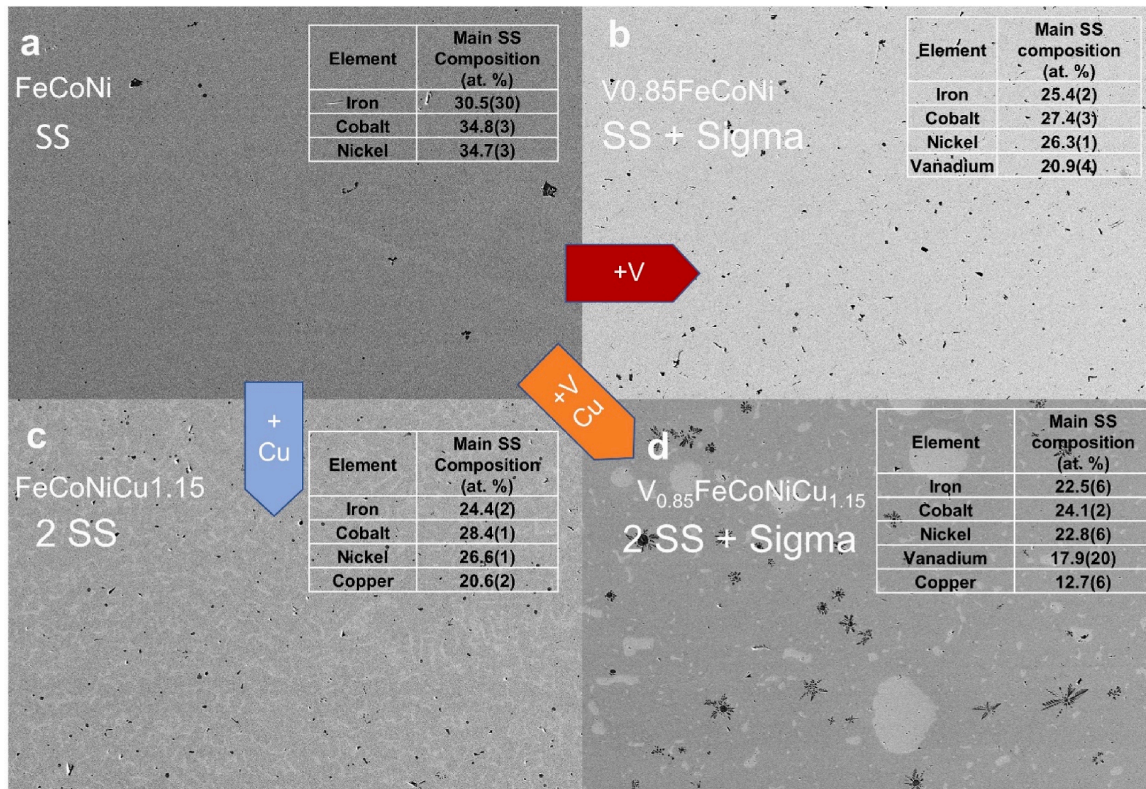


Fig. 1. (Color online.) Scanning electron micrographs obtained in BSE mode with a magnification of 250x, showing the microstructure of four solid solutions: (a) FeCoNi, (b) V_{0.85}FeCoNi, (c) FeCoNiCu_{1.15} and (d) V_{0.85}FeCoNiCu_{1.15}. Either one or two solid solutions (SS) or a mix of SS and a sigma intermetallic are observed. The atomic composition of the main ccp solid solution is shown in the insert for each of the four studied alloys.

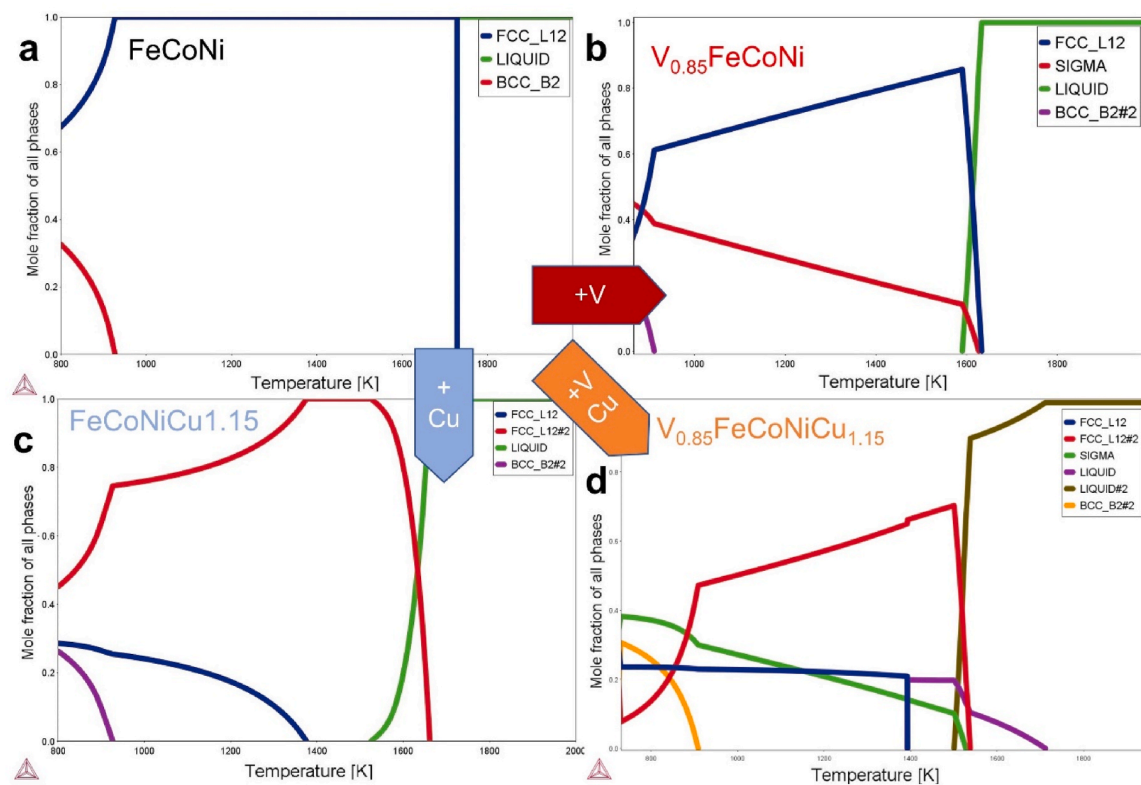


Fig. 2. (Color online.) CALPHAD plots indicating the phase presence as a function of temperature for the four studied FeCoNi-based alloys.

plot in Fig. 2(a) predicts the formation of a secondary phase at temperatures below 950 K. Since solidification occurs with a high cooling rate, however, there is not enough thermal activation for the segregation to occur. The addition of V in $V_{0.85}FeCoNi$ modifies the solidification process, as is illustrated in the upper-right corner in Fig. 1(b). A sigma phase is present during early stages of sample preparation together with the cubic close-packed (ccp) solid solution (also known as face-centered cubic, space group $Fm\bar{3}m$); however, it is removed after polishing. The sigma phase is an intermetallic with a tetragonal structure (space group $P4_2/mnm$), and composition A_2B , where A and B are transition metals. The removal can be ascribed to the very different crystal structures, creating incoherence between the ccp structure of the solid solution and the tetragonal structure of the sigma phase [32]. Sigma phases are typically precipitated from solid solutions during heat treatments, but they can also precipitate during solidification. This appears to be the case for the studied V-containing alloys and agrees well with calculated phase fraction plots as a function of temperature obtained by CALPHAD, see Fig. 2(b). By employing image area analysis due to the contrast between the removed phase and the alloy, it is possible to estimate the phase fraction of the sigma phase using ImageJ, with an average value of 0.8% in volume for $V_{0.85}FeCoNi$. Precipitates are seen with a spheroid or polyhedral shape morphology, another indication of the small coherence between the precipitates and the main solid solution. In the V-containing 4-element alloy, displayed in Fig. 1(b), up to 21 at. % V is observed in the main ccp solid solution, together with Fe (25 at. %), Co (27 at. %), and Ni (26 at. %). The chemical compositions of the main solid solutions measured by EDS are shown in the lower section of Table 1.

When Cu is introduced into FeCoNi, as shown in Fig. 1(c), the solubility of Cu in the solid solution decreases as the temperature drops after arc melting. This is confirmed by the CALPHAD prediction for phase presence as a function of temperature in Fig. 2(c), which shows the formation of a secondary ccp phase at temperatures below approximately 1400 K. As a result, dendrites with a composition of $FeCoNiCu_x$ are formed. Once the solubility limit is reached, the remaining Cu solidifies in an inter-dendritic secondary ccp phase. BSE images confirm this, shown in Fig. 1(c), in the clearer inter-dendritic regions. The average chemical composition of the $FeCoNiCu_{1.15}$ solid solution features up to 21 at. % Cu together with Fe (24 at. %), Co (28 at. %) and Ni (27 at. %). The remaining copper precipitates in the Cu-rich phase, together with a small amount of Ni, Fe, and Co.

When V and Cu are both combined with Fe, Co and Ni, the solidification process changes once again, see Fig. 1(d). A solid solution is formed that contains V–Fe–Co–Ni–Cu. However, its chemical composition differs from the nominal composition due to the lack of solubility between V and Cu, which induces a decrease in Cu-content from 21 at. % in $FeCoNiCu_{1.15}$ to 13 at. %. The ratio of the remaining ferromagnetic elements is Fe (22 at. %), Co (24 at. %) and Ni (23 at. %), while V remains close to 17 at. %. The remaining Cu is seen as spheres and rounded elements in a Cu-rich phase in Fig. 1(d). This could be an indication of liquid phase immiscibility between a Cu-rich liquid and V–Fe–Co–Ni–Cu solid solution, as Fe, Co and especially V tend to phase-separate with Cu (see also Fig. 2). A similar morphology is observed in $Nb_xFeCoNiCu$ [33]. This secondary liquid formation is also observed in the CALPHAD plot in Fig. 2(d), as it predicts the segregation of a secondary Cu-rich liquid from a main liquid at around 1500 K.

In addition to the two ccp phases, an amount of removed sample is seen, related to the formation of the sigma phase. The sigma phase appears around a ccp phase containing V–Fe–Co–Ni–Cu (main SS) and the Cu-rich phase. The sigma phase fraction estimated from image analysis is 1.1% in volume. This time, it exhibits a different morphology than the one seen for the 4-element $V_{0.85}FeCoNi$ alloy. It is precipitated in spheres or dendrites (snowflakes), see Fig. 1(d). This can be related to a different interfacial energy between the liquid and the solid formation of the V-containing intermetallic. A three-phase system is thus present, with a Cu-rich SS, a sigma intermetallic and a main V–Fe–Co–Ni–Cu

solid solution.

The different elements present in each of the solid solutions allows for studying 4 different magnetic systems: (i) purely ferromagnetic interactions in the 3-element alloy (FeCoNi), (ii) ferromagnetic elements (FeCoNi) alloyed with a diamagnetic element (Cu) which dilutes the moments, (iii) ferromagnetic elements (FeCoNi) alloyed with an element that induces antiparallel interactions (V), and finally, (iv) the combination of dilution and antiparallel coupling in the 5-element ferromagnetic alloy (V–Fe–Co–Ni–Cu).

With the main compositions identified, it is necessary to determine the lattice parameters of the phases present. The PXD patterns of the four solid solutions are shown in Fig. 3 and are primarily attributed to ccp structures with no other observed reflections. The lattice parameters are presented in Table 2. In the as-cast state, FeCoNi has an a -axis of 3.571(2) Å. By addition of V and Cu, a is slightly altered to 3.595(2) Å for both. Upon simultaneous addition of V and Cu, the a -axis increases slightly to 3.604(2) Å. The stacking faults probability in the ccp lattice is obtained from the FAULTS software refinement, and shown in Table 2. Stacking faults in HEAs are common due to the high number of elements, as they tend to lower the stacking fault energy [34,35]. The stacking fault probabilities ranged from 8 to 14% between the alloys and the change in values may be ascribed to the presence of different elements and the level of strain in the powder for the PXD sample preparation.

3.2. Magnetic properties of the main solid solutions

Fig. 4 depicts magnetization as a function of temperature for the four alloys in the vicinity of T_C with applied fields of 1 T. Data was obtained with a VSM in the range from 300 to 1100 K and by PPMS from 10 to 370 K. To facilitate comparison to the DFT results, magnetization values are expressed in Bohr magnetons in the left axis, and in Am^2/kg on the right axis. High magnetic fields were selected to better correlate to the intended application, where fields of at least 1 T will be employed to generate the magnetocaloric effect. By normalizing the temperature by T_C , one can compare materials with different T_C and gain insight on the thermal dependence of the magnetic moments in the solid solution. The ΔS_m of $V_{0.85}FeCoNiCu_{1.15}$ alloys was investigated in a previous report [14] and therefore ΔS_m calculations are not performed in this study. Instead, the absolute derivative of magnetization as a function of temperature is depicted in Fig. 4(b) with an applied magnetic field of $\mu_0H = 1$ T. While it does not replace the ΔS_m curves, high $|dM/dT|$ values are an indication of a high ΔS_m . The high field $|dM/dT|$ can provide insight

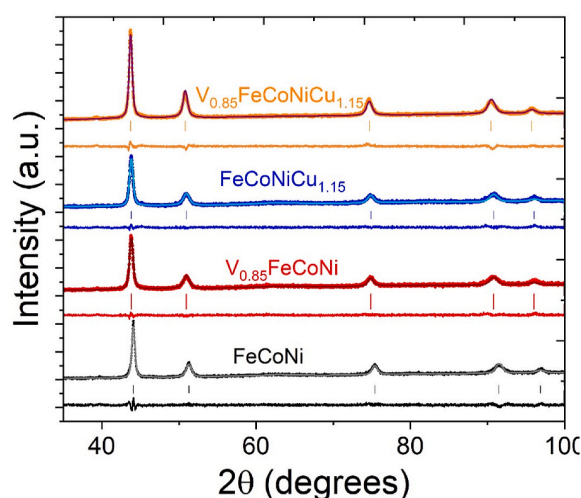


Fig. 3. (Color online.) PXD patterns and Rietveld refinements of the four studied alloys measured with Cu- $K\alpha$ radiation ($\lambda = 1.5409$ Å). Observed intensities are shown as points, calculated intensities as lines and difference plots are shown below each pattern.

Table 2

Experimental lattice parameters (a), Curie temperatures (T_C), and saturation magnetizations (M_S) of the studied FeCoNi-based alloys.

main phase composition (formula units)	Exp. a (Å)	Stacking fault probability (%)	χ^2	exp. T_C (K)	Exp. M_S (μ_B /atom)
Fe ₁ Co _{1.14} Ni _{1.14}	3.571 (2)	8.4%	1.39	997	1.47
FeCo _{1.16} Ni _{1.09} Cu _{0.84}	3.595 (2)	14.2%	1.38	957	1.16
V _{0.82} FeCo _{1.07} Ni _{1.03}	3.595 (2)	13.6%	1.26	245	0.58
V _{0.75} FeCo _{1.07} Ni _{1.01} Cu _{0.56}	3.604 (2)	8.4%	1.7	278	0.54

on the shape of ΔS_m curves, and approximate values if the $|dM/dT|$ values are multiplied by the applied field in T, without the arduous process of obtaining a series of isofield or isotherm curves for a ΔS_m calculation.

In the FeCoNi base alloy, a ferromagnetic-to-paramagnetic transition is observed. The ferromagnetic state is stabilized due to the large external magnetic field, leading to a broad curve that spans tens of K. The maximum change of magnetization is observed at 997 K, as shown in Table 2 together with all experimentally observed T_C 's. The total saturation magnetization (M_S) for this alloy is 1.47 μ_B /atom. With the introduction of Cu, M_S is decreased to 1.16 μ_B /atom, and the derivative (dM/dT) is slightly smaller; however, the overall behaviour characteristic of a ferromagnetic material is kept. This is also evident from Fig. 4 (b) which shows the derivative of magnetization as a function of temperature, (dM/dT) as FeCoNiCu_{1.15} ($T_C = 957$ K) exhibits a similar behaviour as FeCoNi. This leads to the conclusion that other elements besides Cu such as Cr, V and Mn are necessary to lower T_C , confirming the work by Kurniawan et al. [7].

In samples containing V, where antiparallel interactions are inserted into the magnetic system, the temperature dependence of magnetization changes drastically and the magnetic transition becomes much broader than for FeCoNi and FeCoNiCu_{1.15}. Furthermore, M_S is largely decreased to 0.58 and 0.54 μ_B /atom in V_{0.85}FeCoNi and V_{0.85}FeCoNiCu_{1.15}, respectively.

The magnetic transitions for V_{0.85}FeCoNi and V_{0.85}FeCoNiCu_{1.15} are presented in Fig. 5, in the temperature range from 10 to 375 K. A measurement artifact is observed as a slight increase in magnetization at

$T = 50$ K for both samples. In the case of V_{0.85}FeCoNi, the measured T_C is 245 K, while V_{0.85}FeCoNiCu_{1.15} presents a T_C of approx. 280 K. The absolute magnetization values are higher for the sample without Cu, as it acts as a dilutant for the ferromagnetic moments. On both V-containing alloys there is still some remaining magnetization after the end of the measurement range due to the large number of exchange interactions and inhomogeneity in the alloy. Surprisingly, the (dM/dT) derivative of the 5-element alloy is higher. This can be explained by the smaller V-content in the 5-element solid solution (18 at. %) compared to the 4-element alloy (21 at. %). The decrease in (dM/dT) seen in Fig. 4(b) due to the introduction of V is a hindrance to the magnetocaloric properties. This can be correlated to local inhomogeneities between V and the other elements, creating a distribution of T_C 's. The slightly larger derivative seen in Fig. 5 for V_{0.85}FeCoNiCu_{1.15} compared to V_{0.85}FeCoNi could hint at a pathway for improving the magnetocaloric

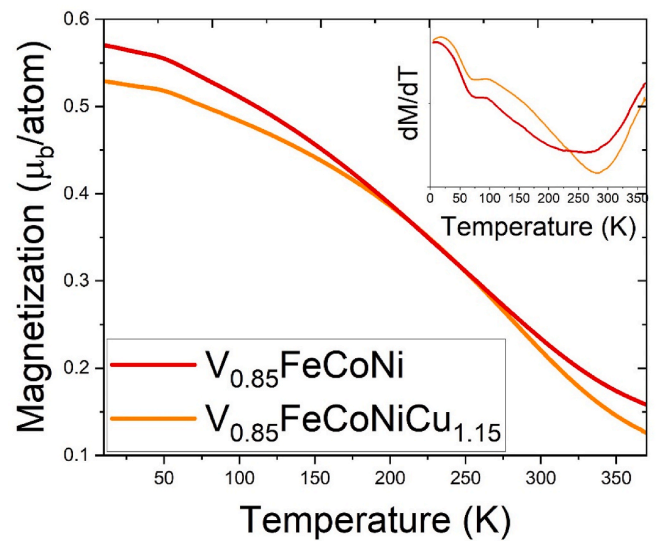


Fig. 5. (Color online.) Magnetization as a function of temperature for two V-containing alloys, with applied field of $\mu_0H = 1$ T. The inset shows the derivative of magnetization (dM/dT) as a function of temperature. A measurement artifact occurring due to impurities in the sample chamber is seen at $T = 50$ K.

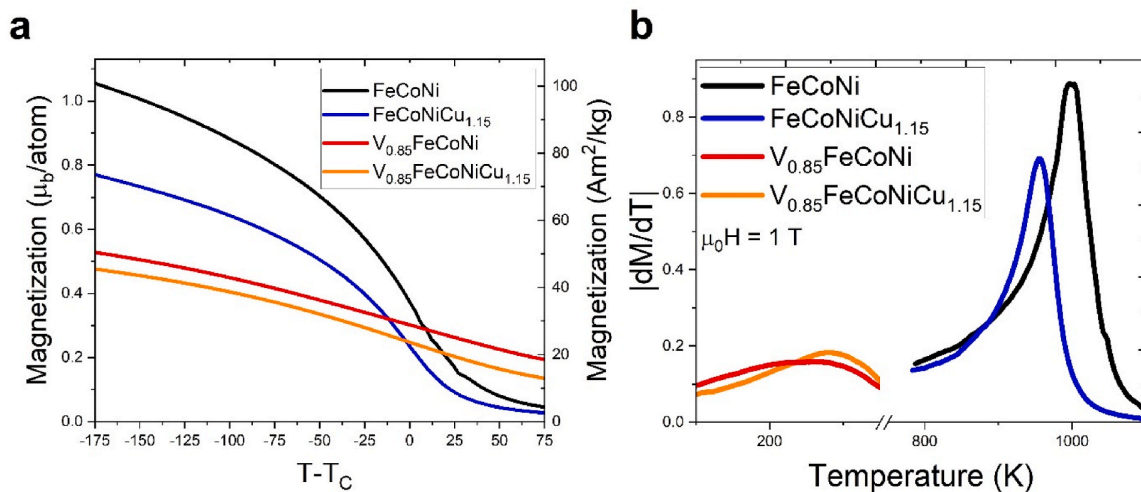


Fig. 4. (Color online.) (a) Magnetization as a function of temperature for the four studied alloys with applied fields of $\mu_0H = 1$ T, in Bohr magneton/atom on the left, and in Am^2/kg on the right. (b) Absolute derivative of magnetization as a function of temperature for the studied alloys, allowing one to compare the transitions with each modification. With the introduction of Cu, a decrease in absolute magnetization is observed, but the overall behaviour is unchanged. In V-containing alloys, absolute magnetization, and derivatives of magnetization (dM/dT) are strongly modified, which is harmful to the magnetocaloric effect.

properties by modifying the ratio between dilution and antiferromagnetic elements and the ferromagnetic elements. This is exactly the case observed by Belyea et al. in CrFeCoNiPd_x . With larger contents of Pd, the nominal content of Cr decreases from 25 at. % ($x = 0$) to 22.2 at. % ($x = 0.5$). This modifies T_C 's from around 100 K to 300 K [5].

3.3. Theoretical results

Electronic structure calculations and Monte Carlo simulations are presented in detail for the nominal composition of the 3-, 4- and 5-element alloys, where the Fe, Co and Ni content is equal. The nominal atomic concentrations of the elements are listed in the upper section of Table 1. For these alloys, the 0 K equilibrium lattice parameters, a , were estimated from a Morse type of equation of state as described in Section 2.1. Due to the quick solidification of the as-cast samples, we expect a solid solution with the greatest extent of randomness of the constituting elements, and we can furthermore assume that the composition of the FeCoNi sample in the as-cast state is very close to the nominal composition. Within this set of assumptions, we find that the lattice parameter of FeCoNi (3.56 Å) is in good agreement with the measured data (3.57 Å) while its total magnetic moment (m_{tot}) per 1 atom calculated at 0 K is $1.64 \mu_B$. This compares well to the measured value of $1.47 \mu_B$ at RT. These results give us confidence in the theoretical framework and allow us to investigate how the addition of Cu and V affect the magnetic properties of FeCoNi-based alloys.

Fig. 6 presents the element resolved partial densities of states (DOS) for Fe, Co, and Ni in the equiatomic FeCoNi base alloy. The difference in DOS modifies the individual magnetic moments for each of the elements, depicted in Table 3. The largest exchange splitting between the spin-up and spin-down DOS is manifested for Fe. The spin-up channel is almost filled, and the remaining number of electrons occupy the spin-down channel resulting in a magnetic moment of $2.51 \mu_B$ for Fe. Co and Ni possess more electrons than Fe, that will result in a complete filling of the spin-up states showing larger values of DOS in the energy range of -0.25 to -0.05 Ry for Co and Ni than for Fe. Also, the peak at -0.05 Ry is slightly shifted towards lower energies for Co and Ni compared to Fe. The extra electrons for Co and Ni are accommodated by the spin-down channel resulting in decreased local magnetic moments of $1.69 \mu_B$ (Co) and $0.72 \mu_B$ (Ni), respectively, compared to Fe.

To compare the effect of adding Cu and V to FeCoNi, we turn our attention to FeCoNiCu_{1.15} and V_{1.15}FeCoNi, where the nominal atomic concentration and the ratio of Fe, Co and Ni are identical. The modelled lattice parameters of FeCoNiCu_{1.15} and V_{1.15}FeCoNi are both slightly larger than for FeCoNi. The V-containing 4 element alloy has a lattice parameter of 3.59 Å due to the larger volume of the element V. In the case of FeCoNiCu_{1.15}, the calculated lattice parameter of 3.59 Å can be

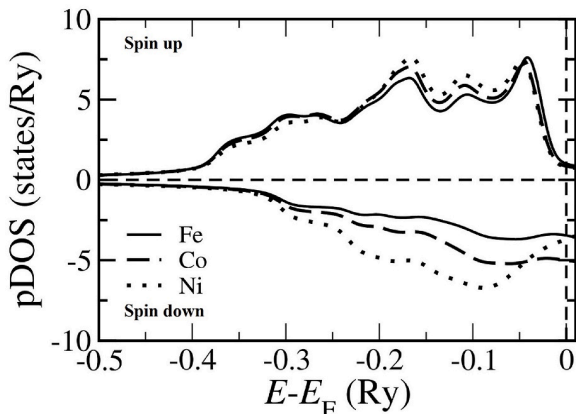


Fig. 6. Partial density of states (pDOS) for Fe (full line), Co (dashed line), and Ni (dots) in the FeCoNi equiatomic base alloy.

ascribed to filled d -orbitals of Cu, imposing larger bond lengths. In the 5-element alloy, the combined effect of V and Cu increases the calculated lattice parameter slightly to 3.60 Å.

The element-resolved and total magnetic moments for different FeCoNi-based multicomponent alloys are listed in Table 3. The addition of electrons to FeCoNi, e.g., via Cu in FeCoNiCu_{1.15}, affects the local magnetic moments of Fe, Co, and Ni differently. The extra electrons from Cu fill completely the spin-up states for Fe, see the upper panel of Fig. 7, inducing a subtle increase of m_{Fe} . The filled spin-up channel of Co and Ni cannot accommodate more electrons; here the spin-down states receive the extra electrons (see middle and lower panels of Fig. 7 for Co and Ni, respectively) resulting in a decrease of m_{Co} and m_{Ni} . The addition of V in V_{1.15}FeCoNi has the opposite effect: electrons are removed from both spin-up and spin-down channels of the pDOS of Fe, Co, and Ni, resulting in a drastic decrease of m_{Fe} , m_{Co} and m_{Ni} . The induced moment on Cu is very small for all compounds ($< 0.05 \mu_B$). On the other hand, the local moment induced on V is quite substantial and comparable to m_{Ni} (see Table 3), and it couples antiparallel to the moments of the magnetic elements (Fe, Co, Ni), thereby reducing the ferromagnetic character of the alloy.

These changes in the electronic structure and magnetic moments translate to the exchange integrals calculated for the 3- and 4-component alloys plotted in Figs. 8 and 9. All magnetic pair interactions are positive in case of FeCoNi establishing a ferromagnetic ground state. $J_{\text{Fe-Fe}}$, $J_{\text{Fe-Co}}$ and $J_{\text{Co-Co}}$ have the largest values while $J_{\text{Fe-Ni}}$ and $J_{\text{Co-Ni}}$ are half of them. Adding Cu to FeCoNi results in a very small increase of the 1st nearest neighbor (NN) $J_{\text{Fe-Fe}}$, $J_{\text{Fe-Co}}$ and $J_{\text{Co-Co}}$ while their 2nd NN pair interactions are decreased. $J_{\text{Fe-Ni}}$ and $J_{\text{Co-Ni}}$ are not affected by the addition of Cu. Since the nominal concentration of Fe, Co and Ni decreases considerably in FeCoNiCu_{1.15} (24.1 at. %) compared to the equiatomic alloy (33 at. %), and Cu does not contribute to the magnetic properties (due to its very small induced magnetic moment), we expect a lower T_C for FeCoNiCu_{1.15} than for FeCoNi.

In contrast, adding V largely affects the magnetic exchange interactions in two ways. Firstly, we observe a significant decrease in all pair interactions between Fe, Co, and Ni for V_{1.15}FeCoNi. Secondly, V couples antiferromagnetically to Fe and Co. Due to this drastic change we can anticipate a large decrease of T_C for V_{1.15}FeCoNi compared to both FeCoNi and FeCoNiCu_{1.15}. Decreasing the amount of V in V_{0.85}FeCoNi leads to an increase of J_{ij} 's, anticipating a larger T_C than for V_{1.15}FeCoNi.

The combination of V and Cu in the 5-element alloy V_{0.85}FeCoNiCu_{1.15} will result in intermediate values for $J_{\text{Fe-Fe}}$, $J_{\text{Fe-Co}}$ and $J_{\text{Co-Co}}$ compared to the 3- and 4-element alloys FeCoNi, FeCoNiCu_{1.15} and V_{0.85}FeCoNi, respectively. Compared to V_{0.85}FeCoNi, the dilution with Cu in the 5-element alloy has no large effect on $J_{\text{Fe-Ni}}$ and $J_{\text{Co-Ni}}$. However, they are still low (0.25 mRy) when compared to $J_{\text{Fe-Ni}}$ and $J_{\text{Co-Ni}}$ in FeCoNi and FeCoNiCu_{1.15} (See the top-left part of Fig. 9). In the 5-element alloy, $J_{\text{Fe-V}}$ and $J_{\text{Co-V}}$ have the largest negative values (antiparallel couplings).

The Curie temperatures calculated by the Monte Carlo method from ferromagnetic exchange interactions for the 3-, 4- and 5-element alloys assuming nominal compositions are listed in Table 3. The magnetic transition temperature for FeCoNi is calculated to 1009 K based on the theoretical lattice parameter. Cu-addition increases the 1st NN J_{i-j} 's slightly compared to that of FeCoNi. However, T_C of FeCoNiCu_{1.15} (820 K) is lower than for the FeCoNi alloy. This is the result of a dilution effect caused by Cu since the concentration of the magnetic elements are lower in FeCoNiCu_{1.15} than in FeCoNi (see Table 1). In addition, Cu does not contribute to the magnetism, due to its filled d -orbitals that manifest in a negligible induced magnetic moment. As expected from the analysis of the exchange interactions, the lowest Curie temperature (233 K) is obtained for V_{1.15}FeCoNi while increasing Fe, Co, and Ni concentrations in V_{0.85}FeCoNi, compared to V_{1.15}FeCoNi (see Table 1) increases T_C to 350 K (see Table 3). The addition of Cu to the V-alloy decreases not only the atomic concentration of V, but also the concentration of the magnetic

Table 3

Element resolved magnetic moments, m_i (μ_B /atom), total magnetic moment, m_{tot} (μ_B /atom), and calculated T_C (K) for the nominal and measured compositions of the solid solutions. Nominal compositions are written in *italic*.

System	Composition	m_{Fe} (μ_B /atom)	m_{Co} (μ_B /atom)	m_{Ni} (μ_B /atom)	m_{V} (μ_B /atom)	m_{tot} (μ_B /atom)	Calc. T_C (K)	Experimental T_C (K)
Fe-Co-Ni	<i>FeCoNi</i>	2.51	1.69	0.72		1.64	1009	
	<i>FeCo_{1.14}Ni_{1.14}</i>	2.65	1.67	0.64	-	1.61	997	1018
Fe-Co-Ni-Cu	<i>FeCoNiCu_{1.15}</i>	2.56	1.65	0.61	-	1.19	820	
	<i>FeCo_{1.16}Ni_{1.09}Cu_{0.84}</i>	2.70	1.66	0.58	-	1.29	871	957
V-Fe-Co-Ni	<i>V_{1.15}FeCoNi</i>	1.93	1.00	0.23	-0.44	0.64	233	
	<i>V_{0.85}FeCoNi</i>	2.05	1.16	0.31	-0.56	0.79	350	
	<i>V_{0.82}FeCo_{1.07}Ni_{1.03}</i>	2.22	1.22	0.31	-0.74	0.83	384	245
V-Fe-Co-Ni-Cu	<i>V_{0.85}FeCoNiCu_{1.15}</i>	2.21	1.23	0.29	-0.54	0.66	362	
	<i>V_{0.75}FeCo_{1.07}Ni_{1.01}Cu_{0.56}</i>	2.32	1.27	0.31	-0.75	0.76	403	278

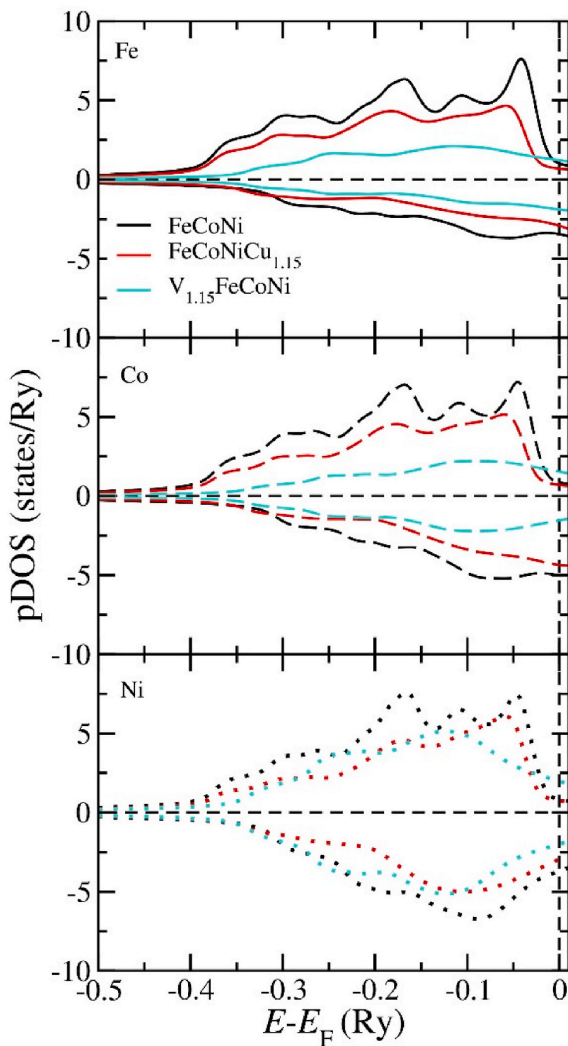


Fig. 7. (Color online.) pDOS for Fe, Co, and Ni in various multicomponent alloys. Black line stands for FeCoNi, the red line for FeCoNiCu_{1.15} and the blue line for V_{1.15}FeCoNi. Full line stands for Fe, the dashed line for Co and the dotted line for Ni.

elements (see Table 1). Therefore, the T_C of V_{0.85}FeCoNiCu_{1.15} (362 K) is higher compared to the V-alloys.

From the above analysis based on the nominal compositions, we can conclude that Cu moderately dilutes the ferromagnetic interactions between Fe, Co and Ni and shields the negative coupling of V, resulting in moderate changes in T_C of FeCoNiCu_{1.15} compared to FeCoNi, and of

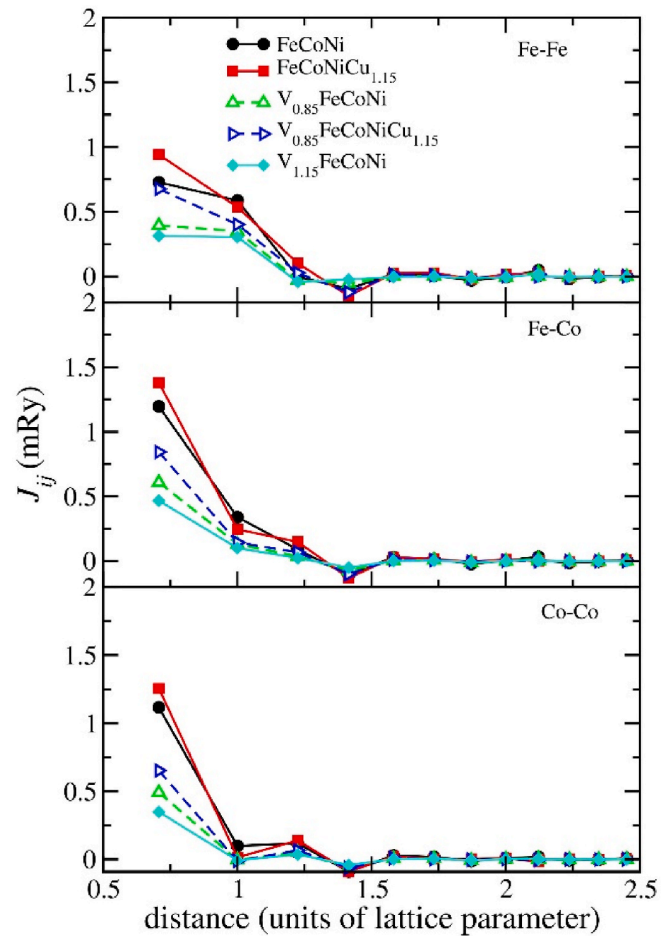


Fig. 8. (Color online.) Calculated magnetic pair exchange interactions for (Fe-Fe), (Fe-Co), and (Co-Co) in the FeCoNi base alloy and selected V- and Cu-doped based solid solutions.

V_{0.85}FeCoNiCu_{1.15} compared to V_{1.15/0.85}FeCoNi. On the other hand, V acts in three different ways: it dilutes the concentration of the magnetic elements, decreases their pair magnetic interactions and couples anti-parallel to them. This leads to a drastic decrease of T_C for the V-containing alloys.

The effect of other 3d metals such as Ti, Cr and Mn on the magnetism of the FeCoNi-base alloy is now briefly discussed. In X_{1.15}FeCoNi, where X = Ti, Cr and Mn, the randomly distributed X-elements have a similar effect on the local magnetic moments of Fe, Co, and Ni as V; namely, m_{Fe} , m_{Co} and m_{Ni} decrease. In addition, a quite substantial induced local moment develops on Ti ($-0.34 \mu_B$), comparable with the Ni moment

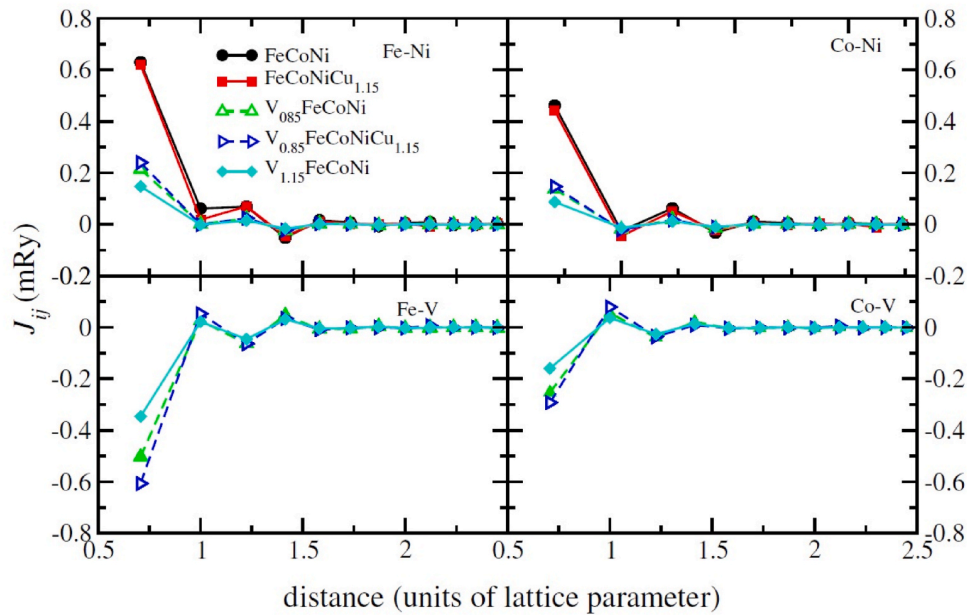


Fig. 9. (Color online.) Calculated magnetic pair exchange interactions for (Fe–Ni), (Co–Ni), (Fe–V) and (Co–V) in the FeCoNi base alloy and selected V- and Cu-doped based solid solutions.

(0.24 μ_B), that couples antiparallel to the local moment of the ferromagnetic elements. m_{Cr} and m_{Mn} are also quite high, with $-0.62 \mu_B$ (Cr) and $-1.72 \mu_B$ (Mn), respectively, and couple antiparallel to the moments of Fe, Co, and Ni, as expected. Therefore, we expect that the effect of Ti, Cr, and Mn on the high temperature magnetism of $X_{1.15}FeCoNi$ is like that of V. Consequently, we foresee a large decrease of T_C for these compounds. Indeed, the decrease of T_C for $X_{1.15}FeCoNi$ ($X = Ti, Cr$ and Mn , respectively), estimated via mean field approximation is large as in the case of V. However, a detailed investigation on the effect of Ti, Cr and Mn is beyond the scope of the present study.

Magnetic properties have also been calculated for the experimentally measured compositions and lattice parameters and are also listed in Table 3. The total magnetic moment calculated for $FeCo_{1.14}Ni_{1.14}$ at 0 K is about 10% larger than at RT. This discrepancy is even larger for the alloys that contain V and Cu. The experimental trends are however captured by the theory. The calculated T_C s for $FeCo_{1.14}Ni_{1.14}$ and $FeCo_{1.16}Ni_{1.09}Cu_{0.84}$ based on the experimental lattice parameters, are 996 K and 871 K, respectively. They are in good agreement with the measured data, 997 K and 957 K, respectively. In contrast, we find a large discrepancy for the V-containing alloys. This is not surprising considering the applied unavoidable assumptions and approximations. Firstly, J_{i-j} 's are calculated for the ideal atomic positions, e.g., unrelaxed lattice positions neglecting the local lattice relaxations due to the size differences between the elements. The second assumption is the random distribution of the elements that does not consider the effect of short-range order or segregation that are possibly present in real alloys. Finally, the temperature effect on the magnitude of the local magnetic moments and as a consequence on the exchange parameters (non-Heisenberg behaviour), that is widely discussed recently [36–41], is also not investigated in this study.

Although the actual values of the total magnetic moment and T_C for the as-cast alloys with V addition do not agree with the measured data, these properties are a direct consequence of the average interactions across the material. In the calculations, the modelled system is still an idealized solid solution. On the other hand, a closer look on the enthalpies of mixing of the studied alloys can shed some light on the trends observed in the experiments. As is known from literature, an enthalpy of mixing, ΔH_{mix} , very close to 0 in connection with atomic size differences $\leq 6.6\%$ favours the formation of solid solutions [42]. This is the case for

the nominal composition of $V_{0.85}FeCoNiCu_{1.15}$, with a ΔH_{mix} of 0.32 J/K. However, this value is only accidentally close to 0 because it results from a combination of pairs with large negative ΔH_{mix} (Co–V and Ni–V), and others with a large positive ΔH_{mix} (Fe–Cu, Co–Cu and Cu–V) that can individually promote segregation. Nevertheless, we are confident that the conclusions drawn for the nominal compositions are also valid for the as-cast samples.

4. Conclusion

Four ferromagnetic transition-metal based alloys were studied to understand how structure and microstructure affect the steepness of the magnetic transition, which is an indication of the magnetocaloric effects in the materials. All alloys were studied in metastable states after casting. Pure ferromagnetic, diluted ferromagnetic, ferromagnetic-antiferromagnetic and diluted ferromagnetic-antiferromagnetic systems were investigated.

The FeCoNi base alloy exhibits a monophasic microstructure. With the addition of V, a sigma intermetallic is introduced, while with Cu, a secondary Cu-rich phase is precipitated in an inter-dendritic region due to the lack of solubility at lower temperatures. In the 5-element alloy $V_{0.85}FeCoNiCu_{1.15}$, a sigma intermetallic and secondary ccp phase are both present. However, instead of precipitating from a main solid solution, the Cu-rich phase is solidified from a secondary liquid phase, as indicated from the morphology of the Cu-rich phase.

The precipitation of secondary phases impacts the chemical composition of the main solid solutions, which is directly responsible for the macroscopic magnetization behaviour. All studied solid solutions feature ferromagnetism at lower temperatures and undergo ferro-to-paramagnetic transitions. The temperature dependent magnetization curves show that FeCoNi has a typical second order transition, with a continuous decrease in magnetization. The dilution induced by the addition of Cu in $FeCoNiCu_{1.15}$ mostly impacts the magnetization values, and slightly effects T_C values and the steepness of the magnetic transition. The introduction of V, however, in V–FeCoNi strongly modifies T_C , decreasing it below room temperature in $V_{0.85}FeCoNi$. The absolute magnetization values are reduced, and the transition is broadened, which are both detrimental for magnetocaloric properties. The 5-element alloy $V_{0.85}FeCoNiCu_{1.15}$ boasts a similar magnetic behaviour,

though with a slightly increased derivative of magnetization that is credited to the reduced V content.

Analysis of the magnetic properties by DFT shows that the addition of Cu to FeCoNi dilutes the magnetic exchange and results in a slight decrease of T_C . In contrast, the addition of V acts in three different ways: (i) V dilutes the amount of the ferromagnetic elements; (ii) its induced moment couples antiparallel to the moments of Fe, Co, and Ni; (iii) the addition of V leads to a decrease of the magnetic exchange interactions between the ferromagnetic elements. These combined effects result in a large decrease of the magnetic transition temperature in the studied $V_{0.85}FeCoNi$ and $V_{0.85}Fe_1Co_1Ni_1Cu_{1.15}$ alloys. A similar behaviour is predicted for other early 3 *d*-transition metals based on a brief investigation of their effect on the local magnetic moments of $X_{1.15}FeCoNi$ ($X = Ti, Cr$ and Mn), though in different strengths.

To make high entropy alloys viable for magnetocaloric applications, the strength of ferromagnetic interactions is of key importance, together with the abruptness of the transition (high dM/dT). The drastic reduction of T_C that is caused by the addition of V, Mn, Cr and Ti to the FeCoNi base alloy is remarkable. However, such elements are also responsible for a large decrease in the moments of Fe, Co, and Ni. Pathways to improvement of the magnetocaloric effect lie in optimizing the content of antiferromagnetic coupling and diluting elements.

Credit roles

Bruno G. F. Eggert: Conceptualization (equal) Data curation (equal) Formal analysis (equal) Investigation (equal) Methodology (equal) Visualization (equal) Writing - original draft (equal) Writing - review & editing (equal) **Erna K. Delczeg-Czirjak:** Software (equal) Methodology (equal) Formal analysis (equal) Resources (equal) Visualization (equal) Writing - original draft (equal) Writing - review & editing (equal) **Bjørn Hauback:** Supervision (equal) Writing - review & editing (equal) **Christoph Frommen:** Funding acquisition (equal) Project administration (equal) Supervision (equal) Writing - review & editing (equal).

Declaration of competing interest

The authors declare that they have no known competing financial interests or personal relationships that could have appeared to influence the work reported in this paper.

Data availability

Data will be made available on request.

Acknowledgements

This work was financed by The Research Council of Norway through the NANO2021 program, Project No. 287150. E. K. D.-Cz. acknowledges the Swedish National Infrastructure for Computing (SNIC) for computational resources (snic2021-1-36 and snic2021-5-340) and the Swedish Foundation for Strategic Research (SSF) (contract EM-16-0039) for financial support. Valuable discussions with A.V. Ruban from KTH Royal Institute of Technology and M. Pereiro from Uppsala University are also acknowledged. B. G. F. Eggert also acknowledges Bjørn M. Valldor for his skillful assistance on performing magnetic measurements at low temperatures.

References

[1] A. Kitanovski, Energy Applications of Magnetocaloric Materials, 2020: 1903741, <https://doi.org/10.1002/aenm.201903741>.
 [2] V. Franco, J.S. Blázquez, J.J. Ipus, J.Y. Law, L.M. Moreno-Ramírez, A. Conde, Magnetocaloric effect: from materials research to refrigeration devices, Prog. Mater. Sci. 93 (2018) 112–232, <https://doi.org/10.1016/j.pmatsci.2017.10.005>.

[3] M.C. Gao, D.B. Miracle, D. Maurice, X. Yan, Y. Zhang, J.A. Hawk, High-entropy functional materials, J. Mater. Res. 33 (2018) 3138–3155, <https://doi.org/10.1557/jmr.2018.323>.
 [4] S.M. Na, P.K. Lambert, H. Kim, J. Paglione, N.J. Jones, Thermomagnetic properties and magnetocaloric effect of FeCoNiCrAl-type high-entropy alloys, AIP Adv. 9 (2019), <https://doi.org/10.1063/1.5079394>.
 [5] D.D. Belyea, M.S. Lucas, E. Michel, J. Horwath, C.W. Miller, Tunable magnetocaloric effect in transition metal alloys, Sci. Rep. 5 (2015) 1–8, <https://doi.org/10.1038/srep15755>.
 [6] A. Perrin, M. Sorescu, M.T. Burton, D.E. Laughlin, M. McHenry, The role of compositional tuning of the distributed exchange on magnetocaloric properties of high-entropy alloys, Jom 69 (2017) 2125–2129, <https://doi.org/10.1007/s11837-017-2523-3>.
 [7] M. Kurniawan, A. Perrin, P. Xu, V. Keylin, M. McHenry, Curie temperature engineering in high entropy alloys for magnetocaloric applications, IEEE Magn. Lett. 7 (2016) 1–5, <https://doi.org/10.1109/LMAG.2016.2592462>.
 [8] N.A. Morley, B. Lim, J. Xi, A. Quintana-Nedelcos, Z. Leong, Magnetic properties of the complex concentrated alloy system CoFeNi0.5Cr0.5Alx, Sci. Rep. 10 (2020) 1–12, <https://doi.org/10.1038/s41598-020-71463-3>.
 [9] D.B. Miracle, O.N. Senkov, A critical review of high entropy alloys and related concepts, Acta Mater. 122 (2017) 448–511, <https://doi.org/10.1016/j.actamat.2016.08.081>.
 [10] Z. Dong, S. Huang, V. Ström, G. Chai, L.K. Varga, O. Eriksson, L. Vitos, MnxCr0.3Fe0.5Co0.2Ni0.5Al0.3 high entropy alloys for magnetocaloric refrigeration near room temperature, J. Mater. Sci. Technol. 79 (2021) 15–20, <https://doi.org/10.1016/j.jmst.2020.10.071>.
 [11] A. Phys, Magnetocaloric Properties of Melt-Spun MnFe-Rich High-Entropy Alloy Magnetocaloric Properties of Melt-Spun MnFe-Rich High-Entropy Alloy, 2021: 141909, <https://doi.org/10.1063/5.0065067>.
 [12] M.S. Lucas, D. Belyea, C. Bauer, N. Bryant, E. Michel, Z. Turgut, S.O. Leontsev, J. Horwath, S.L. Semiatin, M.E. McHenry, C.W. Miller, Thermomagnetic analysis of FeCoCrNi alloys: magnetic entropy of high-entropy alloys, J. Appl. Phys. 113 (2013) 2011–2014, <https://doi.org/10.1063/1.4798340>.
 [13] A. Quintana-Nedelcos, Z. Leong, N.A. Morley, Study of dual-phase functionalisation of NiCoFeCr-Alx multicomponent alloys for the enhancement of magnetic properties and magneto-caloric effect, Mater. Today Energy 20 (2021): 100621, <https://doi.org/10.1016/j.mtener.2020.100621>.
 [14] B.G.F. Eggert, E.K. Delczeg-czirjak, F. Maccari, S. Kumar, O. Gutfleisch, H. Fjellvåg, B.C. Hauback, C. Frommen, Exploring V-Fe-Co-Ni-Al and V-Fe-Co-Ni-Cu high entropy alloys for magnetocaloric applications, J. Alloys Compd. 921 (2022): 166040, <https://doi.org/10.1016/j.jallcom.2022.166040>.
 [15] T. Gottschall, K.P. Skokov, M. Fries, A. Taubel, I. Radulov, F. Scheibel, D. Benke, S. Riegg, O. Gutfleisch, Making a cool choice: the materials library of magnetic refrigeration, Adv. Energy Mater. 9 (2019), <https://doi.org/10.1002/aenm.201901322>.
 [16] J.P. Perdew, K. Burke, M. Ernzerhof, Generalized gradient approximation made simple, Phys. Rev. Lett. 77 (1996) 3865–3868, <https://doi.org/10.1103/PhysRevLett.77.3865>.
 [17] J. Rodriguez-Carvajal, Recent developments of the program FULLPROF, commission on powder diffraction, IUCr Newsl. (Int. Union Crystallogr.) 26 (2001) 12–19. <http://www.iucr.org/iucr-top/comm/cpd/html/newsletter26.html>.
 [18] C.A. Schneider, W.S. Rasband, K.W. Eliceiri, NIH Image to ImageJ: 25 years of image analysis, Nat. Methods 9 (2012) 671–675, [https://doi.org/10.1016/S0031-8914\(53\)80099-6](https://doi.org/10.1016/S0031-8914(53)80099-6).
 [19] O.K. Andersen, O. Jepsen, G. Krier, Lectures on Methods of Electronic Structure Calculation, 1994.
 [20] L. Vitos, The EMTO Method and Applications in Computational Quantum Mechanics for Materials Engineers, Springer-Verlag London, 2007.
 [21] P. Soven, Coherent-potential model of substitutional disordered alloys, Phys. Rev. 156 (1967) 809–813, <https://doi.org/10.1103/PhysRev.156.809>.
 [22] B.L. Gyorffy, Coherent-potential approximation for a nonoverlapping-muffin-tin-potential model of random substitutional alloys, Phys. Rev. B 5 (1972) 2382–2384, <https://doi.org/10.1103/PhysRevB.5.2382>.
 [23] L. Vitos, Total-energy method based on the exact muffin-tin orbitals theory, Phys. Rev. B 64 (2001): 14107, <https://doi.org/10.1103/PhysRevB.64.014107>.
 [24] A. V Ruban, M. Dehghani, Atomic configuration and properties of austenitic steels at finite temperature: effect of longitudinal spin fluctuations, Phys. Rev. B 94 (2016): 104111, <https://doi.org/10.1103/PhysRevB.94.104111>.
 [25] A. V Ruban, H.L. Skriver, Screened Coulomb interactions in metallic alloys. I. Universal screening in the atomic-sphere approximation, Phys. Rev. B 66 (2002): 24201, <https://doi.org/10.1103/PhysRevB.66.024201>.
 [26] A. V Ruban, S.I. Simak, P.A. Korzhavii, H.L. Skriver, Screened Coulomb interactions in metallic alloys. II. Screening beyond the single-site and atomic-sphere approximations, Phys. Rev. B 66 (2002): 24202, <https://doi.org/10.1103/PhysRevB.66.024202>.
 [27] J. Kollar, L. Vitos, H.L. Skriver, From ASA towards the Full Potential, Springer-Verlag, Berlin Heidelberg New York Tokyo, 2000.
 [28] H.J. Monkhorst, J.D. Pack, Special points for Brillouin-zone integrations, Phys. Rev. B 13 (1976) 5188–5192, <https://doi.org/10.1103/PhysRevB.13.5188>.
 [29] V.L. Moruzzi, J.F. Janak, K. Schwarz, Calculated thermal properties of metals, Phys. Rev. B 37 (1988) 790–799, <https://doi.org/10.1103/PhysRevB.37.790>.
 [30] B. Skubic, J. Hellsvik, L. Nordstrom, O. Eriksson, A method for atomistic spin dynamics simulations: implementation and examples, J. Phys. Condens. Matter. 20 (2008): 315203, <https://doi.org/10.1088/0953-8984/20/31/315203>.

- [31] O. Eriksson, A. Bergman, L. Bergqvist, J. Hellsvik, *Atomistic Spin Dynamics*, Oxford University Press, 2016. <https://global.oup.com/academic/product/atomistic-spin-dynamics-9780198788669>.
- [32] J.M. Joubert, Crystal chemistry and Calphad modeling of the σ phase, *Prog. Mater. Sci.* 53 (2008) 528–583, <https://doi.org/10.1016/j.pmatsci.2007.04.001>.
- [33] M.R. Rahul, S. Samal, G. Phanikumar, Effect of niobium addition in FeCoNiCuNb_x high-entropy alloys, *J. Mater. Res.* 34 (2019) 700–708, <https://doi.org/10.1557/jmr.2019.36>.
- [34] S.F. Liu, Y. Wu, H.T. Wang, J.Y. He, J.B. Liu, C.X. Chen, X.J. Liu, H. Wang, Z.P. Lu, Stacking fault energy of face-centered-cubic high entropy alloys, *Intermetallics* 93 (2018) 269–273, <https://doi.org/10.1016/j.intermet.2017.10.004>.
- [35] A.J. Zaddach, C. Niu, C.C. Koch, D.L. Irving, Mechanical properties and stacking fault energies of NiFeCrCoMn high-entropy alloy, *Jom* 65 (2013) 1780–1789, <https://doi.org/10.1007/s11837-013-0771-4>.
- [36] A. V. Ruban, S. Shallcross, S.I. Simak, H.L. Skriver, Atomic and magnetic configurational energetics by the generalized perturbation method, *Phys. Rev. B* 70 (2004): 125115, <https://doi.org/10.1103/PhysRevB.70.125115>.
- [37] A. V. Ruban, S. Khmelevskiy, P. Mohn, B. Johansson, Temperature-induced longitudinal spin fluctuations in Fe and Ni, *Phys. Rev. B* 75 (2007): 54402, <https://doi.org/10.1103/PhysRevB.75.054402>.
- [38] A. V. Ruban, A.B. Belonoshko, N. V. Skorodumova, Impact of magnetism on Fe under Earth's core conditions, *Phys. Rev. B* 87 (2013): 14405, <https://doi.org/10.1103/PhysRevB.87.014405>.
- [39] R. Cardias, A. Szilva, A. Bergman, Y. Kvashnin, J. Fransson, S. Streib, A. Delin, M. I. Katsnelson, D. Thonig, A.B. Klautau, O. Eriksson, L. Nordström, Comment on “Proper and improper chiral magnetic interactions”, *Phys. Rev. B* 105 (2022): 26401 <https://doi.org/10.1103/PhysRevB.105.026401>.
- [40] M. dos Santos Dias, S. Brinker, A. Lászlóffy, B. Nyári, S. Blügel, L. Szunyogh, S. Lounis, Proper and improper chiral magnetic interactions, *Phys. Rev. B* 103 (2021) L140408, <https://doi.org/10.1103/PhysRevB.103.L140408>.
- [41] S. Khmelevskiy, P. Mohn, Longitudinal fluctuations of Co spin moments and their impact on the Curie temperature of the Heusler alloy Co₂FeSi, *J. Magn. Magn. Mater.* 560 (2022): 169615, <https://doi.org/10.1016/j.jmmm.2022.169615>.
- [42] M.C. Gao, C. Zhang, P. Gao, F. Zhang, L.Z. Ouyang, M. Widom, J.A. Hawk, Thermodynamics of concentrated solid solution alloys, *Curr. Opin. Solid State Mater. Sci.* 21 (2017) 238–251, <https://doi.org/10.1016/j.cossms.2017.08.001>.

Paper III

Structural transitions and magnetocaloric properties of low-cost MnNiSi-based intermetallics



Structural transitions and magnetocaloric properties of low-cost MnNiSi-based intermetallics

B.G.F. Eggert^a, J.F.H. Belo^b, J.P. Araújo^b, B.C. Hauback^a, C. Frommen^{a,*}

^a Department for Hydrogen Technology, Institute for Energy Technology (IFE), P.O. Box 40, NO-2027, Kjeller, Norway

^b Institute of Physics of Advanced Materials, Nanotechnology and Nanophotonics (IFIMUP), Departamento de Física e Astronomia da Faculdade de Ciências da Universidade do Porto, Rua do Campo Alegre, 687, 4169-007, Porto, Portugal

ARTICLE INFO

Keywords:

A. intermetallics
Functional alloys
B. Martensitic transformation
Magnetic properties
D. microstructure
F. Electron microscopy
Scanning

ABSTRACT

A series of $\text{Mn}_{1-x}\text{Ni}_x\text{Fe}_{2x}\text{Si}_{0.95}\text{Al}_{0.05}$ MM'X-type compounds (with $x = 0.28, 0.3, 0.32$ and 0.35) were investigated for their potential as magnetocaloric materials. Structural and magnetic properties were studied by magnetometry, microscopy and X-ray diffraction. Double substitution of Fe in Mn and Ni sites allowed to tune martensitic transition temperatures between low temperature orthorhombic and high temperature hexagonal structures from 373 K in $x = 0.28$ –183 K in $x = 0.35$ during cooling. Transition temperatures occur around room temperature for $x = 0.30$ (300 K for cooling transformation) and 0.32 (270 K for heating transformation). Isothermal entropy changes of $-8, -19$ and -26 J/kg.K were calculated for field changes of $\mu_0H = 0-2, 0-5$ and $0-7$ T for $x = 0.30$. The values are comparable to those reported for MnNi(SiAl)-based compounds with single site substitutions (Mn and Ni) by Fe. Further analyses show that high magnetic fields are necessary to induce the magnetostructural transition in all studied compounds, which can be attributed to the presence of secondary phases and/or disorder at a local level.

1. Introduction

Materials featuring magneto-responsive effects can be employed in a variety of applications. As an example, magnetostriction effects occur when magnetic fields modify internal strain in the crystal structure, giving rise to core components of transducers and actuators [1]. For magnetoresistance effects, the electrical resistance is modified by varying degrees of magnetic fields, which enables devices such as microelectromechanical systems and spin-valves [2,3]. Besides changes in strain and electrical resistivity, the reorientation of magnetic moments also brings a modification in temperature. In some materials, known as magnetocaloric materials, external magnetic fields induce a large variation in temperature compared to regular materials [4]. In some magnetocaloric materials, these large variations are created due to coupled magnetization and volume changes, undergoing transitions known as First Order Phase Transitions (FOPTs).

Such magnetocaloric phase transitions can be achieved by composition tuning of known systems, enabling concurrent electronic [5–8] and structural changes [9–11] in relation to magnetic transitions. In magnetocaloric materials with FOPTs, the latent heat associated with symmetry and/or volume changes around the coupled structural

transition temperature T_{str} is the driving force for alternative energy conversion technologies. In order to evaluate the performance of such magnetocaloric materials, two properties are commonly considered: the adiabatic temperature change (ΔT_{ad}) and the isothermal entropy change (ΔS_m) [4,12]. If one considers the use of such materials for wide spread technologies such as domestic refrigeration and air conditioning, masses in the order of kilograms of magnetocaloric materials will be needed in each unit [13,14]. Therefore, magnetocaloric materials should be produced with non-expensive, non-critical elements, i.e., elements that are not at a supply risk, that do not feature major environmental implications in its production, and that do not feature a large vulnerability to supply restriction [15]. Such materials should also be inserted within a sustainable life cycle [14].

One of the most interesting and versatile class of materials which exhibit magneto-responsive effects are the MM'X compounds, where M and M' are transition metals, and X is a p-block element. Typical examples include MnCoGe, MnCoSi, MnNiGe among others [16]. These materials crystallize either in the orthorhombic (orth.) TiNiSi structure-type (space group $Pnma$) or the hexagonal Ni_2In structure-type (space group $P6_3/mmc$) at higher temperatures, as schematically illustrated for $\text{MnNiSi } 2 \times 2 \times 2$ supercells in Fig. 1. To ease comprehension,

* Corresponding author.

E-mail address: Christoph.frommen@ife.no (C. Frommen).

<https://doi.org/10.1016/j.intermet.2023.107823>

Received 12 October 2022; Received in revised form 20 December 2022; Accepted 2 January 2023

Available online 13 January 2023

0966-9795/© 2023 The Authors. Published by Elsevier Ltd. This is an open access article under the CC BY license (<http://creativecommons.org/licenses/by/4.0/>).

$TiNiSi$ and the Ni_2In structures will be referred to as orth. and hex. respectively. The $TiNiSi$ structure-type is a ternary silicide with 3 different $4c$ positions, with half-chair configuration in Ni-Si bonds. Ni and Si are also bonded to Mn, which itself is arranged with other Mn atoms in spiral/hexagonal coordination, if seen along the b direction. This spiral/hexagonal coordination is emphasized in Fig. 1a. It is known to be responsible for a high magnetic moment in this structure [17,18]. In the hex. Ni_2In type structure illustrated in Fig. 1b, the Mn atoms stay in layered positions along vertices and edges of the unit-cell ($2a$ site), with Ni and Si remaining in $2d$ and $2c$ sites, respectively [19]. The orth. and hex. unit cells are related in the following manner: $c_{hex} \rightarrow a_{orth}$, $\sqrt{3} a_{hex} \rightarrow c_{orth}$, and $c_{hex} \rightarrow a_{orth}$. By appropriate elemental substitution, a magnetostructural transition (MST) can be achieved in $MM'X$ systems across a wide compositional space [1,20–22]. Given a sufficiently high magnetic field, a metamagnetic transition can occur from a hex. paramagnetic (PM) to an orth. ferromagnetic phase (FM) [19].

Among the commonly studied $MnMX$ compounds, $MnNiSi$ features the more abundant Si element as a p-block, compared to critical Ge, regularly used in $MM'X$ reports. The use of Ge as a main element in magnetocaloric devices would require a much larger demand than the possible future production, making its use inviable [14]. Also, the price of Ge is much larger than Si. Therefore, $MnNiSi$ should be used as a starting $MM'X$ compound. Its structural transition temperature (T_{str}) is close to 1200 K, while its T_C is around 600 K [19], and different elements can partially substitute the $2a$, $2d$, or $2c$ sites according to the Hume-Rothery rules (referring to the hex. structure). In some compounds, it is possible to completely substitute one element for another while remaining in the same space groups, yielding different forms of magnetism i.e. antiferromagnetism in $MnNiGe$ [19], paramagnetism in $FeNiSi$ [23] or ferromagnetism in $MnCoGe$ and $MnNiSi$ [17,24]). This is another indication of the versatility of this class of materials. In the case of $MnNiSi$, at least two substitutions in the lattice must be performed to induce an MST around room temperature (RT); one on either the $2a$ or $2d$ sites, and a second on the $2c$ sites (when referring to the Ni_2In structure type).

$2d$ and $2a$ site substitutions in $MM'X$ systems are usually performed by other transition metals, where the T_{str} modifications are site and content dependent [25]. With regards to the effect of substitution in $2c$ sites, different p-block elements can be used, mainly from groups 3a and 4a i.e. Ge [26–28], Ga [29,30], Sn [31] and Al [32–34]. The substitutions aim to lower T_C and T_{str} , thus creating coupled structural and magnetic transitions at RT.

In this article, we investigate a series of $MM'X$ compositions with abundant elements, featuring the least expensive $MM'X$ possible: $Mn_{1-x}Ni_xFe_{2x}Si_{0.95}Al_{0.05}$ with $x = 0.28, 0.3, 0.32$ and 0.35 . All reports so far have dealt with single site substitutions. To the best of our knowledge, no concurrent Al ($2c$) substitutions with double ($2a, 2d$) site substitutions by Fe have been reported.

The structures, phase content, and morphology are described by the help of powder X-ray diffraction and microscopy techniques. In addition, a comprehensive analysis of structural transitions, magnetic and magnetostructural properties are presented. This enables a fundamental understanding of the $MnNiSi_{0.95}Al_{0.05}$ intermetallic with double substitution of $2a$ and $2d$ sites by Fe featuring transitions across RT.

2. Materials and methods

$MnNiSi$ -based intermetallics were synthesized with pre-alloyed $MnNiSi$ intermetallic ingots together with elemental Fe, Si and Al in a Ti-gettered arc melting furnace. $MnNiSi$ pre-alloys were utilized instead of the pure elements as the samples featured a smaller mass loss. Mass losses due to Mn evaporation were smaller than 1 wt% in all samples. The as-cast ingots were subsequently sealed in quartz tubes under vacuum, heat treated at 1073 K for 7 days and quenched in water.

Synchrotron radiation powder X-ray diffraction (SR-PXD) experiments were carried out at the Swiss-Norwegian Beamline (SNBL), station BM-01, ($\lambda = 0.69217 \text{ \AA}$) at the European Synchrotron Radiation Facility (ESRF) in Grenoble, France. Heating and cooling of the capillaries was performed using a cryostat or a furnace with heating/cooling rates of 2K/min. Structural characterization was performed in Topas Academic v6. In all refinements, the peak resolution function was described by an algorithm developed by Chernyshov et al. [35] for area detectors, such as the one at BM-01. The background was described by a Chebyshev polynomial with 10 parameters. The main parameters refined were zero error, lattice parameters, general positions and isotropic displacement factors for individual sites. Size broadening of the peaks was described using a Lorentzian function. Preferential Orientation was addressed by the use of the March-Dollase model whose pole density profile is given by

$$P_{p^*}(r, \rho) = \left(r^3 \cos^2 \rho + \frac{\sin^2 \rho}{r} \right)^{-3/2} \quad (1)$$

Where p^* represents the preferred orientation direction, defined as $p^* = ha^* + kb^* + lc^*$ for the reciprocal lattice vectors a^* , b^* and c^* , and r is a parameter for description of crystallites impacting the preferred orientation, where values smaller than 1 describe rod-shaped crystallites, and r larger than 1 describe plate-shaped crystallites. The angle ρ is the polar angle between the preferred orientation direction p^* and the direction s^*

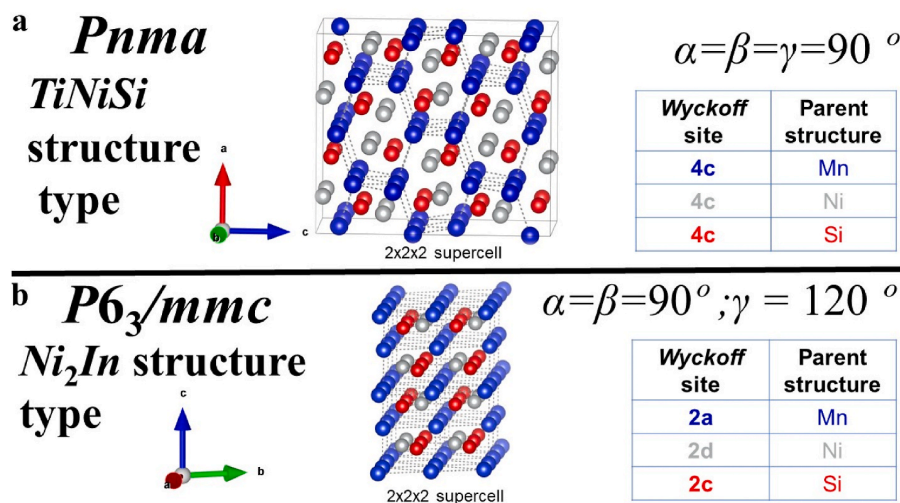


Fig. 1. Representation of the structure and description of the main parameters of the orth. and hex. structures adopted in $MnNiSi$ compounds.

that specifies the direction of the specimen [36].

Optical micrographs were obtained from a Zeiss Axioskop 2 with a polarizer lens. Scanning electron microscopy (SEM) and energy dispersive X-ray spectroscopy (EDS) were done in a Hitachi SU8230 ultra-high resolution cold-field emission scanning electron microscope.

Differential scanning calorimetry (DSC) measurements were carried out with a Discovery DSC 25 from TA Instruments using a heating/cooling rate of 10 K/min in ingots with masses in the range of 5–15 mg. Heat capacity measurements were performed by a “classical” three step procedure [37]. Magnetic measurements were performed by a Quantum Design MPMS 3, where temperature dependent curves had applied fields of $\mu_0H = 0.5$ T, and heating rates of 2 K/min from 50 to 375 K. Field dependent curves were performed by the discontinuous method [38] with temperature intervals of 2 K/min in magnetic fields in the range of $\mu_0H = 0-7$ T across the magnetic transitions. The samples had masses ranging from 20 to 40 mg and were not corrected for demagnetization.

3. Results and discussion

3.1. Crystal structure and microstructure

The SR-PXD patterns at RT presented in Fig. 2 show the presence of both orth. and hex. phases for all compositions. The partial Fe substitution in both Mn and Ni sites acts to stabilize the hex. Ni_2In structure type at RT. This is confirmed by the gradual growth of all hex. peaks, but most notably the $(102)_{hex}$ and $(110)_{hex}$ planes seen between $2\theta = 19-20^\circ$, see Fig. 2. This growth occurs in detriment of the orth. peaks. A third set of peaks, which corresponds to $Mn_{1.0}Ni_{1.25}Si_{0.75}$ in the hexagonal $MgZn_2$ structure-type ($P6_3/mmc$), can be observed for all samples [39]. For the $x = 0.28$ sample, a small peak associated with the $(\bar{3}10)$ reflection for the Fe_5Si_3 -type hexagonal phase is present in the pattern in $2\theta = 17.87^\circ$. Other Fe_5Si_3 peaks are overlapping with reflections from other structures.

Rietveld refinements were carried out on all X-ray patterns and are also shown in Fig. 2. The results show that the phase content at RT is modified as a function of Fe substitution, increasing the amount of hex. phase with higher Fe contents seen in Fig. 3. The main lattice parameters, standard deviations, volume of the orth. and hex. unit cells, and

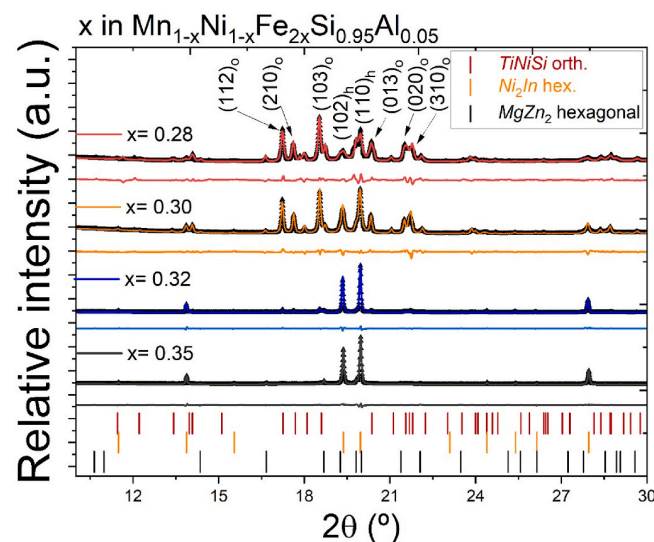


Fig. 2. Rietveld refinement results of SR-PXD data ($\lambda = 0.69217$ Å) of $Mn_{1-x}Ni_{1-x}Fe_{2x}Si_{0.95}Al_{0.05}$ with $x = 0.28, 0.3, 0.32,$ and 0.35 , displaying the main phases present at RT on the bottom of the graph, and the main miller indices of the orth. and hex. phases between $2\theta = 17-23^\circ$. Experimental data is represented by symbols, the best fit as continuous lines and the difference plot is shown under each diffraction pattern.

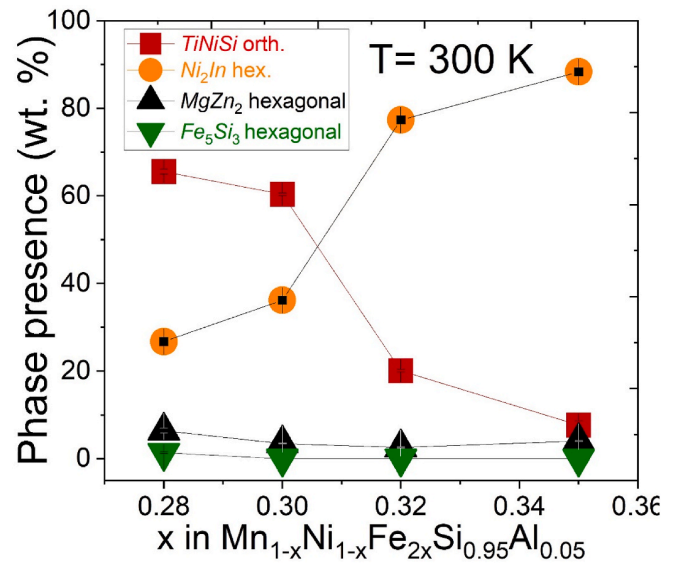


Fig. 3. Phase presence for different compositions of $Mn_{1-x}Ni_{1-x}Fe_{2x}Si_{0.95}Al_{0.05}$ as a function of Fe content as determined by Rietveld refinement.

weighted profile R-factors (R_{wp}) for all samples are displayed in Table 1. A small reduction of the unit cell volume with increasing Fe substitution can be observed for both the hex. and orth. cell.

There was a challenge to fit the observed intensities for the (102) and (110) peaks for the Ni_2In structure, which could be an indication of preferential orientation in the samples. A March-Dollase model was used and successfully described the intensity mismatches with (hkl) of (110) , and r values ranging from 0.76 to 0.85, see eqn. (1) above. Such preferential orientation in the sample can be attributed to the solidification process. The arc melting process occurs by opening an electric arc through the sample and into a Cu coated cooled hearth. As the melting is finished, the grains quickly crystallize from the colder Cu interface, inducing columnar growth, which in turn aligns the grains. This should create a texture in the microstructure, which is confirmed by polarized optical microscopy technique, employed for the $Mn_{0.68}Ni_{0.68}Fe_{0.64}Si_{0.95}Al_{0.05}$ ($x = 0.32$) sample, see Fig. 4a. Polarized images are a helpful tool as different grain orientations can be differentiated by different grey hues.

Fig. 4a shows that the microstructure is composed of long, slab-like grains with lengths in the order of hundreds of micrometers, following the solidification front. Higher magnifications (63x) provide a better understanding of the microstructure in Fig. 4b. The grains of the main phase appear to be surrounded by dark boundary regions. The same tone is observed in inclusions, as seen within the “matrix” composed of the Ni_2In hex. phase.

These inclusions and dark boundary areas could be an indication of a secondary phase. Using SEM imaging and EDS measurements, this suspicion can be further elucidated. Indeed, the presence of a chemically different phase in the grain boundaries is confirmed by SEM measurements in Back-scattered electron mode, see Fig. 4c. This is because different atomic densities are observed between the “matrix phase” and the secondary phase, indicating different elemental compositions. This secondary phase is present in the grain boundaries of the Ni_2In structure and inside the grains. With the aid of composition maps, shown in Fig. 4d, one can clearly note a lower presence of Fe in the secondary phase and a higher presence of Mn and Ni (not shown for the sake of brevity). EDS measurements determined the chemical composition of the secondary phase as $Mn_{0.97}Ni_{0.97}Fe_{0.28}Si_{0.78}$. This is very similar to the nominal composition of the hexagonal $MgZn_2$ phase ($Mn_{1.0}Ni_{1.25}Si_{0.75}$), with a small amount of Fe substitution that was also observed by SR-PXD (see Figs. 2 and 3).

Table 1

Structural parameters of the studied samples obtained by Rietveld refinement: lattice parameters, volume of the orth. and hex. unit cells, and weighted profile R-factors (R_{wp}) with standard deviations in brackets.

Composition $Mn_{1-x}Ni_{1-x}Fe_{2x}Si_{0.95}Al_{0.05}$	a orth (Å)	b orth (Å)	c orth (Å)	V_{orth} (Å ³)	a hex (Å)	c hex (Å)	V_{hex} (Å ³)	R_{wp} (%)
x=0.28	5.7452(4)	3.6643(2)	6.958(5)	146.41(2)	3.9997(4)	5.1200(8)	70.93(2)	8.29
x=0.30	5.7302(3)	3.6713(2)	6.9576(3)	145.34(1)	3.9958(1)	5.1275(2)	70.901(6)	5.52
x=0.32	5.7367(4)	3.668(2)	6.950(5)	146.27(1)	3.9935(5)	5.1299(7)	70.852(2)	7.45
x=0.35	5.693(4)	3.677(2)	6.952(4)	145.1(2)	3.9913(5)	5.1200(7)	70.640(2)	8.02

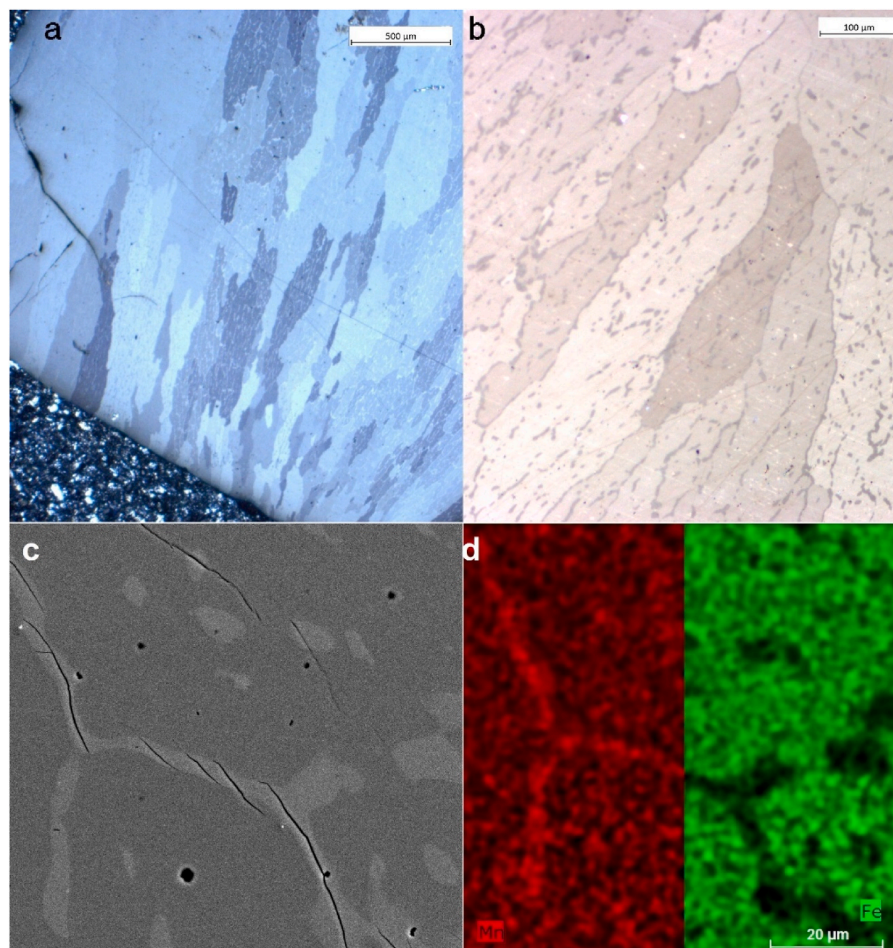


Fig. 4. Microstructure of the $Mn_{0.68}Ni_{0.68}Fe_{0.64}Si_{0.95}Al_{0.05}$ heat treated sample observed by a) polarized optical microscopy with a 16x magnification exhibiting elongated grains due to preferential orientation; b) Higher (63x) magnification which displays the biphasic nature of the sample; c) Back-scattered electron image which shows the different atomic densities, confirming the biphasic nature of the microstructure and d) Mn/Fe EDS maps of the same area, confirming the presence of a Mn-rich, Fe-poor phase – the composition traces it back to the $MnNiFeSi$ phase with a hexagonal $MgZn_2$ -type structure.

The presence of such $MgZn_2$ Laves structure can be rationalized by the following reasons: Firstly, in the $MnNiSi$ parent compound, the stabilization of the hex. structure at RT can only be performed by the presence of (at least) two substitutions to the lattice. In the case of Al substitution in the Si sites, the required amounts for stabilization are small, close to 1 wt %. As such, small inhomogeneities in the Al or Fe contents around the grains could stabilize the $MgZn_2$ Laves phase in the grain boundary or inside the grain regions. Secondly, the thermodynamic equilibrium of the proposed composition is inside a biphasic field. A third possibility is that the $MgZn_2$ Laves phase is segregated upon solidification and not solubilized during heat treatment. Additional EDS measurements on a series of areas encompassing the dark and bright phases were carried out, thereby determining the composition of the alloy, to be $Mn_{0.7}Ni_{0.67}Fe_{0.67}Si_{0.90}Al_{0.06}$, and thus in good agreement with the nominal composition $Mn_{0.68}Ni_{0.68}Fe_{0.64}Si_{0.95}Al_{0.05}$.

3.2. Structural transitions characterized by SR-PXD and DSC

In-situ SR-PXD is a powerful technique to study structural transitions as a function of temperature. An example of the transition in $Mn_{0.7}Ni_{0.7}Fe_{0.6}Si_{0.95}Al_{0.05}$ is shown in Fig. 5 during heating with a heating rate of 2 K per minute. In this contour plot, the peaks associated with the orth. phase are disappearing with increasing temperature while the hex. peaks are becoming stronger in intensity. Small peaks associated with the $MgZn_2$ structure-type can also be observed in the vicinity of the peaks from the Ni_2In structure-type. The reduction and gradual disappearance of the orth. peaks occur between 320 and 380 K, respectively. This large temperature range could be an indication of the level of disorder associated with the structure, as Mn/Fe/Ni can interchangeably occupy 2a and 2d sites, respectively. This can also be a reason for the presence of hex. peaks at lower temperatures, before the majority of the sample undergoes the phase transition. By analysing the derivative of the intensity of the $(110)_{hex}$ peak with temperature, one can observe the temperature regions where the transition takes place.

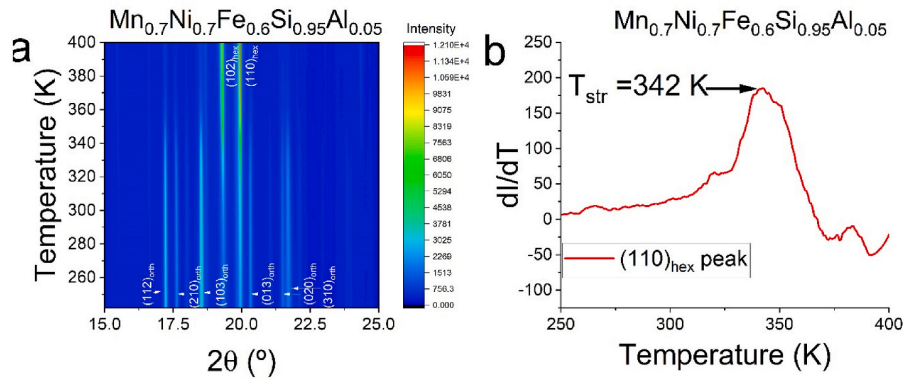


Fig. 5. a) Contour plot for the diffraction patterns as a function of temperature for $\text{Mn}_{0.7}\text{Ni}_{0.7}\text{Fe}_{0.6}\text{Si}_{0.95}\text{Al}_{0.05}$. ($\lambda = 0.69217 \text{ \AA}$) The plot displays the transition from the orth. to hex. structure occurring across the measured temperatures. b) derivative of intensity as a function of temperature for the $(110)_{\text{hex}}$ peak, indicating the transition temperature occurring in the measured composition.

The T_{str} is found to be around 342 K in Fig. 5b.

An alternative method to characterize structural transitions in a material is by capturing the latent heat associated with such transitions in a DSC device. By modification of the Fe content in $\text{Mn}_{1-x}\text{Ni}_x\text{Fe}_{2x}\text{Si}_{0.95}\text{Al}_{0.05}$, the transition temperatures between orth. and hex. structures changes from above to significantly below RT by decreasing x , see the DSC curves in Fig. 6a. Transition temperatures for orth. to hex. structure ($T_{\text{str}_{\text{orth-hex}}}$) during heating, hex. to orth. ($T_{\text{str}_{\text{hex-orth}}}$) during cooling, and thermal hysteresis values are displayed in Table 2. Values for the transformation temperatures are obtained from the maximum/minimum value of heat flow for each sample. The samples with $x = 0.28$ and 0.30 feature transitions above RT, with transitions between 373 and 419 K, and 313 and 351 K, respectively. The $x = 0.32$ and 0.35 samples feature transitions below RT, between 226–270 K and 183–217 K, respectively. Therefore, going from $x = 0.28$ to $x = 0.35$ substantially impacts T_{str} , modifying it by almost 200 K. The peaks are broad across the transitions for $x = 0.32$, 0.3 and 0.28, which is another indication of the local disorder in the system. For the $x = 0.35$ sample, a sharp transition is observed, which can be associated with a smaller disorder in the small ingot measured. Thermal hysteresis is noticeable in these measurements, which range from 46, 42, 44 and 34 K for the samples with $x = 0.28$, 0.30, 0.32 and 0.35, respectively. Such values are relatively high and can be attributed to extrinsic and intrinsic factors [40], but also due to the thermal inertia component, as calorimetry measurements are dynamic measuring processes, with high heating and cooling rates (10 K/min in the performed measurements).

Another method to extract information from scanning calorimetry experiments is by measuring the heat capacity of a sample, obtained through a “classical” three-step procedure, seen in the cooling transition of Fig. 7a for $\text{Mn}_{0.7}\text{Ni}_{0.7}\text{Fe}_{0.6}\text{Si}_{0.95}\text{Al}_{0.05}$. By doing this, it is possible to

Table 2

Transition temperatures during heating and during cooling in $\text{Mn}_{1-x}\text{Ni}_x\text{Fe}_{2x}\text{Si}_{0.95}\text{Al}_{0.05}$ obtained by DSC and by temperature dependent magnetization, and T_{hys} values for the produced samples.

Composition $\text{Mn}_{1-x}\text{Ni}_x\text{Fe}_{2x}\text{Si}_{0.95}\text{Al}_{0.05}$	Transition temperature (K)		T_{hys} (K)	Transition temperature (K)		T_{hys} (K)
			DSC	VSM	VSM	VSM
	Heating	Cooling	T_{hys}	Heating	Cooling	T_{hys}
$x = 0.28$	419	373	46	–	–	–
$x = 0.3$	351	313	38	347	324	23
$x = 0.32$	270	226	44	270	240	30
$x = 0.35$	217	183	34	219	183	36

extract the absolute entropy variation before and after the structural transition ΔS_{str} . To determine the entropy change associated to the event, two lines are drawn from the curve before and after the transition event. By drawing a line from the inflection point of the transition and connecting it to the two aforementioned curves, the associated entropy values from initial (T_i) and final (T_f) points can be subtracted, obtaining the entropy variation before and after the transition. For the $\text{Mn}_{0.7}\text{Ni}_{0.7}\text{Fe}_{0.6}\text{Si}_{0.95}\text{Al}_{0.05}$ composition, the variation of entropy is approximately 51 J/Kg.K.

3.3. Magnetic and magnetocaloric properties

Temperature-dependent magnetization curves for samples with $x = 0.30$, 0.32 and 0.35 are shown in Fig. 6b. The sample with $x = 0.28$ features a transition beyond the measuring capacity of the MPMS system, and thus it has been excluded here. To capture the transitions in the

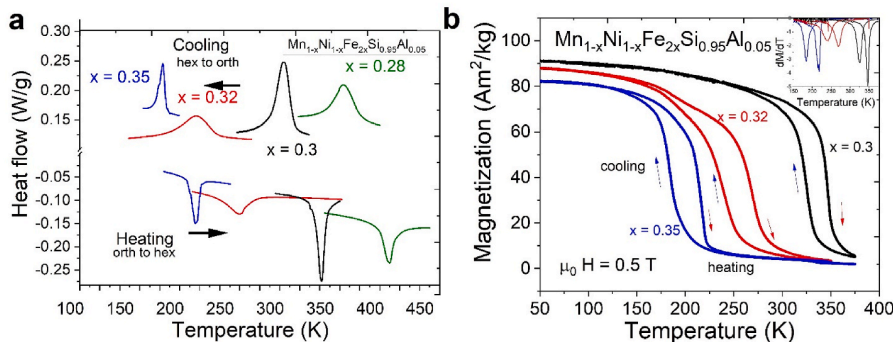


Fig. 6. The MST observed in $\text{Mn}_{1-x}\text{Ni}_x\text{Fe}_{2x}\text{Si}_{0.95}\text{Al}_{0.05}$ ($x = 0.28$, 0.30, 0.32 and 0.35) by means of a) DSC and b) temperature-dependent magnetization measurements.

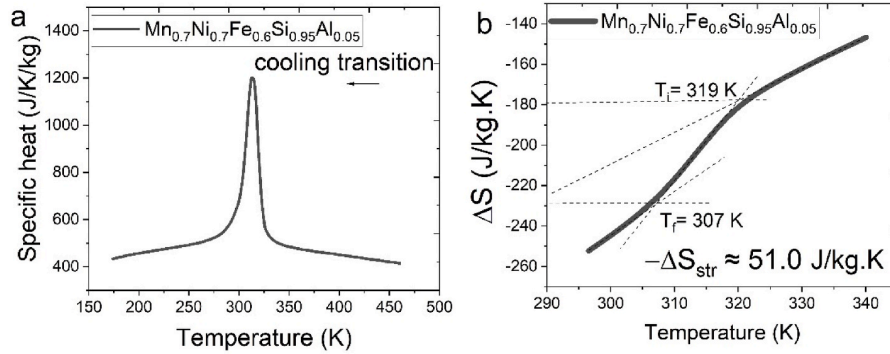


Fig. 7. a) Heat capacity obtained from DSC measurements for the cooling transition of $\text{Mn}_{0.7}\text{Ni}_{0.7}\text{Fe}_{0.6}\text{Si}_{0.95}\text{Al}_{0.05}$. b) Absolute variation in entropy for the structural transition region of the sample $\text{Mn}_{0.7}\text{Ni}_{0.7}\text{Fe}_{0.6}\text{Si}_{0.95}\text{Al}_{0.05}$, which allows for the determination of the entropy change due to the latent heat of the transition.

examined samples, applied fields of $\mu_0 H = 0.5$ T were used. With higher Fe substitution, the absolute magnetization decreases, which might seem counterintuitive. In fact, due to the interatomic distances in the lattices, the Mn atom carries a higher FM moment than Fe in the TiNiSi and the Ni_2In structures. Generally, the presence of transition metals in Mn sites impacts the magnetization by changing the average interatomic distances between Mn–Mn atoms, and through modification of the band structure. Nevertheless, Fe substitution results in the smallest decrease of magnetization [32]. The abrupt change of magnetization at temperatures close to the latent heat peaks seen in the DSC, as the samples are heated/cooled, is a clear indication of an MST. The presence of a small dip between 180 and 230 K and a wider transition in the $x = 0.32$ sample could be an indication of a higher degree of inhomogeneity, displaying more than a single magnetic phase undergoing a transition inside that temperature region. As the MnNiSi system features a wide solid solubility region when Fe is incorporated into the lattice, compositional variations can occur within the small amounts of mass present (between 10 and 30 mg) in the magnetization measurements. Nevertheless, the other samples appear to feature only one magnetic phase transition. Another interesting feature of the martensitic transformation in such compositions is the difference in transition temperature width between heating and cooling steps, indicating different mechanisms for each event. During the heating transformation, an anisotropic contraction of the cell volume is observed, inducing tensile residual stress. On the cooling transformation, the stress is released by the expansion, and by the formation of new surface area i.e., cracking of the sample.

The magnetic transition temperatures measured by magnetometry are displayed in Table 2. Temperatures obtained by VSM during cooling are 324, 240 and 183 K, and 347, 270 K and 219 K during heating, for $x = 0.3, 0.32,$ and $0.35,$ respectively. The transitions measured by magnetometry feature smaller hysteresis than those obtained by DSC measurements, with 23 and 30 K for $x = 30$ and $x = 0.32,$ respectively. This is due to the fact that the magnetic measurements were performed

with a lower heating/cooling rate of 2 K/min, instead of 10 K/min used in the DSC. Further analysis of the magnetocaloric properties requires the use of field dependent curves, which allow the determination of the isothermal entropy change. As the $x = 0.3$ sample is the one that features most of its transition close to RT, we analyse its cooling transition in detail.

3.4. Magnetocaloric effect of $\text{Mn}_{0.7}\text{Ni}_{0.7}\text{Fe}_{0.6}\text{Si}_{0.95}\text{Al}_{0.05}$

In order to avoid the presence of mixed magnetic states during the measurements [38], the sample was always heated up to temperatures far above $T_{\text{strorth-hex}}$ and cooled down to the isotherm temperature without any applied field. By this method, magnetization isotherms were obtained from 310 to 364 K with a temperature step of 2 K, and are displayed in Fig. 8a to describe the cooling transformation.

The isotherms describe FM behavior at initial temperatures, with saturation magnetization reaching up to $80 \text{ Am}^2/\text{kg}$. As the temperature increase, a higher fraction of sample becomes PM, which leads to a decrease in magnetization. As magnetic fields increase, however, magnetization rises again after a certain applied field threshold, signaling the transition from the hex. (PM) to the orth. (FM) phase. This behavior can be seen up to 344 K, when the transformation can no longer be induced by the applied fields. When comparing the behavior with other MM'X compounds such as MnCoGe or La–Fe–Si based materials, we find that much higher fields are necessary to fully transform the material [7,22]. By employing the Maxwell relation, ΔS_m is obtained and displayed in Fig. 8b. Calculated values of ΔS_m are $-8.15, -19.15$ and -26.45 J/kg.K for $\mu_0 H = 0-2, 0-5$ and $0-7$ T, respectively. The negative values are an indication of conventional magnetocaloric effect.

The metamagnetic transition (PM-to-FM) seen during isotherms, the shift of ΔS_m towards higher temperatures as higher fields are applied, and the presence of hysteresis are clear indications of a FOPT. However, ΔS_m increases linearly with applied field, as shown in Fig. 8c, which is

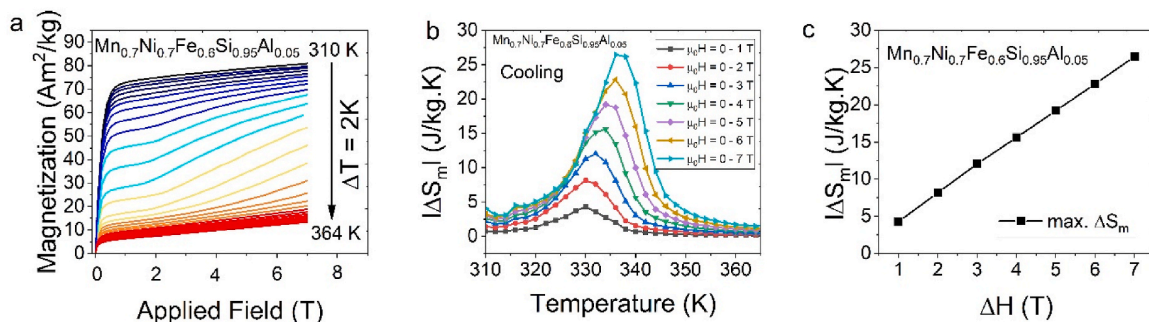


Fig. 8. Magnetic analyses for the $\text{Mn}_{0.7}\text{Ni}_{0.7}\text{Fe}_{0.6}\text{Si}_{0.95}\text{Al}_{0.05}$ sample. a) Field dependent curves across the MST, with temperature steps of 2K. b) Calculated isothermal entropy (ΔS_m) in magnetic fields up to 7 T. c) Maximum variation of ΔS_m as a function of applied field, showing a linear trend.

characteristic for materials undergoing a second order phase transition [4,41]. This occurs as the maximum applied field is apparently not high enough to fully transform the material from the PM to the FM state, as can be seen from Fig. 8a. Across the temperatures where metamagnetic transitions occur, the magnetization curve does not saturate, and only reaches a fraction of the saturation magnetization seen at lower temperatures. Therefore, as higher fields transform bigger volume fractions of the sample to the FM state, the entropy change contribution associated to the martensitic transformation is higher, thus yielding a linear correlation. Assuming that the value of $|\Delta S_m|$ is the sum of the magnetic entropy due to magnetic moment reorientation ΔS_{mag} , and the fraction of the structural transition contribution ΔS_{str} due to the magnetization, one can conclude that even with applied fields of $\mu_0 H = 0-7$ T, the total $|\Delta S_m|$ is smaller than $|\Delta S_{str}|$, an indication of a low magnetostructural coupling of the studied sample.

To further investigate this MST, an Arrott plot analysis (M^2 (H/M) curves) was performed and the result is shown in Fig. 9a. Typically, an S-shaped curve or a negative slope in such plots are a qualitative indication of FOPTs [42]. A slight negative slope can be observed at $T = 338$ K, indicating a FOPT character. Such analysis can be useful for a qualitative evaluation of the transitions. A more sensitive method that yields a quantitative analysis has been utilized by Law et al. when studying the n exponent from the field dependence of the magnetic entropy change [41,43]. The n exponent can be calculated as follows:

$$n = \frac{d \ln(\Delta S_m)}{d \ln(\Delta H)}$$

Values of n above 2 are exhibited for compounds undergoing FOPTs. From the n analysis of the $Mn_{0.7}Ni_{0.7}Fe_{0.6}Si_{0.95}Al_{0.05}$ sample (Fig. 9b), n is higher than 2 only in fields above 3 T. This is another indication of the low magnetostructural coupling of the samples to the MST. The shift of T with the ΔS peak with field is also only observed when the applied field is above 3 T (see also Fig. 8b). When comparing the ΔS_m values of $Mn_{0.7}Ni_{0.7}Fe_{0.6}Si_{0.95}Al_{0.05}$ with other reported quantities in the literature, they are similar to compositions with substitutions in the Mn (2a) sites, in (MnFe)NiSi $_{1-y}Al_y$ [32,34,44,45]; and higher than the reported compositions with a substitution on Ni (2d) sites Mn(FeNi)Si $_{1-y}Al_y$ [33]. For the $Mn_{1-x}Fe_{1-x}NiSiAl_{1-y}$ samples, very different values are reported for similar compositions with Fe substitution on Mn. ΔS_m values of 20–50 J/kg.K in $\mu_0 H = 0-5$ T, or between $\Delta S_m = -8$ to -22 J/kg.K in $\mu_0 H = 0-2$ T are reported, for variations of 10% of Fe substitution in Mn, or 3–4% substitution in Al [20,32]. A possible reason for the variation in values are different processing conditions such as arc-melting or melt-spinning, which modifies the structure/microstructure. Another possible reason for the variations reported in literature is how the magnetic measurements have been performed, as different starting materials placed in the magnetometer (i.e. ingots/coarse powders/fine powders) are known to modify the MSTs [46].

These variations on reported values of ΔS_m in $Mn_{1-x}Fe_{1-x}NiSiAl_{1-y}$ shed light on how sensitive the MST of (MnFe)Ni(SiAl) and (MnFe)(NiFe)(SiAl) compounds can be to different processing conditions that will impact ΔS_m values. Pertaining extrinsic factors, the presence of phase impurities would change the susceptibilities and magnetization of the orth. phase. In the presently studied $Mn_{1-x}Ni_{1-x}Fe_{2x}Si_{0.95}Al_{0.05}$ compositions, the secondary $Mn_{0.97}Ni_{0.97}Fe_{0.28}Si_{0.78}$ phase with a hexagonal $MgZn_2$ structure is known to display antiferromagnetic (AFM) ordering [39]. This could interfere with the internal magnetization of the main hex. phase by lowering the total magnetization of the system. Therefore, removing secondary phases can help maximizing internal magnetization. To further understand this interaction between the primary and secondary magnetic phases, micromagnetic simulations could be carried out. Regarding intrinsic properties, the degree of chemical disorder in the phases is also a factor that contributes to diminished ΔS_m values, as Mn/Fe/Ni can theoretically substitute 2a and 2d sites interchangeably [32,33], while Al could substitute 2a and 2c sites [32]. This could result in a small distribution of T_{str} 's, which in turn requires a higher applied field to induce the transformation, and thus lead to a decrease in overall ΔS_m values [47]. The broad transition captured by in-situ SR-PXD as well as by DSC measurements also hint towards a distribution of T_{str} 's as a result of chemical disorder. However, such disorder can only be probed at the local level by techniques such as total scattering or X-ray absorption spectroscopy which is outside the scope of this work.

Another concern is the known effect of Mn loss during arc melting (the most reported technique for synthesis of MM'X compounds) and to a small extent during heat treatment (as it applies only to the surface areas), making it difficult to accurately track Mn concentrations across the sample. This is very important as very small variations in Mn content have a huge impact on T_{str} , altering it by 80 K for variations of 0.03 per formula unit [24]. A better microstructural design and composition control could lead to improved magnetostructural coupling and therefore higher magnetocaloric effect under lower fields. A suggestion would be to employ different synthesis and processing techniques e.g., reactive/fast sintering methods, avoiding Mn loss issues coupled with different disorder/defect concentrations.

4. Conclusion

Ingots of critical-element free $Mn_{1-x}Ni_{1-x}Fe_{2x}Si_{0.95}Al_{0.05}$ compounds ($x = 0.28, 0.3, 0.32$ and 0.35) were synthesized by arc-melting. The increase in Fe content lowers the cell volumes slightly and shifts magnetostructural transitions from above RT in $x = 0.28$ to significantly below RT in $x = 0.35$. The samples with $x = 0.3$ and 0.32 display a transition around RT.

SR-PXD at RT shows the presence of an orth. $TiNiSi$ -type and a hex. Ni_2In -type phase, as well as a secondary hexagonal $MgZn_2$ -type phase for all samples. Rietveld analysis evidences the presence of texture in the

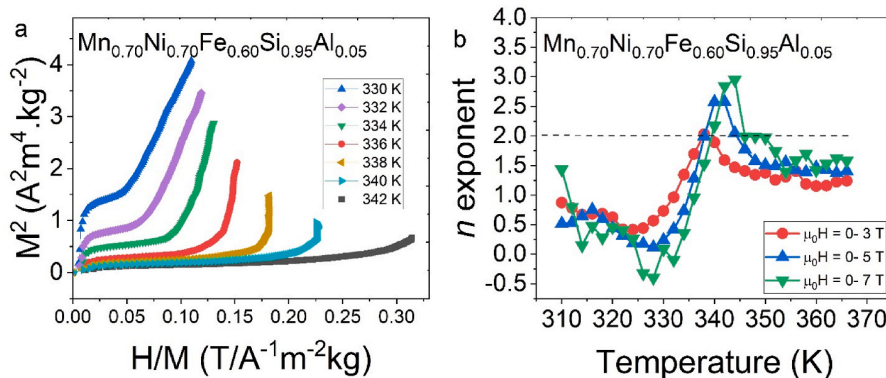


Fig. 9. Magnetic analyses for the $Mn_{0.7}Ni_{0.7}Fe_{0.6}Si_{0.95}Al_{0.05}$ sample: a) Arrott plot of the MST. b) n exponent analysis of the magnetic entropy change.

hex. Ni_2In -type main phase. In order to evaluate the presence of the secondary phase, and its relationship with the main phases, optical and electron microscopy techniques were applied for the sample with $x = 0.32$. Microscopy supports the presence of texture in the samples, which is in direct relation with formation of a solidification front during arc melting, confirming previous results from SR-PXD. The secondary $MgZn_2$ -type phase is primarily located at the grain boundaries and to a lesser extent, is also present inside the grains of the main phase. The composition of the secondary $MgZn_2$ -type phase obtained by EDS measurements is $Mn_{0.97}Ni_{0.97}Fe_{0.28}Si_{0.78}$.

The magnetostructural transitions are evaluated by in-situ SR-PXD, heat capacity and heat flow measurements by DSC, and magnetic measurements. Transformation temperatures for the orth. to hex. transition span a broad region from above to below RT and were determined as 419, 351, 270 and 217 K for $x = 0.28, 0.30, 0.32,$ and $0.35,$ respectively. Magnetic measurements show magnetic transitions at 347, 270 and 219 for $x = 0.3, 0.32$ and $0.35,$ respectively, under an applied field of $\mu_0H = 0.5$ T. Differences between the transformation temperatures obtained by DSC and magnetometry can be attributed to small compositional variations, different heating rates and the influence of the magnetic field.

The hex. to orth. transition i.e., cooling transformation is evaluated for the $Mn_{0.7}Ni_{0.7}Fe_{0.6}Si_{0.95}Al_{0.05}$ composition by field dependent isotherms, with temperature steps of 2 K, from 310 to 364 K. Entropy changes of $\Delta S_m = -8.15, -19.15$ and -26.45 J/kg.K are obtained for field changes of $\mu_0H = 0-2, 5$ and 7 T, respectively. The results are comparable to other reported (MnFe)NiSi $_{1-y}$ Al $_y$ compounds produced by arc melting and melt spinning. When comparing the results to other known MM'X systems with Fe/Al substitution, however, discrepancies are seen in the ΔS_m values, mostly due to the apparent low magnetostructural coupling of the MM'X materials seen in reported Mn $_{1-x}$ Fe $_x$ NiSi $_1$ Al $_{1-y}$ alloys and in our samples, as confirmed by n exponent analysis. Such insensitivity could be caused by a combination of intrinsic or extrinsic effects. Therefore, more research on understanding and modifying the local structure is required to obtain critical-element free MM'X systems which can be competitive with other available magnetocaloric materials.

CRedit roles

Bruno G. F. Eggert: Conceptualization (equal) Data curation (equal) Formal analysis (equal) Investigation (equal) Methodology (equal) Visualization (equal) Writing - original draft (equal) Writing - review & editing (equal) **J. F. H. Belo:** Investigation (equal) Resources (equal) Writing - review & editing (equal) **J. P. Araújo:** Resources (equal) Writing - review & editing (equal) **Bjørn Hauback:** Supervision (equal) Writing - review & editing (equal) **Christoph Frommen:** Funding acquisition (equal) Project administration (equal) Supervision (equal) Writing - review & editing (equal)

Declaration of competing interest

The authors declare that they have no known competing financial interests or personal relationships that could have appeared to influence the work reported in this paper.

Data availability

Data will be made available on request.

Acknowledgements

This work was financed by The Research Council of Norway through the NANO2021 program, Project No. 287150. J. H. Belo thanks projects financed by EEA grants, via the project FBR OC1 85 and the national funding agency for science, research and technology (FCT) for the

projects UIDB/50011/2020, PTDC/EME-TED/3099/2020, and PTDC/FISMAC/31302/2017. J. H. Belo also thanks CERN/FISTEC/0003/2019 and for his contract DL57/2016 reference SFRH-BPD-87430/2012. The authors thank the staff at the Swiss-Norwegian beamline (BM01) of the European Synchrotron Radiation Facility (ESRF) for their skillful assistance during the X-ray diffraction measurements.

References

- [1] C.L. Zhang, Y.X. Zheng, H.C. Xuan, S.C. Ma, Q.Q. Cao, D.H. Wang, Y.W. Du, Large and highly reversible magnetic field-induced strains in textured Co $_{1-x}$ Ni $_x$ MnSi alloys at room temperature, *J. Phys. D Appl. Phys.* 44 (2011), <https://doi.org/10.1088/0022-3727/44/13/135003>.
- [2] Q. Zhang, W.F. Li, N.K. Sun, J. Du, Y.B. Li, D. Li, Y.Q. Zhang, Z.D. Zhang, Large magnetoresistance over an entire region from 5 to 380 K in double helical CoMnSi compound, *J. Phys. D Appl. Phys.* 41 (2008), <https://doi.org/10.1088/0022-3727/41/12/125001>.
- [3] C. Biswas, R. Rawat, S.R. Barman, Large negative magnetoresistance in a ferromagnetic shape memory alloy: Ni $_{2+x}$ Mn $_{1-x}$ Ga, *Appl. Phys. Lett.* 86 (2005) 1–3, <https://doi.org/10.1063/1.1925757>.
- [4] A. Smith, C.R.H. Bahl, R. Bjørk, K. Engelbrecht, K.K. Nielsen, N. Pryds, Materials challenges for high performance magnetocaloric refrigeration devices, *Adv. Energy Mater.* 2 (2012) 1288–1318, <https://doi.org/10.1002/aenm.201200167>.
- [5] J.S. Kouvel, C.C. Hartelius, Anomalous magnetic moments and transformations in the ordered alloy FeRh, *J. Appl. Phys.* 33 (1962) 1343–1344, <https://doi.org/10.1063/1.1728721>.
- [6] A. Chirkova, K.P. Skokov, L. Schultz, N.V. Baranov, O. Gutfleisch, T.G. Woodcock, Giant adiabatic temperature change in FeRh alloys evidenced by direct measurements under cyclic conditions, *Acta Mater.* 106 (2016) 15–21, <https://doi.org/10.1016/j.actamat.2015.11.054>.
- [7] J. Liu, J.D. Moore, K.P. Skokov, M. Krautz, K. Löwe, A. Barcza, M. Katter, O. Gutfleisch, Exploring La(Fe,Si) $_{13}$ -based magnetic refrigerants towards application, *Scripta Mater.* 67 (2012) 584–589, <https://doi.org/10.1016/j.scriptamat.2012.05.039>.
- [8] Y. Liu, X. Fu, Q. Yu, M. Zhang, J. Liu, Significant reduction of phase-transition hysteresis for magnetocaloric (La $_{1-x}$ Ce $_x$) $_{2}$ Fe $_{11}$ Si $_{12}$ Hy alloys by microstructural manipulation, *Acta Mater.* 207 (2021), <https://doi.org/10.1016/j.actamat.2021.116687>.
- [9] V.K. Pecharsky, K. a Gschneidner, Giant magnetocaloric effect in Gd $_{5}$ Si $_2$ Ge $_2$, *Phys. Rev. Lett.* 78 (1997) 3–6, <https://doi.org/10.1103/PhysRevLett.78.4494>.
- [10] A. Planes, L. Mäosa, M. Acet, Magnetocaloric effect and its relation to shape-memory properties in ferromagnetic Heusler alloys, *J. Phys. Condens. Matter* 21 (2009), <https://doi.org/10.1088/0953-8984/21/23/233201>.
- [11] J. Liu, T. Gottschall, K.P. Skokov, J.D. Moore, O. Gutfleisch, Giant magnetocaloric effect driven by structural transitions, *Nat. Mater.* 11 (2012) 620–626, <https://doi.org/10.1038/nmat3334>.
- [12] T. Gottschall, K.P. Skokov, M. Fries, A. Taubel, I. Radulov, F. Scheibel, D. Benke, S. Riegg, O. Gutfleisch, Making a cool choice: the materials library of magnetic refrigeration, *Adv. Energy Mater.* 9 (2019), <https://doi.org/10.1002/aenm.201901322>.
- [13] H. Johra, K. Filonenko, P. Heiselberg, C. Veje, S. Dall'Olivo, K. Engelbrecht, C. Bahl, Integration of a magnetocaloric heat pump in an energy flexible residential building, *Renew. Energy* 136 (2019) 115–126, <https://doi.org/10.1016/j.renene.2018.12.102>.
- [14] R. Gauß, G. Himm, O. Gutfleisch, The resource basis of magnetic refrigeration, *J. Ind. Ecol.* 21 (2017) 1291–1300, <https://doi.org/10.1111/jiec.12488>.
- [15] T.E. Graedel, R. Barr, C. Chandler, T. Chase, J. Choi, L. Christoffersen, E. Friedlander, C. Henly, C. Jun, N.T. Nassar, D. Schechner, S. Warren, M.Y. Yang, C. Zhu, Methodology of metal criticality determination, *Environ. Sci. Technol.* 46 (2012) 1063–1070, <https://doi.org/10.1021/es203534z>.
- [16] C.J. Müller, On Evil Twins and Their Absent Friends Ternary Intermetallic Ni 2 in Type, 2015.
- [17] G.A. Landrum, R. Hoffmann, J. Evers, H. Boysen, The TiNiSi family of compounds: structure and bonding, *Inorg. Chem.* 37 (1998) 5754–5763, <https://doi.org/10.1021/ic980223e>.
- [18] F.R. Shen, F.X. Hu, Z.B. Yu, H.B. Zhou, H. Wu, Q.Z. Huang, J.Z. Hao, Y.H. Gao, K. M. Qiao, J. Li, C. Zhang, W.H. Liang, L.H. He, J. Wang, T.J. Liang, J.R. Sun, B. G. Shen, Neutron diffraction study on hydrostatic pressure regulated magnetostructural transition and magnetocaloric effect in MnNi $_{1-x}$ FeSi $_1-y$ Ge $_y$ alloys, *J. Appl. Phys.* 127 (2020), <https://doi.org/10.1063/5.0003056>.
- [19] W. Bažela, A. Szytula, J. Todorović, A. Zięba, Crystal and magnetic structure of the NiMnGe 1–nSn System, *Phys. Status Solidi* 64 (1981) 367–378, <https://doi.org/10.1002/pssa.2210640140>.
- [20] C.L. Zhang, H.F. Shi, Y.G. Nie, E.J. Ye, Z.D. Han, D.H. Wang, Thermal-cycling-dependent magnetostructural transitions in a Ge-free system Mn $_{0.5}$ Fe $_{0.5}$ Ni(Si,Al), *Appl. Phys. Lett.* 105 (2014), <https://doi.org/10.1063/1.4904464>, 0–4.
- [21] S.C. Ma, Y.X. Zheng, H.C. Xuan, L.J. Shen, Q.Q. Cao, D.H. Wang, Z.C. Zhong, Y. W. Du, Large roomtemperature magnetocaloric effect with negligible magnetic hysteresis losses in Mn $_{1-x}$ V $_x$ Co $_6$ alloys, *J. Magn. Magn Mater.* 324 (2012) 135–139, <https://doi.org/10.1016/j.jmmm.2011.07.047>.
- [22] S.K. Pal, C. Frommen, S. Kumar, B.C. Hauback, H. Fjellvåg, G. Helgesen, Enhancing giant magnetocaloric effect near room temperature by inducing magnetostructural

- coupling in Cu-doped MnCoGe, *Mater. Des.* 195 (2020), 109036, <https://doi.org/10.1016/j.matdes.2020.109036>.
- [23] A. Taubel, T. Gottschall, M. Fries, T. Faske, K.P. Skokov, O. Gutfleisch, Influence of magnetic field, chemical pressure and hydrostatic pressure on the structural and magnetocaloric properties of the Mn-Ni-Ge system, *J. Phys. D Appl. Phys.* 50 (2017), <https://doi.org/10.1088/1361-6463/aa8e89>.
- [24] E.K. Liu, W. Zhu, L. Feng, J.L. Chen, W.H. Wang, G.H. Wu, H.Y. Liu, F.B. Meng, H. Z. Luo, Y.X. Li, Vacancy-tuned paramagnetic/ferromagnetic martensitic transformation in Mn-poor Mn_{1-x}CoGe alloys, *EPL* 91 (2010), <https://doi.org/10.1209/0295-5075/91/17003>, 0–5.
- [25] S.K. Pal, C. Frommen, S. Kumar, B.C. Hauback, H. Fjellvåg, T.G. Woodcock, K. Nielsch, G. Helgesen, Comparative phase transformation and magnetocaloric effect study of Co and Mn substitution by Cu in MnCoGe compounds, *J. Alloys Compd.* 775 (2019) 22–29, <https://doi.org/10.1016/j.jallcom.2018.10.040>.
- [26] C.L. Zhang, H.F. Shi, E.J. Ye, Y.G. Nie, Z.D. Han, B. Qian, D.H. Wang, Magnetostructural transition and magnetocaloric effect in MnNiSi-Fe₂Ge system, *Appl. Phys. Lett.* 107 (2015) 2–6, <https://doi.org/10.1063/1.4936610>.
- [27] L.M. Moreno-Ramírez, Díaz-García, J.Y. Law, A.K. Giri, V. Franco, Hysteresis, latent heat and cycling effects on the magnetocaloric response of (NiMnSi)_{0.66}(Fe₂Ge)_{0.34} alloy, *Intermetallics* 131 (2021), <https://doi.org/10.1016/j.intermet.2020.107083>.
- [28] E. Palacios, R. Burriel, C.L. Zhang, Calorimetric study of the giant magnetocaloric effect in (MnNiSi)_{0.56}(FeNiGe)_{0.44}, *Phys. Rev. B* 103 (2021) 1–8, <https://doi.org/10.1103/PhysRevB.103.104402>.
- [29] C.L. Zhang, Y.G. Nie, H.F. Shi, E.J. Ye, J.Q. Zhao, Z.D. Han, H.C. Xuan, D.H. Wang, Tunable magnetostructural coupling and large magnetocaloric effect in Mn_{1-x}Ni_{1-x}Fe_{2x}Si_{1-x}Gax, *J. Magn. Magn. Mater.* 432 (2017) 527–531, <https://doi.org/10.1016/j.jmmm.2017.02.046>.
- [30] H. Imam, H.G. Zhang, J. Chen, M. Yue, Q.M. Lu, D.T. Zhang, W.Q. Liu, Powdering and SPS sintering effect on the magnetocaloric properties of MnNiSi-based compounds, *AIP Adv.* 9 (2019), <https://doi.org/10.1063/1.5070084>, 0–4.
- [31] K. Deepak, R.V. Ramanujan, Magnetocaloric properties of low-cost Fe and Sn substituted mnnisi-based alloys exhibiting a magnetostructural transition near room temperature, *IEEE Trans. Magn.* 54 (2018), <https://doi.org/10.1109/TMAG.2018.2832090>.
- [32] A. Biswas, A.K. Pathak, N.A. Zarkevich, X. Liu, Y. Mudryk, V. Balema, D. D. Johnson, V.K. Pecharsky, Designed materials with the giant magnetocaloric effect near room temperature, *Acta Mater.* 180 (2019) 341–348, <https://doi.org/10.1016/j.actamat.2019.09.023>.
- [33] B. Nuendute, W. Hanggai, H. Yibole, B. Tana, O. Tegus, F. Guillou, Drastic influence of synthesis conditions on structural, magnetic, and magnetocaloric properties of Mn(Fe,Ni)(Si,Al) compounds, *Crystals* 12 (2022), <https://doi.org/10.3390/cryst12020233>.
- [34] L. Lei, Z.G. Zheng, S. Jin, W.H. Wang, C.F. Li, J.Y. Liu, Z.G. Qiu, D.C. Zeng, The magnetostructural transition and magnetocaloric properties in Fe_{0.6}Mn_{0.4}NiSi_{1-x}Al_x alloys, *J. Appl. Phys.* 128 (2020), <https://doi.org/10.1063/5.0003261>, 0–9.
- [35] D. Chernyshov, V. Dyadkin, H. Emerich, G. Valkovskiy, C.J. McMonagle, W. van Beek, On the resolution function for powder diffraction with area detectors, *Acta Crystallogr. Sect. A Found. Adv.* 77 (2021) 497–505, <https://doi.org/10.1107/s2053273321007506>.
- [36] T. Ida, in: Effect of Preferred Orientation in Synchrotron X-ray Powder Diffraction, 2, 2013, pp. 7–11. http://www.crl.nitech.ac.jp/ar/2013/0711_accr_ar2013_review.pdf.
- [37] G.W.H. Höhne, W. Hemminger, H.-J. Flammersheim, Differential Scanning Calorimetry, Springer Berlin Heidelberg, 1996, <https://doi.org/10.1007/978-3-662-03302-9>.
- [38] L. Caron, Z.Q. Ou, T.T. Nguyen, D.T. Cam Thanh, O. Tegus, E. Brück, On the determination of the magnetic entropy change in materials with first-order transitions, *J. Magn. Magn. Mater.* 321 (2009) 3559–3566, <https://doi.org/10.1016/j.jmmm.2009.06.086>.
- [39] X. Yan, M.W. Pieper, H. Michor, G. Hilscher, M. Reissner, A. Grytsiv, P. Rogl, V. Pomjakushin, G. Giester, E. Bauer, S. Paschen, Phase relations, crystal chemistry, and physical properties of MgZn 2-type Laves phases in the Mn-Cu-Si and Mn-Ni-Si systems, *Phys. Rev. B Condens. Matter* 88 (2013) 1–13, <https://doi.org/10.1103/PhysRevB.88.174416>.
- [40] O. Gutfleisch, T. Gottschall, M. Fries, D. Benke, I. Radulov, K.P. Skokov, H. Wende, M. Gruner, M. Acet, P. Entel, M. Farle, Mastering hysteresis in magnetocaloric materials, *Philos. Trans. R. Soc. A Math. Phys. Eng. Sci.* 374 (2016), <https://doi.org/10.1098/rsta.2015.0308>.
- [41] V. Franco, J.S. Blázquez, A. Conde, Field dependence of the magnetocaloric effect in materials with a second order phase transition: a master curve for the magnetic entropy change, *Appl. Phys. Lett.* 89 (2006) 1–4, <https://doi.org/10.1063/1.2399361>.
- [42] B.K. Banerjee, On a generalised approach to first and second order magnetic transitions, *Phys. Lett.* 12 (1964) 16–17, [https://doi.org/10.1016/0031-9163\(64\)91158-8](https://doi.org/10.1016/0031-9163(64)91158-8).
- [43] J.Y. Law, V. Franco, L.M. Moreno-Ramírez, A. Conde, D.Y. Karpenkov, I. Radulov, K.P. Skokov, O. Gutfleisch, A quantitative criterion for determining the order of magnetic phase transitions using the magnetocaloric effect, *Nat. Commun.* 9 (2018), <https://doi.org/10.1038/s41467-018-05111-w>.
- [44] M.L. Arreguin-Hernández, C.F. Sánchez-Valdés, J.L. Sánchez Llamazares, Magnetostructural transition and magnetocaloric effect in thermally annealed Mn_{0.5}Fe_{0.5}NiSi_{0.945}Al_{0.055} melt-spun ribbons, *J. Magn. Magn. Mater.* 533 (2021), <https://doi.org/10.1016/j.jmmm.2021.168021>.
- [45] S. Ghosh, P. Sen, K. Mandal, Magnetostructural transition and large magnetocaloric effect in (Mn_{0.6}Fe_{0.4})NiSi_{1-x}Al_x (x = 0.06–0.08) alloys, *J. Magn. Magn. Mater.* 500 (2020) 23–26, <https://doi.org/10.1016/j.jmmm.2019.166345>.
- [46] T. Gottschall, D. Benke, M. Fries, A. Taubel, I.A. Radulov, K.P. Skokov, O. Gutfleisch, A matter of size and stress: understanding the first-order transition in materials for solid-state refrigeration, *Adv. Funct. Mater.* 27 (2017) 1–6, <https://doi.org/10.1002/adfm.201606735>.
- [47] J.S. Amaral, V.S. Amaral, Disorder effects in giant magnetocaloric materials, *Phys. Status Solidi Appl. Mater. Sci.* 211 (2014) 971–974, <https://doi.org/10.1002/pssa.201300749>.

Paper IV

Structure and magnetism of Fe-substituted $\text{MnNiSi}_{0.95}\text{Al}_{0.05}$ compounds

Paper V

**Study of the magnetostructural
transition in critical-element free**



Study of the magnetostructural transition in critical-element free $\text{Mn}_{1-x}\text{Ni}_{1-x}\text{Fe}_{2x}\text{Si}_{0.95}\text{Al}_{0.05}$

Cite as: AIP Advances 13, 025215 (2023); doi: 10.1063/9.0000511

Submitted: 3 October 2022 • Accepted: 25 November 2022 •

Published Online: 3 February 2023









View Online



Export Citation



CrossMark

Bruno G. F. Eggert,¹  Kun Wang,²  Sina Jafarzadeh,²  Christian R. Bahl,²  Bjørn C. Hauback,¹  and Christoph Frommen^{1,a)} 

AFFILIATIONS

¹Department for Hydrogen Technology, Institute for Energy Technology (IFE), P.O. Box 40, NO-2027 Kjeller, Norway

²Department of Energy Conversion and Storage, Technical University of Denmark (DTU), Anker Engeldunds Vej B301, DK-2800 Kgs. Lyngby, Denmark

Note: This paper was presented at the 67th Annual Conference on Magnetism and Magnetic Materials.

^{a)}Author to whom correspondence should be addressed: Christoph.frommen@ife.no

ABSTRACT

Two different heat treatments have been carried out on similar $\text{Mn}_{1-x}\text{Ni}_{1-x}\text{Fe}_{2x}\text{Si}_{0.95}\text{Al}_{0.05}$ compositions with magnetostructural transitions between hexagonal and orthorhombic crystal structures around room temperature. The samples were analyzed concerning their structural, microstructural, magnetic, and caloric properties. The results show that the introduction of a high-temperature step, before the heat treatment (1073 K/7 days) usually used in the literature for such compounds modifies the microstructure, leading to sharper transitions with shorter transition widths, and stronger latent heat peaks. Magnetic field-assisted calorimetry and vibrating sample magnetometry provide methods to assess the effect of magnetic field on the broad transitions for the sample with $x = 0.32$ and the sharp transitions seen in the sample with $x = 0.31$.

© 2023 Author(s). All article content, except where otherwise noted, is licensed under a Creative Commons Attribution (CC BY) license (<http://creativecommons.org/licenses/by/4.0/>). <https://doi.org/10.1063/9.0000511>

INTRODUCTION

To fully realize solid-state cooling by magnetic refrigeration, further understanding of the impact of microstructure on the magnetocaloric effect is required. Modification of the microstructure can influence transition kinetics, leading to stronger, more efficient transformations, while lowering hysteresis.¹ Besides microstructure, new compositions that modify the intrinsic aspects of transitions and allow for higher reversibility also need to be explored.

In this context, the $\text{MM}'\text{X}$ compounds (where M and M' are transition metals and X is a p-block element) are promising candidates for use with room temperature (RT) magnetic heat conversion technologies.^{2–5} This is due to their versatile martensitic (diffusionless) transitions between a ferromagnetic martensite orthorhombic (TiNiSi structure-type, space group: $Pnma$) crystal structure and a paramagnetic austenite with a hexagonal structure (Ni_2In structure-type, space group: $P6_3/mmc$). This can lead to a strong isothermal entropy change (ΔS_m) and reasonable adiabatic temperature change (ΔT_{ad}). Such magnetostructural transitions (MSTs) are only possible

by substituting one or more elements from the parent $\text{MM}'\text{X}$ compound, which in turn modifies the structural transition temperature (T_{str}) and Curie Temperature (T_C) of both structures, making them coincide.

Recently, modifications of the (2a) Mn site by Fe and (2c) Si site by Al (when referring to the hexagonal crystal structure) successfully induced T_{str} towards RT.^{2,4,6} Similarly, (2d) Ni site substitution by Fe has also been discussed.⁷ In previous reports, $\text{MM}'\text{X}$ materials have been produced by arc melting succeeded by thermal treatment at temperatures around 1073 K (800 °C) for an extended period of time (4–7 days), followed by quenching to RT.^{2,4,8,9} However, little attention has been given to alternative heat treatment procedures for this kind of materials.

In this article, we report on the properties of two $\text{Mn}_{1-x}\text{Ni}_{1-x}\text{Fe}_{2x}\text{Si}_{0.95}\text{Al}_{0.05}$ compounds synthesized by arc melting which are heat treated by two different methods: with a single 1073 K step for 168 hours (sample A), and a 1073 K step for 168 hours preceded by a high temperature step at 1323 K for 5 hours (sample B), being quenched in water afterwards. Further

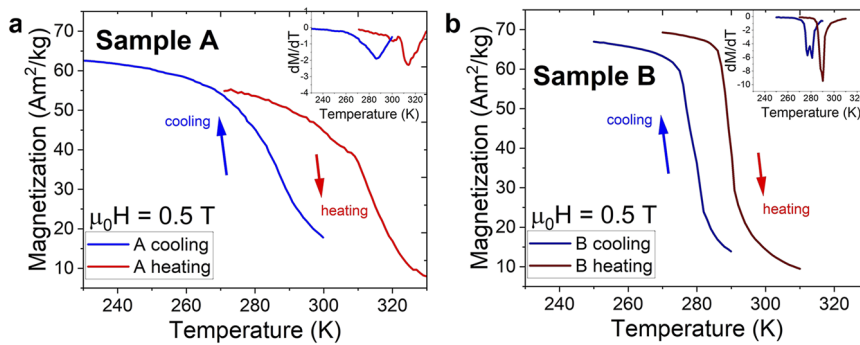


FIG. 1. Temperature-dependent magnetization for sample A and B evidencing the change in the magnetic transition due to the two different heat treatment procedures.

description of experimental and characterization methods is given in the supplementary information.

RESULTS

The magnetic transitions with an applied field of 0.5 T are presented in the temperature-dependent curves in Fig. 1. They are characterized by a decrease (or increase) of the magnetization during heating (or cooling) of the ingots. Transition values obtained from VSM are summarized in Table S1 in the [supplementary material](#). The T_{str} value is determined from the derivative of the magnetization. The transitions in sample A (Fig. 1(a)) are broad and occur at 314 and 286 K during heating and cooling, respectively. The magnetization values during heating are changing from 55 to 8 Am²/kg ($\Delta M = 47$ Am²/kg) in a temperature range of 57 K, from 272 to 329 K. The hysteresis values are also very high, reaching up to 27 K between the two transformations. In sample B, the transitions occur

at 290 and 278 K during heating and cooling respectively, and are sharper, as indicated by the higher derivative of magnetization with temperature, seen in the inset of Fig. 1(b). The hysteresis values for sample B are also smaller than for sample A, reaching up to 11.3 K. An interesting feature of the cooling curve is the presence of two derivatives, indicating two different values for T_{str} . During the heating procedure, the magnetization in sample B changes from 66 to 17 Am²/kg ($\Delta M = 49$ Am²/kg) in a temperature interval of 15 K, between 282 and 297 K. Therefore, the shifts in magnetization occur within smaller temperature spans in sample B, compared to sample A. To understand the difference between the transitions for the two samples, Powder X-ray Diffraction was carried out at RT, and is referred to in the [supplementary material](#). The results indicate very similar phase contents between sample A and B. The way that such phases are distributed along the microstructure could shed light on its magnetic behavior. Therefore, optical microscopy and SEM measurements were performed.

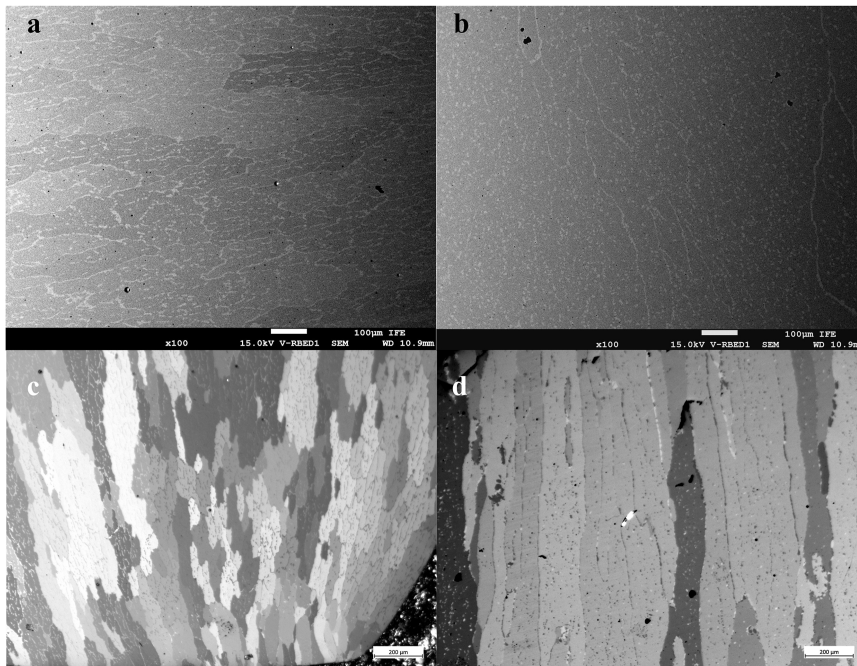


FIG. 2. Back-scattered SEM micrographs for (a) sample A and (b) sample B with 100 times magnification. Polarized optical microscopy images in (c) sample A and (d) sample B with 31.5 x magnification.

TABLE I. Chemical composition of $Mn_{1-x}Ni_{1-x}Fe_{2x}Si_{0.95}Al_{0.05}$ with $x = 0.32$ (sample A) and 0.31 (sample B) as measured by EDS.

Sample	Nominal composition of the alloy (formula units)	Area comp. (formula units)	Main phase composition (formula units)	Sample	Nominal composition of the alloy (formula units)	Area comp. (formula units)	Main phase composition (formula units)
A				B			
Mn(1 - x)	0.68	0.69 ± 0.01	0.67 ± 0.01	Mn(1 - x)	0.69	0.72 ± 0.01	0.69 ± 0.01
Ni(1 - x)	0.68	0.69 ± 0.01	0.66 ± 0.01	Ni(1 - x)	0.69	0.68 ± 0.01	0.64 ± 0.01
Fe(2x)	0.64 (x = 0.32)	0.64 ± 0.01	0.68 ± 0.01	Fe(2x)	0.62 (x = 0.31)	0.61 ± 0.01	0.66 ± 0.01
Si(0.95)	0.95	0.93 ± 0.01	0.94 ± 0.01	Si(0.95)	0.95	0.94 ± 0.01	0.95 ± 0.01
Al(0.05)	0.05	0.05 ± 0.01	0.05 ± 0.01	Al(0.05)	0.05	0.05 ± 0.01	0.06 ± 0.01

Back-scattered SEM micrographs for samples A and B are shown in Fig. 2. The ingots were prepared to display the solidification front of the alloys, i.e., the cross-section parallel to the arc direction during the arc melting process. For sample A (Fig. 2(a)) two phases can be seen from the contrast in the images, which correspond to the $Ni_2In/TiNiSi$ (dark areas, the main phase) and $MgZn_2$ hexagonal (clear areas) phases, respectively. Additionally, the secondary $MgZn_2$ hexagonal phase can be seen inside the grains in different morphologies: as lines in sample A, and as lines and rounded precipitates in sample B (seen in Fig 2(b)).

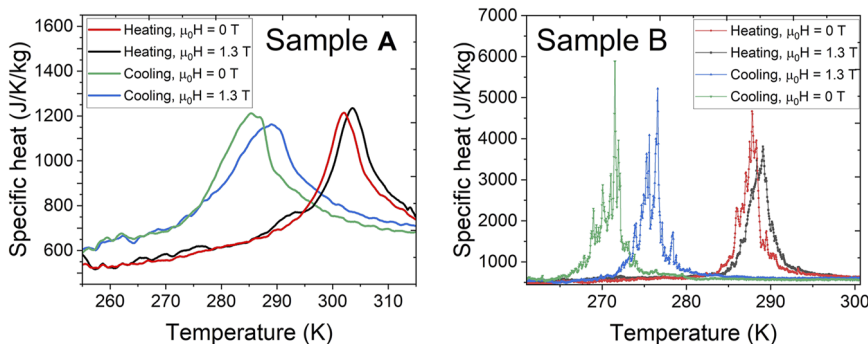
The average composition for sample A and B as determined by area EDS measurements is similar to the nominal composition (see Table I). Regarding the area composition of the main phase (Ni_2In hexagonal/ $TiNiSi$ orthorhombic structure-type), the results display some differences from nominal compositions regarding the Ni content, which is slightly smaller than the nominal alloy composition. This can be correlated to the effect of different heat treatments, which might induce different phase fractions. The composition of the hexagonal Ni_2In phase is correlated to T_{str} , where higher modifications of the parent compound (Fe and Al modification) bring T_{str} to lower values. Between Fe and Al, Al has a stronger influence on the modification of T_{str} , which could explain the slightly lower T_{str} observed in sample B.

Due to the large grain sizes, the effect of the two different heat treatments can be better understood under lower magnifications in polarized light microscopy, see Figs. 2(c) and 2(d). The microstructure yielding from the regular heat treatment process is shown in Fig. 2(c), with columnar long grains yielding from the arc melting process. Different grey hues seen in the image represent different

orientations in the grains, making it possible to estimate the grain sizes. The grain sizes feature great dispersion, ranging in length from tens of microns to several hundred microns.

The additional high-temperature step for sample B modifies the microstructure, as seen in Fig. 2(d). The grains have smaller variations in their crystallographic orientations, which leads to a smaller grey hue variation. Furthermore, the grains are larger compared to sample A, but with smaller size dispersion. Therefore, the higher temperature step of 5 hours at 1323 K creates substantial grain growth before the 168 hour (1 week) step. With bigger grains, a smaller amount of grain boundary areas is present in sample B compared to sample A. To further the understanding of the differences between the two samples, the transitions were analyzed with in-field DSC experiments.

Two ingots were selected, with masses of 6.41 and 4.41 mg for sample A and B, respectively. These small masses were chosen in order to minimize the risk of sample movement due to the applied field. A comparison of the transitions observed in both samples with a heating rate of 1 K/min is shown in Fig. 3, for applied fields of 0 and 1.3 T. The T_{str} and the hysteresis values for both samples are displayed in Table S1. It is possible to observe larger transition widths during cooling transformations than on heating for both samples. A broad transition spanning between 25–30 K is observed for sample A, with the cooling transformation temperature ($T_{str_{h-o}}$) occurring at 287.8 K. The heating transformation temperature ($T_{str_{o-h}}$) occurs at 302.0 K. Sample B features a sharper transition, with a width of 7–10 K occurring at $T_{str_{h-o}}$ of 271.5 upon cooling and $T_{str_{o-h}}$ of 287.8 K during heating. The absolute latent heat peak associated with the transitions in sample A is between

**FIG. 3.** Specific heat curves for sample A and B obtained from in-field DSC with applied fields of $\mu_0H = 0$ and 1.3 T.

600–700 J/K⁻¹kg⁻¹, compared to 4000–5000 J/K.kg in sample B, which is a remarkable difference. Both samples appear to display a large thermal hysteresis of around 16 K between heating and cooling transformations.

A shift of peak positions to higher temperatures as the magnetic field is increased occurs for both transitions, with smaller shifts occurring during the heating transformation than compared to the cooling, for both samples. In both samples, the shift of $T_{\text{str}_{\text{o-h}}}$ is around 1 K/T, whereas $T_{\text{str}_{\text{h-o}}}$ is 2.9 and 3.9 K/T for samples A and B, respectively. This leads to smaller hysteresis values with higher applied fields.

DISCUSSION

The transformations during cooling and heating need to be analyzed separately. During heating transformation (ortho-to-hex), an anisotropic contraction occurs, with the compression along the *a* direction and an expansion in the *c* direction (based on the hexagonal unit cell).¹⁰ This leads to an overall compression of the lattice, which induces a residual tensile stress. This residual stress impacts the material in addition to the expansion of the lattice during the hexagonal to orthorhombic (cooling) transformation, creating new surface area (cracking) to accommodate for the stresses in the brittle material. After several cycles, this will lower the cohesion between the particles, eventually pulverizing them, lowering the reversibility. However, some recent studies show promising results employing ductile metal composites that can keep cohesion of the particles and accommodate for the transformation stresses appropriately.¹¹

Regarding the larger width of cooling transformations compared to heating, the release of residual tensile stress during the cooling transformation could contribute to lower the nucleation threshold of the orthorhombic phase, thus acting differently on the transitions during cooling than during heating. With a lower nucleation threshold for the martensitic phase, each grain would transition more easily, thereby spreading the transformation during cooling.

The sharp peaks in the specific heat curves for sample B (Fig. 3 and S3) can be associated to more homogeneous (lower) dispersion of the elements in the lattice (at the local level, not easily detectable by regular EDS techniques), since Mn, Ni and Fe can interchangeably occupy *2a* and *2d* sites in the *Ni₂In* crystal structure. This would lower the dispersion of the T_{str} values. A second reason is the increase of average grain sizes and decrease of its dispersion, which could modify the growth of new orth./hex. phases. As the mechanism of the growth of martensitic phase fronts is only deterred by interphase and grain boundaries, it would lead to a smaller volume of inhibiting agents during the transformation of sample B (with decreased volume of grain boundary areas) compared to sample A, and therefore easily transforming bigger volumes at once.

A more homogeneous structure and bigger grain sizes results in higher latent heat spikes (up to 5000 J/K⁻¹kg⁻¹), higher magnetization derivatives, and sharper transitions widths (7–10 K) for sample B. In comparison, the transitions measured by DSC for sample A span between 20–25 K, with a much smaller latent heat peak. While the transition appears broader, it is of first order, as a large thermal hysteresis is observed. A supporting evidence for the effect of grain size on the transition width is that in other MM'X system, (Mn,Fe)Ni(SiAl), melt-spun ribbons with small grain size in range of

10 microns feature much wider transition width, and subsequently, lower ΔS_{m} than arc-melted/bulk (Mn,Fe)Ni(Si,Al) samples undergoing long heat-treatment steps with large grain sizes.^{8,9} Another method to compare both samples could be by analyzing the structural transition by temperature-dependent PXD. As the sample is typically grinded to submicrometric particles, they are not susceptible to the influence of different grain sizes, allowing each particle to transition on its own. If a sample features better homogeneity, all particles will transition within a smaller transition width.

CONCLUSION

The MST of $\text{Mn}_{1-x}\text{Ni}_{1-x}\text{Fe}_{2x}\text{Si}_{0.95}\text{Al}_{0.05}$ alloys was studied as a function of two different heat treatment procedures. The conventional heat treatment plateau at 1073 K (sample A) has been compared to a heat treatment where a high temperature step (1323 K) is introduced right before the regular heat treatment plateau, also at 1073 K (sample B). Temperature-dependent magnetization results reveal that sample A features a broad magnetization change across RT, with transitions occurring between 314 to 286 K, for heating and cooling transformations, while sample B features a sharper magnetization variation, occurring at 290 and 280 K for heating and cooling, respectively.

Despite similar phase presences, average structures and compositions as measured by PXD and SEM/EDS, much larger grains are observed for sample B than for sample A. The results indicate that the high temperature step induced better homogeneity and increased grain sizes, which would induce higher volume fractions to transform at once, leading to increased latent heat spikes. Nevertheless, a more detailed study on the isothermal entropy changes of heating and cooling transitions is required to obtain a full picture of the effect of heat treatment on the properties of $\text{Mn}_{1-x}\text{Ni}_{1-x}\text{Fe}_{2x}\text{Si}_{0.95}\text{Al}_{0.05}$ compounds.

SUPPLEMENTARY MATERIAL

See [supplementary material](#) for the description of experimental methods and further data analysis.

ACKNOWLEDGMENTS

This work was financed by The Research Council of Norway through the NANO2021 program, Project No. 287150.

AUTHOR DECLARATIONS

Conflict of Interest

The authors have no conflicts to disclose.

Author Contributions

Bruno G. F. Eggert: Conceptualization (equal); Data curation (equal); Formal analysis (equal); Investigation (equal); Methodology (equal); Visualization (equal); Writing – original draft (equal); Writing – review & editing (equal). **Kun Wang:** Investigation (equal); Resources (equal); Writing – review & editing (equal). **Sina Jafarzadeh:** Investigation (equal); Resources (equal). **Christian R. Bahl:** Investigation (equal); Resources (equal); Writing – review &

editing (equal). **Bjørn C. Hauback**: Supervision (equal); Writing – review & editing (equal). **Christoph Frommen**: Funding acquisition (equal); Project administration (equal); Supervision (equal); Writing – review & editing (equal).

DATA AVAILABILITY

The data that support the findings of this study are available from the corresponding author upon reasonable request.

REFERENCES

- ¹O. Gutfleisch, T. Gottschall, M. Fries, D. Benke, I. Radulov, K. P. Skokov, H. Wende, M. Gruner, M. Acet, P. Entel, and M. Farle, *Philos. Trans. R. Soc. A Math. Phys. Eng. Sci.* **374**, 6607 (2016).
- ²A. Biswas, N. A. Zarkevich, Y. Mudryk, A. K. Pathak, A. V. Smirnov, V. P. Balema, D. D. Johnson, and V. K. Pecharsky, *J. Appl. Phys.* **129**, 193901 (2021).
- ³S. K. Pal, C. Frommen, S. Kumar, B. C. Hauback, H. Fjellvåg, and G. Helgesen, *Mater. Des.* **195**, 109036 (2020).
- ⁴C. L. Zhang, H. F. Shi, Y. G. Nie, E. J. Ye, Z. D. Han, and D. H. Wang, *Appl. Phys. Lett.* **105**, 242403 (2014).
- ⁵L. M. Moreno-Ramírez, Á. Díaz-García, J. Y. Law, A. K. Giri, and V. Franco, *Intermetallics* **131**, 107083 (2021).
- ⁶M. L. Arreguín-Hernández, C. F. Sánchez-Valdés, and J. L. Sánchez Llamazares, *J. Magn. Magn. Mater.* **533**, 168021 (2021).
- ⁷B. Nuendute, W. Hanggai, H. Yibole, B. Tana, O. Tegus, and F. Guillou, *Crystals* **12**, 233 (2022).
- ⁸C. L. Zhang, Y. G. Nie, H. F. Shi, E. J. Ye, J. Q. Zhao, Z. D. Han, H. C. Xuan, and D. H. Wang, *J. Magn. Magn. Mater.* **432**, 527 (2017).
- ⁹A. Biswas, A. K. Pathak, N. A. Zarkevich, X. Liu, Y. Mudryk, V. Balema, D. D. Johnson, and V. K. Pecharsky, *Acta Mater.* **180**, 341 (2019).
- ¹⁰T. Zhang, Y. Gong, B. Wang, D. Cen, and F. Xu, *J. Mater. Sci. Technol.* **104**, 59 (2022).
- ¹¹H. Zhou, K. Tao, B. Chen, H. Chen, K. Qiao, Z. Yu, J. Cong, R. Huang, S. V. Taskaev, and H. Zhang, *Acta Mater.* **229**, 117830 (2022).

Appendix B: Supplementary material for “Study Of The Magnetostructural Transition In Critical-Element Free $Mn_{1-x}Ni_xFe_{2x}Si_{0.95}Al_{0.05}$ ”

MATERIALS AND METHODS

MnNiSi-based intermetallics were synthesized with ingots of Mn, Ni, Fe, Si, and Al in a Ti-gettered arc melting furnace, with nominal compositions of $Mn_{1-x}Ni_xFe_{2x}Si_{0.95}Al_{0.05}$, where $x = 0.31$ and 0.32 . An excess of 5 wt. % of Mn was added to account for evaporation. The mass losses after arc melting were smaller than 1 wt. %. Ingots were later sealed in quartz tubes under vacuum and heat treated according to the two different routes described in Fig. S1: In sample A, the ingot was kept at 1073 K for 7 days and quenched in water. In sample B, the sample was heat treated at 1323 K for 5 hours, and then kept at 1073 K for 7 days (168 hours), followed by quenching. We selected two samples with T_{str} around RT, with slightly different nominal compositions, namely $Mn_{0.68}Ni_{0.68}Fe_{0.64}Si_{0.95}Al_{0.05}$, (sample A), and $Mn_{0.69}Ni_{0.69}Fe_{0.62}Si_{0.95}Al_{0.05}$, (sample B). The effects of the two different heat treatments were studied by diffraction, microstructure, caloric and magnetic measurements.

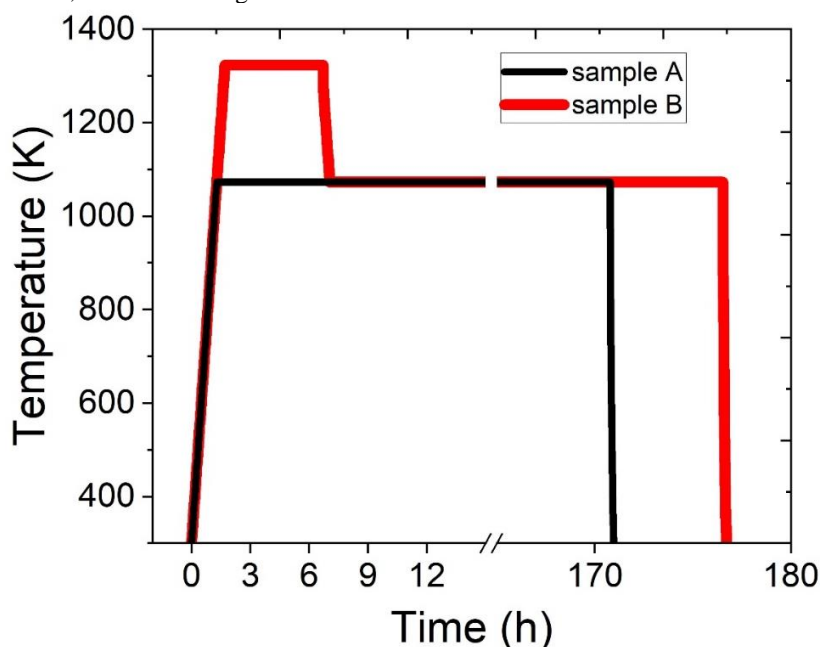


Figure S1. Description of heat treatment performed on sample A and B.

Powder X-ray Diffraction (PXD) was carried out with a Bruker D2 diffractometer with Cu-K α radiation ($\lambda = 1.5405 \text{ \AA}$) in Bragg-Brentano geometry. Rietveld refinements were performed in Topas Academic v6. Light Microscopy images were taken from a Zeiss Axioskop, while Scanning Electron Microscopy (SEM) and X-ray Energy Dispersive Spectroscopy (EDS) were performed by a JEOL JSM-7900F instrument. Specific heat of the transitions as a function of magnetic field was examined using a home-built Difference Scanning Calorimetry (DSC) device with Peltier cells, being described elsewhere ¹. During the measurements, external magnetic fields from 0 to 1.3 T were used. Temperature-dependent magnetization curves were obtained from a Vibrating Sample Magnetometer (VSM) from LakeShore across the T_{str} , with an applied field of $\mu_0H = 0.5 \text{ T}$.

TRANSITION TEMPERATURES OBTAINED FROM DSC AND VSM

TABLE S1. T_{str} during heating and cooling transitions for samples A and B as obtained by in-field DSC and VSM.

	VSM 0.5 T	DSC 0 T	DSC 1.3 T	T_{str} shift (K/T)
Sample A $T_{\text{str}_{\text{o-h}}}$	314.0	302.0	303.6	1.2
Sample A $T_{\text{str}_{\text{h-o}}}$	286.0	285.3	288.3	2.4
Sample A hysteresis	27.0	16.7	15.3	-
Sample B $T_{\text{str}_{\text{o-h}}}$	290.2	287.8	289.1	1.0
Sample B $T_{\text{str}_{\text{h-o}}}$	278.9	271.5	276.6	3.9
Sample B hysteresis	11.3	16.3	12.5	-

STRUCTURAL RESULTS

PXD in Fig. S2 shows a majority phase with the hexagonal Ni_2In structure-type, a minority phase with the orthorhombic $TiNiSi$ structure-type, and a minority of Laves-type phase with the $MgZn_2$ structure-type. Lattice parameters for the two main phases are presented in Table S2. This shows that both samples are very similar at RT with respect to average crystal structure and ratio between the three structures, as also indicated in the figure.

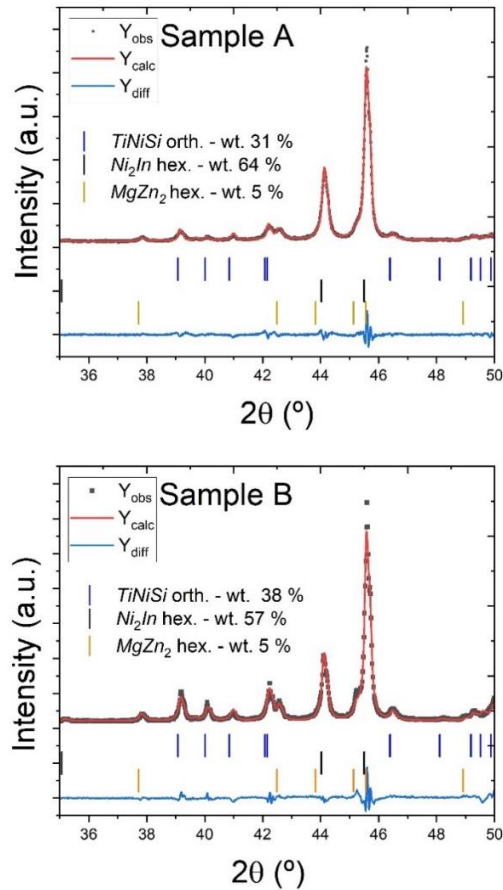


Figure S2. PXD from Cu $K\alpha$ ($\lambda = 1.5405 \text{ \AA}$) patterns of samples A and B, respectively, showing the majority of the Ni_2In structure-type hexagonal phase on both measurements. The bars below the intensities refer to the Bragg peaks for the orthorhombic, hexagonal and minority phases, respectively.

TABLE S2. Rietveld refinement results from samples A and B at room temperature, displaying the main lattice parameters on the two main phases.

Composition	Sample	a_{ortho} (Å)	b_{ortho} (Å)	c_{ortho} (Å)	a_{hex} (Å)	c_{hex} (Å)	wRp (%)
$Mn_{0.68}Ni_{0.68}Fe_{0.64}Si_{0.95}Al_{0.05}$	A	5.736(7)	3.667(4)	6.953(9)	3.992(4)	5.124(6)	7.14
$Mn_{0.69}Ni_{0.69}Fe_{0.62}Si_{0.95}Al_{0.05}$	B	5.731(4)	3.660(2)	6.959(6)	3.992(1)	5.127(2)	7.34

ADDITIONAL CALORIC RESULTS

Transitions on cooling are captured in detail with different applied fields, ranging from 0 to 1.3 T, and are shown in Fig. S3. For both samples, the peaks appear to shift gradually to higher temperatures as the ferromagnetic state is stabilized by the application of the magnetic field. In sample A, this gradual shift is not easily discernible throughout the different applied fields, therefore a line is drawn, indicating $T_{str_{h-o}}$ with $\mu_0H = 0$ T. For sample B, the transitions are seen as a group of peaks that shifts towards higher temperatures for different fields. Each field thus exhibits a seemingly different group of peaks during the transition, with absolute latent heat values changing from one field to the other. This occurs as different compositions across the ingot respond differently to the applied fields. This behavior is similar to what has been shown by Erbesdobler et al. in La-Fe-Si samples². However, one of the peaks can be followed across all cooling transitions, and it can be used to determine the shift of $T_{str_{h-o}}$ with different applied fields on sample B. Thus, one can determine the shift of the transition temperatures as a function of magnetic field. **Figure S3.** Specific heat curves during cooling with in-field DSC for samples A and B with $\mu_0H = 0, 0.3, 0.8, 1.05$ and 1.3 T.

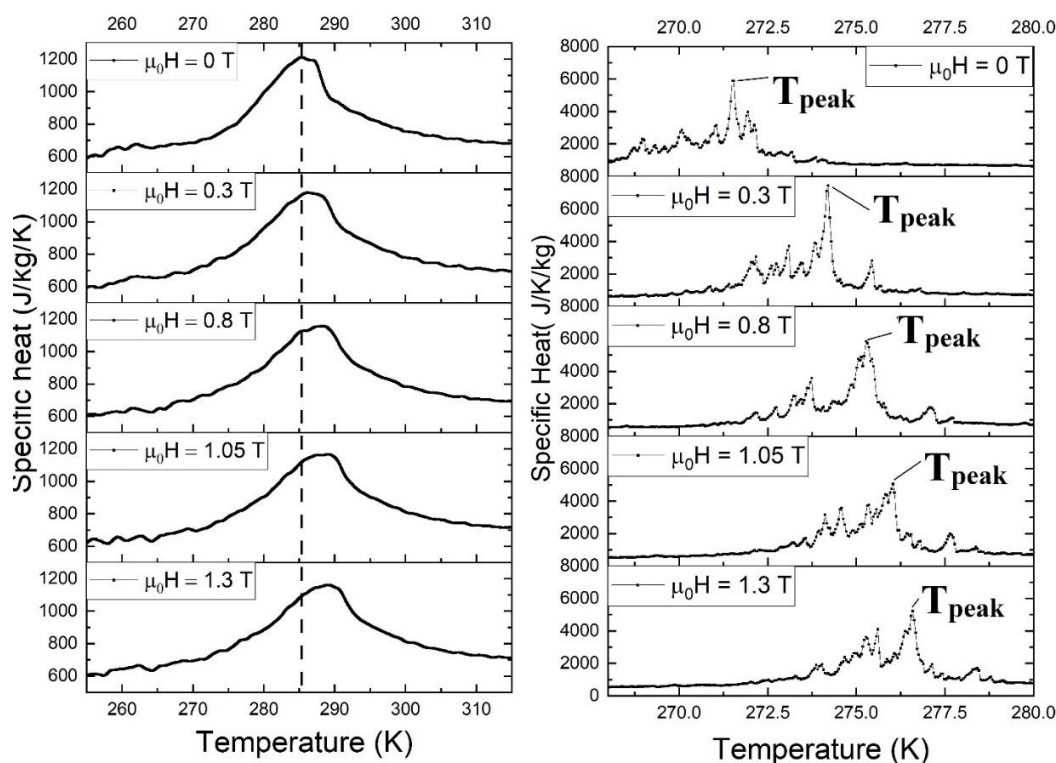


Fig. S4 displays the shift in $T_{str_{h-o}}$ as a function of applied field. For sample A, the variation of peak positions reaches up to 3.0 K from 285.3 to 288.3 K from 0 to 1.3 T in a linear trend. For sample B, the shifts also occur

linearly with respect to applied field, but with higher jumps, reaching up to 5.1 K with 1.3 T applied field from 271.5 to 276.6 K.

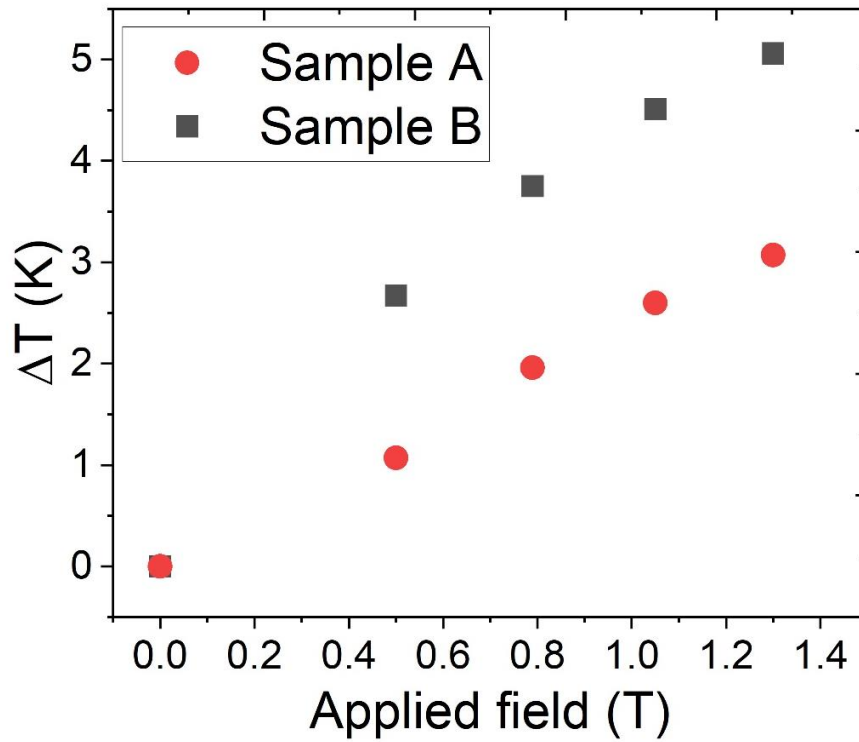


Figure S4. Temperature shift of T_{str} for applied fields $\mu_0H = 0 - 1.3$ T from the in-field DSC during cooling for samples A and B.

REFERENCES

- ¹ K.K. Nielsen, H.N. Bez, L. Von Moos, R. Bjørk, D. Eriksen, and C.R.H. Bahl, *Rev. Sci. Instrum.* **86**, (2015).
- ² F. Erbesdobler, C.R.H. Bahl, R. Bjørk, and K.K. Nielsen, *J. Appl. Phys.* **127**, (2020).

